

# Immune cell-mediated drug delivery for the treatment of inflammatory diseases

Junyi Che

Imperial College London  
Department of Materials

Submitted in accordance with the requirements for the degree of  
Doctor of Philosophy

August 2020



## Declaration of Originality

I declare that the original scientific content in this thesis is my own, unless otherwise stated or referenced within. Experimental work or data analysis done in collaboration with, or with the assistance of others is appropriately acknowledged within the text and relevant figure captions. The work presented in this thesis was performed at Imperial College London and Massachusetts Institute of Technology.

## Copyright Declaration

The copyright of this thesis rests with the author and is made available under a Creative Commons Attribution Non-Commercial No Derivatives license. Researchers are free to copy, distribute or transmit the thesis on the condition that they attribute it, that they do not use it for commercial purposes and that they do not alter, transform or build upon it. For any reuse or redistribution, researchers must make clear to others the license terms of this work.

# Acknowledgements

I would like to express all my gratitude to my PhD advisor, Professor Molly Stevens, for all her support and guidance during the last three years. Thank you for building such an amazing group that is international, collaborative and friendly, which really inspired and helped me during my Ph.D. journey. Thank you for giving me freedom to pursue my ideas, which let me grow up independently. I have also learned a great deal from her enthusiasm and professionalism for science.

I have been very lucky to work with many talented researchers. First, I would like to sincerely thank Dr. Adrian Najer, who has helped me unconditionally throughout my Ph.D. life. He is an extremely critical mentor that made every step of my research solid; he is also the researcher I always want to become in the future. His contributions to my Ph.D. with all his time, assistance and advice are too numerous to recount. Dr. Susanne Sattler has been a great supervisor for all my *in vivo* studies and gave me precious help and suggestions on experiment design and data analysis. Dr. Tim Keane offered the best support to help me start all my Ph.D. projects. Dr. Anna Blakney and Dr. Paul McKay have been the best collaborators. Thank you for always finding the time to help me whenever I needed. Dr. Mohamed Bellahcene performed the myocardial ischemia reperfusion injury model, echocardiography and pressure-volume loop measurements. Dr. Charlie Winter helped with 3D structural illumination microscopy. Jiaqing Tang helped with high resolution transmission electron microscopy. Amalia Sintou helped with neutrophil isolation.

My Ph.D. journey wouldn't have been so fun without my lovely friends. Valeria has been an amazing friend, bringing countless joys to my life and always encouraging me during my bad times. Cecile has always been my "plus one" during the last year of my Ph.D.; I wish you could have joined our group when I started. Alice has been a precious friend and office mate, always willing to listen and give advice. Lilianna and Maria João with full of Portuguese energy that made my lab days colourful. Lucia and Marco have been the most fun and enthusiasm Italian; I missed our noisy corner in the lab. Mike has been always thinking about me and encouraging me during my hard times. Jono, Omar and Chris have made my life 'tougher'; we 'made fun of each other' and cared about each other so much. Brian has been a comrade in my Ph.D.



career. Charlie has been helping me no matter the problems I had in personal life or research. I would also like to thank Raya, Maxine, Dan, Renee, Marta, Kaili, Alessandra, Jelle, Kaja, Sirli, and Kun for creating every single unforgettable moment that I will miss so much.

Without family, work would be without purpose. Thanks to my mom and dad for their unconditional love and support. I have never felt the distance between UK and China because our hearts are always together.

# Abstract

Uncontrolled inflammation is a major pathological factor underlying a range of diseases including autoimmune conditions, cardiovascular disease and cancer. Improving localised delivery of immunosuppressive drugs to inflamed tissue in a non-invasive manner offers significant promise to reduce severe side effects caused by systemic administration. Employing immune cells for active transport of drugs and drug-loaded nanocarriers to a target site is a promising recent approach. Particularly, in the context of drug delivery for anti-inflammation therapy, immune cells have the intrinsic functions to migrate to and infiltrate the inflamed tissue. Here, a delivery strategy using neutrophils loaded with methotrexate (MTX)-liposomes *ex vivo* to deliver MTX to target sites was first investigated *in vitro*. This hybrid system efficiently migrated following an inflammatory chemokine gradient and triggered release of loaded liposomes *via* neutrophil extracellular traps (NETs) formation in an inflammatory environment was achieved. Subsequent re-uptake of the released liposomes by target macrophages provided detailed support for *in vivo* treatment studies. In parallel, macrophages were evaluated as alternative immune cells to carry nanoparticles. Given the advantage of a well-defined release mechanism (NETs formation), MTX-liposome loaded neutrophils were chosen over a macrophage-based system to be further validated *in vivo* using two mouse models of inflammation, a lipopolysaccharide (LPS)-injury skeletal muscle model and a myocardial ischemia reperfusion injury (IRI) model. The migratory behaviour of liposome-loaded neutrophils was confirmed by demonstrating the neutrophil-mediated delivery of liposomes to the inflamed muscle and the injured heart. A single low-dose injection of the hybrid system locally reduced inflammatory cytokine levels in the inflamed muscle and slightly improved the pumping efficiency of the IRI heart. These results highlight the advantages of immune cell-mediated drug delivery, which is a versatile strategy that allows combinations with different types of nanoparticles encapsulating various drugs to reduce tissue inflammation and actively promote repair in inflammatory diseases.

# Publications

The work presented in Chapter 2 and Chapter 4 has been accepted in *Advanced Materials*:

**J Che**, A Najer, A K. Blakney, P F. McKay, M Bellahcene, C W. Winter, A Sintou, J Tang, T J. Keane, M D. Schneider, R J. Shattock, S Sattler, M M. Stevens. "Neutrophils Enable Local and Non-Invasive Liposome Delivery to Inflamed Skeletal Muscle and Ischemic Heart" (In press).

L. Massi, A. Najer, R. Chapman, C. D. Spicer, V. Nele, **J. Che**, M. A. Booth, J. J. Douth, M. M. Stevens. "Tuneable peptide cross-linked nanogels for enzyme-triggered protein delivery." *Journal of Materials Chemistry B* (accepted).

# Table of Contents

Declaration of Originality .....	3
Copyright Declaration .....	3
Acknowledgements.....	4
Abstract.....	6
Publications.....	7
List of Figures .....	11
List of Tables .....	14
List of abbreviations.....	15
1. Introduction.....	19
1.1. Inflammation.....	19
1.1.1. Molecular and cellular mechanisms involved in inflammation .....	19
1.1.2. Inflammation-induced organ injury .....	28
1.2. Treatments of inflammation .....	34
1.2.1. Anti-inflammatory drugs.....	35
1.2.2. Challenges of using anti-inflammatory drugs .....	39
1.3. Nanoparticle-based drug delivery for inflammatory diseases.....	40
1.3.1. The history of nanoparticle-based delivery systems .....	40
1.3.2. Liposomes .....	42
1.3.3. Polymeric nanoparticles.....	45
1.3.4. Inorganic nanoparticles.....	46
1.3.5. Virus nanoparticles .....	49
1.3.6. Challenges of using nanoparticle-based drug delivery systems .....	51
1.4. Cell-mediated drug delivery.....	55
1.4.1. Different types of cell carriers.....	56
1.4.2. Methods of cell carrier loading with nanoparticles .....	61
1.4.3. Applications of cell-mediated drug delivery .....	64
1.5. Scope of the thesis.....	68
2. <i>In vitro</i> development of a neutrophil-mediated drug delivery system.....	72
2.1. Introduction .....	72
2.2. Materials and methods.....	74
2.2.1. Materials .....	74
2.2.2. Liposome preparation and characterisation.....	74

2.2.3.	Drug loading and retaining in liposomes .....	75
2.2.4.	Neutrophil isolation .....	77
2.2.5.	Uptake of liposomes by neutrophils .....	78
2.2.6.	Neutrophil viability.....	80
2.2.7.	Physiological functions of neutrophils .....	80
2.2.8.	NETs formation imaging.....	81
2.2.9.	Quantification of liposome and MTX release from neutrophils .....	82
2.2.10.	Co-culture of liposome loaded neutrophils with RAW 264.7 cells .....	83
2.2.11.	Statistics .....	84
2.3.	Results and discussion .....	85
2.3.1.	Preparation and characterisation of liposome loaded neutrophils.....	86
2.3.2.	Physiological functions of neutrophils after loading with blank liposomes .....	92
2.3.3.	Inflammation-responsive release of liposomes from neutrophils and delivery to macrophages.....	98
2.3.4.	Optimising drug loading and release properties of liposomes.....	105
2.3.5.	Preparation and characterisation of MTX-liposome loaded neutrophils .....	110
2.3.6.	Physiological functions of neutrophils after loading with MTX-liposomes .....	115
2.3.7.	Inflammation-responsive transfer of MTX-liposomes from neutrophils to macrophages.....	120
2.4.	Conclusions .....	126
3.	Cellular interactions of different types of nanoparticles with macrophages .....	130
3.1.	Introduction .....	130
3.2.	Materials and methods.....	132
3.2.1.	Materials .....	132
3.2.2.	Nanoparticle preparation and characterisation .....	133
3.2.3.	Uptake of nanoparticles by RAW 264.7 cells .....	136
3.2.4.	Cell viability .....	136
3.2.5.	Cell migration assay .....	137
3.2.6.	Identification of RAW 264.7 cell phenotype .....	137
3.2.7.	Statistics .....	138
3.3.	Results and discussion .....	138
3.3.1.	Preparation and characterisation of nanoparticle loaded macrophages.....	139
3.3.2.	Physiological functions of macrophages after loading with different nanoparticles .	149
3.4.	Conclusions .....	155
4.	<i>In vivo</i> validation of the neutrophil-mediated drug delivery system for the treatment of inflammatory diseases .....	159

4.1.	Introduction .....	159
4.2.	Materials and methods.....	161
4.2.1.	Animals.....	161
4.2.2.	LPS-injury skeletal muscle model and flow cytometry .....	161
4.2.3.	ELISA (Luminex) assay .....	162
4.2.4.	Quadriceps histology.....	163
4.2.5.	Myocardial ischemia-reperfusion injury (IRI) model .....	163
4.2.6.	Fluorescence Molecular Tomography.....	164
4.2.7.	Cardiac functional assessment.....	165
4.2.8.	Statistics .....	167
4.3.	Results and discussions.....	167
4.3.1.	<i>In vivo</i> migration of liposome/neutrophils to inflamed skeletal muscle .....	169
4.3.2.	<i>In vivo</i> migration of liposome/neutrophils to the IRI heart .....	178
4.3.3.	<i>In vivo</i> anti-inflammatory treatment <i>via</i> neutrophil-mediated delivery in the LPS-injury skeletal muscle model.....	184
4.3.4.	<i>In vivo</i> improvement of cardiac function <i>via</i> neutrophil-mediated delivery in the myocardial IRI model .....	190
5.	Conclusions and future work.....	214
5.1.	Conclusions .....	214
5.1.1.	<i>In vitro</i> development of immune cell-mediated drug delivery systems.....	214
5.1.2.	<i>In vivo</i> anti-inflammation treatments.....	216
5.2.	Future work.....	218
5.3.	Perspectives .....	218
	References .....	222
	Appendix .....	241

# List of Figures

Figure 1.1 The category of different inflammatory inducers. ....	20
Figure 1.2 Timeline of the recruitment of different types of cells to the injured tissue. ....	23
Figure 1.3 Different stages of neutrophil migration. ....	24
Figure 1.4 2D confocal images of a live bacteria captured by a neutrophil and 3D reconstruction analysis. ....	25
Figure 1.5 Structural and functional changes of different organs due to acute or chronic inflammation and associated diseases. ....	29
Figure 1.6 Different points of inhibition by anti-inflammatory drugs. ....	35
Figure 1.7 The timeline of therapeutic nanosystems. ....	41
Figure 1.8 Structure and surface modifications of liposome-mediated drug delivery systems. ....	42
Figure 1.9 Inorganic nanoparticles used in different biomedical applications. ....	47
Figure 1.10 Different cargoes attached to virus nanoparticles. ....	50
Figure 1.11 Medical applications for approved nanomedicines. ....	52
Figure 1.12 Physiological barriers hindering nanoparticle-based drug delivery. ....	55
Figure 1.13 Neutrophil-mediated PTX-liposome delivery for anti-cancer treatment. ....	65
Figure 1.14 Schematic illustration of the concept of this work. ....	69
Figure 2.1 Schematic illustration of preparation of drug-encapsulated liposome loaded neutrophils and evaluation of activity. ....	86
Figure 2.2 Preparation and characterisation of cationic liposomes. ....	87
Figure 2.3 Isolation and characterisation of neutrophils. ....	89
Figure 2.4 Liposome loading of neutrophils. ....	91
Figure 2.5 Cytocompatibility of liposomes to neutrophils after incubation for 4 h and 8 h. ...	92
Figure 2.6 Change in the CD11b expression of liposome loaded neutrophils after treatment with fMLP at different concentrations. ....	93
Figure 2.7 Change in the superoxide generation of liposome-loaded neutrophils with and without fMLP treatment. ....	94
Figure 2.8 Migration ability of liposome loaded neutrophils with and without fMLP treatment. ....	95
Figure 2.9 Representative images of neutrophils at the bottom side of the transwell membrane after the migration test. ....	96
Figure 2.10 CLSM images of liposome/neutrophils on the transwell membrane. ....	97
Figure 2.11 Schematic illustration of NETs formation and resulting delivery of liposomes from neutrophils to macrophages. ....	99
Figure 2.12 CLSM representative images of liposome/neutrophils (liposomes were labelled with DiD and loaded with FITC-BSA) before and after treatment with fMLP or PMA. ....	100
Figure 2.13 Stimulated release of liposomes (DiD labelled) from neutrophils after treatment with PMA detected by FCS. ....	102
Figure 2.14 Delivery of liposomes to co-cultured macrophages (RAW 264.7 cells) when transported <i>via</i> neutrophils. ....	104

Figure 2.15 CLSM representative images of RAW 264.7 cells after incubation with liposome/neutrophils at 0 h, 4 h and 8 h in the absence of PMA. ....	105
Figure 2.16 Structures and calibration curves of MTX and DEX. ....	106
Figure 2.17 Preparation and characterisation of MTX-liposomes. ....	109
Figure 2.18 The effect of cholesterol percentage of liposomes (liposome composition: 16:0-18:1 PC (POPC), 18:0 TAP and cholesterol) on drug retention behaviour. ....	110
Figure 2.19 CLSM representative images of MTX-liposome/neutrophils. ....	112
Figure 2.20 Fluorescence representative images of a single MTX-liposome/neutrophil. ....	113
Figure 2.21 Neutrophil uptake and viability for MTX-loaded liposomes and subsequent loading amount of MTX with neutrophils. ....	114
Figure 2.22 Physiological functions of neutrophils after loading with MTX-liposomes. ....	116
Figure 2.23 Representative images of neutrophils at the bottom side of the transwell membrane after the migration test. ....	118
Figure 2.24 CLSM representative images of MTX-liposome/neutrophils on the transwell membrane. ....	119
Figure 2.25 Stimulated release of MTX-liposomes (DiD labelled) from neutrophils after treatment with PMA detected by FCS. ....	121
Figure 2.26 Percentage of released MTX from neutrophils. ....	122
Figure 2.27 Flow cytometry analysis of macrophages after co-culture with MTX-liposome/neutrophils (liposomes were labelled with DiD). ....	123
Figure 2.28 TNF- $\alpha$ inhibition effect of MTX-liposome on co-cultured macrophages (RAW 264.7 cells). ....	125
Figure 2.29 Anti-proliferation effect of MTX-liposome on co-cultured macrophages (RAW 264.7 cells) when transported <i>via</i> neutrophils. ....	126
Figure 3.1 Schematic illustration of different types of nanoparticles loaded into macrophages and evaluation of cellular responses. ....	139
Figure 3.2 Characterisation of different types of nanoparticles. ....	141
Figure 3.3 Nanoparticle loading into macrophages. ....	143
Figure 3.4 Co-localisation of nanoparticles with macrophages using CLSM. ....	145
Figure 3.5 Super resolution representative images (SIM) of cationic liposome loaded macrophages. ....	146
Figure 3.6 Cytocompatibility of nanoparticles to macrophages after incubation for 4 h and 8 h. ....	148
Figure 3.7 Effect of different types of nanoparticles on migration of macrophages. ....	151
Figure 3.8 Polarisation of macrophages after loading with different types of nanoparticles. ....	153
Figure 4.1 Schematic illustration of two different mouse models used to determine the migration behaviour of loaded neutrophils and the treatment effect after intravenous injection of MTX-liposome/neutrophils. ....	168
Figure 4.2 H&E staining of healthy quadriceps and LPS-injected quadriceps after different timepoints. ....	170
Figure 4.3 Schematic illustration of sample preparation process of quadriceps and blood collected after LPS injection. ....	171



Figure 4.4 Flow cytometry analysis of quadriceps with or without neutrophil injection (labelled with VivoTrack 680). .....	173
Figure 4.5 Quantification of endogenous neutrophils and injected neutrophils in healthy quadriceps and LPS-injected quadriceps after neutrophil injection. ....	175
Figure 4.6 Quantification of endogenous neutrophils and injected neutrophils in the blood after neutrophil injection.....	176
Figure 4.7 Quantification of liposome loaded neutrophils in healthy quadriceps and LPS-injected quadriceps after injection. ....	177
Figure 4.8 Schematic illustration of myocardial IRI surgery, the following treatment and sample analysis process in the myocardial IRI mouse model.....	178
Figure 4.9 <i>In vivo</i> accumulation of neutrophils (labelled with VivoTrack 680) in the heart after myocardial IRI surgery and biodistribution in other organs at 1 h post neutrophil injection. ....	180
Figure 4.10 <i>In vivo</i> accumulation of neutrophils (labelled with VivoTrack 680) in the heart after myocardial IRI surgery and biodistribution in other organs at 2 h post neutrophil injection. ....	181
Figure 4.11 <i>In vivo</i> accumulation of liposome/neutrophils in the heart after myocardial IRI surgery and biodistribution in other organs at 1 h post injection.....	183
Figure 4.12 Schematic illustration of the anti-inflammation treatment <i>via</i> neutrophil-mediated delivery in the LPS-injury skeletal muscle model. ....	185
Figure 4.13 Inflammatory cytokine levels in healthy quadriceps and LPS-injected quadriceps after different treatments measured by ELISA assay. ....	187
Figure 4.14 IL-6 levels in inflamed versus healthy quadriceps after different treatments. ...	188
Figure 4.15 Schematic illustration of myocardial IRI surgery and subsequent treatment....	191
Figure 4.16 Images of IRI hearts with/without the treatment after PFA fixation. ....	192
Figure 4.17 Representative brightfield images of Sirius red stained slices from the IRI group. ....	194
Figure 4.18 Representative brightfield images of Sirius red stained slices from the IRI + treatment group. ....	195
Figure 4.19 Quantification of collagen deposition in histological slices at different levels. .	196
Figure 4.20 Graphic representation of body weight and muscular contractility related parameters.....	198
Figure 4.21 Graphic representation of heart dimension related parameters.....	199
Figure 4.22 Graphic representation of LV mass, heart rate, normalised cardiac output, and stroke volume. ....	200
Figure 4.23 Graphic representation of Tibia length (mm).....	202
Figure 4.24 Graphic representation of ejection fraction (EF in %) and heart rate (bmp). ....	203
Figure 4.25 Graphic representation of arterial load related parameters.....	204
Figure 4.26 Graphic representation of diastolic function related parameters. ....	205
Figure 4.27 Graphic representation of systolic function related parameters. ....	206
Figure 4.28 Graphic representation of load-independent parameters.....	207

# List of Tables

Table 1-1 FDA classified commercial products for different applications.....	51
Table 1-2 Neutrophil-mediated delivery systems deliver drug-loaded nanoparticles to different disease sites. ....	59
Table 2-1 Different compositions and ratios used to prepare liposomes. ....	75
Table 2-2 The effect of liposome composition and initial DEX amount on the loading of DEX with liposomes. ....	107
Table 4-1 Cardiac parameters assessed through 2D echocardiography. ....	201
Table 4-2 Cardiac functions assessed through PV loop measurements.....	208

# List of abbreviations

PAMPs	Pathogen-associated molecular patterns
NALP	NACHT-, leucine-rich-repeat- and pyrin-domain-containing protein
ROS	Reactive oxygen species
IgE	Immunoglobulin E
LPSs	Lipopolysaccharides
ATP	Adenosine triphosphate
HMGB1	High-mobility group box 1 protein
TLRs	Toll-like receptors
ECM	Extracellular matrix
AGEs	Advanced glycation end products
OxLDL	Oxidized low-density lipoprotein
IL-1 $\beta$	Interleukin 1- $\beta$
TNF- $\alpha$	Tumour necrosis factor- $\alpha$
IFN- $\gamma$	Interferon- $\gamma$
fMLP	N-formyl-methionyl-leucyl-phenylalanine
NETs	Neutrophil extracellular traps
MIP-1 $\alpha$	Macrophage inflammatory protein 1 $\alpha$
VEGF	Vascular endothelial growth factor
TGF- $\beta$	Transforming growth factor- $\beta$
MHC	Major histocompatibility complex
ICAM-1	Intercellular adhesion molecule 1
APCs	Antigen-presenting cells
NKT cells	Natural killer T cells
MAIT cells	Mucosal associated invariant T cells
RA	Rheumatoid arthritis
ADAMTS	Metalloproteinase with thrombospondin-like motifs
MMPs	Matrix metalloproteinases
PRRs	Pattern recognition receptors
MI	Myocardial infarction
PPCI	Primary percutaneous coronary intervention
IRI	Ischemia reperfusion injury
NAFLD	Non-alcoholic fatty liver disease
HCV	Hepatitis C virus
COPD	Chronic obstructive pulmonary disease
CNS	Central nervous system
PD	Parkinson's disease
AD	Alzheimer's disease
BBB	Blood brain barrier
MTX	Methotrexate
DEX	Dexamethasone
ADHF	Acute decompensated heart failure
COX	Cyclooxygenase
AP-1	Activator protein 1

CAPS	Cryopyrin-associated periodic syndromes	
LTB5	Leukotriene B5	
HDACs	Histone deacetylases	
HATs	Histone hyperacetylases	
NO	Nitric oxide	
NSAIDs	Nonsteroidal anti-inflammatory drugs	
PML	Progressive multifocal leukoencephalopathy	
EPR	Enhanced permeability and retention	
MLVs	Multilamellar vesicles	
PEG	Poly(ethylene glycol)	
PGE-1	Prostaglandin E-1	
MRI	Magnetic resonance imaging	
CT	Computed tomography	
SPR	Surface plasmon resonance	
MSNs	Mesoporous silica nanoparticles	
QDs	Quantum dots	
HSV	Herpes simplex virus	
MPS	Mononuclear phagocyte system	
cRGD	Cyclic arginine-glycine-aspartate	
MSCs	Mesenchymal stem cells	
NHS	N-hydroxysuccinimide	
PTX	Paclitaxel	
DOPC	1,2-dioleoyl-sn-glycero-3-phosphocholine	
18:0 TAP (DSTAP)	1,2-stearoyl-3-trimethylammonium-propane	
POPC	1-palmitoyl-2-oleoyl-glycero-3-phosphocholine	
DiD	1,1'-Dioctadecyl-3,3,3',3'-Tetramethylindodicarbocyanine, Chlorobenzenesulfonate Salt	4-
DAPI	2-[4-(Aminoiminomethyl)phenyl]-1H-Indole-6-carboximidamide hydrochloride	
WGA	Wheat germ agglutinin	
FITC-BSA	Albumin-fluorescein isothiocyanate conjugate	
DLS	Dynamic light scattering	
TEM	Transmission electron microscopy	
LC-MS	Liquid chromatography–mass spectrometry	
PFA	Paraformaldehyde	
CLSM	Confocal Laser Scanning Microscopy	
3D-SIM	3D structural illumination microscopy	
FCS	Fluorescence Correlation Spectroscopy	
PMA	Phorbol myristate acetate	
DSPE-PEG 2000	1,2-distearoyl-sn-glycero-3-phosphoethanolamine-N- (azido(poly(ethylene glycol)-2000)	
PDLLA-PAA	poly(D,L-lactide)-block-poly(acrylic acid)	
ATA	(2-Aminoethyl)trimethylammonium chloride hydrochloride	
EDC	1-ethyl-3-(3-dimethylaminopropyl)carbodiimide	
PEG-PCL	Poly(ethylene glycol)-poly( $\epsilon$ -caprolactone)	
CTAC	Cetrimonium chloride	
TEA	Triethanolamine	

TEOS	Tetraethyl orthosilicate
HCl	Hydrochloric acid
NHS	N-hydroxysuccinimide
APTES	3-triethoxysilylpropylamine
MES	2-(N-Morpholino)ethanesulfonic acid hydrate
PMOXA-PDMS- PMOXA	Poly(2-methyl-2-oxazoline)-block-poly(dimethylsiloxane)-block-poly(2- methyl-2-oxazoline)
PDMS-PAA	Poly(dimethylsiloxane)-block-poly(acrylic acid)
MeO-PEG-COOH	$\alpha$ -methoxy- $\omega$ -carboxylic acid poly(ethylene glycol)
THF	Tetrahydrofuran
DOX	Doxorubicin
HIV	Human immunodeficiency virus
BMDMs	Bone marrow derived macrophages
MPTP	1-methyl-4-phenyl-1,2,3,6-tetrahydropyridine
FMT	Fluorescent Molecular Tomography
LAD	Left anterior descending
ECG	Electrocardiogram
PV loop	Pressure–volume (PV) loop
DiI	1,1'-Dioctadecyl-3,3,3',3'-Tetramethylindocarbocyanine Perchlorate
CPPs	Cell-penetrating peptides
EF	Ejection fraction
LV	Left ventricle
FS	Fractional shortening
DAP	Diastolic arterial pressure
SAP	Systolic arterial pressure
SOD1	Superoxide dismutase

# Chapter 1

## Introduction

## 1. Introduction

### 1.1. Inflammation

Inflammation is the natural defence mechanism of our immune system to respond to harmful stimuli such as dead cells, toxic substances, and pathogens.<sup>1</sup> In physiological conditions, these harmful stimuli trigger the release of inflammation-inducing molecules into the extracellular environment, activating various types of cells (*e.g.* neutrophils and macrophages) that migrate to the inflammatory site.<sup>2,3</sup> These cells aim to remove pathogens and clear out the damaged cells to allow subsequent tissue repair.<sup>4,5</sup> A successful host defence achieves a balance between pro- and anti-inflammatory responses, which act cooperatively, to eliminate the harmful stimuli and to stop further damage.<sup>6</sup> However, if left unchecked, acute and/or chronic inflammatory responses can cause extensive tissue damage. In this section, the molecular and cellular events involved in the inflammatory response, as well as the relationship between inflammation and disease will be presented.

#### 1.1.1. Molecular and cellular mechanisms involved in inflammation

An inflammation response is usually triggered by tissue damage or infection and is mediated by a complex network of biomolecules and immune cells. The inducers activate specific sensors to produce mediators to activate and recruit immune cells to the injury or infection site, eventually eliminating damaged tissue or microbes.

##### 1.1.1.1. Inducers of inflammation

###### *Exogenous inducers*

Exogenous inducers are generally divided into two categories: non-microbial and microbial inducers. Microbial inducers can be further classified into two groups: virulence factors (produced by microorganisms such as toxins) and pathogen-associated molecular patterns (PAMPs) (Figure 1.1).<sup>7</sup>

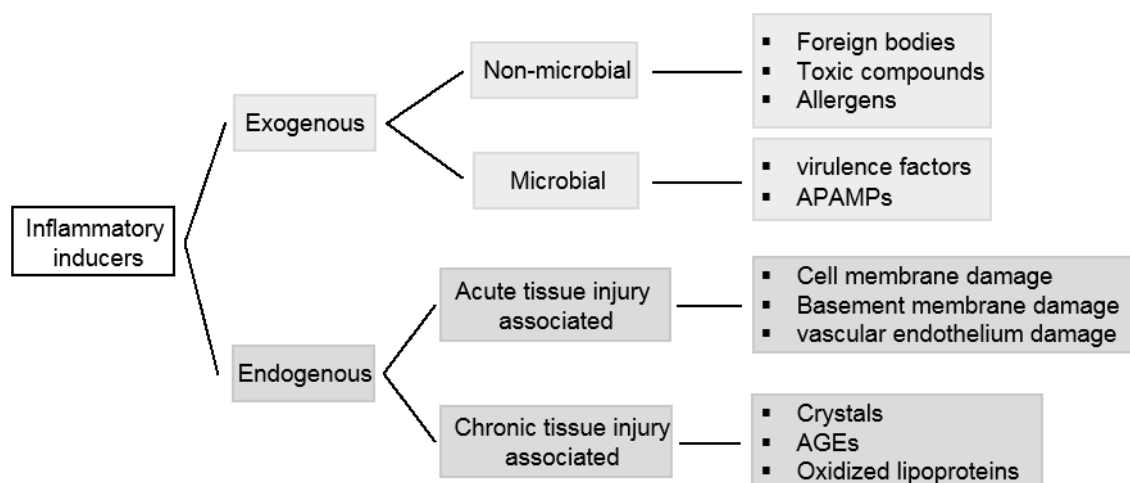


**Figure 1.1** The category of different inflammatory inducers. *Inflammatory inducers can be classified into exogenous inducers and endogenous inducers. Within each category, they are further classified into non-microbial inducers and microbial inducers (exogenous inducers), and acute or chronic tissue injury associated inducers (endogenous inducers). Adapted with permission from Springer Nature.<sup>7</sup>*

Foreign bodies, toxic compounds, and allergens are the most common non-microbial inducers. Foreign bodies are typically particles that cannot be digested by macrophages. A good example of foreign bodies are silica particles.<sup>8</sup> Due to the absence of phagocytosis-inhibitors on their surface, silica particles are readily recognised by macrophages following exposure to the biological environment. However, because of their large particle size (larger than 6  $\mu\text{m}$ ), silica particles cannot be phagocytised by macrophages or may damage the phagosomal membrane during digestion. As a result, the NALP3 (NACHT-, leucine-rich-repeat- and pyrin-domain-containing protein) inflammasome, a multiprotein complex detecting various stimuli including PAMPs, will be activated.<sup>8</sup> Toxic chemicals such as benzene, halocarbons, and nitrosamines cause chemical-induced inflammation. These chemicals produce reactive oxygen species (ROS) which damage the cell structure or generate neoantigens or reactive intermediates when metabolised, which initiate immunotoxic effects.<sup>9</sup> Allergens can be classified into two groups: the first one comprises non-infectious environmental molecules which can induce immunoglobulin E (IgE) production while the second group comprises molecules able to elicit an adaptive immune response related to local inflammation. Following allergen exposure, mast cells release mediators and cause functional changes within the affected tissues. Some mediators can also activate and recruit immune cells to the allergic site, which aggravates the inflammation response.<sup>10</sup>



Microbial inducers comprise of different virulence factors produced by specific pathogens such as bacteria, viruses, and fungi. These pathogens produce adhesins and surface proteins which allow them to enter the host cells and to exploit them for survival. This process initiates the host's immune response.<sup>11,12</sup> Another type of microbial inducers are PAMPs, which are conserved small molecular motifs carried by microorganisms. PAMPs can activate the immune response to protect the host from the infection. Lipopolysaccharides (LPSs), which are found in the outer membrane of Gram-negative bacteria, are a classic example of PAMPs. LPSs are able to bind to the receptor of many immune cell types such as monocytes, macrophages, and B cells, promoting the secretion of pro-inflammatory cytokines.<sup>13</sup>

### *Endogenous inducers*

Stress, damage, and tissue dysfunction are the main causes of endogenous inducers. One important example is the acute tissue injury, which can damage cellular membranes (*e.g.*, the plasma membrane), basement membranes, or vascular endothelium.<sup>7</sup> Any of these damages will immediately initiate an inflammatory response. Cell necrosis caused by tissue injury disrupts the integrity of the cellular membrane and leads to the release of dead cell components, such as adenosine triphosphate (ATP), potassium ions, HMGB1 (high-mobility group box 1 protein), and members of the S100 calcium-binding protein family.<sup>14,15</sup> ATP binds to the surface of macrophages to help the efflux of potassium ions and work with other signals to activate the NALP3 inflammasome.<sup>16</sup> At the same time, members of the S100 calcium-binding protein family also cooperate with TLRs (Toll-like receptors) to initiate an inflammatory response.<sup>17,18</sup> When the basement membrane is destroyed, mesenchymal cells and epithelial cells come into contact, and the disorder of mesenchymal and epithelial interaction induces an inflammatory response. In some organs, the epithelial surface plays an important role to separate the internal and external environment. For example, in the intestine, the basement membrane separates commensal microorganisms from the inner sterile environment. When the basement membrane is destroyed, commensal microorganisms are able to enter the sterile environment, binding to TLRs present on the macrophages in the lamina propria, which leads to intestinal inflammation.<sup>19,20</sup> Another example is the vascular endothelial damage, which allows platelets and plasma proteins to enter the extravascular space. When these species encounter the extracellular matrix (ECM),

an important plasma-derived regulator of inflammation, the Hageman factor, is activated. The Hageman factor will then promote the generation of inflammatory mediators.<sup>21</sup>

As outlined above, endogenous inducers are generated during an acute inflammation process following tissue injury. Other inducers, such as crystals of monosodium urate and calcium pyrophosphate dehydrate, AGEs (advanced glycation end products), and oxidized lipoproteins, are involved in chronic inflammation processes. Crystals of monosodium urate and calcium pyrophosphate dehydrate are usually formed in connective tissues, such as joints.<sup>14</sup> When these crystals reach a certain size, macrophages recognise them as foreign bodies to be phagocytosed and the NALP3 inflammasome is activated.<sup>22</sup> AGEs are a group of glycosylated molecules produced when sugars react with proteins and can cause damage by crosslinking proteins, compromising their functionality.<sup>23,24</sup> AGEs are involved in the development of many degenerative diseases like diabetes, Alzheimer's diseases, and cardiovascular disease. Oxidized lipoproteins play a dominant role in the inflammation cascade of many chronic diseases related to thrombus. For example, oxidized low-density lipoprotein (OxLDL) generated from dying cells and microvesicles were found to have antigenic properties and resulted in atherosclerosis-associated inflammation.<sup>25</sup>

#### 1.1.1.2. Cellular responses during inflammation

All the inducers of inflammation discussed above are typically produced by harmful stimuli such as tissue injury, toxic chemicals, and bacterial infection. These inducers trigger the production of various inflammatory mediators to activate and recruit several types of cells to the inflammatory site for tissue repair. In this section, the temporal inflammatory cell response will be discussed and is summarised in the following scheme (Figure 1.2).

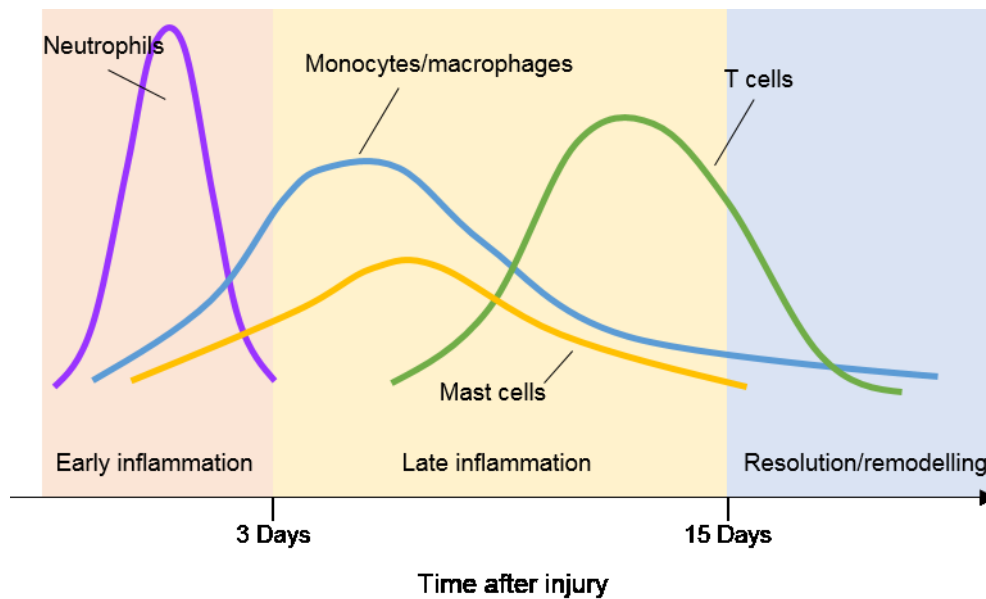


**Figure 1.2** Timeline of the recruitment of different types of cells to the injured tissue. Neutrophils are firstly recruited to the injury site, followed by monocytes/macrophages in the early stage of inflammation. In the late stage of inflammation, mast cells are recruited sequentially. T cells also appear in the late stage of inflammation to influence the resolution and remodelling of the tissue.

#### *Neutrophils-one of the first responders during inflammation*

Neutrophils are commonly considered short-lived cells with a half-life of 1.5 h in mice and 8 h in humans.<sup>26</sup> During the inflammation response, neutrophils are the first and the most abundant cells that reach and infiltrate the injury site in the early stage of inflammation. Immediately after tissue injury or infection, endothelial cells are activated to express adhesion molecules. Neutrophils freely circulating in the bloodstream are tethered by these molecules on the surface of the endothelium and slowly roll on its surface; at the same time, they are activated by pro-inflammatory factors interleukin 1- $\beta$  (IL-1 $\beta$ ), tumour necrosis factor- $\alpha$  (TNF- $\alpha$ ), and interferon- $\gamma$  (IFN- $\gamma$ ) to express several adhesion molecules.<sup>27</sup> Adhesion molecules on the surface of neutrophils interact with integrins on the surface of endothelial cells, ensuring firm adhesion. Among all the integrins, CD11b is the most important; it dominates adhesion and migration functions of neutrophils.<sup>28,29</sup> Once tightly adhered to the endothelium, neutrophils are guided by chemokine gradients, such as bacteria-derived N-formyl-methionyl-leucyl-phenylalanine (fMLP), along the endothelium to transmigrate across the basement membrane.<sup>30</sup> To observe this process, Yipp *et al.* used intravital microscopy to

image neutrophils at different stages of migration: free circulating neutrophils in the blood, rolling neutrophils on the surface of the endothelium, adhering neutrophils, and extravasated neutrophils inside the tissue (Figure 1.3).<sup>31</sup> Eventually, neutrophils aggregate at the injury site to release a variety of factors to initiate the activation and recruit more neutrophils and other cells involved in the inflammation process.<sup>32</sup>

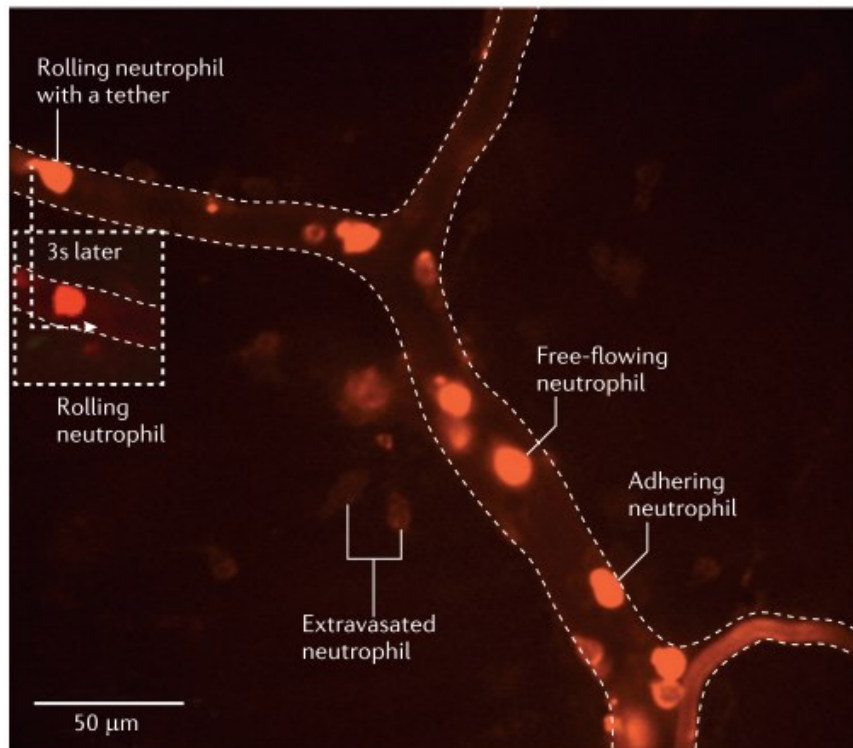


**Figure 1.3 Different stages of neutrophil migration.** Mouse skin was infected with *Staphylococcus aureus* and the image was taken 2 h after the infection. Neutrophils were labelled with anti-Gr-1 antibody conjugated to phycoerythrin (red). Mouse skin was detected under an intravital microscope to visualise the process of neutrophil migration. The image was adapted with permission from Springer Nature.<sup>31</sup>

After migrating to the inflammatory site, neutrophils start clearing the damaged tissue and killing pathogens. There are two main killing mechanisms involved in this process: intracellular killing by phagocytosis and extracellular killing by releasing neutrophil extracellular traps (NETs). Microorganisms are phagocytosed by neutrophils when they encounter each other. Neutrophils trap microorganisms inside phagosomes, releasing ROS factors and antibiotic proteins to kill them.<sup>33,34</sup> When neutrophils are highly activated, they can also kill microorganisms by releasing NETs. NETs are neutrophil intracellular constituents composed of DNA, histones, and granular proteins. NETs can immobilise pathogens to favour

subsequent phagocytosis by other cells or kill them directly by antibiotic histones and proteases.<sup>35</sup> Yipp *et al.* captured 2D confocal images (Figure 1.4) of a NET-forming neutrophil and a NETosing (the neutrophils capable of forming NETs) neutrophil *in vivo* after incubation with *S. aureus*.<sup>36</sup> 3D reconstruction analysis clearly revealed a neutrophil trapping a live bacteria; additionally, the neutrophil continuously released an extracellular NET after capturing the bacteria. The formation of NETs also occurs during chronic inflammatory diseases,<sup>37</sup> thrombosis,<sup>38</sup> autoimmune diseases,<sup>39</sup> and cancer.<sup>40</sup> These functions of neutrophils help to remove dead cells and pathogens for subsequent tissue repair.

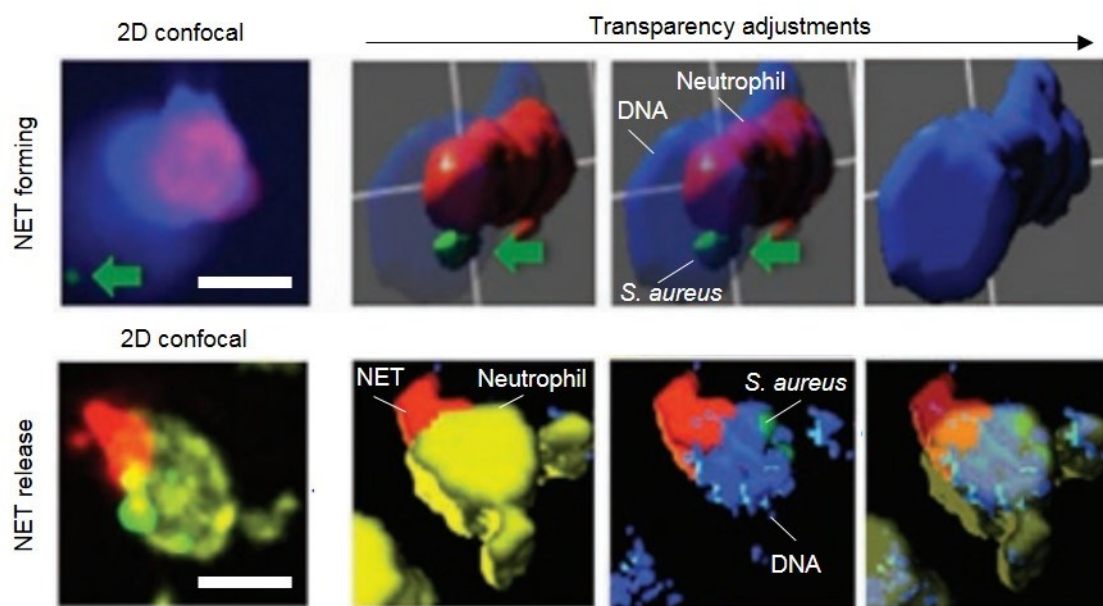


**Figure 1.4 2D confocal images of a live bacteria captured by a neutrophil and 3D reconstruction analysis.** A NET-forming neutrophil (red) captured a live *S. aureus* bacterium (Green) as imaged by confocal microscopy (top left image). Different 3D transparency images showed the live bacterium was inside DNA (blue) of the NET-forming neutrophil. A NETosing neutrophil (yellow) captured a live *S. aureus* bacterium (Green) was imaged by confocal microscopy (bottom left image). Different 3D transparency images showed the NETosing neutrophil still released an extracellular NET when bacteria had been trapped inside. Scale bar = 10  $\mu\text{m}$ . Adapted from Springer Nature.<sup>36</sup>

After completing their task, most neutrophils die after they form NETs in the inflammatory tissue and are subsequently cleared by macrophages. Nevertheless, reverse neutrophil transmigration back into the vasculature has been shown in zebrafish embryo and mouse models.<sup>41,42</sup> Furthermore, Buckley *et al.* recently observed that approximately 1-2% of peripheral blood neutrophils undergo reverse transmigration in patients suffering from

rheumatoid arthritis.<sup>43</sup> There are two different explanations regarding this phenomenon. One explanation claims that these reverse transmigrated neutrophils are extra neutrophils that do not need to fight with pathogens or clear damaged tissue, so they migrate from the inflamed tissue back to the bloodstream. Another explanation is that the neutrophils that re-enter into the blood circulation are intended to spread the inflammation to other organs and lead to systemic inflammation.<sup>26</sup>

#### *Monocytes/Macrophages-dual functions associated with pro- and anti-inflammation*

Similarly to neutrophils, monocyte recruitment and transmigration involves the sequential steps of endothelial cell activation, monocytes adhesion, and monocytes transmigration.<sup>44</sup> Apart from a small fraction of monocytes that are recruited to phagocytose exhausted neutrophils, the majority of monocytes in the injured tissue are recruited from the bloodstream to phagocytose cell debris and pathogens, and, more importantly, to contribute to tissue repair.<sup>45</sup> Monocyte infiltration into the injured tissue is tightly controlled by gradients of several chemotactic factors, which include pro-inflammatory cytokines, growth factors, and macrophage inflammatory protein 1 $\alpha$  (MIP-1 $\alpha$ ).<sup>46</sup> During the transmigration process, monocytes become activated following exposure to the chemotactic factors and differentiate into mature tissue macrophages of the pro-inflammatory phenotype (M1 phenotype).<sup>47</sup> M1 macrophages can produce a large number of inflammatory cytokines and mediators including IL-1, IL-6, IL-12, and TNF- $\alpha$  to amplify the inflammation response and phagocytose pathogens and dead cells.<sup>48</sup>

Following removal of cell debris and pathogens, M1 macrophages transform to and/or are replaced by macrophages of a reparative phenotype (M2 phenotype). M2 phenotype macrophages are featured by producing anti-inflammatory growth factors including transforming growth factor- $\beta$  (TGF- $\beta$ ), IL-1, and vascular endothelial growth factor (VEGF).<sup>46,49</sup> This transition happens over time and several studies suggest that predominance of the M1 phenotype is found in the early stage of inflammation whereas M2 macrophages are more predominant in the late stage of inflammation and during the resolution/remodelling phase. The main functions of M2 macrophages are to promote functional cell proliferation and protein synthesis, and secrete proteases and their inhibitors to affect the ECM components and remodelling.<sup>50,51</sup>

In contrast to neutrophils, macrophages are long-lived cells with complex functions during inflammation. Unlike neutrophils that undergo apoptosis after completing their tasks, the fate of macrophages during the inflammation resolution/remodelling phase is to migrate to the draining lymph nodes.<sup>52</sup>

#### *Mast cells-mediate allergic and anaphylactic reactions*

Mast cells are another type of leukocytes that play an important role in allergic and anaphylactic reactions, as well as innate immunity.<sup>53</sup> Once activated, mast cells migrate to the injured site and secrete a variety of pro-inflammatory and vasoactive molecules including TNF, histamine, serotonin, and proteases.<sup>54,55</sup>

Recent studies demonstrated that mast cells are capable of providing signals to potentially initiate and sustain T cell priming. Mast cells have also been shown to express IL-4 in the presence of IgE, IL-33, and lectins; in particular, IL-4 in conjunction with dendritic cells can stimulate naïve T cells towards a Th2 phenotype.<sup>56,57</sup> Exosomes released from mast cells can also activate T cells; exosomes isolated from IL-4-treated, bone marrow-derived mast cells expressed several molecules including major histocompatibility complex (MHC) class II, CD86, CD40, CD40L, lymphocyte function-associated antigen 1 (LFA-1), and intercellular adhesion molecule 1 (ICAM-1),<sup>58</sup> which are known to be important for T cell activation. Another study also used the same source of mast cells and found that when mast cells and T cells are co-cultured in the presence of IL-4, mast cells increase the frequency of Th2 cell differentiation.<sup>59</sup>

#### *T cells-control and shape the immune response*

T cells are a type of lymphocytes derived from the thymus gland and they can differentiate into different subsets that regulate the outcome of inflammation. Differentiated T cells secrete distinct cytokines to recruit other cells to mediate the inflammation response or directly attacking virus-infected cells.<sup>60,61</sup>

Based on the different functions of their subsets, T cells can be classified into two main groups: conventional adaptive T cells and innate-like T cells. Conventional adaptive T cells comprise helper CD4+ T cells, cytotoxic CD8+ T cells, memory T cells, and regulatory CD4+ T cells. When helper CD4+ T cells encounter antigen-presenting cells (APCs), they become activated and rapidly secrete cytokines that can favour B cell maturation and activate other cells (*e.g.*



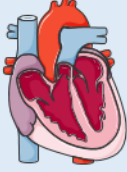
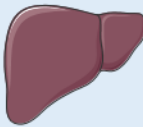



cytotoxic T cells and macrophages).<sup>62</sup> Cytotoxic CD8+ T cells, as the name implies, can attack virus-infected cells and cancer cells by binding to short peptide sequences bound to MHC class I molecules present on the surface of these cells. Cytotoxic CD8+ T cells can also produce IL-2 and IFN- $\gamma$  cytokines to affect other cells, particularly macrophages. Memory T cells can provide the immune system a 'memory' of previously encountered pathogens so that when these pathogens invade the body again, memory T cells immediately recognise and attack them.<sup>63</sup> Regulatory CD4+ T cells are crucial at the late stage of the immune response as they stop the T cells-mediated immunity by suppressing autoreactive T cells, maintaining immunological tolerance.<sup>64</sup>

Innate-like T cells include natural killer T cells (NKT cells) and mucosal associated invariant T cells (MAIT cells). NKT cells can produce cytokines, release cell killing molecules, and recognise and eliminate certain tumour cells and infected cells. Similarly, MAIT cells are able to lyse bacteria-infected cells.<sup>65,66</sup>

### 1.1.2. Inflammation-induced organ injury

A successful host defence mechanism relies on the spatially- and temporally-controlled production of inflammatory mediators and recruitment of cells. However, in many cases of acute inflammation, failure to suppress the inflammatory response leads to additional tissue damage and progress from acute to chronic inflammation, which is the major cause of diseases and death. In the next section, tissue injury in different organs including the articulation, digestive system, heart, liver, lung, kidney, and brain caused by acute and chronic inflammation will be discussed (Figure 1.5).



Geometric and functional changes	Examples of inflammation-associated diseases
<ul style="list-style-type: none"> <li>▪ Hyperplastic cartilage</li> <li>▪ Formation of spurs</li> <li>▪ Degradation of cartilage matrix</li> <li>▪ Change of joint shape</li> </ul>	 <ul style="list-style-type: none"> <li>▪ Osteoarthritis</li> <li>▪ Rheumatoid arthritis</li> </ul>
<ul style="list-style-type: none"> <li>▪ Diarrhea</li> <li>▪ Change of metabolic status</li> <li>▪ Internal cramps/muscle spasms</li> </ul>	 <ul style="list-style-type: none"> <li>▪ Ulcerative colitis</li> <li>▪ Crohn's disease</li> </ul>
<ul style="list-style-type: none"> <li>▪ Non-infarcted myocardium</li> <li>▪ Ventricular dilatation</li> <li>▪ Thinner infarcted wall</li> <li>▪ Inhibition of cardiomyocyte contraction</li> </ul>	 <ul style="list-style-type: none"> <li>▪ Myocardial ischemia heart injury</li> <li>▪ Adverse LV remodelling</li> <li>▪ Heart failure</li> </ul>
<ul style="list-style-type: none"> <li>▪ Hepatocyte damage</li> <li>▪ Cholestasis</li> </ul>	 <ul style="list-style-type: none"> <li>▪ Systemic metabolic alterations</li> <li>▪ Alcoholic hepatitis</li> <li>▪ Ischemia reperfusion injury</li> </ul>
<ul style="list-style-type: none"> <li>▪ Pulmonary fibrosis</li> <li>▪ Impaired gas exchange</li> <li>▪ Pulmonary vascular dysfunction</li> </ul>	 <ul style="list-style-type: none"> <li>▪ Obstructive pulmonary disease</li> <li>▪ Asthma</li> </ul>
<ul style="list-style-type: none"> <li>▪ Loss of glomeruli</li> <li>▪ Tubular injury and fibrosis</li> <li>▪ Reduced glomerular filter rate and creatinine clearance</li> </ul>	 <ul style="list-style-type: none"> <li>▪ Glomerulonephritis</li> <li>▪ Interstitial nephritis</li> <li>▪ Pyelonephritis</li> </ul>
<ul style="list-style-type: none"> <li>▪ Enhanced BBB permeability</li> <li>▪ Damaged neural cells</li> </ul>	 <ul style="list-style-type: none"> <li>▪ Parkinson's disease</li> <li>▪ Alzheimer's disease</li> <li>▪ Autoimmune encephalitis</li> <li>▪ Central nervous system vasculitis</li> </ul>

**Figure 1.5 Structural and functional changes of different organs due to acute or chronic inflammation and associated diseases.** *The images of organs were adapted from the Servier Medical Art website.*

### Articulation

Joint inflammation, also called arthritis, can exist in one or more joints and has many forms and includes diseases like osteoarthritis and rheumatoid arthritis (RA). Osteoarthritis is the most common form affecting around 28% of people over the age of 60 worldwide with the hallmark of cartilage destruction.<sup>67</sup> Inflamed cartilage, synovium, and subchondral bone are

the main pathogenesis, sometimes accompanied by systemic inflammation. Chondrocytes, a unique cell type present in the articular cartilage of adults, become activated following exposure to DAMPs and produce matrix-degrading proteinases (*e.g.* disintegrin and metalloproteinase with thrombospondin-like motifs (ADAMTS)) and several inflammatory cytokines (*e.g.* IL-1 $\beta$ , IL-6 and TNF- $\alpha$ ).<sup>68,69</sup> These matrix-degrading proteinases are considered the main enzymes contributing to cartilage degradation while inflammatory cytokines can upregulate the expression of matrix metalloproteinases (MMPs) to inhibit ECM remodelling. Similarly, synoviocytes in the synovium and the cells in other joint tissue release inflammatory cytokines and degradative enzymes to further destruct the joint tissue.<sup>70</sup>

RA is an autoimmune disorder that affects 1% of people in the world and it happens when the immune system starts attacking the synovium. Infiltration and accumulation of T cells, macrophages, mast cells, and other immune cells in the synovial compartment trigger the synovitis. The production of cytokines from these cells is crucial to the pathogenesis of RA including IL-4, IL-13, IL-15, and TNF- $\alpha$  in the early stage and IL-6 in the late stage. Sustained inflammation and dysfunction of synoviocytes result in a hyperplastic synovium. Loss of protection from the normal synovium further damages the cartilage surface and promote the degradation of cartilage matrix. Moreover, the prolonged inflammation response in the joint also lead to bone erosion.<sup>71,72</sup>

### *The digestive system*

Inflammatory bowel disease is the most common disease occurring in the digestive system and featuring inflammation; it comprises two main forms: Crohn's disease (can affect any part of the bowel) and ulcerative colitis (only affects the colon and rectum). The main cause is a defective mucosal immune system that inappropriately responds to luminal antigens and indigenous microflora. Upon inflammatory bowel disease, the leaky epithelial barrier gives luminal antigens access to the mucosal tissue. Consequently, luminal antigens such as microbial antigens from commensals induce an inflammatory response in various ways. For example, myeloid dendritic cells misidentify commensals as pathogens, upregulating their expression of pattern recognition receptors (PRRs) and co-stimulatory molecules on the surface. These cells also alter their functions to promote the differentiation of T cells from naïve T cells to NKT cells and effector T cells that are known as active subtypes contributing to inflammation.<sup>73</sup> Activated T cells release inflammatory cytokines such as IL-12, IL-13, IL-18,

and IFN- $\gamma$  and further promote inflammatory cells migrating from the bloodstream to the intestinal mucosa, which may intensify and persist inflammation.<sup>74</sup>

### *Heart*

Cardiovascular diseases are one of the major causes of death and disability worldwide, with 37% of heart failures attributable to acute myocardial infarction (MI).<sup>75</sup> The standard treatment to minimise the injury from MI is myocardial reperfusion using primary percutaneous coronary intervention (PPCI). However, myocardial reperfusion can lead to severe cardiomyocyte death and further myocardial injury that contributes up to 50% of the final infarct size.<sup>76</sup> Therefore, the mortality and morbidity following acute MI are dramatically high with 7% and 42%, respectively.<sup>77</sup>

The inflammatory response following acute MI plays an important role in inducing ischemia reperfusion injury (IRI). There are different stages involved in the MI cascade: at first, the lack of oxygen supply following myocardial infarction causes the death of a large number of working cardiomyocytes (cell necrosis and apoptosis phase). After the cells have died by necrosis or apoptosis, they release their cytoplasmic content into the extracellular environment, instigating a severe inflammatory reaction through the engagement of PRRs.<sup>78</sup> When PRRs on immune cells encounter PAMPs or DAMPs, an ensemble of pro-inflammatory cytokines and chemotactic factors are activated and trigger the release of *e.g.* nuclear factor- $\kappa$ B (NF- $\kappa$ B), IL-1 $\beta$ , IL-18, and TNF- $\alpha$ . Pro-inflammatory cytokines and chemotactic factors recruit leukocytes to the area of injury; typically, neutrophils are the first innate immune cells recruited to the myocardium. The recruitment process comprises two steps: peripheral activation and infiltration. Formylated peptides (such as fMLP) and mitochondrial DNA released by necrotic cells are sensed by formyl peptide receptor 1 (FPR1) and TLR9, respectively, which leads to neutrophil activation and tissue infiltration.<sup>79</sup> The second step relies on cardiac endothelial cells, which are activated by pro-inflammatory cytokines that can induce overexpression of adhesion molecules responsible for the migration of neutrophils to the injured site and through the endothelial cell layer.<sup>79</sup> After arriving at the injured site, neutrophils phagocytose damaged cells and form NETs. In this case, NETs serve as scaffolds for the aggregation of erythrocytes and platelets to grow thrombus, or interact with monocytes.<sup>80</sup> Following this, monocytes and macrophages are recruited to internalise cellular debris and engulf apoptotic cardiomyocytes. This inflammatory response aims at removing

dead cells and matrix debris to create a clean environment for the next proliferative phase. However, the inflammatory response is usually overactive, with infiltrating immune cells spreading beyond the border of the MI area, and prolonged, which can lead to expansion of the injury.<sup>81,82</sup>

An anti-inflammatory reparative phase, during which inflammation is suppressed to help wound healing and scar formation, follows the pro-inflammatory phase. During the anti-inflammatory reparative phase, neutrophils, monocytes, macrophages, and other immune cells either undergo apoptosis or retreat from MI area (the fate of immune cells was discussed in detail in section 1.1.1),<sup>83</sup> whilst mesenchymal stem cells deposit extracellular proteins to preserve the structural integrity of the infarcted heart. The adult mammalian heart has a limited number of stem cells able to form new tissue but contains an abundant population of interstitial and perivascular fibroblasts. These cells can transdifferentiate into myofibroblasts to secrete matrix proteins. In addition, cardiac fibroblasts, bone marrow-derived fibroblast progenitors, and endothelial cells can transdifferentiate into mesenchymal cells, smooth muscle cells, and pericytes and these cells might also contribute to the infarct myofibroblast population. All these cells start to proliferate and finally culminate in reparative myocardial fibrosis and scar formation. These phenomena affect the structure of the ventricular chamber, which exhibits a thinner wall and a larger heart size. These structural changes lead to ventricular dilatation and reduced ejection fraction,<sup>84</sup> which often culminates in total heart failure and death.<sup>85</sup>

### *Liver*

Excessive inflammation in the liver is detrimental, as it can cause liver fibrosis, systemic metabolic alterations (*e.g.* obesity, diabetes), alcoholic hepatitis, ischemia reperfusion injury and eventually lead to irreversible liver damage.<sup>86</sup> Chronic liver diseases developed from inflammation such as non-alcoholic fatty liver disease (NAFLD) are one of the leading causes of mortality and morbidity in the United States.<sup>87</sup>

The liver is the largest internal organ in the body and its main function is to filter the blood coming from the digestive organs, in order to break down substances, extract nutrients and energy, and detoxify toxins. As such, the liver may also absorb toxic compounds, cell debris and dangerous molecules from pathogens, which lead to infectious inflammation and sterile

inflammation.<sup>88</sup> Infectious inflammation in the liver is usually caused by microorganisms. For example, the persistence of hepatitis C virus (HCV) infection may cause chronic inflammation in the liver and eventually lead to cirrhosis and hepatocellular carcinoma.<sup>89</sup> Sterile inflammation in the liver typically results from alcoholic or non-alcoholic steatohepatitis,<sup>90,91</sup> ischemia reperfusion injury, and exposure to toxic drugs.<sup>92</sup>

In terms of the underlying molecular and cellular mechanisms, infectious inflammation and sterile inflammation possess similar receptors and pathways, many of which are activated by both PAMPs and DAMPs. For example, both bacterial LPS and cellular HMBG1 are able to activate TLR4, which is involved in the NF- $\kappa$ B pathway and in the production of inflammatory cytokines. Following PAMP and DAMP activation, pro-inflammatory cytokines are produced, which activate and recruit Kupffer cells (a specific type of macrophages in the liver) and immune cells. Sustained recruitment of these cells prolongs the inflammation response, eventually leading to hepatocyte damage and/or cholestasis.<sup>93,94</sup>

### *Lung*

The lung is the primary organ of the respiratory system. Usually, lung inflammation is caused by exposure to bacteria, viruses, and environmental pollution. Acute inflammation can cause pulmonary fibrosis and impair gas exchange while chronic inflammation is associated with many diseases such as cystic fibrosis, asthma, and chronic obstructive pulmonary disease (COPD) that lead to lung injury.<sup>95,96</sup> Smoking, one of the biggest causes of illness and death in the United Kingdom, is the main risk factor for the development of COPD as it can induce inflammation of the small airways and lung parenchyma.<sup>97</sup> During the chronic inflammation caused by smoking, neutrophils, macrophages, and activated T lymphocytes infiltrate into the airways and induce the production of ROS, proteases, chemokines, and cytokines in the lung, which aggravate the inflammation response and ultimately lead to irreversible lung damage.<sup>98</sup>

### *Kidney*

Kidney inflammation often contributes to renal injury that can result in a variety of diseases such as glomerulonephritis, acute and chronic kidney diseases.<sup>99</sup> According to a recent study, around 10-12% of people are suffering from chronic kidney diseases; furthermore, approximately 50% of elderly patients shows signs of kidney dysfunction.<sup>100</sup> Infection, ischemia reperfusion, and immune-complex *in situ* formation or deposition are the main

inducers of kidney inflammation. During the inflammation process, stimuli such as PAMPs, DAMPs, and TLRs activate transcription factors (NF- $\kappa$ B or MAPK), which mediate genes for the innate and adaptive immune response. Renal tubular epithelial cells promote the secretion of different inflammatory cytokines, and these cytokines trigger leukocytes infiltration into renal tubules and corpuscles.<sup>101,102</sup> Acute and chronic kidney inflammation lead to extensive loss of glomeruli, tubular injury and fibrosis.

### *Brain*

Brain inflammation occurs in several central nervous system (CNS) diseases including neurodegenerative diseases (*e.g.* Parkinson's disease (PD) and Alzheimer's disease (AD)), autoimmune diseases (*e.g.* autoimmune encephalitis and central nervous system vasculitis), and epilepsy.<sup>103,104</sup> The inflammatory response in the brain can cause the up-regulation of neuronal excitability, neural cell damage, and enhancement of blood brain barrier (BBB) permeability, a highly selective semipermeable membrane formed by endothelial cells and astrocytes to separate the brain from the peripheral tissues. CNS diseases-concomitant inflammation originates from either the activation of immune cells and microglia in the brain or from the attack of the damaged brain tissue by immune cells activated from innate and adaptive immune system.<sup>105</sup> Stimuli such as TLRs and DAMPs can trigger an inflammation response in the brain; for example, DAMPs (*e.g.* heat-shock proteins) can easily enter the brain through the damaged BBB and initiate pro-inflammatory cascades. Similarly, the activation of PRRs, TLRs, and RAGE contribute to the NF- $\kappa$ B pathway activation, promoting cell death and participating in neuro-inflammatory processes.<sup>106</sup>

## 1.2. Treatments of inflammation

Inflammation is implicated in the pathogenesis of many diseases including autoimmune conditions (*e.g.* RA), cardiovascular disease (*e.g.* MI), and CNS diseases (*e.g.* AD). Chronic inflammation may lead to irreversible tissue damage, making these diseases a major cause of mortality globally, which account for three out of five deaths.<sup>107</sup> As such, a variety of effective anti-inflammatory drugs have been developed to suppress inflammation *via* different pathways for the treatment of acute or chronic inflammation (Figure 1.6). In the next section, different anti-inflammatory drugs in clinical trials or available on the market will be discussed.

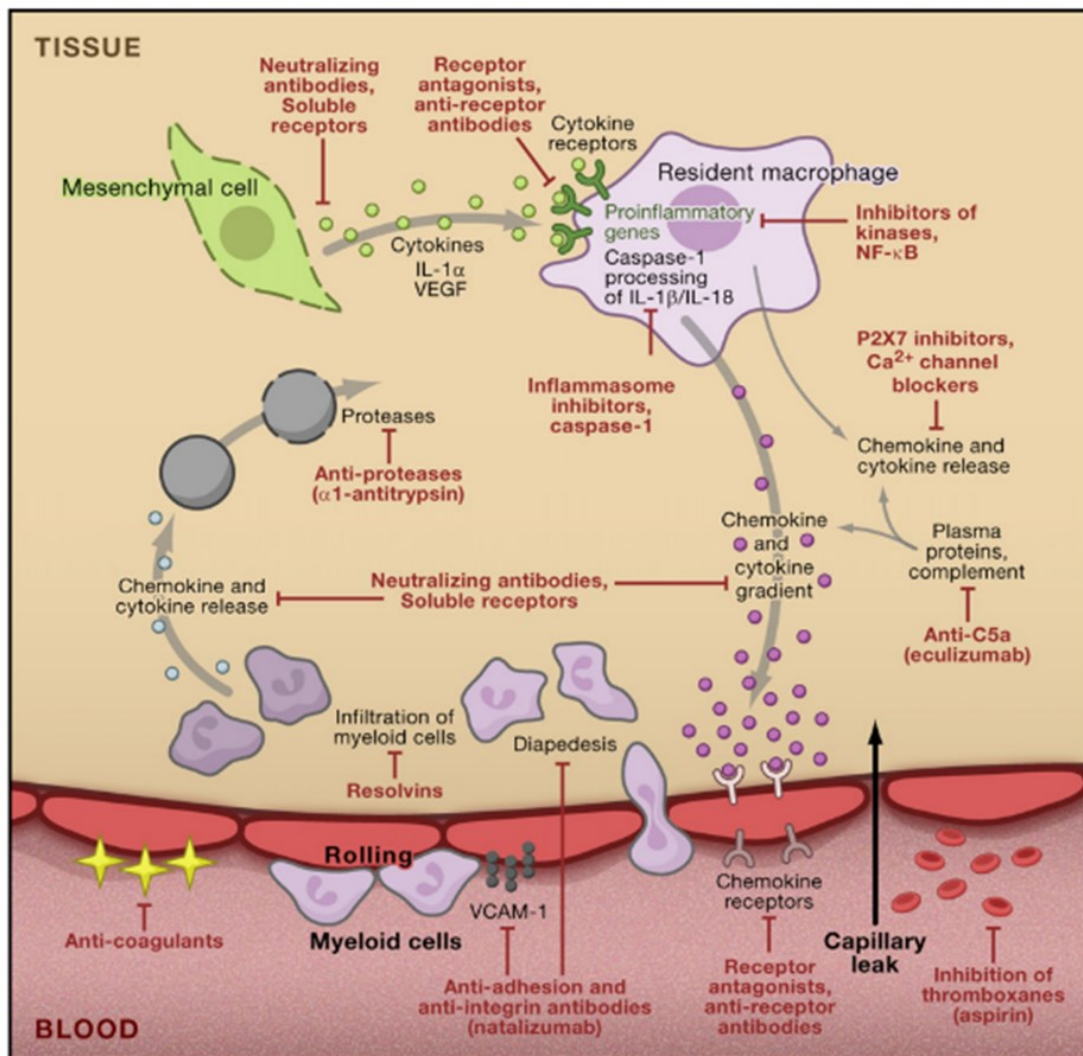


**Figure 1.6 Different points of inhibition by anti-inflammatory drugs.** The image is showing different inflammatory pathways involved in ischemia-induced tissue injury. Different types of drugs that will be discussed below can suppress inflammation via blocking one or several different points in the pathway. Adapted from Dinarello et al. with permission from Elsevier.<sup>108</sup>

### 1.2.1. Anti-inflammatory drugs

#### *Orally active drugs*

Several drugs that can be administered orally such as methotrexate (MTX), dexamethasone (DEX), cyclosporine, and tacrolimus, are usually employed for the treatment of autoimmune diseases. Because of their broad immune suppression properties, they also possess anti-inflammatory properties and have been used to treat many acute and chronic inflammatory

diseases such as cardiovascular disease and inflammatory bowel disease. The most widely used drug is MTX. At high doses, MTX is able to inhibit folic acid synthesis, which has been shown to reduce cell proliferation;<sup>109</sup> this mechanism is utilised when MTX is administered at high concentrations ( $\sim 350 \mu\text{g mL}^{-1}$ ) for cancer treatment. However, at lower doses (10 times lower), MTX can also decrease the production of TNF- $\alpha$ , IL-6, and other chemokines, which is the mechanism exploited for anti-inflammatory applications.<sup>110</sup> For example, MTX has been used to treat chronic heart failure post MI: after 3 months of treatment, patients exhibited decreased levels of TNF- $\alpha$ , IL-16, MCP-1, and IL-10.<sup>111</sup> DEX, another immune suppressant, achieves anti-inflammation effects primarily by inhibiting leukocytes infiltration at the inflammation site and suppressing the expression of inflammatory mediators.<sup>112</sup> 19 months after DEX treatment post acute decompensated heart failure (ADHF), patients had lower cardiac mortality, which is the result from the anti-inflammation effect of DEX.<sup>113</sup> Cyclosporine and tacrolimus are also used broadly for different clinical applications, such as the treatment of allograft rejection and T cell-mediated diseases. Their mechanism is to inhibit the production of IL-2 and IFN- $\gamma$ , which can further suppress the production of TNF- $\alpha$  from lymphocytes.<sup>108</sup>

#### *Prostaglandin inhibitors*

Inflammatory prostaglandins (PGE<sub>2</sub>) lower the pain threshold and their production can be reduced by prostaglandin inhibitors during the inflammation to decrease pain. Two pathways are involved in the synthesis of PGE<sub>2</sub>: the cyclooxygenase (COX)-1 pathway, which is responsible for low levels of PGE<sub>2</sub> and mediates homeostasis in healthy conditions, and the COX-2 pathway, which induces high levels of PGE<sub>2</sub> associated with inflammatory diseases. Hence, the COX-2 pathway is the main target of this type of anti-inflammatory drugs.<sup>114</sup> Drugs such as aspirin can inhibit both the COX-1 and COX-2 pathways,<sup>115</sup> while some specific COX-2 inhibitors, such as celecoxib, have shown effective pain reduction in patients with osteoarthritis or RA.<sup>116</sup>

#### *Glucocorticoids*

Glucocorticoids are widely used for the treatment of autoimmune diseases and are able to mitigate inflammation by lowering the expression of several cytokine-induced genes. Glucocorticoids can enter cells and bind to steroid receptors in the cytoplasm; the formed



complex translocates to the nucleus and is recognised by DNA, which binds to it. This binding suppresses the activation of transcription factors activator protein 1 (AP-1) and NF- $\kappa$ B, which account for the expression of genes that encode almost all the pro-inflammatory cytokines. Glucocorticoids are also able to affect T cell growth by suppressing the expression of IL-2, IL-4, IL-15, and IFN- $\gamma$  or to inhibit the COX-2 pathway to reduce inflammation.<sup>117,118</sup>

### *IL-1 blockers*

IL-1 blockers have been shown to be effective for auto-inflammatory diseases, which are chronic inflammatory diseases characterised by macrophage dysfunction and local or systemic inflammation. Some of these auto-inflammatory diseases result from gain-of-function mutations that can activate caspase-1 to induce the release of IL-1 $\beta$ .<sup>119</sup> For example, the auto-inflammatory disease hyper IgD syndrome has mutations encoding mevalonate kinase<sup>120</sup> and can be managed by blocking IL-1 $\beta$  expression. IL-1 blockers have also been shown to be effective for the treatment of brain diseases: the decrease of the IL-1 $\beta$  activity reduces the number of circulating neutrophils and the level of IL-6 in stroke patients. Moreover, less neurological impairment is observed.<sup>121</sup> In the case of heart diseases, animal studies have shown that the reduction of IL-1 expression prevents post-MI remodelling<sup>122</sup> whilst a study on MI patients demonstrated improved left ventricular end-systolic volume index after treatment with anakinra, a human IL-1 receptor antagonist, for 14 d.<sup>123</sup> Among all the IL-1 blockers, canakinumab and Xoma 502 are the most effective. Canakinumab was approved by the FDA in 2009 to treat cryopyrin-associated periodic syndromes (CAPS) including familial cold autoinflammatory syndrome, Muckle-Wells syndrome, and neonatal onset multi-inflammatory disease.<sup>124</sup> Canakinumab and Xoma 502 are now in clinical trials for the treatment of gout, Behcet's disease, and coronary artery disease.

### *Resolvins*

During inflammation, besides main pro-inflammatory molecules, infiltrating neutrophils and monocytes also release anti-inflammatory molecules such as eicosapentanoic acid (omega-3), PGE<sub>3</sub>, and leukotriene B<sub>5</sub> (LTB<sub>5</sub>). Resolvins of E series (RvE1 and RvE2) derived from the oxidation of omega-3 fatty acids are ubiquitous across inflammatory sites in mammals.<sup>125</sup> RvE1 molecules downregulate the expression of leukocyte adhesion molecules and induce neutrophil apoptosis, which accelerates the anti-inflammation phase, and can also reduce the

production of IL-12 by dendritic cells.<sup>126</sup> Recently, synthetic RvE1 was successful in a Phase II clinical trial for the treatment of dry eye inflammation. In many animal studies, resolvins have been shown to decrease the number of migrating neutrophils and macrophages at the inflammatory site and also downregulate TNF- $\alpha$  and IL-1 $\beta$  gene expression.<sup>127</sup> Resolvins of D series are derived from docosahexaenoic acids and have been shown to activate specific receptors, which result in an anti-inflammatory effect.<sup>128</sup> Apart from their anti-inflammation properties, resolvins can also have an effect on many inflammation-concomitant diseases. For example, in different debris tumour models, a reduction in the chemotherapy-induced tumour debris was observed after the administration of RvE1, RvED1 or RvD2,<sup>129</sup> whilst biosynthesised RvE1 inhibited the development of 2,4,6-trinitrobenzene sulfonic acid-induced bowel inflammation in a colitis mouse model.<sup>130</sup>

#### *Histone deacetylase inhibitors*

Histone deacetylases (HDACs) and histone hyperacetylases (HATs) are two classes of enzymes that have opposite effects in chromatin compacting. HDACs can improve histone DNA wrapping, thus inhibiting the binding of transcription factors to gene promoters which down-regulate gene expression, while HATs loosen histones-DNA complex to initiate gene expression.<sup>131</sup> Currently, synthetic HDAC inhibitors have been extensively studied for the treatment of several solid tumours,<sup>132</sup> parasitic,<sup>133</sup> and inflammatory diseases.<sup>134</sup> Some *in vitro* and *in vivo* studies suggested that HDAC inhibitors can reduce the secretion of inflammatory cytokines and nitric oxide (NO), which are mediators that usually initiate and sustain inflammation in a variety of inflammatory diseases. For instance, HDAC inhibitor butyrate reduced IL-8 expression in colonic epithelial cells by 80%, which suggests that the use of butyrate could be effective for the treatment of ulcerative colitis.<sup>135</sup> Additionally, butyrate was shown to prevent LPS-induced maturation of dendritic cells<sup>134</sup> and reduce the expression of IL-2 in T-cells,<sup>136</sup> thus highlighting the ability of butyrate to regulate inflammatory cells. Another HDAC inhibitor, uberoylanilide hydroxamic acid (SAHA), was tested in a colitis disease model where it induced a decrease in the production of proinflammatory cytokines such as TNF- $\alpha$ , IL-6, and IFN- $\gamma$ .<sup>137</sup> Some HDAC inhibitors have also been studied clinically as anti-inflammatory drugs with positive outcomes. A good example is ITF2357, an orally active inhibitor, which was administered at a daily oral dose of 1.5mg/kg to patients with active systemic onset juvenile idiopathic arthritis in a Phase II clinical trial. After

receiving the treatment for 12 weeks, more than 75% of patients reported a reduction in joint pain and a significant suppression of systemic symptoms was detected.<sup>138</sup>

### 1.2.2. Challenges of using anti-inflammatory drugs

Although suppression of inflammation using anti-inflammatory drugs has been achieved in studies and clinic trials, achieving sufficiently high systemic concentrations of these drugs is still hampered by poor bioavailability and bio-stability<sup>139</sup>, undesirable off-target effects<sup>140</sup>, and obstacles of biological barriers<sup>141</sup>. At the same time, using these anti-inflammatory drugs often causes a lot of severe side effects.

The first challenge is solubility and bio-stability of these drugs. Most of the nonsteroidal anti-inflammatory drugs (NSAIDs) exhibit low solubility in water and limited drug absorption at the disease site. Some anti-inflammatory proteins such as IL-1Ra suffer from decreased potency over time because of reduced bioactivity in biological environments.<sup>139</sup> Another challenge is non-specific absorption by healthy tissues upon systemic administration of the drugs. Most of the injected dose will be cleared *via* hepatic metabolism, which results in a lower drug concentration in the target tissue while the extra drug cleared in the liver can cause hepatotoxicity. Oral drugs for colon-associated diseases might lose their activity in the acidic environment of the stomach or might be absorbed in an upper segment of the intestine before reaching the target site. Furthermore, biological barriers such as the BBB, blood vessels, skin, or small intestines dramatically reduce the delivery efficiency of anti-inflammatory drugs to the inflamed tissue. For example, the BBB prevents most of the drugs to be taken up by the brain. Small molecular drugs may be able to cross the BBB through lipid-mediated free diffusion but only when the molecular weight of the drug is below 400 Da and forms < 8 hydrogen bonds.<sup>141</sup>

The use of anti-inflammatory drugs often causes side effects, such as suppression of the host defence against infections. For example, progressive multifocal leukoencephalopathy (PML), a rare and fatal viral disease which causes brain damage and inflammation, often occurs in patients following treatment with immunosuppressive drugs.<sup>142</sup> Orally-active drugs such as MTX and DEX have serious side effects including hepatotoxicity, opportunistic infections, bone marrow suppression, and pulmonary hypersensitivity,<sup>143,144</sup> which are caused by rapid drug clearance in the liver and host immune suppression. NSAIDs such as prostaglandin

inhibitors were reported to induce gastroduodenal toxicity, cardiovascular toxicity, hypertension, and acute renal failure.<sup>140</sup> Histone deacetylase inhibitors such as SAHA and MS275 failed in clinical trials because of their cytotoxicity, which can lead to cell-cycle arrest and apoptosis.<sup>140</sup> Therefore, the development of a drug delivery system that can encapsulate different poorly soluble or toxic anti-inflammatory drugs and locally deliver drugs to the inflammatory site with minimum exposure to undesired tissues is an avenue of research with great potential.

### 1.3. Nanoparticle-based drug delivery for inflammatory diseases

During the past two decades, several nanoparticle-based drug delivery strategies have been successfully developed for the treatment of various cancers, cardiovascular disorders, and inflammatory diseases.<sup>145</sup> These strategies utilise synthetic or naturally-derived materials, or a combination of both, as the base materials for nanoparticle fabrication. The use of nanoparticles to encapsulate drugs has enabled to modulate some key properties of the drug, such as solubility, stability, blood circulation half-life, toxicity, and immunogenicity. Furthermore, nanoparticles surface functionalisation with moieties including antibodies, peptides, and aptamers has increased the targeting efficiency of nanoparticles.<sup>146,147</sup>

#### 1.3.1. The history of nanoparticle-based delivery systems

The first report of a nanoparticle therapeutic system can be traced back to 1954 when Jatzkewitz *et al.* used a short peptide spacer to conjugate mescaline to polyvinylpyrrolidone to control its release profile *in vivo*.<sup>148</sup> In the mid-1960s, Bangham discovered liposomes.<sup>149</sup> These two events marked the birth of the nanoparticle-based drug delivery field. Many nanoparticle formulations have been investigated, of which liposomes and polymeric nanoparticles are the most widely-used nanoparticle-based therapeutics on the market (Figure 1.7).

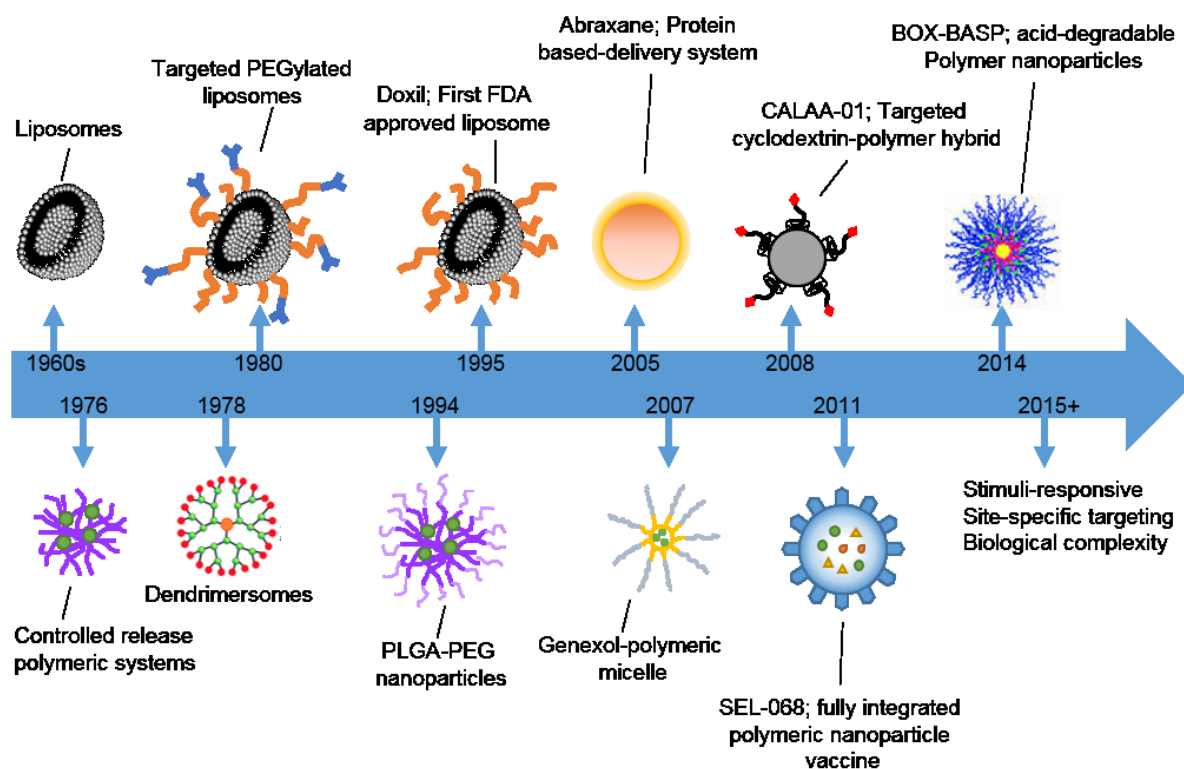


**Figure 1.7** The timeline of therapeutic nanosystems. Reproduced from Brittany L. Banik *et al* with permission from Wiley.<sup>150</sup>

In the 1980s, when Maeda *et al.* conjugated poly(styrene-co-maleic acid) with the cytotoxic drug neocarzinostatin (SMANCS), they found that the SMANCS conjugate had enhanced accumulation at the tumour site compared to the free drug. This phenomenon is known as the enhanced permeability and retention (EPR) effect<sup>151</sup> and is based on the assumption that the inherently leaky tumour vasculature allows nanoparticles to escape from blood circulation and accumulate in the tumour tissue. However, this phenomenon is only observed when the nanoparticle has a size ranging from 10 to 100 nm.<sup>152</sup> The smaller nanoparticles will be rapidly cleared by the kidneys whereas the larger ones will be removed by the reticuloendothelial system. This crucial breakthrough has given researchers a powerful tool in the design parameters of drug delivery vehicles.

In the same decade, the first nanoparticle therapeutic Sandimmune (a mixture of cyclosporine and Cremophor encapsulated in micelles) was approved by the FDA and marketed by Novartis. In 1989, the FDA approved the first controlled-release polymer formulation, an implantable form of goserelin acetate marketed as Zoladex by AstraZeneca to treat certain types of

prostate and breast cancer.<sup>153</sup> Since then, several types of nanocarriers have been investigated for drug delivery, with current efforts focussing on the development of smart drug delivery systems that incorporate several chemical modifications for increased targeting efficiency or stimuli-responsiveness.<sup>154,155</sup> A few selected ones with relevance to the anti-inflammation applications are discussed below.

### 1.3.2. Liposomes

In 1965, Alec Bangham and colleagues reported the discovery of a swollen phospholipid system, which later became known as liposome.<sup>156</sup> In the next few years, Gregoriadis *et al.* developed various liposomal formulations for drug encapsulation, thus highlighting the potential of liposomes as drug delivery platforms.<sup>157,158,159</sup>

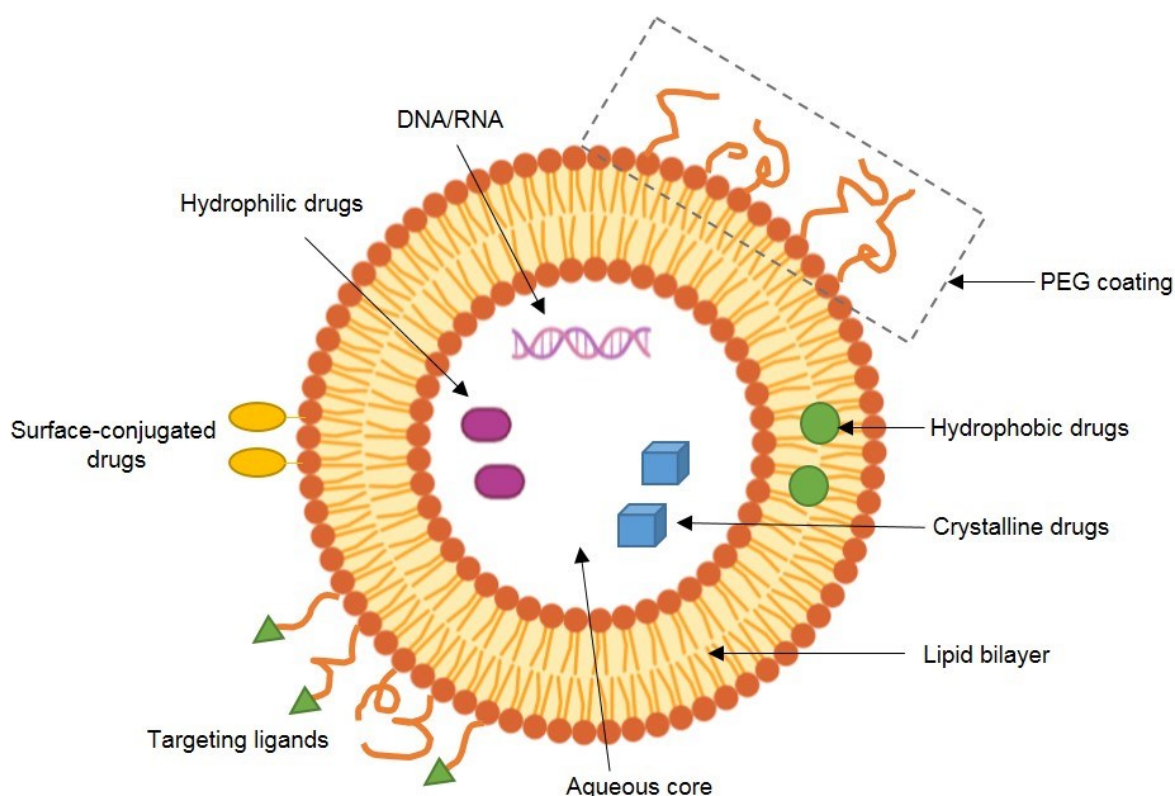


**Figure 1.8 Structure and surface modifications of liposome-mediated drug delivery systems.** Drugs with different properties can be encapsulated in the aqueous core, incorporated into the lipid membrane or conjugated to the surface of liposomes. Different surface functionalisation strategies including the use of targeting molecules, PEG and stimuli-responsive molecules can improve drug delivery efficiencies mediated by liposomes. The surface of liposomes can be functionalised with PEG to increase liposomal circulation times, whilst targeting ligands can be conjugated on the surface to enhance receptor-mediated endocytosis by desired cells.

Liposomes are spherical nanoparticles formed by one or several lipid bilayers enclosing an aqueous core. According to their structure, liposomes can be classified as: 1) Multilamellar vesicles (MLVs), which comprise several concentric bilayers and exhibit sizes ranging from 500 to 5000 nm. 2) Unilamellar vesicles, which have only one lipid bilayer and can be formulated in the size range from 50 to 1000 nm depending on the envisaged application. Liposomes can load hydrophilic drugs in their aqueous core and hydrophobic drugs in the lipid bilayer. Hydrophobic drugs can easily be inserted into the fatty acyl chain region of the lipid bilayer of liposomes. The loaded hydrophobic drugs can also be released easily since the hydrophobic membrane does not act as a barrier for these drugs. In contrast, drugs of high hydrophilicity are retained in the aqueous core of the liposomes and are only slowly released over hours to days, due to the hydrophobic barrier of the liposome membrane. Some drugs of intermediate solubility can readily move between the lipid bilayer, the aqueous core and the exterior aqueous phase, which leads to their rapid release from liposomes. However, manipulating pH of the aqueous core of liposomes or formulating drug complexes within liposomes can increase loading and extend the retention time of weak bases, such as doxorubicin, in liposomes.<sup>160,161</sup> Liposomes have many favourable biological properties when used as drug carriers: 1) they increase the stability of encapsulated drugs; 2) they are biocompatible, biodegradable and non-immunogenic for either systemic or non-systemic administration; 3) when loading toxic drugs like Doxorubicin, liposomes can decrease the toxicity to other tissues; and 4) surface modifications can be performed to introduce active targeting.<sup>162</sup> As such, some liposomal formulations have been approved as medicines. Two best known examples are liposomal doxorubicin named as Doxil that is used for the cancer treatment,<sup>163</sup> and liposomal amphotericin B named as AmBisome, used for fungal infections.<sup>164</sup>

Liposomes are also a very popular drug carrier in the applications of treating inflammatory diseases such as RA, multiple sclerosis, uveitis, and inflammatory bowel disease. The first study using a liposomal formulation for the treatment of inflammation was conducted by Dingle *et al.* in 1970s, which used liposomes composed of lectin and phosphatidic acid to deliver cortisol palmitate in a rabbit model of RA and observed a reduction of the joint temperature and joint diameter after intra-articular administration. More studies on local administration of different liposomal formulations were carried out swiftly. Korting *et al.* reported the earliest work using a liposomal formulation loaded with corticosteroids to treat

inflamed skin *via* applying the gel on the skin surface,<sup>165</sup> whilst Tremblay *et al.* firstly used DEX encapsulated liposomes to treat lung inflammation *via* intranasal instillation.<sup>166</sup> PEG-coated liposomes were also shown to have sustained drug release properties after intraocular injection in a rat model of uveitis, thus could reduce repeated injections.<sup>167</sup> Another study used MTX loaded liposomes to treat MI in rats for 6 weeks *via* intraperitoneal injection and achieved a 40% improvement of systolic function in left ventricle, reduced cardiac dilation and smaller infarction size.<sup>168</sup>

Furthermore, chemical modification strategies that involve the use of targeting molecules, stimuli-responsive molecules, poly(ethylene glycol) PEG and so on have greatly accomplished better targetability, controlled drug release, and longer *in vivo* circulation upon systemic administration (Figure 1.8). One example is a study using Arg-Gly-Asp modified PEG-liposomes to deliver DEX in a rat model of adjuvant-induced arthritis.<sup>169</sup> Liposomes were shown to bind to the vascular endothelial cells at the site of inflammation after a single *i.v.* administration, which provided a prolonged anti-inflammatory effect. Varying the surface charge of liposomes can be used to modulate targeting of mucosa. Positively charged liposomes showed better adhesion to healthy mucosa and negatively charged liposomes preferably adhered to inflamed mucosa,<sup>170</sup> thus targeting inflamed mucosa can be achieved by modifying liposome surfaces with negative charges. In another study, DEX loaded liposomes were conjugated with sialyl-Lewis X to target activated endothelial cells and this system showed a two-fold higher DEX concentration accumulated in the inflamed eyes *in vivo*.<sup>171</sup>

Currently, some liposome-based products developed for the treatment of inflammatory diseases are in different stages of clinical trials. For example, prostaglandin E-1 (PGE-1) encapsulated liposomes named as Liprostin<sup>TM</sup> have been developed for treating various cardiovascular diseases. PGE-1 can suppress inflammation and reduce the formation of thrombi, and Liprostin<sup>TM</sup> achieved great outcomes in peripheral vascular disorder in phase II trials.<sup>172</sup> However, some disadvantages of liposomes still remain. Liposomes have low chemical and physical stability due to potential oxidation and hydrolysis of the phospholipids and a membrane thickness of about 4 nm. Low versatility compared to polymer-based nanoparticles and the issue of drug leakage are other limitations of liposomes.



### 1.3.3. Polymeric nanoparticles

Polymeric nanoparticles such as micelles, dendrimers, and vesicles (called polymersomes), have been developed to readily introduce different properties to the nanoparticles due to the chemical versatility of polymers. The design of polymeric nanoparticles started from the simple micelle structures to smart multi-stimuli responsive systems.

Several formulation parameters such as the fabrication temperature, the solvent in which the polymer is dissolved, or the polymer hydrophilicity and stability, as well as structural parameters such as particle size, zeta potential, and morphology need to be tailored to the specific application.<sup>173</sup> Polymeric nanoparticles can be formulated by either inducing macromers self-assembly in solution *via* solvent evaporation, nanoprecipitation, dialysis, and super critical fluid techniques, or *via* direct monomer polymerisation, which is based on emulsion, interfacial, or controlled/living radical polymerisation techniques.<sup>173</sup> In the drug delivery field, several biodegradable polymers have been shown to self-assemble into a myriad of structures able to encapsulate and controllably release chemical drugs and biological cargos. These systems can be designed to achieve target-specific nanoparticle accumulation, protection of sensitive drugs, controlled release, and prolonged blood circulation time.<sup>174</sup>

Polymeric micelles and polymersomes are the most widely used polymeric nanoparticles in the drug delivery field. Polymeric micelles are formed by amphiphilic block copolymers with a core-shell structure. A variety of drugs including hydrophobic molecules, nucleic acids, and proteins can be encapsulated into the core *via* incorporation of different core-forming blocks in the copolymers. Polymeric micelles have some advantages as a drug delivery system; they have a high drug loading capacity, a slow dissociation rate to retain drugs for a long time, and allow easy surface functionalisation.<sup>175</sup> When copolymers are designed to have a hydrophilic fraction ranging from about 25% to 40%, they can self-assemble to form polymersomes in aqueous solutions.<sup>176</sup> Similar to liposomes, polymersomes can encapsulate hydrophilic molecules in the aqueous core and hydrophobic molecules in the membrane. However, polymersomes have distinct properties; their membrane thickness can be tuned *via* changing the molecular weight of the hydrophobic block, which then determines the permeability, mechanical stability, and elasticity of the polymersomes. Compared to liposomes,

polymersomes have better stability, longer drug retention times, and surface functionalisation can be achieved by various routes using the diversity of polymer chemistry in combination with coupling strategies.<sup>177</sup> Thus, polymersomes are an interesting nanocarrier to be evaluated for treating chronic inflammatory diseases.

Polymeric nanoparticles have been investigated for the treatment of inflammatory diseases. For example, biodegradable methoxypoly(ethylene glycol)-poly(caprolactone) (mPEG-PCL) micelles were used to encapsulate the poorly water-soluble quercetin for the treatment of acute cystitis in mice and a reduction of inflammatory cell infiltration in the bladder was observed.<sup>178</sup> Hammer *et al.* designed a type of leuko-polymerosome able to mimic leukocyte adhesion in the blood flow towards inflamed sites due to the conjugation of specific leukocyte adhesion molecules on their surface, which can be potentially used for monitoring or treating inflammation and cardiovascular diseases.<sup>179</sup> The main issues associated with polymeric nanoparticles are: polymers are not molecularly define structures and polymer synthesis usually has a big batch-to-batch variation, which currently prevents many polymeric nanoparticle systems to be translated to the clinic. Moreover, smart polymeric nanoparticles with complex polymer structures have scale-up problems.

#### 1.3.4. Inorganic nanoparticles

Inorganic nanoparticles based on silica, gold, silver, and iron oxide have been investigated as platforms for drug delivery and disease detection.<sup>180,181,182</sup> Some of the base inorganic materials used for nanoparticle formulations have already been used clinically for a long time. For example, platinum-based molecules such as cisplatin or carboplatin have been used as drugs for cancer treatment,<sup>183</sup> while silver ions are used to kill bacteria.<sup>184</sup> When formulated as nanoparticles, inorganic materials can exhibit several benefits, such as the ability to load drugs, surface modification, and enhanced tissue targeting through EPR effect. Most importantly, some inorganic materials themselves have unique properties. For instance, gold nanoparticles have the thermal heating property, which has been exploited for cancer thermal therapy.<sup>181</sup> Some functionalised inorganic nanoparticles can be engineered to respond to external stimuli like magnetic fields or light, which can be used to control drug release or for imaging purposes (Figure 1.9).<sup>185</sup>

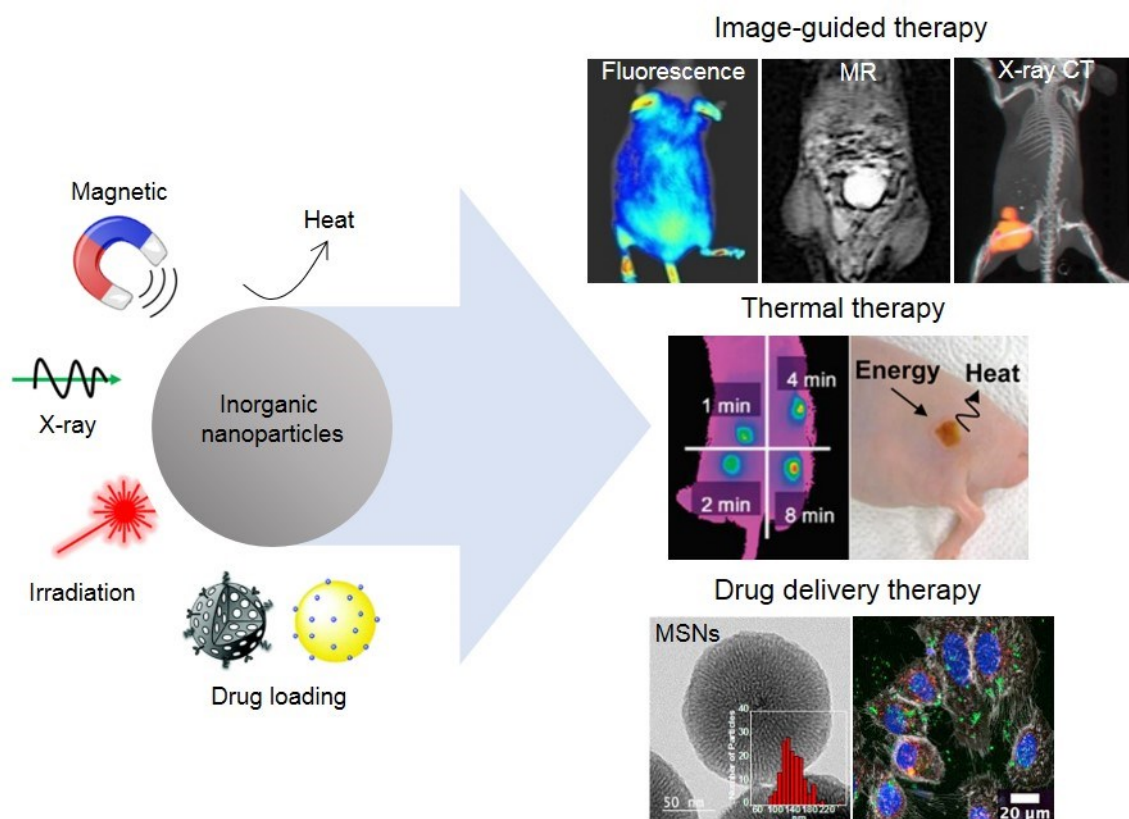


**Figure 1.9 Inorganic nanoparticles used in different biomedical applications.** Many inorganic nanoparticles have favourable intrinsic properties: heat generation upon optical or magnetic excitation, magnetic response, X-ray absorption, irradiation to generate ROS and drug loading. Those properties can be used for fluorescence imaging, magnetic resonance imaging (MRI), computed tomography (CT), thermal therapy and drug delivery applications. Modified from Yoon et al with permissions from ACS Publications.<sup>186</sup>

For drug delivery applications, some solid inorganic nanoparticles can load drugs via surface conjugation. A prominent example are gold nanoparticles. Gold nanoparticles have optical and photothermal functions due to their surface plasmon resonance (SPR) property, which can be precisely controlled by changing size, shape, and structure of gold nanoparticles. These functions provide specific advantages for imaging, diagnosis and therapeutic applications. A variety of therapeutic molecules such as DNA,<sup>187</sup> RNA,<sup>188</sup> proteins,<sup>189</sup> peptides,<sup>190</sup> and drug molecules<sup>191</sup> have been conjugated on the surface of gold nanoparticles *via* covalent or physical absorption. For example, gold nanoparticles conjugated with etanercept, a TNF inhibitor, were shown to successfully deliver the drug to the rheumatic joint and gold nanoparticles played an essential role in enhancing the contrast for photoacoustic imaging to show the delivery process.<sup>192</sup> Currently, few gold nanoparticle products have

entered clinical trials for therapeutic applications and no products have been approved clinically due to the difficulty of optimising surface and physical properties using large animal models<sup>193</sup> and long-term biocompatibility upon systemic administration.<sup>194</sup>

Inorganic nanoparticles can also be formulated to exhibit a porous structure, which allows higher drug encapsulation efficiencies and controlled drug release profiles compared to non-porous structures. A widely explored class of porous inorganic nanoparticles are mesoporous silica nanoparticles (MSNs), which were proposed as a drug delivery platform in 2001, when Vallet-Regí *et al.* encapsulated ibuprofen into MSNs.<sup>195</sup> Because of their tailorable mesoporous structure, high surface area, tuneable geometry, and low polydispersity, MSNs overcome some of the limitations associated to conventional drug delivery systems (organic nanoparticles) such as low and heterogeneous drug encapsulation and uncontrolled pharmacokinetics.<sup>196</sup> The size of the nanoparticle pores determine the molecular size cut-off for drug encapsulation, with macromolecules such as proteins and DNA requiring larger pores.<sup>197</sup> The surface and the mesoporous walls of MSNs can be modified with different functional groups, which allows tuning of surface charge, encapsulation of hydrophilic/hydrophobic drugs, and stimuli-responsive payload release. For example, Lee *et al.* synthesised MSNs functionalised with trimethylammonium able to load and release anionic drug molecules (sulfasalazine) in response to pH changes for the treatment of intestinal inflammation upon oral administration.<sup>198</sup> In another study, Chen *et al.* developed a thermo-responsive MSN drug delivery system. MSNs were coated with poly N-isopropyl acrylamide, which is a thermo-responsive polymer that can change conformation in response to different temperatures to control the cargo release inside MSNs.<sup>199</sup> Moreover, encapsulation of more delicate biological molecules such as proteins and peptides with higher molecular weight within MSNs has been shown to protect these payloads against degradation.<sup>200</sup>

Despite some advantages of using MSNs for drug delivery applications, challenges remain before reaching clinical translation. For example, the long-term *in vivo* fate of MSNs after systemic administration needs to be taken into account since MSNs degrade very slowly.<sup>201</sup> Another concern generates from the large variety of physical properties of MSN. Different parameters such as size, shape, porosity, and surface modification can affect the therapeutic

outcomes for different diseases.<sup>202</sup> Therefore, fundamental studies on the optimization of the physical properties of MSNs are required before entering clinical trials.

### 1.3.5. Virus nanoparticles

Typically, viruses possess a proteinaceous capsid which, in some cases, is covered by a lipid bilayer (enveloped viruses) and are produced inside infected host cells. Using this capsid, the virus can bind to specific receptors on the surface of the host cell to enter the cell; the capsid is then removed and the viral nucleic acid is released in the cytoplasm. The virus exploits the host cell machinery to transcribe, translate, and replicate the viral nucleic acid; the process ends with the assembly of new viruses which exit the host cell to invade new ones.<sup>203</sup> Due to the size of the viral proteinaceous capsid and the possibility of chemically conjugating molecules to the interior and the exterior surface of the capsid, virus-based particles comprising virus coat proteins with defined three-dimensional structures have become one of the most promising candidates for the design of smart drug delivery systems.<sup>204,205</sup>

Functional molecules such as active molecules (*e.g.* small molecular drugs and peptides), targeting molecules (*e.g.* antibodies and proteins), and nanoparticles for imaging (*e.g.* quantum dots and gold nanoparticles) can be conjugated to viral nanoparticles, which can be engineered to release the encapsulated cargo into cells in response to changes in pH, temperature, redox environment or ionic strength (Figure 1.10).<sup>206,207,208</sup>

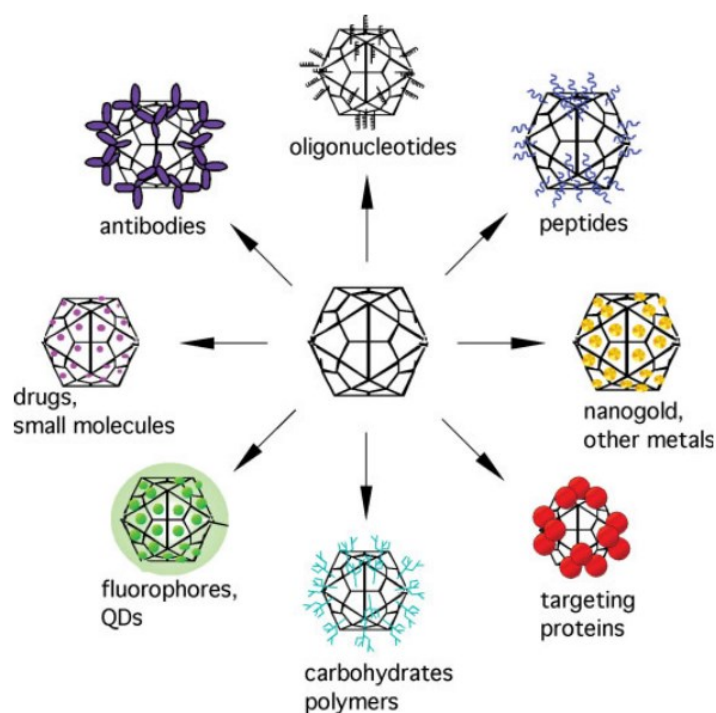


**Figure 1.10 Different cargoes attached to virus nanoparticles.** *Different active molecules, particles, and specific ligands can be attached or genetically modified on the surface of a virus nanoparticle. These includes ligands (such as lysines, peptides, and cysteines), nanoparticles (such as metals and quantum dots (QDs)), and active molecules (such as small molecular drugs, carbohydrates and polymers). The attachment of big molecules such as proteins and antibodies have been achieved without changing their functions. Adapted from Pratik Singh et al with permission from Wiley.<sup>209</sup>*

Virus-based nanoparticles have been evaluated for the treatment of cancer,<sup>210</sup> receptor-targeted delivery,<sup>206,211</sup> and bacterial infection.<sup>212</sup> In the context of inflammation treatment, herpes simplex virus (HSV) has been investigated as a carrier for the delivery of a TNF or IL-1 receptor antagonist and demonstrated inhibited leucocytosis and synovitis in a rabbit arthritis model, which suggests that the HSV-based drug delivery system could be used for the treatment of joint inflammation.<sup>213</sup> Although viruses possess many advantages and design flexibility, their application in nanomedicine is still in its infancy, with only a few products in preclinical trials. The biggest challenge associated with the use of viral vectors is the unpredictability of their immunogenic effect. For example, human adenoviruses have been largely explored for gene delivery but may induce severe toxic effects even at low doses.<sup>214</sup> Additionally, although most of the plant and animal viruses are less likely to induce antiviral

responses as they do not replicate in humans, their regular capsid structure could cause an immunostimulatory response.<sup>215</sup>

### 1.3.6. Challenges of using nanoparticle-based drug delivery systems

A recent study showed that currently 247 nanomedicine products were approved by the FDA or are at various stages of clinical trials.<sup>216</sup> Among them, there are about 100 products currently approved for commercial use (Table 1-1), of which drug delivery systems and medical devices are the two dominant products. Drugs usually represent small therapeutic molecules; biomolecules such as proteins, nucleic acid and sugars have not reached clinical application in nanomedicine. Similarly, very few nanoparticle formulations for gene transfection and recombinant DNA technology have reached the market.

Various nanoparticles have been employed to encapsulate drugs. The three most commonly used platforms are liposomes, polymeric nanoparticles and nanocomposites. Furthermore, each of these formulations were classified into nine categories (Figure 1.11) based on the type of application, for example cancer treatment, infectious diseases, and cardiovascular disorders.

Applications	Commercial	Example		
		Product name	Nanostructure	Use
Biological	7	Focetria®	Emulsion	Influenza vaccine
Device	38	Vitoss®	Nanoscaffold	Bone growth
Drug	32	Doxil®	Liposome	Cancer
		Ambisome®	Liposome	Fungal infection
Genetic	0	/	/	/
Other	0	/	/	/
Research use/Exempt	23	Bio-Conjugated Nanoparticles	Colloidal gold	Research use
Total	100			

**Table 1-1 FDA classified commercial products for different applications.** Adapted from Etheridge, M. L. et al with permission from Elsevier.<sup>216</sup>

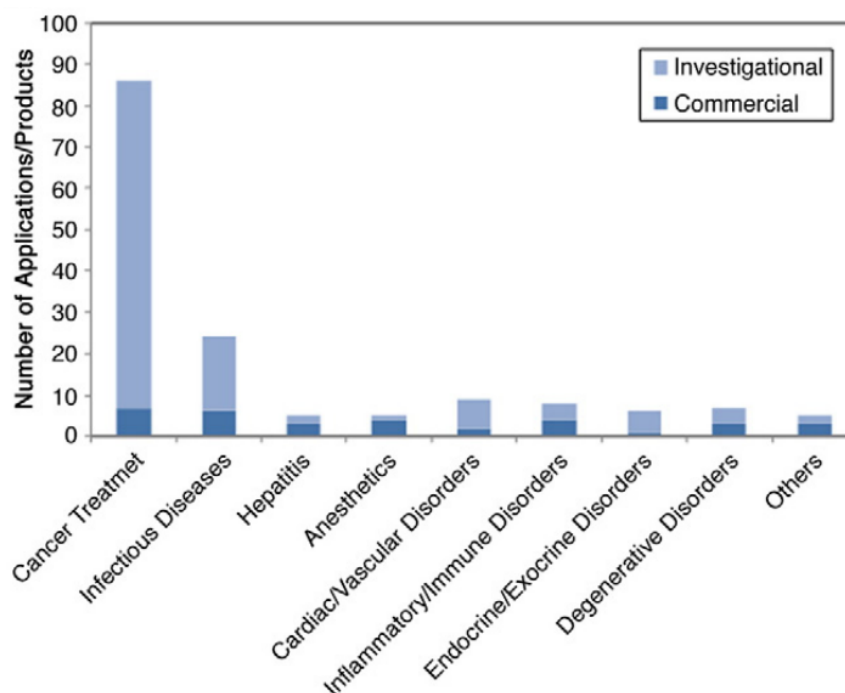


**Figure 1.11 Medical applications for approved nanomedicines.** Adapted from Etheridge, M. L. et al with permission from Elsevier.<sup>216</sup>

Despite more than 700,000 studies on nanomedicines that have been published by the end of 2019, only a few entered clinical trials as described above, which indicates the low yield of nanomedicine products. The main issues for nanoparticle-based drug delivery are the different biological barriers that limit bioavailability of nanoparticles at disease sites (Figure 1.12).

The major barrier is sequestration of nanoparticles by the mononuclear phagocyte system (MPS), which are mainly resident macrophages in the liver, spleen, and lymph nodes phagocytosing nanoparticles immediately after injection. Upon injection into the bloodstream, plasma proteins including serum albumin, immunoglobulins, and apolipoproteins absorb on the surface of nanoparticles to form a protein corona.<sup>171,217</sup> The formed protein corona changes the surface properties of the nanoparticles; as a result, nanoparticles end up in the liver and spleen instead of targeting the disease site because they are recognised by specific receptors on the surface of macrophages. To solve this issue, some ‘stealth’ nanoparticles were developed. The most widely used strategy is conjugating PEG on



the surface of the nanoparticles, wherein ethylene glycol units can form a hydrating layer by absorbing water molecules to prevent/delay plasma protein absorption.<sup>218</sup> The best application of using this approach is PEG functionalised doxorubicin-liposomes, whose blood circulation time was increased from minutes to hours.<sup>219</sup> However, recent studies reported that this strategy generates PEG-specific IgM antibodies that can accelerate the clearance of PEG coated nanoparticles upon repeated administrations.<sup>220,221</sup>

Nanoparticles also encounter several other physiological obstacles including endothelial barrier, the BBB, cell membranes and intracellular clearance before releasing the drug inside the target cells.<sup>222</sup> The endothelial barrier is the first physiological barrier that nanoparticles will encounter before reaching the target tissue. The continuous endothelium forms a barrier between blood vessels and tissue to control the exchange of small molecules, which also limits the transport of nanoparticles from the bloodstream to the target tissue. Under pathological conditions such as cancer, the EPR effect is pronounced to potentially enhance the nanoparticle accumulation in the tumour. However, this effect is mostly seen in artificial mouse models with rapid tumour growth and due to the variable nature of cancer only a small number of patients with tumours have high levels of EPR.<sup>223</sup> In the case of inflammatory diseases, the EPR effect is not observed in most inflamed tissues, thus requiring active targeting approaches to achieve localised delivery of drugs. Another big barrier is the BBB. The BBB is the tightest endothelium that only allows transport of nutrients while blocking harmful substances to protect the brain. When delivering therapeutics to the brain, only nanoparticles with a size smaller than 200 nm have chances to cross the BBB and several parameters such as shape, ligand density and surface charges can dramatically influence the transport efficiency. It is important to note that the highest delivery efficiency to the brain after intravenous administration is no more than 5% of the initial injection dose.<sup>224</sup> As such, brain delivery requires delivery systems able to actively transport drugs.

In term of specific challenges for anti-inflammation therapy, the main issue is that the inflammation-targeted drug delivery systems need to alter and maintain the dynamic balance of pro- and anti-inflammation. Inflammation is a finely dynamic process involving several sensors and feedback pathways. As such, drug delivery systems that only sense and target one inflammation pathway may result in a suppressed host defence or even induce a compensatory pro-inflammation response *via* other pathways.<sup>225</sup> For example, excessive

inflammation following MI usually impairs the infarcted heart; however, using broad-range anti-inflammatory drugs *e.g.* NSAIDs and corticosteroids can disrupt the clearance of dead cells and suppress the functions of fibroblasts, which is harmful for the subsequent heart repair. Thus, altering and maintaining the inflammation balance is the main challenge for the treatment of MI.<sup>226</sup> Moreover, for chronic inflammation, it is necessary to have a sustained drug delivery system to reduce the number of repeated doses.

Thus, immune cell-mediated drug delivery is a promising alternative strategy for the treatment of inflammatory diseases because immune cells have the inherent functions to sense and respond to dynamic inflammatory signals, which allows them to actively migrate to inflammatory sites. Therefore, this strategy might solve one of the main challenges of targeted anti-inflammation therapy.

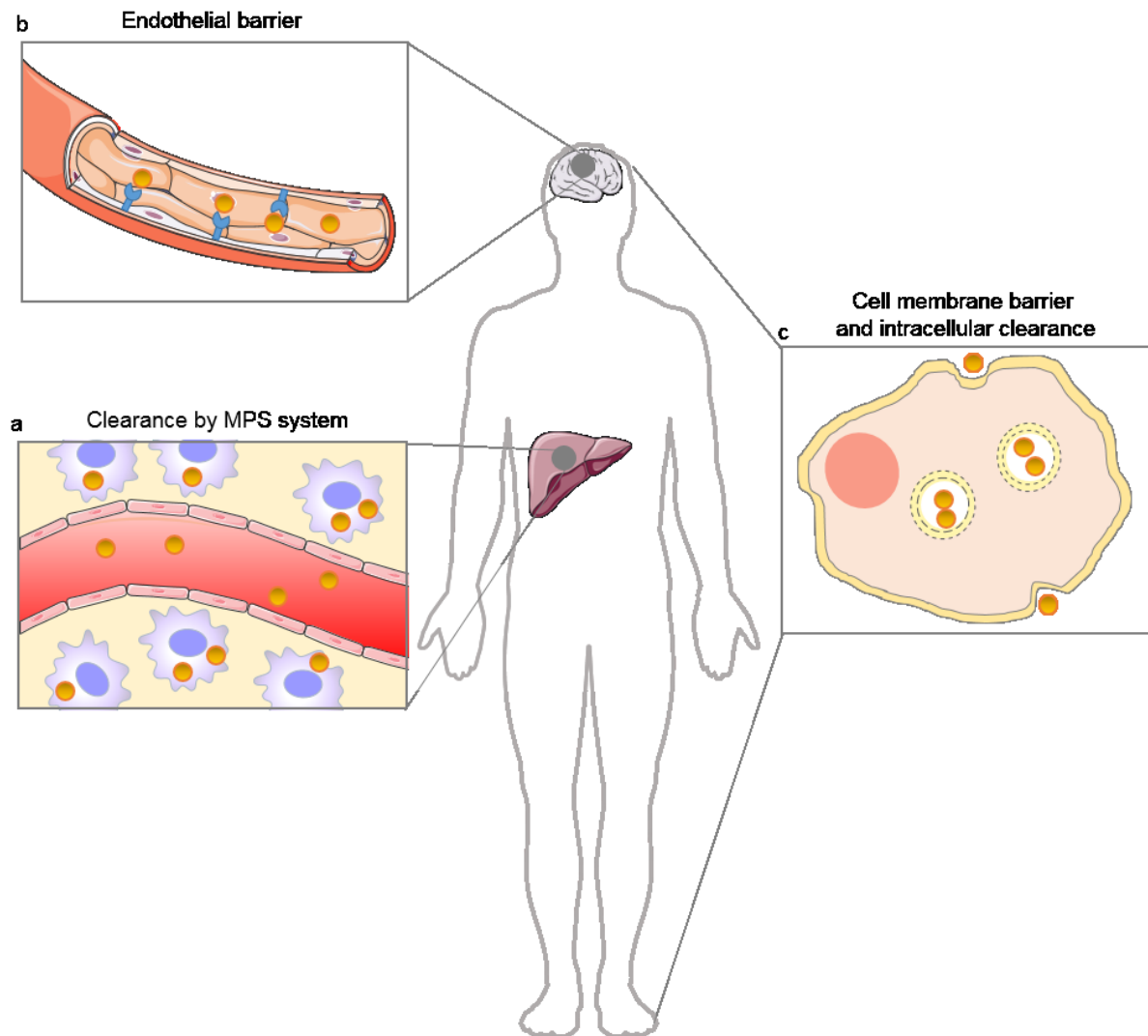


**Figure 1.12 Physiological barriers hindering nanoparticle-based drug delivery.** *a*, Upon intravenous administration, nanoparticles undergo phagocytosis by resident macrophages of the MPS system, which leads to non-specific biodistribution in undesired organs such as the liver and spleen. *b*, Nanoparticles face endothelial barriers that prevent particle extravasation into the target tissue. *c*, After arriving at the target cells, nanoparticles need to be taken up by the cells and escape from the endo-lysosomal system into the cytoplasm to release the payloads.

#### 1.4. Cell-mediated drug delivery

Cell-mediated drug delivery has been recently proposed as an alternative delivery strategy to overcome some of the limitations associated with oral or systemic nanoparticle administration. Cell-mediated drug delivery strategies leverage the natural properties of cells, such as specific tropism to injured sites, flexible morphology and long circulation time to achieve maximum targeting efficiency as well as minimum side effects.

### 1.4.1. Different types of cell carriers

Several cell types including erythrocytes, immune cells, and stem cells have been explored as cell carriers to load drugs or drug-loaded nanocarriers. Each cell type has its unique advantages for different applications such as sustained drug release properties and the ability of targeting inflammatory sites.

#### 1.4.1.1. Erythrocytes

Erythrocytes (or red blood cells) are the most abundant type of blood cells and their main physiological function is to deliver oxygen to tissues *via* blood flow through the circulatory system. Erythrocytes possess unique advantages, including blood circulation times up to 100–120 d before macrophage phagocytosis, the ability to cross capillaries with diameters of 2 – 3  $\mu\text{m}$ , a biconcave flexible shape gives a very high surface to volume ratio with a reversible transformation property, a large inner cavity due to the absence of a nucleus and other organelles, and intrinsic biodegradability.<sup>227</sup> These properties make erythrocytes suitable candidates for the encapsulation of different molecules whilst maintaining their native immunological and biochemical functions. Ihler *et al.* first proposed the use of erythrocytes for enzyme encapsulation in 1973.<sup>228</sup> Since then, erythrocytes have been explored as smart carriers to deliver various pharmacological agents including anti-inflammatory agents,<sup>229</sup> enzymes,<sup>228</sup> peptides, nucleic acids, and drug-loaded nanoparticles.<sup>230,231</sup>

There are two main methods to formulate erythrocyte-based drug delivery systems. The first method entails the encapsulation of payloads inside isolated erythrocytes *ex vivo*; this method is based on the ability of erythrocytes to reversibly open membrane pores under hypotonic conditions. The second method consist of payload conjugation to the surface of erythrocytes.<sup>232</sup> Both methods have been studied and optimised for clinical translation.

There are two main advantages that erythrocytes can offer as biological carriers. First, erythrocytes can provide sustained drug release into the vascular system due to their prolonged circulation time in the blood. For example, erythrocytes loaded with DEX exhibited sustained drug release over 7 d in a patient study.<sup>229</sup> Secondly, erythrocytes are good candidates as carriers for the delivery of drugs to the organs of the reticuloendothelial system, such as the liver and the spleen, as they are eventually degraded in these organs.<sup>233</sup> However, erythrocytes cannot actively migrate across the endothelium, which make them unsuited for

the delivery of drugs to the sites of tumours, inflammation and infection. They are also unable to actively release payloads. Therefore, when the drug needs to be delivered outside the vascular system, immune cells and stem cells are considered more suitable options.

#### 1.4.1.2. Immune cells

In non-pathological conditions, the endothelium forms a monolayer lining the blood vessel wall to regulate the permeability of plasma into tissues. The inter-endothelial passage is usually <3 nm wide, which is smaller than many drugs and most nanoparticles.<sup>234</sup> As such, it is extremely challenging to deliver drugs or drug-loaded nanoparticles across this impermeable barrier to the target site. However, upon occurrence of an infection, tissue injury or cancer, our innate and adaptive system rapidly responds to the concomitant inflammation by activating and recruiting millions of immune cells to cross the endothelial vessels and infiltrate into inflamed tissues (details were discussed in section 1.1). Therefore, immune cells are promising vectors to transport drugs or drug-loaded nanoparticles across the endothelial barrier and release them at the inflamed site.

##### *Neutrophils*

Neutrophils are one of the most abundant immune cells and reach and infiltrate the inflammatory tissue in the early stage of inflammation.<sup>235,236</sup> Additionally, once recruited to the inflammatory site, neutrophils can rupture and release NETs within few hours to eliminate extracellular microorganisms (for more details, see section 1.1).<sup>35</sup> This defined release mechanism enables the potential for the rapid release of neutrophil-loaded drugs or loaded nanocarriers at the early stage of inflammation. However, the development of neutrophils as 'Trojan horses' to deliver therapeutics to different sites is still in its infancy. Previous studies are listed in Table 1-2. There are two strategies to formulate drug/nanocarrier neutrophil hybrids, depending on the place of cargo loading, which is either done *in vivo* or *ex vivo*. In most cases, researchers formulated drug-loaded nanoparticles that can target activated neutrophils in the bloodstream. Following intravenous injection, the nanoparticles are uptaken by activated neutrophils in the bloodstream and carried to the disease site. For example, Chu *et al.* reported that nanoparticles produced from denatured BSA (albumin nanoparticles) can efficiently target activated neutrophils in the bloodstream.<sup>237</sup> They observed that upon intravenous injection, the albumin nanoparticles were internalised by

neutrophils and carried across blood vessels into the inflamed lung in a mouse model of LPS-induced lung inflammation. A similar strategy achieved monocytes/neutrophils targeting in the bloodstream using cyclic arginine-glycine-aspartate (cRGD)-modified liposomes.<sup>238</sup> An alternative approach to formulate drug/nanocarrier neutrophil hybrids is to load the isolated neutrophils with drugs or nanocarriers *ex vivo* and to reinject the hybrids into the bloodstream. A recently published study loaded neutrophils with paclitaxel-liposomes *ex vivo* to deliver paclitaxel to the inflamed brain tissue after *i.v.* injection.<sup>239</sup> However, the lifespan of neutrophils is only about 5 d in circulation and a few hours after isolation from blood, which poses some limitations in terms of applicability. Nonetheless, neutrophils are able to rapidly respond to inflammatory factors and to transport drugs/nanocarriers in a few hours, making them attractive as drug delivery carriers.

Nanoparticles		Drug	Administration	Disease model	Reference
Denatured nanoparticles	BSA	Pyropheophorbide-a	<i>i.v.</i> injection of nanoparticles; target activated neutrophils	Melanoma with TA99 antibody induced inflammation	240
Denatured nanoparticles	BSA	TPCA-1 and cefoperazone acid	<i>i.v.</i> injection of nanoparticles; target activated neutrophils	LPS-induced lung inflammation and bacterial infection	237
Cationic liposomes		Paclitaxel	Formulate liposome loaded neutrophils <i>ex vivo</i> ; <i>i.v.</i> injection of loaded neutrophils	Glioma surgical resection model	239
CI PGP-PEG-DGL/CAT-Aco nanoparticles		No drug	<i>i.v.</i> injection of nanoparticles; target activated neutrophils	Focal cerebral ischemia	241
Poly(sialic acid) decorated liposomes		Pixantrone	<i>i.v.</i> injection of nanoparticles; target activated neutrophils	Xenograft A549 tumour model	242
cRGD liposomes		Edaravone	<i>i.v.</i> injection of nanoparticles; target activated neutrophils	Cerebral ischemia	238
Sialic acid modified liposomes		Dexamethasone and palmitate	<i>i.v.</i> injection of nanoparticles; target activated neutrophils	Adjuvant arthritis model	243

**Table 1-2 Neutrophil-mediated delivery systems deliver drug-loaded nanoparticles to different disease sites.**

### *Monocytes*

Monocytes are white blood cells which can differentiate into macrophages once they leave the blood flow (for more details, see section 1.1). Monocytes/macrophages have been widely investigated as cell carriers due to their ability to reach many sites within the body, such as the hypoxic and necrotic regions of tumours, inflamed brain regions, and tissues releasing inflammatory signals. As such, monocytes/macrophages have been utilised as a cellular Trojan horse for cancer and PD treatment. Brynskikh *et al.* loaded an antioxidant enzyme, catalase, able to attenuate neurodegeneration, into bone marrow-derived macrophages. This system was able to penetrate the BBB and reach the neuro-damaged site.<sup>244</sup> In an anti-tumour study, peritoneum-derived macrophages were loaded with liposomes encapsulating doxorubicin for controlled delivery to the tumour tissue upon systemic administration in a subcutaneous and a metastatic xenograft tumour models.<sup>245</sup> However, it is important to emphasise two points when using monocytes/macrophages as carriers. Firstly, macrophages have two different phenotypes: a pro-inflammatory M1 phenotype and a reparative M2 phenotype. When using macrophages for anti-inflammation applications, such as suppressing neuro-inflammation in the brain, the change of the macrophage phenotype to M1 after drugs/nanocarriers loading can exacerbate inflammation at the disease site. Secondly, while neutrophils form NETs to release loaded drugs within a few hours, the release of internalised drugs from monocytes/macrophages is less defined and can be sustained up to 7 d after reaching the disease site. A possible drug release mechanism for macrophages is to emit/transfer exosomes with encapsulated drugs to adjacent cells.<sup>246</sup>

#### 1.4.1.3. Stem cells

Stem cells can self-renew and differentiate into multiple cell types and play a crucial role in tissue repair and regeneration, which has enabled the use of stem cell therapy for regenerative medicine and tissue engineering. In the drug delivery field, a number of studies have demonstrated that genetically modified stem cells are able to express and release therapeutic molecules such as growth factors and enzymes, making stem cells good candidates for cell-mediated drug/gene delivery.<sup>247</sup> Furthermore, due to the intrinsic reparative and regenerative properties of stem cells, loading drugs with stem cells can be beneficial for current stem cell therapy. For example, mesenchymal stem cells (MSCs) could simultaneously express the functional rolling machinery to target the inflammatory site and



cytokine IL-10 for inflammation suppression upon mRNA transfection.<sup>248</sup> Studeny *et al.* also transduced MSCs with the human IFN- $\beta$  gene and used them to induce tumour regression in a metastatic melanoma model.<sup>249</sup> Another stem cell type, neural stem cells, was employed to carry the oncolytic drug 5-fluorouracil, which migrated to intracerebral melanoma and resulted in a nearly 71% lower tumour burden.<sup>250</sup> Generally, stem cells are easy to harvest and culture *in vitro* and they can be transduced with genes to stably express therapeutic proteins or they can be loaded with drugs. These properties render stem cells a promising tool for targeted drug delivery.

## 1.4.2. Methods of cell carrier loading with nanoparticles

### 1.4.2.1. Internalisation of nanoparticles by cells

The intrinsic ability of cells to phagocytose foreign substances can be utilised for the internalisation of nanoparticles to achieve drug-nanocarrier loaded cells. This method consists of incubating nanoparticles with cells *ex vivo* for sufficiently long times to allow nanoparticle internalisation, followed by removing the excess nanoparticles by centrifugation. Immune cells such as monocytes, macrophages, and neutrophils are phagocytic cells so they are able to internalise a variety of inorganic (*e.g.* gold nanoparticles, silica nanoparticles)<sup>251</sup> and organic nanoparticles (*e.g.* liposomes, polymersomes).<sup>245</sup> Nanoparticle phagocytosis by cells depends on several parameters such as nanoparticle size, morphology, surface charge, and mechanical properties of the materials. Specifically, nanoparticles have been shown to exhibit higher phagocytosis efficiencies compared to a larger size scale.<sup>252</sup> The particle shape at the point of initial contact has been shown to be relevant for macrophage phagocytosis, which is hampered when the angle between the normal to the initial cell/particle contact point is greater than 45°. <sup>253</sup> Rigid structures are preferentially uptaken by macrophages: for example, macrophage internalisation rate of rigid polyacrylamide microbeads was 6 times higher than those soft microbeads.<sup>254</sup> The effect of the nanoparticle surface charge on phagocytosis is still controversial. Generally, positively charged nanoparticles have a higher cell uptake efficiency compared to neutral and negatively charged nanoparticles because of favourable electrostatic interactions between positively charged nanoparticles and the negatively charged cellular membrane. For example, macrophages phagocytose positively charged particles due to positive charges interacting with negatively charged sialic acid groups

on the macrophage membrane. However, in the case of negatively charged, poly(acrylic acid)-conjugated liposomes, a higher macrophage uptake occurred through the scavenger receptor recognition mechanism.<sup>255</sup> It is important to point out that the surface charge may also induce cytotoxicity as positively charged nanoparticles cause membrane damage either directly or by detachment of absorbed polymers.<sup>256</sup> Thus, both the charge density and the particle concentration need to be carefully optimised when incubating with cells. The main advantage of using the internalisation method is that the cell membrane remains intact and prevents the nanoparticles from being cleared or interacting with healthy tissues. The main limitation of this method is that after being internalised the nanoparticles might be destroyed in the complex cytoplasm environment.

#### 1.4.2.2. Non-specific absorption

Nanoparticle conjugation to the cell surface through passive absorption is perhaps the simplest method for nanoparticle loading with cells. Due to the presence of negatively charged phosphate, carboxylate, and sialic acid groups on the surface of mammalian cells, cationic nanoparticles can easily be attached to the cell surface *via* electrostatic interactions.<sup>257</sup> However, the same cytotoxicity issue generated from the positive charge needs to be considered when using this strategy. Apart from electrostatic interactions, passive absorption can be also achieved *via* hydrophobic interactions, Van der Waals forces, and hydrogen bonding. Polystyrene particles, for example, can be absorbed on the surface of erythrocytes to prolong circulation.<sup>258</sup> This absorption is achieved due to the nature of the proteins on the erythrocyte surface binding to the particles *via* hydrogen bonds and Van der Waals interactions. This method requires minimal modification of the cell and the nanoparticle. However, there are two main drawbacks using this method: (1) nanoparticles detachment can occur *in vivo* due to the weak cell-nanoparticle interactions; (2) the nanoparticles on the cell surface are exposed to the biological environment, in essence changing the cell surface that could cause recognition and clearance by the RES system. This method is only suitable for cells without the phagocytosis ability.

#### 1.4.2.3. Ligand-receptor binding

Another method to bind particles to cell surfaces is to utilise specific ligand-receptor interactions. In a recent study, doxorubicin-silica nanoparticles were loaded to MSCs through

the antibody-antigen binding. The silica nanoparticles were conjugated with a monoclonal antibody to specifically bind to CD73 and CD90 proteins on the MSCs membrane, and this strategy finally achieved a loading capacity of 1500 nanoparticles per cell. Importantly, the formed nanoparticle-cell complexes can still perform cell's native functions.<sup>259</sup> Other specific interactions which have been investigated to form particle-cell complexes include Fc receptor interaction<sup>260</sup> and biotin-(strept)avidin interaction.<sup>261</sup> The receptor-ligand binding strategy has several advantages, due to process reproducibility, minimal alteration of the cellular functions and membrane integrity. For some specific receptor-ligand pairs, this method can be translated into *in vivo* binding in the blood circulation. However, the binding affinity may sometimes not be strong enough to support the attachment before complexes reach the target site and low specificity of receptors results in non-specific binding to non-target cells.

#### 1.4.2.4. Covalent conjugation

Covalent nanoparticle conjugation to the cell surface offers stronger stability of the cell-particle interaction compared to either absorption or ligand-receptor binding. This method utilises functional groups present on the cell membrane, for example, thiol and amine groups present on cellular membrane proteins are mostly used due to availability and low toxicity of reaction conditions to form the covalent bonds. The surface of T-cells is rich in free thiol groups, which have been used to covalently conjugate liposomes bearing maleimide groups *via* the thiol-maleimide reaction. More than 100 liposomes were conjugated to each T-cell using this strategy and liposome conjugation did not alter important cell functions, such as proliferation and cytokine secretion.<sup>262</sup> Alternatively, the N-hydroxysuccinimide (NHS) esters are most commonly used for the modification of primary amines on the surface of cells. For example, erythrocytes can be modified with NHS-activated PEG by this method.<sup>263</sup> Among all the available particle attachment techniques to cells, covalent coupling generates the strongest bond between particles and cells. This limits the detachment and uptake of particles in undesired tissues. However, this method requires permanent modification of the cell surface and a specific release mechanism has to be integrated to efficiently liberate the cargo at the target site.

### 1.4.3. Applications of cell-mediated drug delivery

Immune cells can rapidly respond to inflammatory signals in the bloodstream, migrate across the endothelium monolayer, and infiltrate the sites of infections, inflammation, and tumours. By taking advantage of these intrinsic abilities of immune cells, immune cell-mediated drug delivery has the potential to overcome some of the limitations of nanoparticle-based drug delivery for the treatment of various inflammatory diseases.

#### 1.4.3.1. Neutrophil-mediated drug delivery

Neutrophils are the most abundant leukocytes, accounting for 60-70% of the circulating leukocytes. Due to their properties outlined in section 1.1.1.2, neutrophils are an attractive cell carrier to deliver drugs or nanocarriers immediately after inflammation occurs and release loaded drugs/nanocarriers in a short timeframe after forming NETs.

The first study using the neutrophil-mediated delivery strategy for the treatment of lung inflammation was conducted by Chu *et al.* in 2015.<sup>237</sup> They formulated denatured albumin nanoparticles and observed that these nanoparticles can target and be internalised by approximately 30% of activated neutrophils in the bloodstream upon intravenous injection. More importantly, after internalising albumin nanoparticles, neutrophils transported them from blood vessels into inflamed alveoli of mice with LPS-induced lung inflammation. To examine whether neutrophils can deliver therapeutics to improve the treatment of acute lung inflammation, they further loaded albumin nanoparticles with two different therapeutics, a NF- $\kappa$ B inhibitor TPCA-1 and an antibiotic cefoperazone acid (Cefo-A), before intravenously injecting the nanoparticles in the mouse model. TPCA-1 mediated therapy attenuated inflammation by suppressing IL-6 and TNF- $\alpha$  expression, whereas Cefo-A delivery significantly reduced bacterial proliferation in the lung after *pseudomonas aeruginosa* infection.

Another important application of neutrophil-mediated drug delivery is the delivery of drugs across the BBB to reach the brain. Neutrophils are a promising carrier for efficient delivery of drugs to the brain due to their ability to cross the BBB. Xue *et al.* used neutrophils to efficiently deliver paclitaxel (PTX)-loaded liposomes to a tumour site in the brain (Figure 1.13).<sup>239</sup> Compared to the previous example, neutrophils were first isolated and then loaded *ex vivo* before reinjection. They formulated cationic liposomes encapsulating PTX, which were internalised by neutrophils *ex vivo* without altering cellular viability and physiological

functions such as superoxide anion generation and surface protein expression. After surgical tumour resection, neutrophils loaded with PTX-liposomes were guided by inflammatory signals generated from the brain surgery, migrating towards the tumour cells in the inflamed brain after *i.v.* injection. 8h post injection, the highest accumulation of neutrophils in the brain was observed, but the signal was quickly reduced because of NETs formation, which simultaneously resulted in the release of loaded PTX-liposomes. Compared to free PTX-loaded cationic liposomes delivery, neutrophil-mediated PTX-liposomes delivery achieved a much higher PTX accumulation in the brain (Figure 1.13a) and extended the 50% survival rate nearly two times in a postoperative malignant glioma recurrence mouse model.

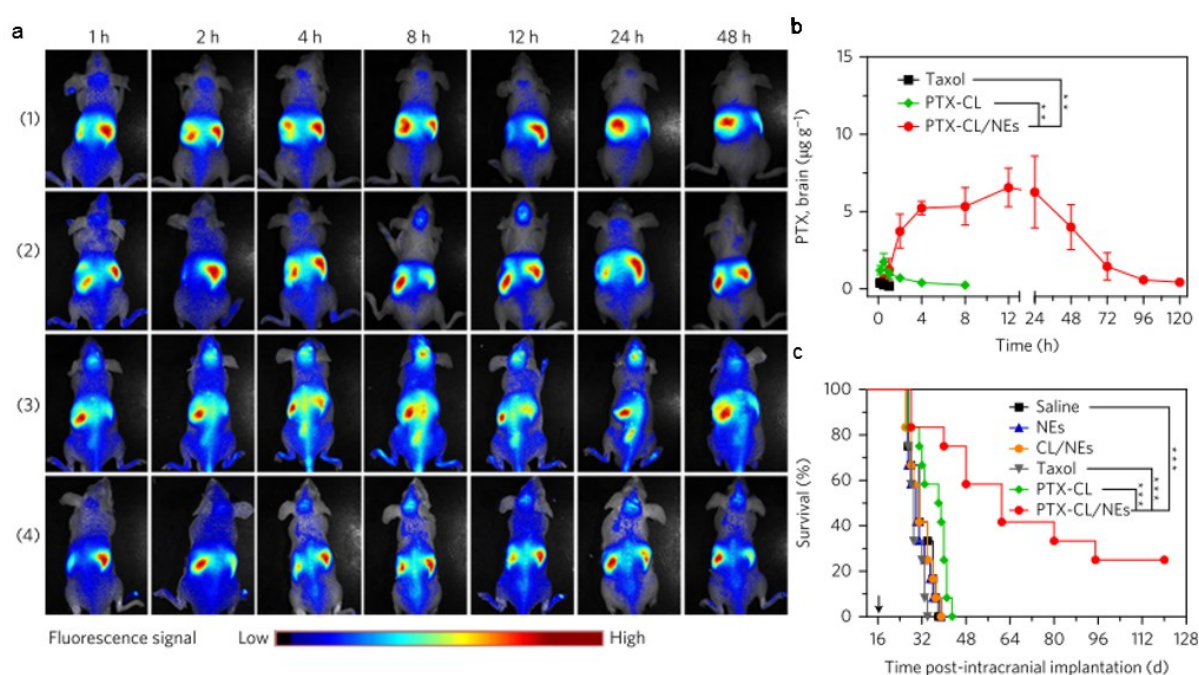


**Figure 1.13 Neutrophil-mediated PTX-liposome delivery for anti-cancer treatment.** *a*, *In vivo* neutrophil migration and accumulation in the brain of (1) healthy mice, (2) brain tumour-bearing mice, (3) surgically treated brain tumour-bearing mice and (4) sham-operated mice after intravenous injection of labelled PTX-liposome loaded neutrophils. *b*, PTX concentration in the brain. *c*, Survival curves of surgically treated brain tumour-bearing mice after different treatments. Adapted from Xue et al with permission from Springer Nature.<sup>239</sup>

Apart from using neutrophil-mediated delivery to target the tumour site in the brain, another study used cRGD-conjugated liposomes to actively target the surface receptors of monocytes/neutrophils in the circulation and these liposomes were carried by monocytes/neutrophils across the BBB to the cerebral parenchyma in a cerebral ischemia model.<sup>238</sup> Reduced neuro impairment was also achieved when loading cRGD-liposomes with

a neuro-protective drug, edaravone. These examples show that neutrophils are a good cell carrier to delivery drugs/nanocarriers to the brain.

The neutrophil-mediated delivery strategy has also been applied to other disease models including adjuvant arthritis and xenograft A949 tumour models, and the loaded nanoparticles were detected in the desired target tissues (Table 1-2). A big advantage of this strategy is that it can overcome the obstacle of the physiological barriers including the BBB and endothelial barrier that hamper most of the nanoparticle-based drug delivery systems used for the delivery of therapeutics to inflammatory sites. Meanwhile, loaded drugs/nanocarriers are also protected by neutrophils from clearance by the MPS system in the bloodstream. However, the active form of drugs or the integrity of nanocarriers might be affected after being loaded into neutrophils, which need to be considered when choosing the drugs or nanocarriers. Overall, neutrophils can be a promising carrier to actively deliver drugs/nanocarriers to the site of inflammation in the early stage of inflammation, and loaded drugs/nanocarriers can be quickly released as soon as neutrophils release NETs. Several inflammation-related diseases such as cancer, tissue injury, PD, and myocardial infarction (inflammation-induced organ diseases was discusses in section 1.1.2) could be potentially treated by using the neutrophil-mediated drug delivery strategy.

#### 1.4.3.2. Macrophage-mediated drug delivery

Unlike neutrophils that are only present in the early stage of inflammation, macrophages remain present much longer during inflammation, starting from the early inflammation stage up to the late resolution/remodelling stage. Macrophages have been proposed as a cell-based carrier in many applications such as cancer therapy and PD treatment. Zhao *et al.* synthesised catalase nanozymes and loaded them into bone marrow-derived macrophages *via* cell phagocytosis. They demonstrated that macrophages protected the nanozymes from being cleared from the bloodstream and also increased their bioavailability in the brain, spleen, liver and kidney. When this macrophage-mediated nanozyme delivery system was applied in a mouse model of PD, macrophages kept migrating and accumulating in the brain for up to 16 d and hence, the loaded nanozymes were transported *via* macrophages across the BBB to the parenchyma.<sup>264</sup> In another study, nanoparticles composed of silica and anticancer drug doxorubicin were internalised by macrophages *ex vivo* with high loading efficiency, without

affecting cellular viability and phenotype. This hybrid system was then intravenously injected into U87MG-tumor-bearing mice and the injected macrophages were observed to accumulate in the tumour. The drug-loaded nanoparticles were released by the macrophages and successfully suppressed tumour growth whilst causing negligible systemic toxicity.<sup>265</sup>

The longer lifespan of macrophages following isolation enables chemical modification of the cell membrane. For example, Xu *et al.* modified the surface of a mouse macrophage cell line (RAW 264.7) with branched polyamidoamine dendrimers *via* click chemistry without altering cell viability, mobility, and expression of signalling molecules.<sup>266</sup> By using the covalent conjugation method, a strong binding between nanoparticles and macrophages ensures the attachment of nanoparticles on the cell surface during the macrophage migration process, which can take several days.

Due to the long-term migration of macrophages to the inflammatory site, it is important to emphasise that it might take up to 2 weeks for macrophages to carry drugs to the target site after intravenous administration. If inflammation needs to be down-regulated urgently, macrophages might not be an ideal carrier. However, in the context of tissue regeneration, the formation of new functional tissues that can take weeks and requires sustained drug release from the delivery system. Administering drug-macrophage hybrids in the resolution/modelling stage of inflammation for tissue regeneration purposes can benefit from long term migration capabilities of macrophages. Overall, macrophages are an attractive carrier for diseases related to inflammation. Compared to neutrophils, more drug/particle attachment methods can be applied to macrophages, and sustained delivery of drugs/drug loaded particles can be achieved due to the long-term migration property of macrophages.

However, the main issues of cell-mediated drug delivery are the complexity of cells and high costs of preparation of drug-cell hybrids. For instance, neutrophil isolation will take several steps and it is very hard to keep neutrophils alive for more than 24 h. More importantly, it is very important to maintain the state of cells after isolation and during the drug/nanocarrier loading steps in order to ensure the physiological functions of the cells are retained.

Overall, immune cells can be very attractive cell carriers for active transport of drugs and drug-loaded nanocarriers to the site of inflammation for the treatment of inflammatory diseases. This strategy exploits the intrinsic properties of immune cells to migrate and

infiltrate inflamed tissue and deliver drugs/drug-loaded carriers locally and non-invasively. Depending on different migration timeframes and release mechanisms of immune cells, the choice of cell carriers and nanocarriers will ultimately determine in which inflammatory stage the drug can be delivered and the release kinetics of the drug from immune cells.

## 1.5. Scope of the thesis

In recent years, increasing efforts have been put on the design of drug delivery systems for actively targeting to remote inflammatory sites for the treatment of inflammation and associated diseases. Nanoparticle-based drug delivery systems are a powerful tool to encapsulate anti-inflammatory drugs and target inflamed tissues. However, major challenges remain including sequestration of nanoparticles by phagocytic cells and biological barriers such as the endothelium hindering infiltration and accumulation in the inflamed tissue ultimately leading to inefficient local delivery. The work presented in this thesis aims to develop immune cell-mediated drug delivery systems that can take advantage of the physiological properties of immune cells to carry anti-inflammatory drug-loaded nanocarriers to remote inflammatory sites, resulting in downregulation of inflammation and active tissue regeneration (Figure 1.14). The herein proposed immune-cell mediated drug delivery systems provide an alternative strategy to achieve active targeting to inflamed tissue using intrinsic functions of immune cells instead of using chemical engineering to conjugate receptor targeting molecules on the nanocarrier surface. A major advantage of this strategy is that simple nanoparticles are combined with immune cells using a one-step incubation method to finally achieve local drug delivery, which offers additional benefits including improved reproducibility and robustness. Moreover, because immune cells can respond to several inflammatory pathways, the formulated nanoparticle-immune cell hybrids are able to better respond and regulate the dynamic balance of inflammation compared to targeted nanoparticle-mediated drug delivery systems. On the other hand, compared with most of studies using cell-mediated drug delivery systems for the treatment of cancer, the novelty of this study lies in the development of immune-cell mediated drug delivery systems to mitigate the underlying inflammation by directly influencing key inflammatory cytokines in the inflamed tissue. Further, this study aims to pave the way for applying such a strategy for the treatment of myocardial IRI, which represents a disease with a long disease progression period and high relevance to human disease, as investigated herein using a myocardial IRI



mouse model. This opens up the possibility for treating a broad range of inflammatory diseases. The developed systems also have the possibility to be loaded with various drugs and drug combinations to actively influence inflammatory cytokine levels to mitigate inflammation and growth factor levels to promote tissue repair at the same time.

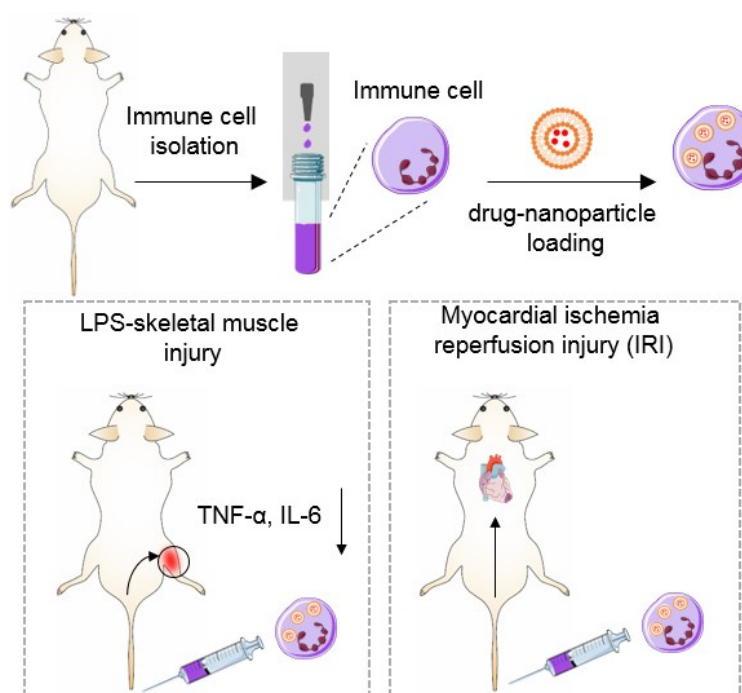


**Figure 1.14 Schematic illustration of the concept of this work.** *Anti-inflammatory drugs are loaded inside nanoparticles. Immune cells (such as neutrophils or macrophages) are isolated from mouse bone marrow and loaded with drug-nanoparticles. The formulated hybrids are intravenously injected to different mouse models of inflammation. In this work, two different models, a LPS-skeletal muscle injury model and a myocardial IRI model, are employed to determine the delivery efficiency of immune cell-mediated delivery systems. After intravenous injection, the hybrids can migrate to the inflamed skeletal muscle and the injured heart respectively. Inflammatory cytokine levels can be down-regulated in the inflamed muscle and cardiac function of the injured heart can be improved after treatment.*

Chapter 1 provides a general overview of inflammation and inflammation induced diseases in organs including a description of inflammatory inducers, cellular responses and organ associated inflammatory diseases. Then, the focus is switched to anti-inflammatory agents and nanoparticle-mediated drug delivery systems developed to improve localised delivery of inflammatory agents and drawbacks of these systems. Finally, cell mediated drug delivery strategies are discussed including cell candidates, methods of nanocarrier loading of cells, and potential applications using immune cell-mediated drug delivery.

Chapter 2 investigates the development of a neutrophil-mediated drug delivery system to deliver an anti-inflammatory agent encapsulated in a nanocarrier to the target cells. Methotrexate (MTX) was chosen to be encapsulated in cationic liposomes (MTX-liposomes) and subsequently loaded into neutrophils *ex vivo*. It is hypothesised that the liposomes protect the carrier neutrophils from premature exposure to the drug to avoid affecting neutrophil physiological functions and viability. In an inflammatory environment mimicking the inflamed tissue site, neutrophils were expected to release loaded MTX-liposomes and subsequently deliver the released MTX-liposomes to target cells (macrophages) where MTX exerts its function.

Chapter 3 investigates cellular interactions of different types of nanoparticles with macrophages to progress towards a macrophage-mediated drug delivery system similar to the neutrophil-mediated system developed in Chapter 2. It is hypothesised that different types of nanoparticles including organic nanoparticles and inorganic nanoparticles with positive and negative surface charges can result in different cellular responses of macrophages after loading *via* phagocytosis, including cell viability and physiological functions. Moreover, after loading with different types of nanoparticles, macrophages can be polarised to pro- or anti-inflammatory phenotypes. The work presented in this chapter aims to optimise various nanoparticle types with modulated surface charge for the development of macrophage-mediated drug delivery systems.

Chapter 4 validates the developed neutrophil-mediated drug delivery system of Chapter 2 in a LPS-injury skeletal muscle mouse model and a myocardial ischemia reperfusion injury mouse model. It is hypothesised that the formulated liposome loaded neutrophils can migrate to the inflamed muscle and the ischemic heart after intravenous injection. After loading the system with MTX and intravenously injecting to the injured mice, it was investigated whether key inflammatory cytokines can be reduced in the LPS injected muscle and cardiac function of the ischemic hearts can be improved after treatment.

Chapter 5 concludes all the findings by briefly describing the major outcomes from this thesis, as well as discussing potential future applications for the systems developed in this thesis.

## Chapter 2

*In vitro* development of a neutrophil-mediated drug delivery system

## 2. *In vitro* development of a neutrophil-mediated drug delivery system

### 2.1. Introduction

Uncontrolled inflammation contributes to a variety of diseases including autoimmunity, myocardial infarction (MI), and cancer.<sup>267</sup> To control the inflammation response, the most common and effective strategy is to deliver anti-inflammatory therapeutics. However, the delivery of such therapeutics locally and in a non-invasive way remains challenging. Many studies have showcased the use of functionalised nanoparticles as nanocarriers to achieve local passive release of therapeutic agents to inflamed tissue.<sup>178,243</sup> Nevertheless, nanoparticle-based drug delivery systems are generally not highly efficient due to sequestration of nanoparticles by phagocytic cells and biological barriers such as the endothelium hindering infiltration and accumulation in the inflamed tissue.<sup>222,268</sup> The mean and medium efficiencies are only 2.24% and 0.76% of the injected dose,<sup>269</sup> which hamper the entry of nanoparticle based drug delivery systems to the clinic.<sup>270</sup>

As illustrated in chapter 1 section 1.1.1.2, immune cells have the inherent properties to migrate and infiltrate inflamed tissue. Thus, immune cells offer a great opportunity as carriers to actively transport drug or drug loaded nanocarriers to inflammatory sites. Among all the different types of immune cells involved in inflammatory responses, neutrophils are one of the most abundant, and also one of the first leukocytes to reach and infiltrate inflamed tissue.<sup>26</sup> More importantly, once recruited to the inflammatory site, neutrophils can rupture and release neutrophil extracellular traps (NETs) within a few hours to eliminate extracellular microorganisms or cell debris.<sup>39</sup> These mechanisms enable site specific and triggered release of cargo from drug- or nanocarrier-loaded neutrophils at early stages of inflammation. For instance, a recent study employed *ex vivo* loaded neutrophils with paclitaxel-encapsulated liposomes to suppress postoperative glioma recurrence after intravenous injection.<sup>239</sup> Another study designed a type of liposomes conjugated with cyclic arginine-glycine-aspartate motif (cRGD) that can attach to neutrophils in the blood circulation.<sup>238</sup> The formulated liposomes were finally delivered to ischemic brain tissue. These examples allow to define the key prerequisites for successful delivery of drug encapsulated nanocarriers *via* neutrophils to the inflammatory site: (1), the chosen nanocarriers can encapsulate a sufficient amount of the therapeutic agents; (2) the formulated drug-loaded nanocarriers can be efficiently

uptaken by neutrophils; (3) the neutrophils can maintain their physiological functions after being loaded with drug-encapsulated nanocarriers; (4) neutrophils can release the loaded nanocarriers in response to inflammatory signals after arriving in the inflamed tissue.

The work presented in this chapter aims at designing, formulating, and optimising a liposome-loaded neutrophil delivery system that meets all the prerequisites described. Liposomes were chosen as the nanocarrier in this chapter because fast drug release properties of liposomes can help mitigating inflammation rapidly in the early stages of inflammation, which is a benefit in case of treating acute inflammation. However, for the treatment of chronic inflammation, nanocarriers with higher stability, such as polymersomes and polymer micelles, can help maintaining nanoparticle integrity inside cells whilst achieving sustained drug release from the hybrid system over longer periods of time. With respect to this, the work of formulation and optimisation of different types of nanoparticles with another type of immune cell will be presented in the next chapter.

In this chapter, it is hypothesised that the liposomes can load sufficient amounts of anti-inflammatory drugs and protect the carrier neutrophils from premature exposure to the drug to avoid affecting neutrophil physiological functions and viability. In an inflammatory environment mimicking the inflamed tissue site, neutrophils can release loaded drug-liposomes and subsequently deliver the released drug-liposomes to target cells where the drug exerts its function. To demonstrate the hypothesis, firstly, the composition of the liposomes was optimised to achieve the highest neutrophil loading efficiency and the lowest cytotoxicity. Particularly, the percentage of cholesterol and the saturation degree of the neutral lipids in the liposome composition were tested to tune lipid membrane properties, aiming at retaining drugs inside liposomes to achieve minimum release within the neutrophils after loading, but efficient release thereafter when delivered at the target site. Secondly, different physiological functions of neutrophils were examined after loading with liposomes (with and without drug), especially functions including cell adhesion and migration that are crucial for their response to inflammatory signals. Thirdly, stimulated formation of NETs and the accompanied release of loaded liposomes from neutrophils were studied. Finally, the delivery of liposomes from neutrophils to target cells existing in the inflamed tissue was investigated by a co-culture system of liposome loaded neutrophils with macrophages in an

inflammatory environment. The subsequent anti-inflammatory effect on the target cells was also investigated. The results provide detailed support to conduct *in vivo* anti-inflammatory treatment using different disease models in mice by injecting this hybrid system as discussed in chapter 4.

## 2.2. Materials and methods

### 2.2.1. Materials

1,2-dioleoyl-sn-glycero-3-phosphocholine (DOPC), 1,2-stearoyl-3-trimethylammonium-propane (18:0 TAP), and 1-palmitoyl-2-oleoyl-glycero-3-phosphocholine (POPC) were purchased from Avanti Polar Lipids. Cholesterol, methotrexate, dexamethasone, bovine serum albumins, edetic acid, Giemsa-Wright stain, 1,1'-Dioctadecyl-3,3',3'-Tetramethylindodicarbocyanine, 4-Chlorobenzenesulfonate Salt (DiD), sucrose, Spectra-Por Float-a-Lyzer G2, 2-[4-(Aminoiminomethyl)phenyl]-1H-Indole-6-carboximidamide hydrochloride (DAPI), wheat germ agglutinin Alexa Fluor 488 conjugate, N-formyl-met-leu-phe, Corning transwell polycarbonate membrane cell culture insert, propidium iodide, cell counting kit-8, TRIzol, Rn18s, TaqMan™ Universal PCR Master Mix, and albumin-fluorescein isothiocyanate conjugate (FITC-BSA) were purchased from Sigma Aldrich. Neutrophil isolation kit, MACS cell separation column, and MACS manual separator were purchased from Miltenyi Biotec. PE anti-mouse CD11b, APC anti-mouse Ly6G/Ly6C, and Zombie green fixable viability kit were purchased from BioLegend. PD-10 minitrap desalting column and PD-10 miditrap desalting column were purchased from GE Healthcare. Dihydroethidium was purchased from MedChemExpress. CellTracker Green CMFDA Dye was purchased from Thermo Fisher Scientific. Direct-zol RNA MiniPrep was purchased from ZYMO RESEARCH. Methotrexate ELISA kit was purchased from Enzo. QuantiTect Reverse Transcription Kit was purchased from QIAGEN.

### 2.2.2. Liposome preparation and characterisation

Cationic liposomes composed of a neutral lipid, a cationic lipid, and cholesterol were prepared using a thin-film hydration method.<sup>271</sup> A variety of lipids and lipid:cholesterol ratios were used in this chapter, which are summarised in Table 2-1.

Composition	Ratio (w:w:w)
DOPC, 18:0 TAP, cholesterol	76:14:10
POPC, 18:0 TAP, cholesterol	76:14:10
POPC, 18:0 TAP, cholesterol	59:16:25
POPC, 18:0 TAP, cholesterol	44:16:40

**Table 2-1 Different compositions and ratios used to prepare liposomes.**

*Preparation of blank liposomes:* neutral lipid, cationic lipid and cholesterol were dissolved in chloroform and organic solvent was removed *via* vacuum rotary evaporation at 65 °C for 2 h. The resulting lipid film was hydrated with PBS at room temperature at a final lipid concentration of 8 mg mL<sup>-1</sup>. Finally, the liposome dispersion was gradually extruded through a 200 nm polycarbonate membrane (Whatman® Nucleopore Track-Etched™ membranes) for 19 times and through a 100 nm polycarbonate membrane for 31 times.

The size of liposomes was measured by Dynamic light scattering (DLS) using a Zetasizer Nano ZS (Malvern). For all the DLS measurements, samples were placed in disposable micro cuvettes and the scattering angle was set at 173°. Each measurement consisted of 35 to 100 runs which were repeated in triplicate at 25 °C. The measurements were averaged and recorded (number mean values). The liposome surface zeta potentials were also measured using a Zetasizer Nano ZS (Malvern). For all the measurements, a 1 mg mL<sup>-1</sup> liposome solution was mixed with 300 mM sucrose at a volume ratio of 5:95 and the mixture was placed in disposable cuvettes. Each measurement consisted of 35 to 100 runs which were repeated in triplicate at 25 °C.

### 2.2.3. Drug loading and retaining in liposomes

Two different drugs, methotrexate (MTX) and dexamethasone (DEX), were encapsulated into liposomes respectively. The loading efficiencies and release profiles were investigated.

*MTX encapsulation:* MTX was first dissolved in PBS. The solubility of MTX in PBS is 1 mg mL<sup>-1</sup>. When preparing MTX solutions with concentrations higher than 1 mg mL<sup>-1</sup>, 0.5 M of NaOH was added portion-wise until the MTX solution was entirely clear. Then, the lipid film was prepared according to the method in 2.2.2 and the MTX solution was added to hydrate the lipid film at room temperature, followed by gradually extruding through a 200 nm

polycarbonate membrane for 19 times and through a 100 nm polycarbonate membrane for 31 times.

*DEX encapsulation:* DEX was first dissolved in a mixture of methanol:chloroform 1:2 (v/v). Then, the lipid solution (lipids and cholesterol were dissolved in methanol:chloroform 1:2 (v/v)) was mixed with the DEX solution and the organic solvent was removed *via* vacuum rotary evaporation at 65 °C for 2 h. PBS was added to hydrate the DEX lipid film for 1 h, followed by gradually extruding through a 200 nm polycarbonate membrane for 19 times and through a 100 nm polycarbonate membrane for 31 times.

The free drug was removed by sequential size exclusion chromatography. 500 µL of the sample after extrusion was added to a PD-10 minitrap desalting column and the flow-through was discarded. Another 1 mL of PBS was added to elute the sample and the eluate was collected in an Eppendorf tube. To improve the efficiency of purification, the eluate was added to a PD 10 miditrap desalting column and was eluted with 1.5 mL of PBS. The final eluate was collected and used for the subsequent study. For imaging purposes, 0.1% 1,1'-Dioctadecyl-3,3,3',3'-Tetramethylindodicarbocyanine, 4-Chlorobenzenesulfonate Salt (DiD) was added to the lipid film to label liposomes. The size and zeta potential of the drug loaded liposomes were measured by DLS and the parameters were set the same as mentioned in 2.2.2.

The size of MTX-liposomes was further confirmed by transmission electron microscopy (TEM). MTX-liposomes were dropped onto a cooper grid (CF400-Cu, Electron Microscopy Science) and stained with 2% fresh ammonium molybdate. After air-dry, the sample was imaged by TEM (JEOL 2100F).<sup>272</sup> TEM was performed by Jiaqing Tang (Imperial College London).

The loading efficiency of the drug into liposomes was measured by liquid chromatography–mass spectrometry (LC-MS). The drug (MTX or DEX) stock solution was diluted with methanol to different concentrations to generate calibration samples. The drug loaded liposomes were prepared and purified following the protocol described above. All the calibration samples and drug-loaded liposome samples were measured by LC-MS. Before measuring samples with LC-MS, an equivalent volume of propanol was added to disintegrate the liposomes. Encapsulation efficiency = encapsulated drug amount / the total amount of drug added;



Loading efficiency = encapsulated drug amount / (encapsulated drug amount + mass of carrier).

The LC-MS system consisted of an Agilent Technologies 1260 Infinity, coupled to an Agilent 6130 Series Quadrupole spectrometer (electrospray ionization mode, ESI+). All the analysis was carried out using a Gemini NX column (5-micron pore size, 150 x 4 mm). A flow rate of 1 mg mL<sup>-1</sup> and a gradient of (10-90) % B over 10 min were used. Eluent A consisted of: water/0.1% NH<sub>3</sub>.H<sub>2</sub>O; eluent B: acetonitrile/0.1% NH<sub>3</sub>.H<sub>2</sub>O. UV detection was performed at 272 nm in a scan mode ranging from 100 to 1000 m/z. MTX was eluted at t<sub>R</sub>=2.01 min (m/z=455[M+H]<sup>+</sup>). The corresponding UV peak at λ=272 nm was integrated and used for quantification based on the established standard curve.

The retention of MTX inside liposomes was determined using a dialysis method. A Float-a-Lyzer G2 (5 mL, MWCO 100kDa) was soaked in deionized water for 15-30 min before use to remove the glycerine on the membrane. MTX loaded liposomes (1 mL) were placed in a Float-a-Lyzer G2. Then, the Float-a-Lyzer G2 with the liposome sample inside was immersed into a PBS solution (50 mL) in a glass beaker. The beaker was kept on a magnetic stirrer and the stirring speed was set at 100 x rpm (Stuart/SSL1) at room temperature. Samples of the dispersion (10 μL) in the beaker was collected at determined timepoints. Propanol (10 μL) was added to each collected sample to disintegrate the liposomes. LC-MS was then used to quantify the retained MTX amount inside liposomes.

To mimic the release of MTX from liposomes in the extracellular environment at the inflammatory site, MTX-liposomes were incubated in 90 % (v/v) FBS for 8 h and then transferred to a dialysis tube (Spectra-Por, 1 mL, MWCO 300 kDa). After an additional 12 h and 44 h dialysis in PBS, samples of the dispersion (100 μL) in the dialysis tube was collected, followed by sonication to release MTX from liposomes. The amount of retained MTX inside liposomes in the dialysis tube was quantified using Methotrexate ELISA kit.

#### 2.2.4. Neutrophil isolation

Mouse neutrophils were isolated from bone marrow by negative selection using a neutrophil isolation kit. Briefly, bones from mouse legs were immersed in RPMI 1640 medium after muscle removal. Mouse bone marrow cells were flashed out with buffer solution (0.5% (w/v)

bovine albumin and 2 mM EDTA), filtered through the cell strainer, centrifuged at 400 g for 10 min and resuspended in the buffer solution. A cocktail of biotin-conjugated monoclonal antibodies was added to magnetically bind to non-target cells, followed by multiple washing steps. The secondary labelling reagent, anti-biotin monoclonal antibodies conjugated to Microbeads, was added and magnetically labelled non-target cells were depleted by retaining them within a MACS cell separation column in the magnetic field of a MACS separator, allowing unlabelled neutrophils to run through the column. The yield was determined using a haemocytometer and the cell viability was calculated by trypan blue exclusion. The purity of isolated neutrophils was measured using immunofluorescence antibody staining with PE anti-mouse CD11b ( $250 \text{ ng } \mu\text{L}^{-1}$ ) and APC anti-mouse Ly6G/Ly6C ( $250 \text{ ng mL}^{-1}$ ), measured using flow cytometry (BD FACSCanto, BD Bioscience). Then, the morphology of neutrophils was observed by widefield microscopy (Zeiss Axio Observer) using Giemsa-Wright stain. To prepare Giemsa-Wright stained samples, 1 mL of Giemsa-Wright solution was added to an ibidi 8-well plate with neutrophils seeded in advance and incubated for 3-4 min at room temperature. 2 mL of distilled water was added and stayed twice as long as the stain solution, followed by washing with distilled water until the edges showed faintly pinkish red. The samples were then kept in PBS and imaged by widefield microscopy (Zeiss Axio Observer).

### 2.2.5. Uptake of liposomes by neutrophils

#### *Flow cytometry analysis*

Neutrophils were isolated from mouse bone marrow and kept in 1640 RPMI medium. Then, the neutrophils were placed into DNA lobind tubes at a density of  $10^6$  cells per tube. DiD labelled liposomes were added to cells at different lipid concentrations and incubated for 1 h, followed by centrifugation at 350 g for 10 min and washed with cold PBS three times to remove free liposomes. Paraformaldehyde (PFA) (4 %) was added to fix the cells for 15 min at room temperature, followed by centrifugation and washing with PBS. 500  $\mu\text{L}$  of PBS was added to resuspend the cells and the samples were measured by flow cytometry. To detect the DiD signal, the samples were excited at 640 nm with a 670/14 emission filter. Ten thousand events were recorded for each sample and the data was analysed by FlowJo (TreeStar) software.

#### *Microscopy analysis*

Neutrophils were isolated from mouse bone marrow and kept in 1640 RPMI medium. The cells were placed into an ibidi 8-well plate (treated bottom) at a density of  $10^5$  cells per well and cultured for 2 h to allow the cell attachment. DiD labelled liposomes were then added at a lipid concentration of  $1 \text{ mg mL}^{-1}$  and incubated for 1 h. This process was followed by washing with cold PBS three times and fixed with 4% PFA for 15 min at room temperature. DAPI ( $100 \text{ ng mL}^{-1}$ ) and wheat germ agglutinin (WGA) alexa fluor 488 conjugate ( $5 \text{ } \mu\text{g mL}^{-1}$ ) were added and incubated for 15 min at room temperature to stain the cell nuclei and membranes. Confocal Laser Scanning Microscopy (CLSM) and 3D structural illumination microscopy (3D-SIM) were used to image the samples. 3D-SIM was performed with the assistance of Dr. Charles W. Winter (Imperial College London).

To further visualise the locations of drug loaded liposomes with neutrophils, DiD was used as a hydrophobic model drug and albumin-fluorescein isothiocyanate conjugate (FITC-BSA) was used as a hydrophilic model drug in this experiment. DiD was encapsulated in the lipid membrane and FITC-BSA was encapsulated in the liposome core at the same time. The sample preparation method was described above (section 2.2.3). After fixing the cells, DAPI was added to stain the cell nuclei and widefield microscopy (Zeiss/HCIImage) was used to image the samples at different magnifications (63x and 100x). To visualise the intracellular location of the model drugs, Z-stack images of a single neutrophil were generated using a constant Z-stack interval, with 100x objective magnification using widefield microscopy (Zeiss/HCIImage). The data was deconvolved to remove the out-of-focus signal collected in each individual image.

#### *Methotrexate ELISA*

The MTX loading efficiency in the neutrophils was measured using a Methotrexate ELISA kit. Neutrophils were incubated with MTX loaded liposomes at different MTX encapsulating concentrations and lipid concentrations for 1 h ( $3.5 \times 10^6$  neutrophils for each sample), followed by washing with cold PBS three times. The supernatants were discarded and the cell pellets were collected for the measurement.  $100 \text{ } \mu\text{L}$  of assay buffer from the ELISA kit was added to the cell pellets, followed by sonication for 10 min until the pellets were completely dissolved. Prior to the measurement, each sample was diluted 10 times. The whole measurement was conducted following the instruction supplied with the ELISA kit. Briefly, MTX standards were diluted from MTX standard stock solution and then all the MTX standards

and diluted samples were added to the ELISA plate. The MTX antibody was added into each well and the plate was incubated at room temperature on a shaker for 30 min at 150 rpm (Stuart/SSL1). After incubation, the solution of each well was emptied and washed with washing buffer from the kit three times. Blue MTX conjugate solution was added to each well and the plate was incubated at room temperature on a shaker for 30 min at the speed of 150 rpm (Stuart/SSL1), followed by washing steps as described. Substrate solution was subsequently added to each well and followed by the same incubation step. After incubation, a stop solution from the kit was added to each well and the whole plate was measured using SpectraMax M5 plate reader (molecular devices). The absorbance of each well was read at 450 nm with a correction filter at 580 nm.

#### 2.2.6. Neutrophil viability

To determine the viability of neutrophils, cells were seeded in DNA low-bind tubes at a density of  $10^6$  cells per tube. Different lipid concentrations of liposome samples were added into tubes and incubated for 4 h and 8 h respectively. The neutrophils were pelleted at 300 g for 10 min and washed three times with cold PBS. Zombie green dye (dilution: 1:100) was diluted to the working concentration and incubated with cells for 15 min at room temperature, followed by washing with cold PBS. Cells were fixed with 4% PFA and resuspended in 500  $\mu$ L PBS. The cell viability was measured using flow cytometry. To detect the presence of zombie green, the samples were excited at 488 nm with a 510/50 emission filter. Simultaneously, the morphology of neutrophils was observed by staining with Giemsa-Wright stain before and after loading as described (section 2.2.4) and detected by widefield microscopy.

#### 2.2.7. Physiological functions of neutrophils

To evaluate the activity of neutrophils, three different physiological functions of neutrophils were evaluated before and after loading with liposomes, including CD11b protein expression on the cell surface, superoxide-anion generation and cell migration.

##### *CD11b expression*

To determine the expression of CD11b, blank neutrophils and liposome-loaded neutrophils were treated with different concentrations of fMLP (1, 10 and 100 nM) at 37 °C for 30 min. After washing with cold PBS three times, PE anti-mouse CD11b ( $250 \text{ ng mL}^{-1}$ ) was added to conjugate to CD11b protein on the cell membrane for 30 min and then washed with cold PBS

three times. 4% of PFA was added to fix the cells for 15 min at room temperature. The fluorescence intensity was measured using flow cytometry. To detect the PE signal, the samples were excited at 561 nm with a 582/15 nm emission filter.

#### *Superoxide-anion generation*

Blank neutrophils and liposome loaded neutrophils were treated with fMLP (1  $\mu\text{M}$ ) at 37 °C for 30 min. After washing with cold PBS three times, dihydroethidium (10  $\mu\text{M}$ ) was added at 37 °C for 30 min to determine the superoxide-generation ability of neutrophils before and after loading with liposomes. Subsequently, the samples were washed again with PBS three times and the fluorescence intensity was measured using flow cytometry. The samples were excited at 488 nm with a 530/30 emission filter.

#### *Cell migration*

The migration ability of blank neutrophils and liposome loaded neutrophils was determined using a transwell cell migration method. For this purpose, cell culture inserts were introduced into a 24-well plate. Blank neutrophils and liposome loaded neutrophils were added into cell culture inserts (polycarbonate membrane, 3.0  $\mu\text{m}$  pore size, 6.5 mm membrane diameter, 0.33  $\text{cm}^2$  surface area) (upper chambers). Meanwhile, the wells of the plate (lower chambers) were filled with different concentrations of fMLP (1 nM and 100 nM). After 3 h, the cell culture inserts were taken out and the cells on the upper side of the membrane were removed. The cells on the bottom side of the membrane were stained with DAPI, imaged and counted. The liposomes in the migrated neutrophils were observed by CLSM (liposomes were labelled with DiD).

#### **2.2.8. NETs formation imaging**

The formation of NETs was imaged by CLSM after treating the samples with PMA. The liposomes were loaded with FITC-BSA and DiD at the same time, followed by incubation with neutrophils to form liposome loaded neutrophils. Formulated liposome loaded neutrophils were incubated in the presence of fMLP or PMA for 0 h and 8 h respectively. Then, the released DNA fragments were stained with propidium iodide (PI, 5  $\mu\text{g mL}^{-1}$ ). In a next step, the samples were fixed with 4% PFA, and the cell nuclei were stained with DAPI. Finally, the samples were imaged by CLSM.

### 2.2.9. Quantification of liposome and MTX release from neutrophils

The stimulated release of MTX-liposomes from neutrophils was determined using Fluorescence Correlation Spectroscopy (FCS). All FCS measurements and data analysis were performed by Dr. Adrian Najer (Imperial College London). FCS MTX-liposome/neutrophils (liposomes were labelled with DiD) were treated with or without PMA for 8 h, followed by centrifugation to collect the supernatant. FCS measurements were run to detect the amount and properties of liposomes after release from neutrophils. FCS was performed on a commercial LSM 880 (Carl Zeiss, Jena, Germany) equipped with an incubation chamber set to 37°C. A HeNe laser at 633nm was used as excitation source combined with an appropriate filter set to detect the fluctuating fluorescence signal. As objective, a 40x C-Apochromat water immersion objective (numeric aperture of 1.2) was used. Glass-bottom ibidi 8-well plates (80827, ibidi, Germany) were used to place 5  $\mu$ L sample droplets and measurements were conducted 200  $\mu$ m above the glass plate. Alexa647 in PBS was used as a standard to calibrate the beam waist ( $D = 3.3 \times 10^{-6} \text{ cm}^2/\text{s}$  (Alexa647) at 25°C was corrected for the higher temperature used:  $D = 4.42 \times 10^{-6} \text{ cm}^2/\text{s}$  at 37°C).<sup>273</sup> Intensity traces of 30x5s were recorded per sample. In the figures, the full intensity curve and the average autocorrelation curves across the whole measurement (both 150 s) were always plotted. Autocorrelation was performed on ZEN software (Carl Zeiss, Jena, Germany) and data was exported for fitting and analysis using PyCorrfit program 1.1.6.<sup>274</sup> using one component fits:

$$G_{1comp}(\tau) = \left( 1 + \frac{T}{1-T} e^{\frac{-\tau}{\tau_{trip}}} \right) * \frac{1}{N * \left( 1 + \frac{\tau}{\tau_D} \right) * \sqrt{1 + \frac{\tau}{SP^2 \tau_D}}}$$

$N$  refers to the effective number of diffusing species in the confocal volume with a height to weight ratio (structural parameter  $SP$ ) fixed to 5.  $\tau_{trip}$  is the triplet time with corresponding triplet fraction  $T$ , and  $\tau_D$  is the diffusion time.

The x-y dimension of the confocal volume ( $\omega_{xy}^2$ ) was calibrated using the calibration solution of Alexa647 in PBS. Diffusion coefficients ( $D$ ) for the sample measurements were then obtained by plugging in the calculated diffusion times ( $\tau_D$ ) from above:

$$D = \frac{\omega_{xy}^2}{4\tau_D}$$

Einstein-Stokes equation was subsequently used with the obtained diffusion coefficients ( $D$ ) to calculate hydrodynamic radii ( $R_h$ ).

The amount of MTX in the released particle solution after incubation of loaded neutrophils in the presence of PMA was quantified using Methotrexate ELISA kit. Formulated MTX-liposome/neutrophils were incubated with and without PMA for 8 h. The supernatants were collected at 0 h, 4 h and 8 h timepoints and sonicated for 30 min before the measurement. The amount of MTX was measured by Methotrexate ELISA kit. The percentage of released MTX was calculated by MTX amount (at different time points)/MTX amount (initial loading).

### 2.2.10. Co-culture of liposome loaded neutrophils with RAW 264.7 cells

#### *Flow cytometry analysis*

In order to distinguish RAW 264.7 cells from neutrophils, the cytoplasm of RAW 264.7 cells was labelled with CellTracker Green CMFDA Dye. RAW 264.7 cells were harvested by centrifugation and resuspended in the pre-warmed CellTracker working solution (1  $\mu$ M). After 30 min incubation, the cells were centrifuged and washed with PBS to remove the free CellTracker dye. Simultaneously, the neutrophils were incubated with DiD-labelled liposomes for 1 h and free liposomes were washed away by centrifugation. The labelled RAW 264.7 cells were then added to co-culture with formulated liposome loaded neutrophils in the FBS-free medium containing PMA (100 nM). After 8 h incubation, the cell samples were fixed using 4% PFA and measured by flow cytometry. To detect the CellTracker signal, the samples were excited at 488 nm with a 530/30 nm emission filter. In addition, to detect the DiD signal, the samples were excited at 640 nm with a 670/14 emission filter.

#### *CLSM analysis*

To visualise the samples by CLSM, RAW 264.7 cells were seeded in a glass bottom 8-well ibidi plate at a density of  $2 \times 10^5$  cells per well. After an overnight incubation, DiD-liposome loaded neutrophils ( $0.3 \times 10^6$  neutrophils) were added to RAW 264.7 cells and incubated in the DMEM medium with or without PMA (100 nM) for 4 h and 8 h respectively. RAW 264.7 cells were washed with cold PBS three times after incubation to remove suspended neutrophils in the

medium. Then, the samples were stained with PI ( $5 \mu\text{g mL}^{-1}$ ) for 30 min. Finally, DAPI was used to stain the cell nuclei and the samples were imaged by CLSM.

#### *Proliferation of RAW 264.7 cells*

To quantify the proliferation of RAW 264.7 cells after treating with MTX-liposome loaded neutrophils, RAW 264.7 cells were seeded in a 96-well plate ( $2 \times 10^4$  cells well $^{-1}$ ). After 12 h incubation, the neutrophils which were loaded with MTX-encapsulated liposomes (MTX-liposome/neutrophils) were added into each well with the growth medium containing LPS and PMA. In this case, LPS ( $100 \text{ ng mL}^{-1}$ ) was used to mimic the inflammatory environment and PMA was used to induce neutrophils forming NETs. After incubating for 24 h, the neutrophils were washed away with PBS and the viability of RAW 264.7 cells was measured using Cell Counting Kit-8. The absorbance of each well was measured at 450 nm using a microplate reader (SpectraMax M5, molecular devices).

#### *TNF- $\alpha$ gene expression of RAW 264.7 cells*

RAW 264.7 cells were seeded in a 24-well plate at a density of  $5 \times 10^4$  cells per well. After 12 h incubation, LPS, PMA, different doses of MTX encapsulated liposomes, and the equivalent amount of MTX were added into each well and incubated for 6 h. The supernatant was then discarded and each well was washed with cold PBS three times. 200  $\mu\text{L}$  of TRizol was added to each well to lyse the cells, followed by pipetting the lysate several times to homogenize. The RNA of each lysate was extracted using Direct-zol RNA MiniPrep according to the kit instruction. The purity and concentration of the extracted RNA was measured using NanoDrop 2000C (Thermo Scientific). To synthesis cDNA from the extracted RNA samples, a QuantiTect Reverse Transcription Kit was employed. 10ng of cDNA was used for qPCR with a TaqMan™ Gene Expression Assay, TaqMan™ Universal PCR Master Mix, and StepOnePlus™ Real-Time PCR System (Life Technologies). The relative gene expression was calculated using the  $\Delta\Delta\text{C}_t$  method normalising to the control and Rn18s was used as a reference gene.

#### 2.2.11. Statistics

All the statistical analyses were conducted in GraphPad 8.0 (Prism). All the statistical tests were specified in the figure legends. Shapiro-Wilk test was used to assess normality and thus determine the statistical test. 'n' refers to technical replicates; 'N' refers to biological replicates.



### 2.3. Results and discussion

The work in this chapter has been divided into three subsections as shown in Figure 2.1. In the first subsection, the preparation of a neutrophil-mediated delivery system with blank liposomes was showcased. For this purpose, blank liposomes were prepared, and neutrophils were isolated and characterised. Then, the neutrophils were loaded with DiD labelled liposomes (DiD-liposomes) and the loading efficiency was determined by flow cytometry and imaged by confocal laser scanning microscopy (CLSM) and 3D structural illumination microscopy (3D-SIM). Moreover, the physiological functions of neutrophils were evaluated after loading with blank liposomes. Furthermore, the stimulated release of loaded liposomes from neutrophils was characterised using fluorescence correlation spectroscopy (FCS) and re-uptake of these released liposomes by target cells was determined using flow cytometry and imaged by CLSM. In the second subsection, two different anti-inflammatory drugs were loaded into the liposomes respectively. The drug loading efficiencies and the release profiles were measured using liquid chromatography–mass spectrometry (LC-MS) aiming to choose a model drug with the highest encapsulation efficiency and a proper release behaviour with liposomes for subsequent experiments. In the third subsection, the optimised methotrexate (MTX)-encapsulated liposomes were loaded into neutrophils and the loading efficiency, the neutrophil's functions and the stimulated liposome release properties were investigated again. Finally, to determine the biological effects of formulated MTX-liposome loaded neutrophils, target cells were tested with MTX-liposome loaded neutrophils using a co-culture method.

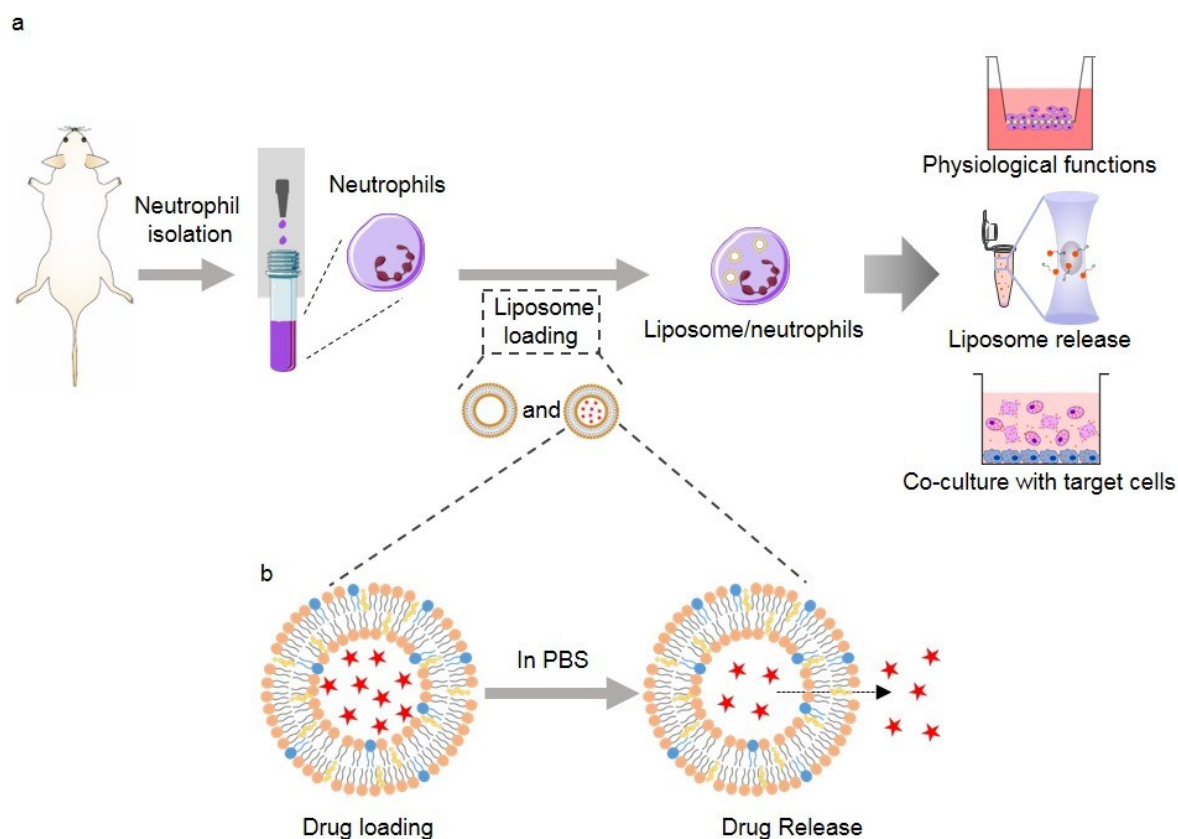


**Figure 2.1 Schematic illustration of preparation of drug-encapsulated liposome loaded neutrophils and evaluation of activity. *a*, In vitro validation of the neutrophil-mediated drug delivery system. Neutrophils were isolated using the negative selection method. Blank liposomes or drug loaded liposomes were prepared and loaded into isolated neutrophils. After loading with liposomes, physiological functions of neutrophils and stimulated release of liposomes from neutrophils were determined. Meanwhile, target cells were co-cultured with liposome loaded neutrophils to investigate the transport of liposomes via neutrophils. *b*, Loading and release of the drug from liposomes was studied.**

### 2.3.1. Preparation and characterisation of liposome loaded neutrophils

Liposomes were chosen for this study because they are an ideal nanocarrier candidate to encapsulate either hydrophilic or hydrophobic drugs due to high biocompatibility and the possibility to scale up the manufacturing process. To promote interactions with neutrophil membranes and achieve high loading efficiencies, a positively charged surface on the liposomes was chosen. However, positive charges on particle surfaces are known to cause cytotoxicity.<sup>256</sup> Therefore, to ensure a compromise between a sufficient positive surface charge to promote interactions while ensuring biocompatibility, different percentages of the cationic lipid 1,2-stearoyl-3-trimethylammonium-propane (18:0 TAP), 1,2-dioleoyl-sn-

glycero-3-phosphocholine (DOPC), and cholesterol were used to formulate liposomes by the thin-film hydration method and extruded to obtain a size of about 100nm (Figure 2.2a and c). To characterise the membrane surface charge, the zeta potential was measured using a Zeta sizer. As expected, with increasing percentage of 18:0 TAP in the composition, the zeta potential of formulated liposomes rose from +9 mV to +31 mV (Figure 2.2b). Thus, 14% (w/w) of the cationic lipid in the composition was decided as the final ratio, yielding a zeta potential of +28 mV (Figure 2.2d). Similar size and zeta potential has also previously been reported to be beneficial and compatible for efficient interactions with cell membranes and subsequent endocytosis.<sup>275</sup>

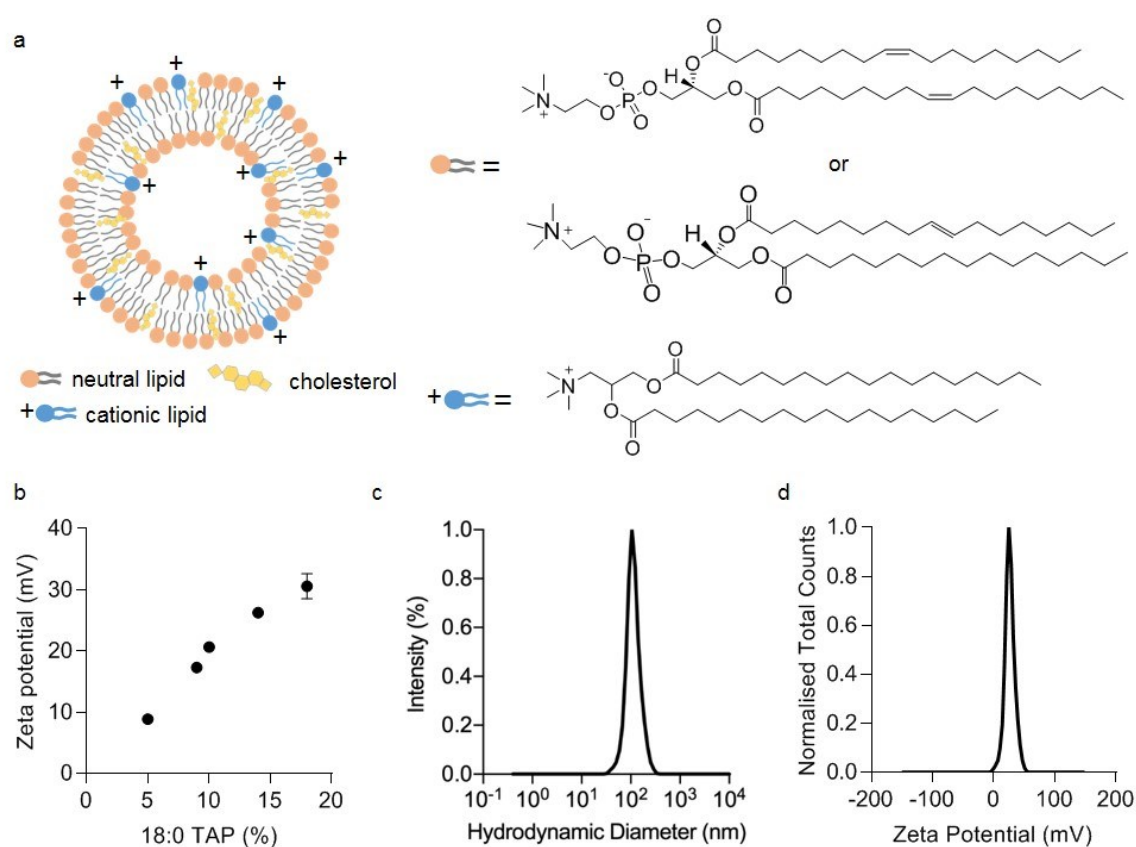


**Figure 2.2** Preparation and characterisation of cationic liposomes. **a**, Schematic illustration of the liposome structure and lipid composition. **b**, Zeta potential distributions of liposomes prepared using different percentages of the cationic lipid (mean  $\pm$  s.d.,  $n = 3$ ). **c** and **d**, Particle-size measured by dynamic light scattering (DLS) and zeta potential distribution of the optimised liposome composition containing 14% (w/w) cationic lipid.

For the cellular component of the delivery system, neutrophils were first isolated from mouse bone marrow using negative selection (Figure 2.3a) and then loaded with liposomes *ex vivo* instead of targeting neutrophils with the nanocarrier *in vivo*.<sup>238</sup> This method has two advantages. First, free liposomes can be easily removed by centrifugation to avoid toxicity or negative effects to other healthy tissues. Second, formulating drug-liposome/neutrophils *ex vivo* can also allow to administer different drug doses by injecting different numbers of neutrophils. Flow cytometry results (Figure 2.3b and c) provided assurance that the isolated neutrophils were clean with a purity of 95% and the Giemsa-Wright stained sample (Romanowsky stain) revealed the typical lobulated shape of the neutrophil nuclei.

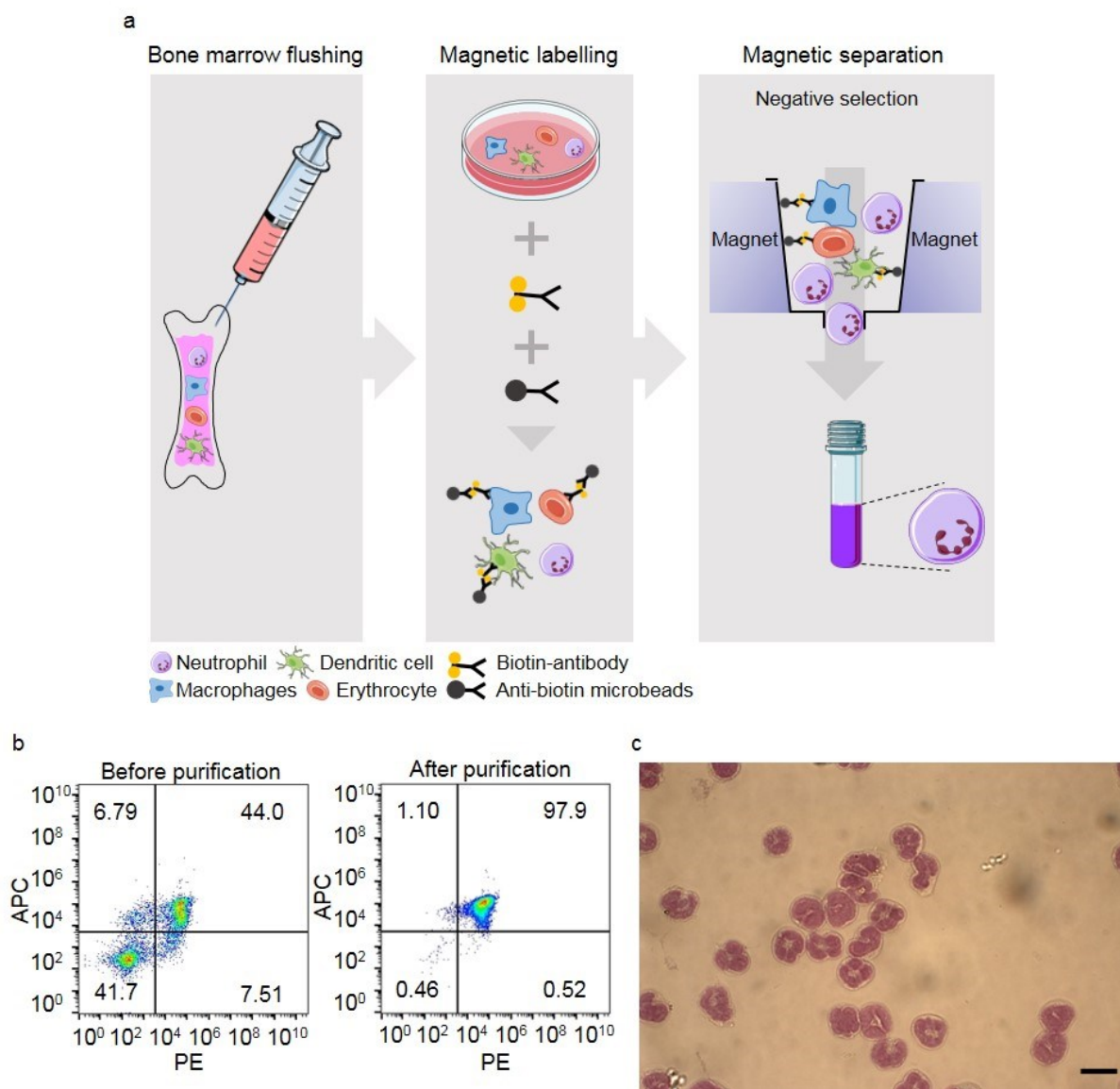


**Figure 2.3 Isolation and characterisation of neutrophils.** **a**, Schematic illustration of the neutrophil isolation process. Mouse bone marrow cells were flushed out with cell culture medium. The cell solution was first mixed with biotin-antibody, followed by incubation with anti-biotin microbeads. Then, a MACS cell separation column in the magnetic field of a MACS separator was used to retain non-target cells and allow unlabelled neutrophils to run through the column. The graphics of cells, syringe and tube were adapted from the Servier Medical Art website. **b**, Flow cytometry analysis of the purity of isolated neutrophils before and after purification. Isolated cells were stained with PE anti-mouse CD11b and APC anti-mouse Ly6G/Ly6C antibodies. **c**, Morphological images (representative) of isolated neutrophils stained with Wright-Giemsa stain. Images were recorded under bright field, 100X. Scale bar: 10  $\mu$ m.

After preparation and characterisation of cationic liposomes and neutrophils separately, a simple loading protocol was used to combine the two. Liposome loaded neutrophils

(liposome/neutrophils) were obtained by incubating liposomes with purified neutrophils for 1 h, and excess liposomes were subsequently washed away by centrifugation. Liposome uptake efficiency for neutrophils was measured using flow cytometry (liposomes were labelled with 1,1'-Diiododecyl-3,3,3',3'-Tetramethylindodicarbocyanine, 4-Chlorobenzenesulfonate Salt (DiD)). Formulated cationic liposomes were readily taken up by neutrophils with more than 95% of the cells being positive for liposomes upon loading (Figure 2.4a), which is expected due to the chosen size and the positively charged surface of liposomes. Co-localisation of liposomes with neutrophils was shown by CLSM images (Figure 2.4b), which correlate well with the flow cytometry data confirming that most cells had taken up liposomes during the 1 h loading procedure. Furthermore, from CLSM images, various spatial locations of liposomes on or within neutrophils were observed. It is clear that in most cases, liposomes were detected absorbed to the cell membrane (grey arrow) while some liposomes were detected inside cells and even close to the nucleus (white arrow).

After this study of loading a hydrophobic model cargo DiD that inserts into the membrane of the liposomes and allowed satisfying cell uptake efficiency, co-loading with another model cargo was also tested. To test whether the liposomes can additionally co-encapsulate a hydrophilic model drug, fluorescein isothiocyanate conjugated bovine serum albumin (FITC-BSA) was co-loaded inside liposomes, which will remain in the aqueous core of the liposomes due to its hydrophilicity. After incubation of neutrophils with these dual loaded liposomes, co-localisation of the cargoes within the neutrophils was visualised using microscopy. A single liposome-loaded neutrophil is shown in widefield microscopy images (Figure 2.4c). The neutrophil took up a large number of liposomes and most of the FITC-BSA and DiD were co-localised in neutrophils (the overlap of FITC-BSA and DiD shows yellow colour), which indicates that liposomes can retain encapsulated FITC-BSA and DiD after being loaded into neutrophils. This highlights the versatility of liposomes able to encapsulate therapeutic combinations as two different molecules can be co-encapsulated inside liposomes, which gives possibilities to reduce inflammation and actively promote repair at the same time for the treatment of inflammation.

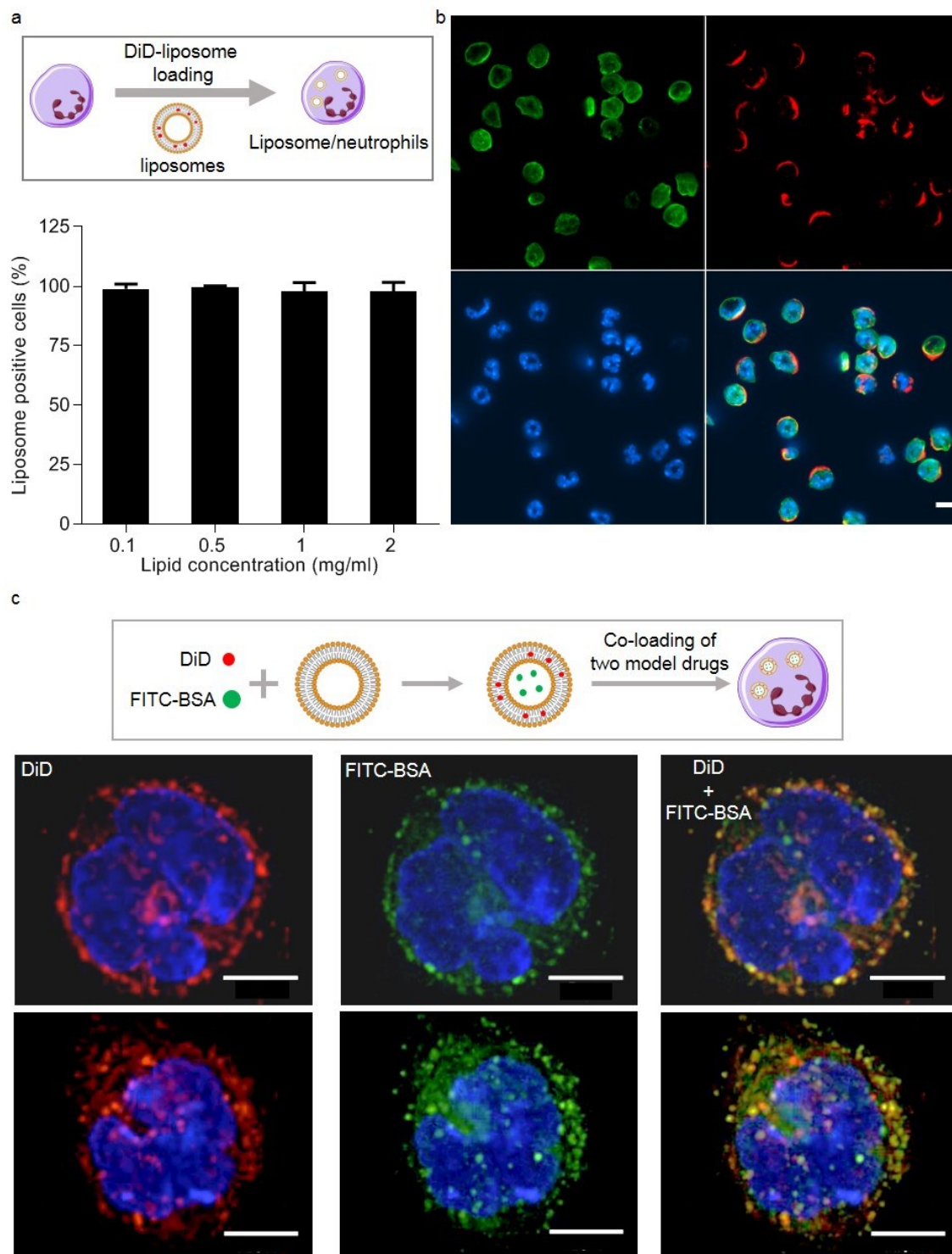


**Figure 2.4 Liposome loading of neutrophils.** *a*, Flow cytometry analysis of liposome loaded neutrophils. Isolated neutrophils were incubated with DiD-liposomes at different lipid concentrations for 1 h (mean  $\pm$  s.d.,  $N = 3$ ). *b*, CLSM representative images of liposome loaded neutrophils (DiD was used to label the liposome membrane (red), wheat germ agglutinin (WGA) was used to stain the cell membrane (green), DAPI was used to stain the cell nuclei (blue)). Scale bar: 10  $\mu$ m. *c*, Widefield microscopy representative images showing the co-localisation of FITC-BSA and DiD in a single neutrophil. Scale bars: 5  $\mu$ m.



A critical parameter is cytocompatibility of formulated cationic liposomes, which determines the loading capacity of liposomes into neutrophils without affecting neutrophil viability. Neutrophil viability was confirmed for different lipid concentrations of liposomes for 4h and 8h incubation post loading (Figure 2.5). More than 80% of neutrophils were alive at the highest lipid concentration after 8 h incubation. Meanwhile, liposome loaded neutrophils (incubated at a lipid concentration of  $2.5 \text{ mg mL}^{-1}$ ) did not reveal any morphological changes with Giemsa-Wright staining, which indicates high cytocompatibility of the used liposome formulation. These results demonstrate that formulated cationic liposomes are a good nanocarrier to encapsulate and retain both hydrophilic and hydrophobic molecules and can successfully and efficiently be loaded into neutrophils with high cytocompatibility.

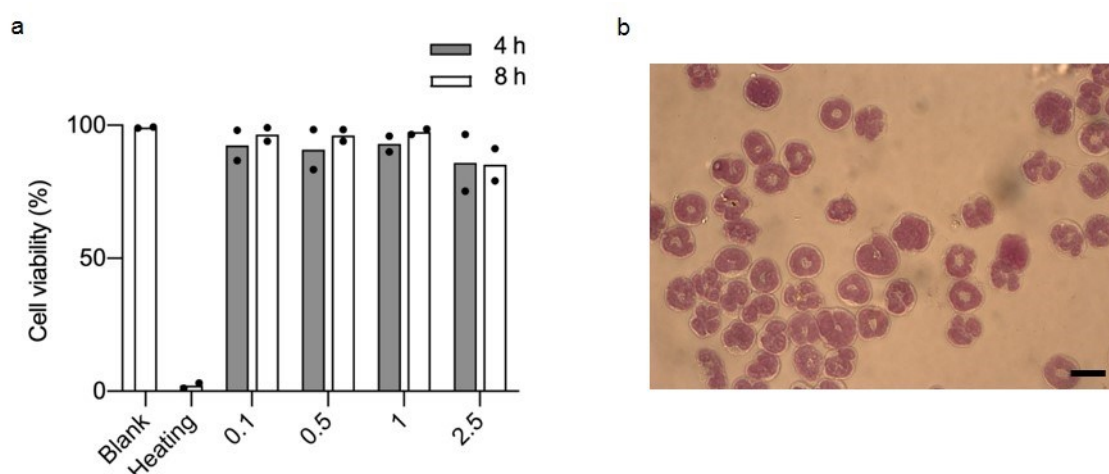


**Figure 2.5 Cytocompatibility of liposomes to neutrophils after incubation for 4 h and 8 h.** *a*, Isolated neutrophils were incubated with blank liposomes at different lipid concentrations for 4 h and 8 h respectively. Zombie green cell viability kit was used to measure neutrophil viability by flow cytometry. Neutrophils heated at  $70 \text{ }^{\circ}\text{C}$  for 10 min were used as the negative control (dead cells) ( $N = 2$ ). *b*, Morphological images (representative) of liposome/neutrophils stained with Giemsa- Wright stain (lipid concentration:  $2.5 \text{ mg mL}^{-1}$ ). Images were recorded under bright field, 100X. Scale bar:  $10 \text{ }\mu\text{m}$ .

### 2.3.2. Physiological functions of neutrophils after loading with blank liposomes

After characterisation and confirmation of the successful and efficient loading of neutrophils with DiD-liposomes, the physiological functions of neutrophils after loading with liposomes including their response to inflammatory factors and migration towards the inflammatory site were investigated. This is crucial because preserving physiological functions after loading with liposomes ensures that neutrophils are able to respond to inflammatory signals and migrate



to the inflamed tissue after intravenous administration *in vivo*. Therefore, several biochemical processes were assessed including CD11b protein expression, superoxide generation ability and cell migration behaviour.

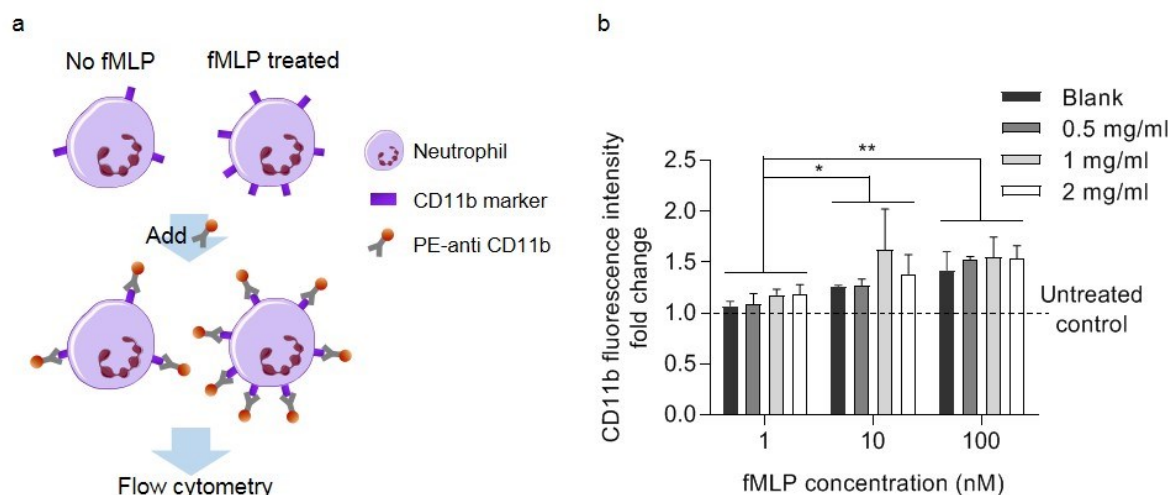


**Figure 2.6** Change in the CD11b expression of liposome loaded neutrophils after treatment with fMLP at different concentrations. **a**, Schematic illustration of the method to determine the CD11b expression of neutrophils. Neutrophils with and without fMLP treatment were incubated with PE anti-mouse CD11b antibody and the PE fluorescent intensity was measured using flow cytometry. **b**, Neutrophils were loaded with blank liposomes at different concentrations and then stained with PE anti-mouse CD11b antibody (mean  $\pm$  s.d.,  $N = 3$ ). \* $P < 0.05$ , \*\* $P < 0.01$ , two-way ANOVA, Bonferroni post hoc test.

CD11b is a neutrophil surface protein that dominates cell adhesion and migration functions to mediate the inflammatory response.<sup>239,29</sup> Once neutrophils are stimulated by inflammatory molecules in the blood, the expression of CD11b is upregulated to enhance cellular adhesion. A neutrophil chemotaxis peptide N-Formyl-Met-Leu-Phe (fMLP), which recruits neutrophils and subsequently initiates inflammation responses at the site of cell/tissue damage,<sup>276</sup> was used to mimic the environment encountered by neutrophils in the blood during inflammation. As expected, the CD11b expression level of neutrophils and liposome/neutrophils significantly increased with increasing fMLP concentration (Figure 2.6). No significant differences were observed between blank neutrophils and liposome/neutrophils, which indicates that after loading with liposomes the neutrophils still responded to an inflammation signal to express a key protein for adhesion and migration, similarly to blank neutrophils.

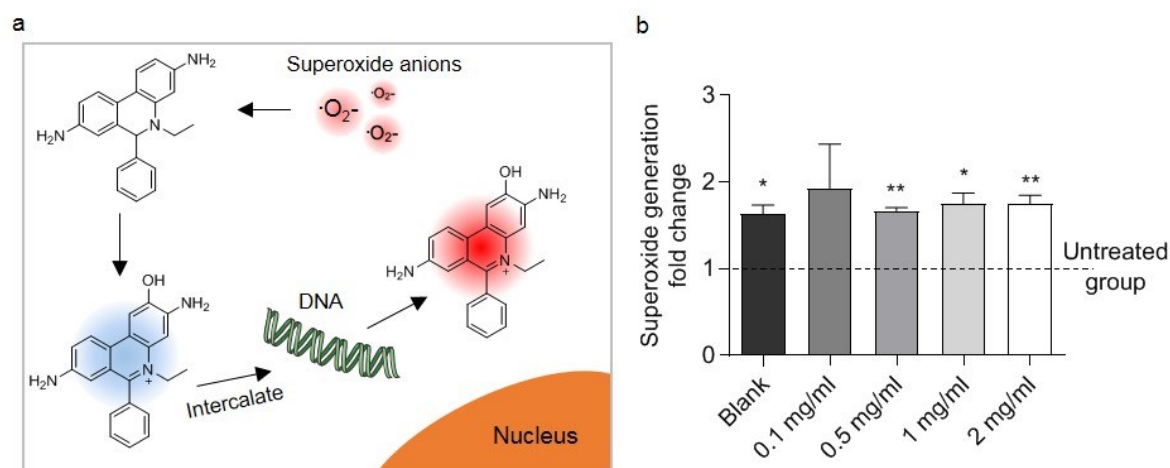


**Figure 2.7** Change in the superoxide generation of liposome-loaded neutrophils with and without fMLP treatment. **a**, Schematic illustration of the mechanism to measure the superoxide generation in neutrophils. The probe dihydroethidium can be oxidised by superoxide anions in cells to exhibit blue fluorescence. It can further intercalate within DNA of the cell to generate a bright fluorescent red signal, which can be detected and quantified by flow cytometry. **b**, The superoxide level of cells treated with fMLP was detected using dihydroethidium and compared to untreated controls (mean  $\pm$  s.d.,  $N = 3$ ). \* $P < 0.05$ , \*\* $P < 0.01$ , unpaired two-tailed Student's  $t$  test.

Furthermore, the superoxide generation capability of neutrophils and liposome/neutrophils was determined using the fluorescent probe dihydroethidium. Dihydroethidium is a cell-permeable dye that can react with superoxide anions inside cells to form oxoethidium, which further interacts with nucleic acids to emit a fluorescent signal quantifiable by flow cytometry.<sup>277</sup> After the neutrophils are activated by inflammatory factors, they generate a large amount of superoxide which is a key component for microbial killing.<sup>278</sup> After treatment with fMLP, a 1.5-fold increase of superoxide generation in blank neutrophils was detected (Figure 2.7). Similarly, the increasing trend of superoxide generation was observed in liposome/neutrophils and there were no significant differences in the superoxide amount produced between blank neutrophils and liposome/neutrophils after fMLP treatment.

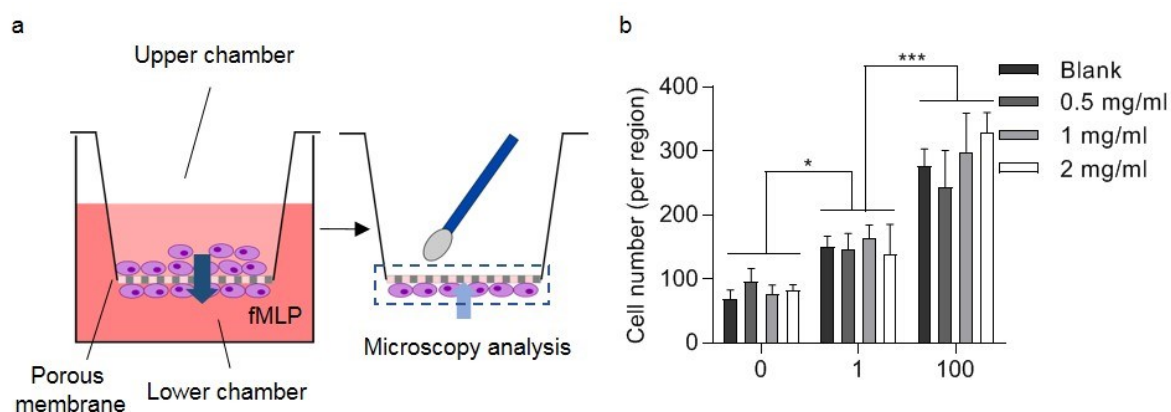


**Figure 2.8 Migration ability of liposome loaded neutrophils with and without fMLP treatment.** **a**, Schematic illustration of the *in vitro* model to evaluate the migration capability of liposome/neutrophils across the porous membrane using a transwell assay. Neutrophils on the bottom side of the membrane were stained with DAPI and imaged using CLSM and analysed by ImageJ. **b**, Number of migrated neutrophils on the bottom side of the membrane (mean  $\pm$  s.d.,  $N = 3$ ). \* $p < 0.05$ , \*\*\* $P < 0.001$ , two-way ANOVA, Bonferroni post hoc test.

The retention of the active migration ability of loaded neutrophils to inflammatory sites is key for the drug delivery purpose described herein. A transwell migration assay was used to explore this migration function of neutrophils *in vitro* (Figure 2.8), in which a porous membrane (pore size 3  $\mu\text{m}$ ) was used to study the transmigration ability of loaded neutrophils.<sup>279</sup> This transwell assay was reported as a valid *in vitro* model to study the migration ability of neutrophils when following a gradient of chemotactic peptides.<sup>279</sup> This transwell assay has also been used in other studies in the field *e.g.* in a study regarding neutrophil-mediated drug delivery to brain tumours.<sup>239</sup> After supplementation of fMLP to the basal medium, more cells migrated through the pores of the transwell membrane (images were taken at the lower side of the membrane to count number of migrated cells), (Figure 2.9). This indicates that after supplying fMLP, the neutrophils were activated and migrated towards the higher fMLP concentration area. This result agrees with previous CD11b expression conclusions (Figure 2.6). Importantly, confocal microscopy images of migrated neutrophils revealed that the signal of DiD-liposomes was still observed in migrated neutrophils (Figure 2.10). This indicates that neutrophils responded to the inflammation signal, migrated, and carried their liposome cargoes across the membrane.

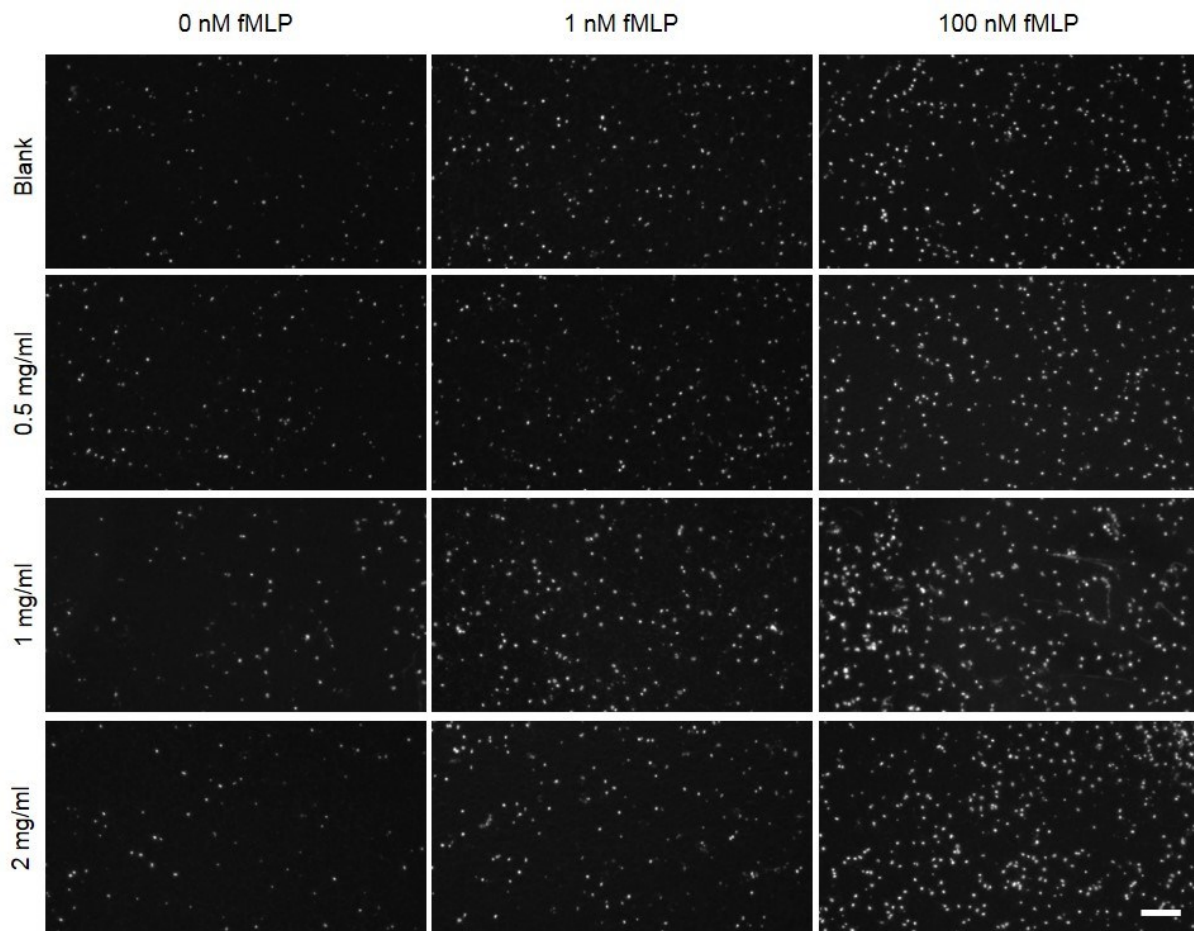


**Figure 2.9** Representative images of neutrophils at the bottom side of the transwell membrane after the migration test. Neutrophils were incubated with DiD-liposomes at different lipid concentrations. Formulated liposome/neutrophils were deposited in the upper chamber of the transwell and activated by fMLP in the lower chamber. Liposome/neutrophils migrated through the pores of the membrane. Membranes were taken out and the cells on the upper side were removed. The nuclei of neutrophils at the bottom side of the membrane were stained with DAPI and imaged by fluorescence microscopy (DAPI channel). Nuclei counts for the different conditions are shown in Figure 2.8b. Scale bar: 100  $\mu$ m.

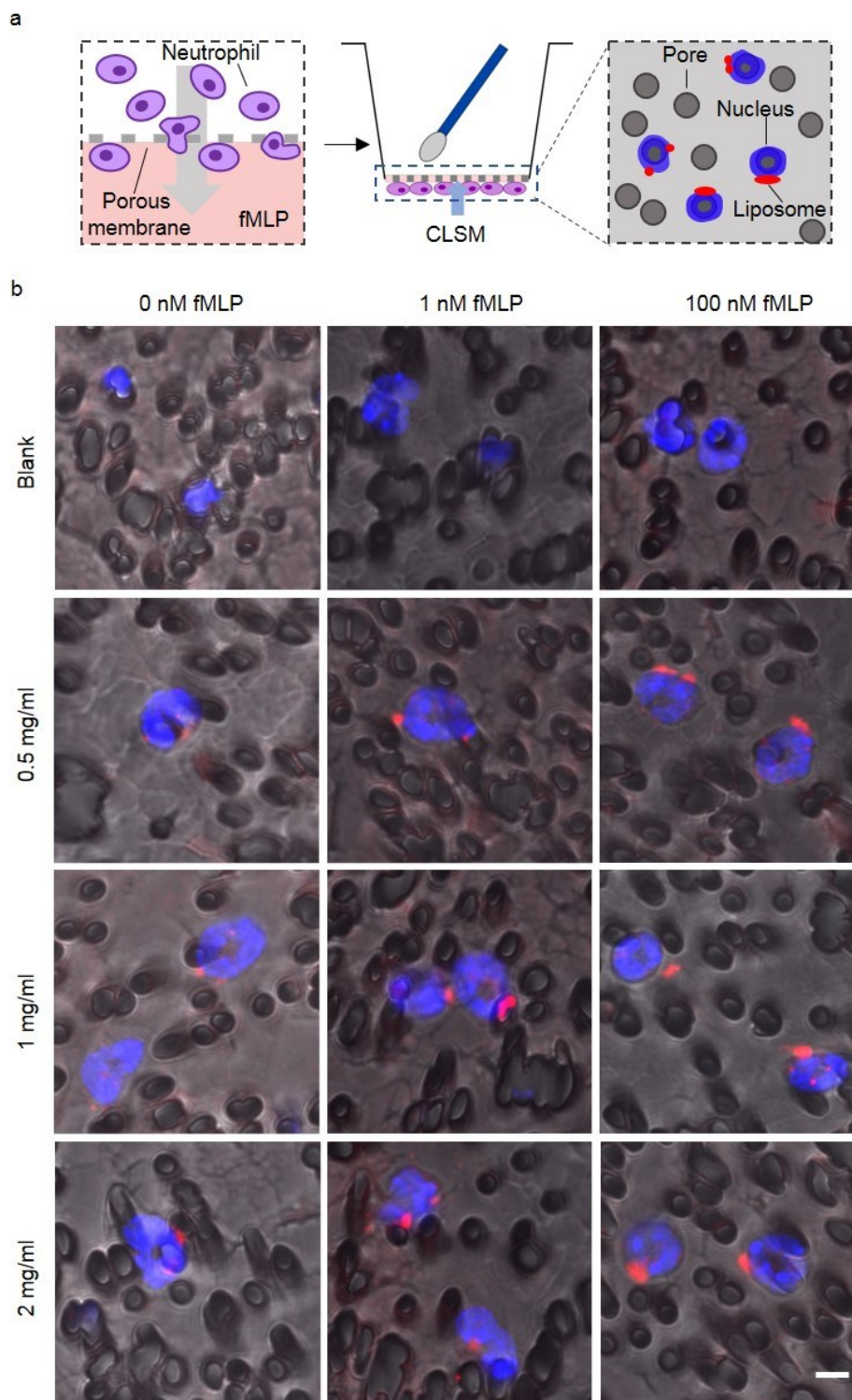


**Figure 2.10 CLSM images of liposome/neutrophils on the transwell membrane.** **a**, Schematic illustration of the sample preparation method. Neutrophils were deposited in the upper chamber of the transwell to measure the cell migration ability. The membranes were cut out and seeded in an ibidi plate and imaged using CLSM. Pores of the membrane (dark grey) were traversed by the liposome/neutrophils. **b**, CLSM representative images of formulated liposome/neutrophils (liposomes were labelled with DiD) and blank neutrophils on the bottom side of the transwell membrane. Scale bar: 5  $\mu$ m.



Taken together, after loading with blank liposomes, neutrophils maintained their adhesion and migration functions in an inflammatory environment, which suggests that they are able to actively respond to inflammatory signals in the blood and migrate to the inflammatory site, whilst carrying their loaded cargoes. These findings also agree with previous published study, in which liposome loading did not impair neutrophil physiological functions and successful recruitment of loaded neutrophils to brain tumours was achieved after *i.v.* injection.<sup>239</sup>

### 2.3.3. Inflammation-responsive release of liposomes from neutrophils and delivery to macrophages

After assessing the physiological functions of liposome/neutrophils and confirming that liposome-loaded neutrophils maintained their adhesion and migration ability in responding to inflammatory signals, the release of liposomes from carrier neutrophils after extended stimulation to initiate NETs formation was studied in detail (Figure 2.11). To initially explore the release of liposomes from neutrophils under the chemotactic environment and under conditions mimicking an inflammatory target site, neutrophils were loaded with liposomes and incubated in either basal medium, in fMLP (to mimic a chemotactic process) or in phorbol myristate acetate (PMA)<sup>35</sup> containing medium (to mimic the inflammatory site). After 8 h incubation, neutrophils formed NETs only in the PMA containing medium. An accompanying decrease in liposome signal inside neutrophils/NETs indicates that neutrophils underwent PMA triggered NETs formation that caused the release of liposomes from neutrophils (Figure 2.12). Due to the small size, even liposomes loosely associated with neutrophil debris (NETs) are prone to be uptaken by other cells, which yields the intended effect of delivering most of the liposomes to target cells at the inflammatory site.

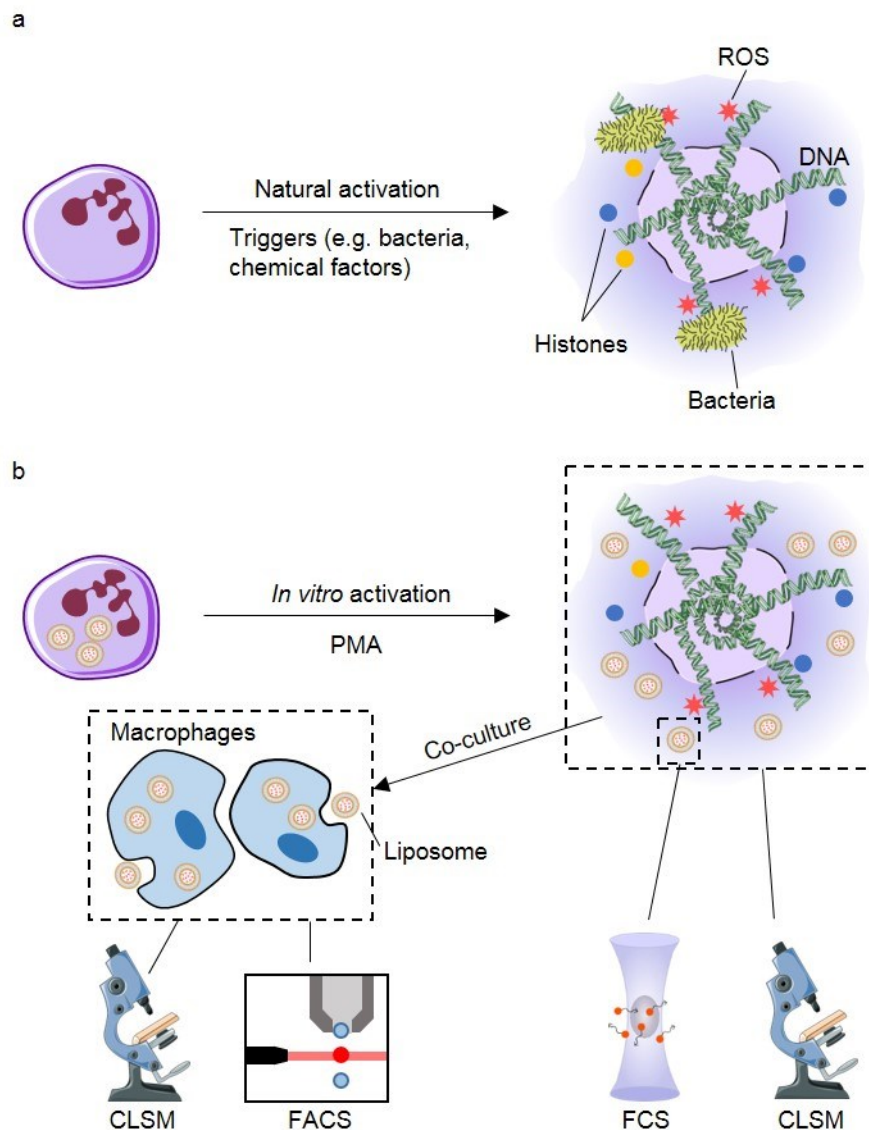


**Figure 2.11 Schematic illustration of NETs formation and resulting delivery of liposomes from neutrophils to macrophages.** *a*, Neutrophils can form NETs after being activated by inflammatory triggers such as bacteria and chemical factors such as PMA. Formed NETs eliminate bacteria with anti-bacterial proteins such as histones and generate reactive oxygen species (ROS). *b*, After loading with liposomes, neutrophils can release loaded liposomes concomitantly with the formation of NETs. In this chapter, the NETs formation process was observed using CLSM and the release of liposomes was characterised using FCS. Furthermore, macrophages were used to investigate the whole cascade of transporting liposomes to target cells (macrophages) via neutrophils, which was characterised using CLSM and flow cytometry. The graphics of neutrophil and microscope were adapted from the Servier Medical Art website.

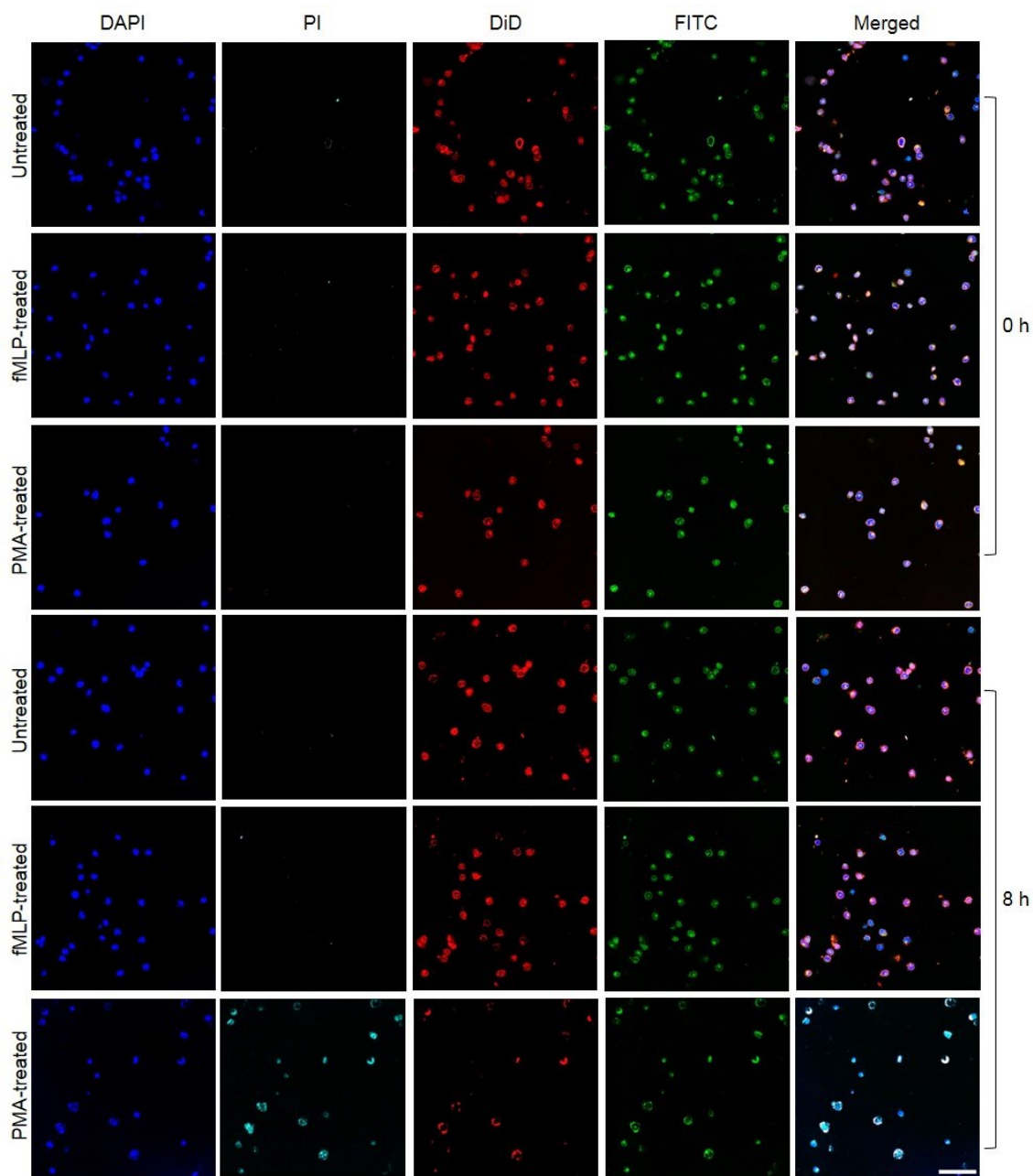


**Figure 2.12** CLSM representative images of liposome/neutrophils (liposomes were labelled with DiD and loaded with FITC-BSA) before and after treatment with fMLP or PMA. Liposomes were loaded with FITC-BSA and DiD simultaneously, followed by incubation with neutrophils to form liposome/neutrophils. Formulated liposome/neutrophils were incubated in the presence of fMLP or PMA for 0 h and 8 h. The nuclei of neutrophils were stained with DAPI and the released DNA fragments were stained with propidium iodide (PI). The merged image is the overlay of the four individual images. Scale bar: 50  $\mu$ m.

To characterise and quantify the number of liposomes released from neutrophils into solution, a sensitive, single-particle detection method called FCS was employed, which allows precisely measuring particles in complex environments such as cell media containing proteins and cell



debris (Figure 2.13a). After 8 h incubation, the detected raw fluorescence intensity was much higher in supernatants of liposome-loaded neutrophils incubated in PMA-containing medium compared to samples from a non-inflammatory control environment (Figure 2.13b). The corresponding autocorrelation curves and calculated hydrodynamic diameters clearly indicate that liposomes were released from the neutrophils (Figure 2.13c). The inflammatory environment induced by PMA caused a large increase of liposome release as seen by the difference in particle counts compared to control groups (Figure 2.13d). Additional information of signal per liposome (CPP in kHz) and diameter ( $D_h$ ) revealed that there were no big differences detectable between the original liposomes and the released liposomes. Similar CPP values for the liposome stock and the PMA-released liposomes indicates that the same number of DiD molecules per liposome were retained during the loading/release processes. Only in some curves partial aggregation of liposomes was found as indicated by high intensity bursts in the intensity trace (Figure 2.13b purple), a two-component autocorrelation curve (Figure 2c purple), and some outliers in the CPP and size plots (Figure 2.13d). This is expected due to the positively charged nature of the liposomes. However, it is not a concern for this type of delivery, because this partial aggregation will happen at the target site and may even be beneficial for subsequent uptake in target cells. Furthermore, the composition of the original liposomes and the released liposomes from loaded neutrophils in the presence of PMA can be assessed using LC-MS to show the differences in membrane composition between the original liposomes and the released liposomes because membrane fusion can happen between liposomes and live cells.<sup>280</sup>

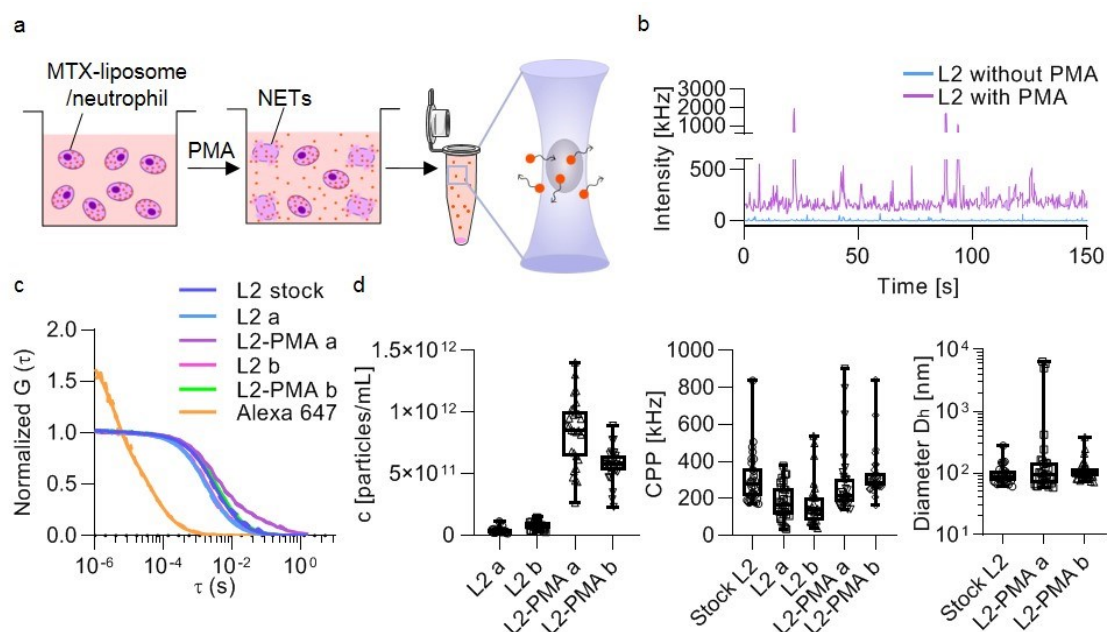


**Figure 2.13 Stimulated release of liposomes (DiD labelled) from neutrophils after treatment with PMA detected by FCS.** *a*, Schematic illustration of the FCS sample preparation. Liposome/neutrophils were prepared and cultured with or without PMA for 8 h, followed by centrifugation to collect the supernatant. FCS measurements were run to detect the amount and properties of liposomes after release from neutrophils. *b*, Raw fluorescence intensity traces recorded for samples collected after incubation of liposomes/neutrophils with and without stimulated release (+/- PMA). *c*, Average autocorrelation curves from FCS measurements ( $n = 30$  independent measurements, 5 s each). *d*, Amount of released liposomes given in particles per mL, signal (counts) per particle (CPP) and hydrodynamic diameter ( $D_h$ ) of liposomes was calculated from the fit parameters obtained in *c*. Centre line, the median; box limits, upper and lower quartiles; whiskers, minimum and maximum values ( $n = 30$  measurements per sample, two repeats were shown as *a* and *b*). The graphics of eppendorf tube was adapted from the Servier Medical Art website. Dr. Adrian Najer performed FCS experiments and FCS data analysis (Imperial College London).

After demonstrating that neutrophils can release loaded liposomes in an inflammatory environment (with PMA), subsequent uptake of the released liposomes by a target cell was studied. This corresponds to the final destination of the nanocarrier where intracellular drug release should finally yield the desired therapeutic effect. Considering the cell types present in the inflamed tissue, which can actively contribute to cause an uncontrolled immune response, a macrophage cell line (RAW 264.7 cells) was employed to represent target cells *in vitro*. Liposome/neutrophils were co-cultured with macrophages for 8 h in a physiological environment (cell medium) and in the presence of PMA (Figure 2.14a). There was negligible

rupture of neutrophils and release of liposomes at 8 h time point under non-inflammatory conditions (Figure 2.15). However, in the medium containing PMA, there was an increased number of dead neutrophils/NETs present in the wells (stained by PI). Simultaneously, the re-uptake of liposomes by the target macrophages was observed (Figure 2.14b). Nearly 97% of the macrophages had taken up liposomes (Figure 2.14c) as measured by flow cytometry. This indicates a successful transport cascade involving carrier neutrophils that undergo rupture to release and deliver the nanocarrier to target macrophages.

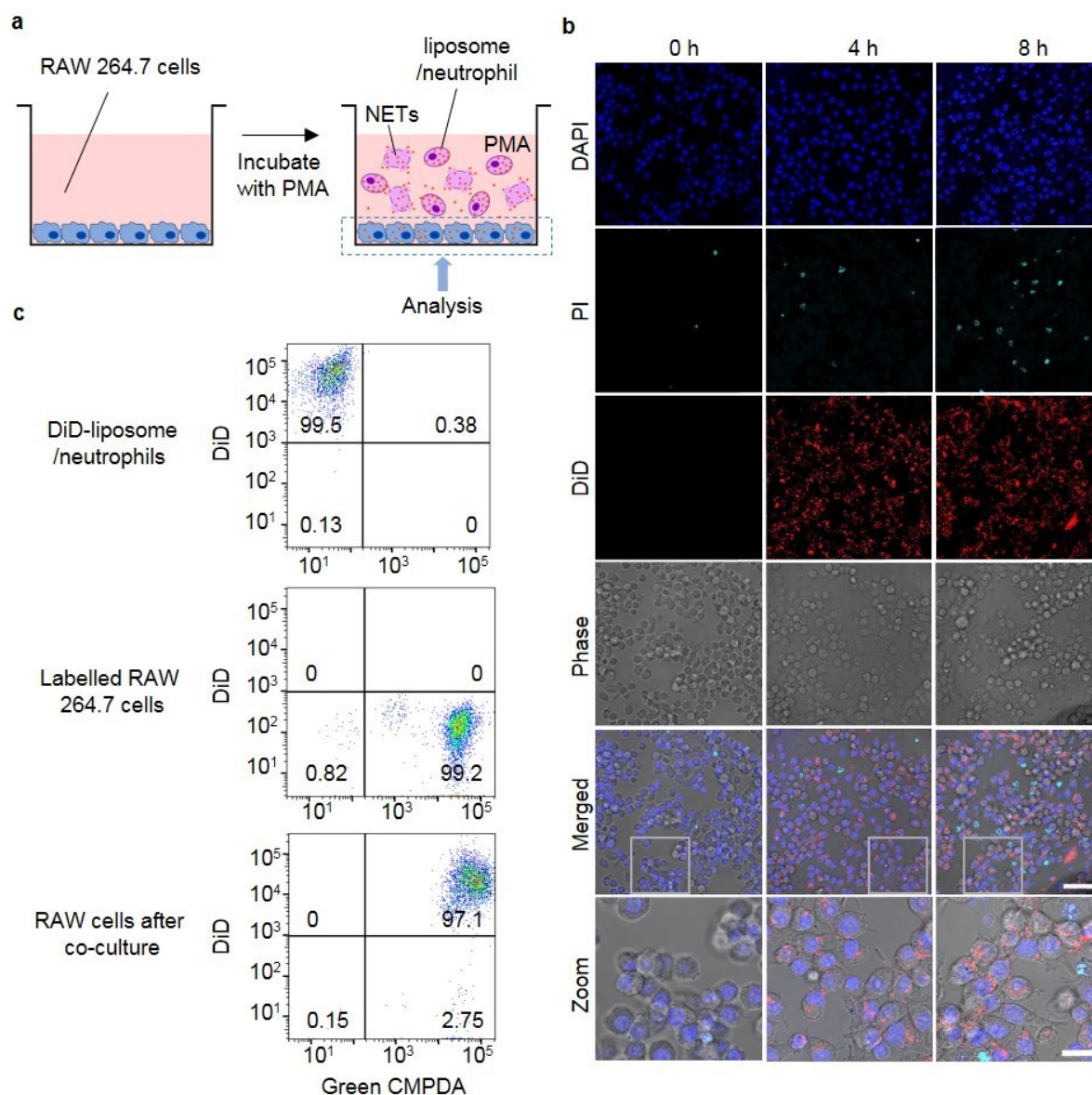


**Figure 2.14 Delivery of liposomes to co-cultured macrophages (RAW 264.7 cells) when transported *via* neutrophils.** **a**, Schematic illustration of the *in vitro* co-culture system of macrophages (RAW 264.7 cells) and liposome/neutrophils. **b**, CLSM representative images of macrophages after incubation with liposome/neutrophils at 0 h, 4 h and 8 h in the presence of PMA. The nuclei of macrophages were stained with DAPI, the released DNA fragments of neutrophils were stained with PI and the liposomes were labelled with DiD. Scale bar: 50  $\mu\text{m}$  in the merged image. The images show that liposomes were released from neutrophils (forming NETs, PI channel) and were subsequently taken up by macrophages. Scale bar: 10  $\mu\text{m}$  in the bottom image. **c**, Flow cytometry analysis of macrophages after co-culture with DiD-liposome/neutrophils. Macrophages were co-cultured with DiD-liposome/neutrophils in the medium containing PMA for 8 h. Green CMPDA channel shows macrophage labelling and DiD channel represents liposome labelling.

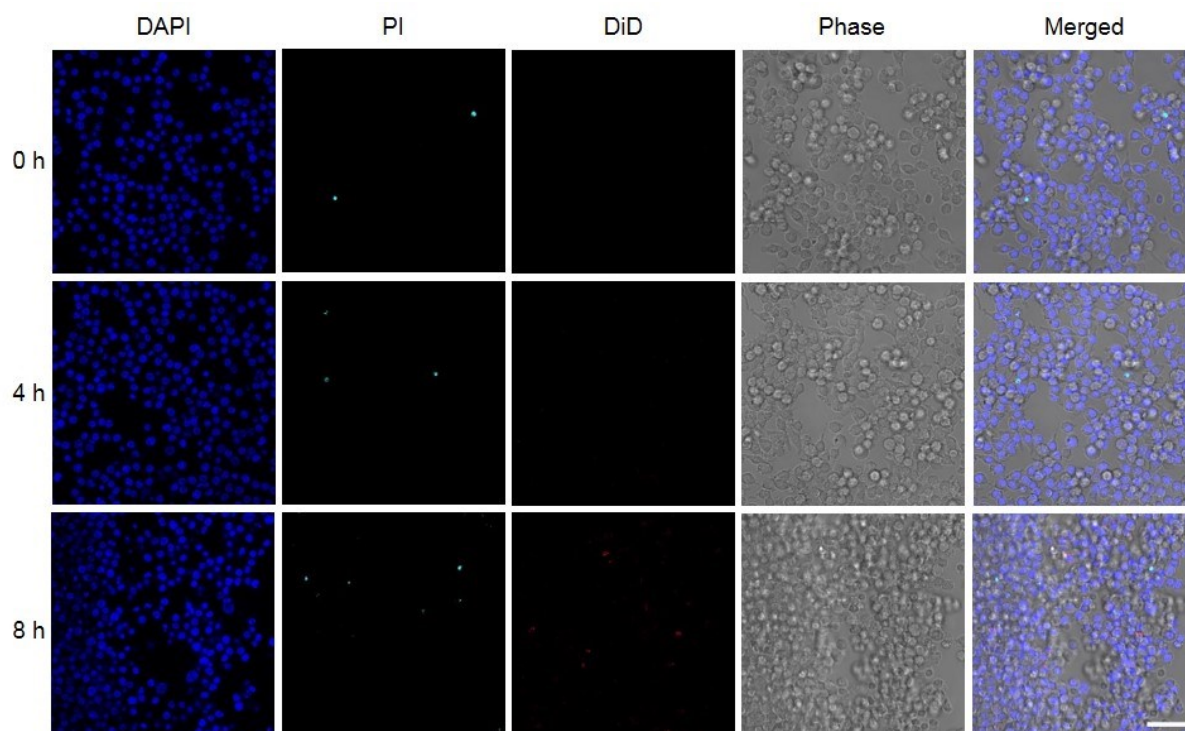


**Figure 2.15** CLSM representative images of RAW 264.7 cells after incubation with liposome/neutrophils at 0 h, 4 h and 8 h in the absence of PMA. The nuclei of RAW 264.7 cells were stained with DAPI, the released DNA fragments were stained with PI and the liposomes were labelled with DiD. The merged image is the overlay of the four individual images. Scale bar: 50  $\mu\text{m}$ .

To summarise, all the *in vitro* data suggests that neutrophils remained viable and retained their physiological properties after being loaded with liposomes. When in an environment mimicking the site of inflammation, loaded neutrophils can rapidly release liposomes under inflammatory stimuli and transport them to macrophages. These results show active migration behaviour of liposome loaded neutrophils towards sources of inflammatory signals, and inflammation triggered release of loaded liposomes and subsequent delivery to target cells, which sets the basis before loading an inflammatory drug into this system and test the anti-inflammatory effects *in vitro* and *in vivo*.

#### 2.3.4. Optimising drug loading and release properties of liposomes

After assessing and confirming that after loading with blank liposomes neutrophils can still respond to inflammatory signals and migrate towards the guidance of the chemokine gradient *in vitro*, and successfully delivering loaded liposomes to target cells, an anti-inflammatory drug was then loaded inside liposomes to test the responses of neutrophils and the resulting

biological effects on target cells. This represents the final delivery system that will later be applied *in vivo* to study anti-inflammatory effects in two relevant mouse models (see chapter 4).

Among all the anti-inflammatory drugs that were discussed in chapter 1 section 1.2, two different orally active drugs methotrexate (MTX) and dexamethasone (DEX) were chosen for several reasons: (1), MTX and DEX are the most widely used drugs with broad immune suppression properties; they have been used to treat many acute and chronic inflammatory diseases such as MI.<sup>109,112</sup> (2), They have serious side effects including hepatotoxicity, generation of opportunistic infections, bone marrow suppression and pulmonary hypersensitive<sup>143,144</sup> because of poor water-solubility and non-specific absorption by healthy tissues after systemic administration. Thus, these two drugs should ideally be delivered locally *via* drug delivery systems to inflamed tissue. To this end, each of these two drugs were tested to be loaded inside liposomes.

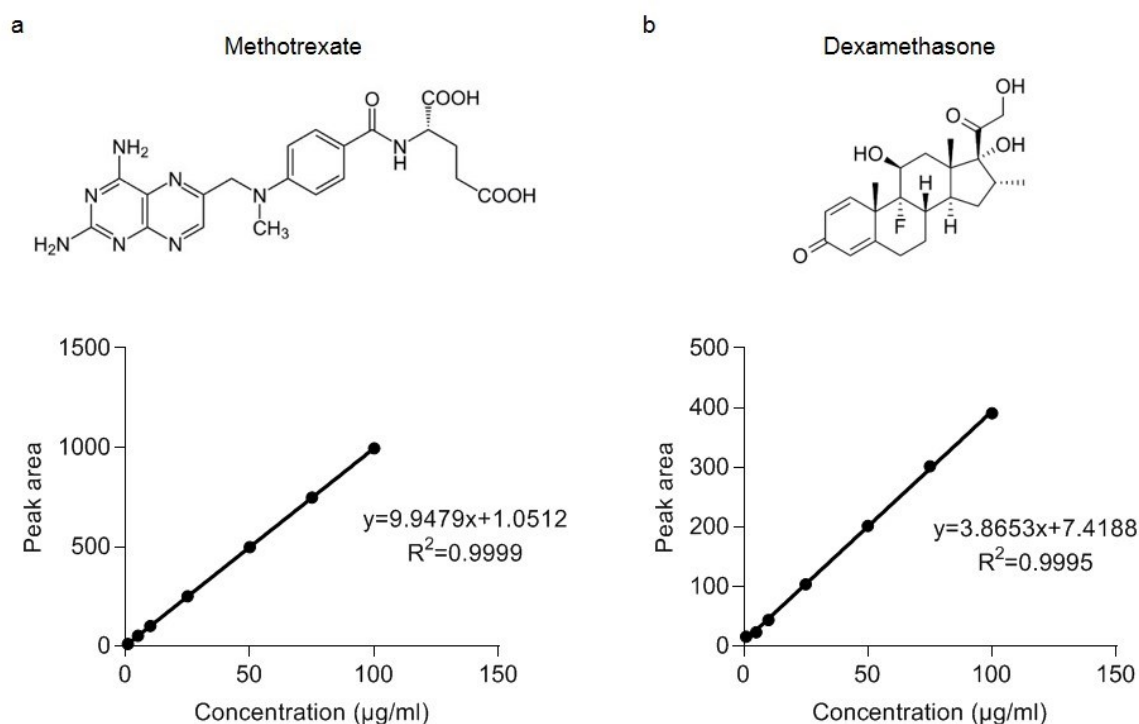


**Figure 2.16 Structures and calibration curves of MTX and DEX.** MTX (a) and DEX (b) dissolved in the mixture of PBS and propanol (v:v=1:1) at different concentrations were measured by LC-MS. The calibration curves were calculated based on the concentrations of the drug and peak areas obtained from LC-MS (mean  $\pm$  s.d., N = 3).



MTX-loaded liposomes and DEX-loaded liposomes were prepared using the thin-film hydration method and subsequent purification by size exclusion chromatography. The amount of loaded MTX and DEX inside liposomes was measured using LC-MS and calculated based on established calibration curves (Figure 2.16). Slight shifts in the baselines might have contributed to non-zero intercept of the standard curves. The resulting loading efficiency of MTX was of 1.25% with the composition of DOPC, DSTAP and cholesterol, in agreement with published studies.<sup>281</sup> The loading efficiency was 1 % and the encapsulation efficiency was 1.25 %, which were low as expected due to the thin-film hydration method used in this study. If needed in the future, the encapsulation efficiency of MTX inside liposomes can be improved by changing the encapsulation method such as using freeze–thaw cycles or the reverse phase evaporation method.<sup>282</sup> On the other hand, no DEX was detected from LC-MS with DEX-loaded liposome samples. Different liposome compositions and initial DEX loading amounts were tested to formulate DEX-loaded liposomes and samples were measured by LC-MS. However, DEX could not be detected by LC-MS in any of the samples (Table 2-2). No further attempts to load DEX were performed, because MTX could be loaded successfully, it was chosen as the anti-inflammatory drug for all the subsequent experiments.

Liposome composition (Weight ratio)	Initial DEX amount (wt% of lipid amount)	LC-MS result
DOPC : DSTAP : Cholesterol=76:14:10	10%, 20% 30%	No peak signal
DOPC : DSTAP=76:14	30%	No peak signal
DOPC : DSTAP: Cholesterol =76:14: 22.5	30%	No peak signal
DPPC : DSTAP=76:14	30%	No peak signal

**Table 2-2 The effect of liposome composition and initial DEX amount on the loading of DEX with liposomes.** *Different neutral lipids, percentages of lipids and cholesterol were used to formulate liposomes. Different initial DEX amounts were added when preparing liposomes. Propanol was added to disintegrate liposomes before measuring samples with LC-MS. DEX calibration curve was used from Figure 2.16 for calculation.*

MTX-loaded liposomes were obtained with a diameter of about 100 nm and a zeta potential of +28 mV (Figure 2.17a and b), which is similar to the DiD-liposomes that have shown high cell uptake efficiency and compatibility in previous *in vitro* experiments (Chapter 2 section

2.3.1). Transmission electron microscopy (TEM) further confirmed that the size of MTX-liposomes was  $111 \pm 46$  nm (Figure 2.17c). After loading MTX inside liposomes, the retention of MTX inside liposomes was critical to minimise premature exposure of neutrophils to the drug. Since it was previously shown that  $2.5 \mu\text{g mL}^{-1}$  of MTX could markedly influence neutrophil chemotaxis,<sup>283</sup> adherence and accumulation at the site of inflammation,<sup>284,285</sup> minimising rapid MTX release from the liposomes is particularly important. As neutrophils have a remarkably short half-life in the blood circulation of approximately 1.5 h and 8 h in mice and humans,<sup>26</sup> 8 h was chosen as the critical timeframe to retain most of the MTX inside the liposomes. To achieve a slow release of MTX from the liposomes within the first 8 h, three different cholesterol percentages between 10% to 40% were tested to tune membrane properties and, hence, the release profile (Figure 2.18a and b). By increasing the cholesterol percentage in the liposome composition, the phase of the lipid membrane changes from a lipid disordered phase to an ordered phase,<sup>286</sup> which successfully slowed down the MTX release from the liposomes. At a cholesterol percentage of 40%, only approximately 5% of the drug was released within the first 8 h during 20 d incubation, which turned out to be sufficiently stable for the intended application (Figure 2.18c). This composition is also in good agreement with the compositions reported in the literature to form stable liposome formulations with a controlled and reproducible release for loaded drugs.<sup>287</sup> In terms of the amount of drug released during this time,  $1.2 \mu\text{g}$  of MTX ( $2.4 \mu\text{g mL}^{-1}$  in the medium) was the maximum amount exposed to neutrophils during incubation. This is lower than concentrations that were previously found to have an effect on neutrophil chemotaxis.<sup>288</sup> However, in a more complex biological environment, mimicked by incubating MTX-liposomes in 90% fetal bovine serum (FBS),  $67 \pm 4\%$  of MTX was released from liposomes after 20 h incubation, reaching  $85 \pm 7\%$  release after 52 h. This suggests efficient release of MTX from liposomes after MTX-liposomes are released from neutrophils at the inflammatory site. This is key for the application, because if the drug stays entrapped inside the nanocarrier it cannot have the desired effect, even if delivered to the correct site via neutrophils. Subsequently, the effect of this optimised composition on the physiological functions of neutrophils was tested similarly to blank liposomes (see chapter 2 section 2.3.2).



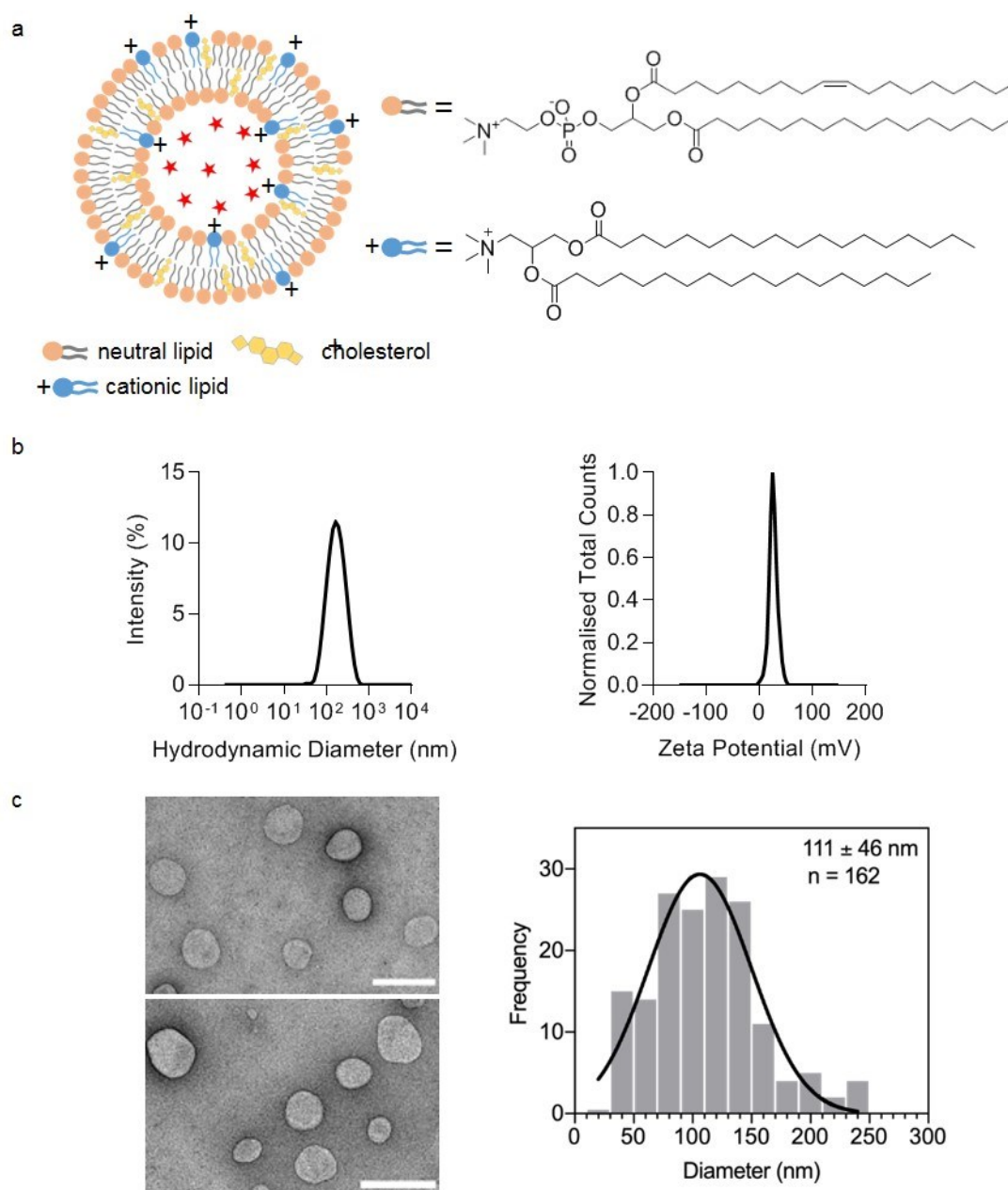


**Figure 2.17 Preparation and characterisation of MTX-liposomes.** *a*, Schematic illustration of the liposome structure and lipid molecules. *b*, Particle-size measured by DLS and zeta potential distribution of MTX-liposomes. *c*, TEM representative images and corresponding histogram for MTX-liposomes. Scale bars: 200 nm. TEM performed by Jiaqing Tang (Imperial College London).

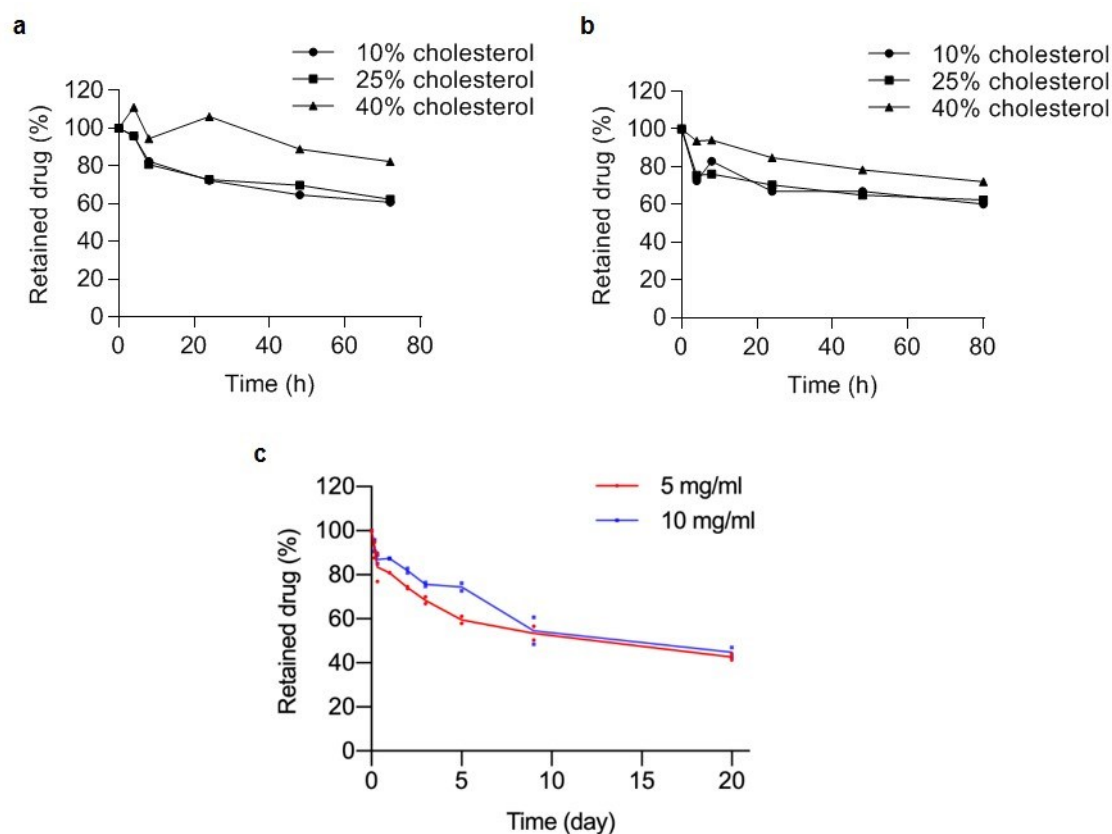


**Figure 2.18** The effect of cholesterol percentage of liposomes (liposome composition: 16:0-18:1 PC (POPC), 18:0 TAP and cholesterol) on drug retention behaviour. *a* and *b*, Quantity of retained drug (MTX concentration used during liposome formation: *b*: 5 mg mL<sup>-1</sup>; *c*: 10 mg mL<sup>-1</sup>) inside liposomes with different cholesterol percentages over 3 d in PBS pH 7.4 at room temperature measured by LC-MS. *c*, Quantity of retained MTX inside liposomes over 20 d in PBS pH 7.4 at room temperature measured by LC-MS (N = 2).

### 2.3.5. Preparation and characterisation of MTX-liposome loaded neutrophils

To test whether MTX incorporated in liposomes could be carried by neutrophils without affecting their viability and physiological functions various conditions were tested. Different MTX concentrations inside the liposomes (5 mg mL<sup>-1</sup>: MTX5; 10 mg mL<sup>-1</sup>: MTX10, initial hydrating concentrations) and different lipid concentrations of liposomes (1 mg mL<sup>-1</sup>: LP1; 2 mg mL<sup>-1</sup>: LP2, initial concentrations) were incubated with neutrophils. The MTX-liposome uptake efficiency for neutrophils was measured using flow cytometry. The MTX-liposomes were taken up by neutrophils with more than 98% of the neutrophils being positive for liposomes upon loading (Figure 2.21a), which matches previous neutrophil uptake results. Co-localisation of MTX-liposomes with neutrophils is shown in CLSM images, corresponding to flow cytometry data demonstrating that most of the neutrophils had taken up MTX-liposomes

during the 1 h incubation (Figure 2.19). A high-resolution fluorescence imaging technique 3D-SIM was employed to spatially localise MTX-liposomes in neutrophils, which revealed greater details of the subcellular particle localisation. It is clear that liposomes ended up in various locations on or within neutrophils (Figure 2.20). In most cases, liposomes were detected adjacent to the cell membrane, with some also clearly detected inside cells and even close to the nucleus. Furthermore, neutrophil viability was confirmed in all groups for 4 h and 8 h incubation post loading (Figure 2.21c). More than 85% of neutrophils were still alive after incubating with the highest MTX hydrating concentration and lipid concentration for 8h. Meanwhile, blank neutrophils and liposome-loaded neutrophils (lipid concentration at 2 mg mL<sup>-1</sup>) did not reveal any morphological difference with Giemsa-Wright staining (Figure 2.21b), which indicates high cytocompatibility of the MTX-liposome formulation. The neutrophil uptake and viability results demonstrate that loading MTX inside liposomes does not affect neutrophil phagocytosis of liposomes and the amount of MTX loaded inside was compatible with neutrophils.

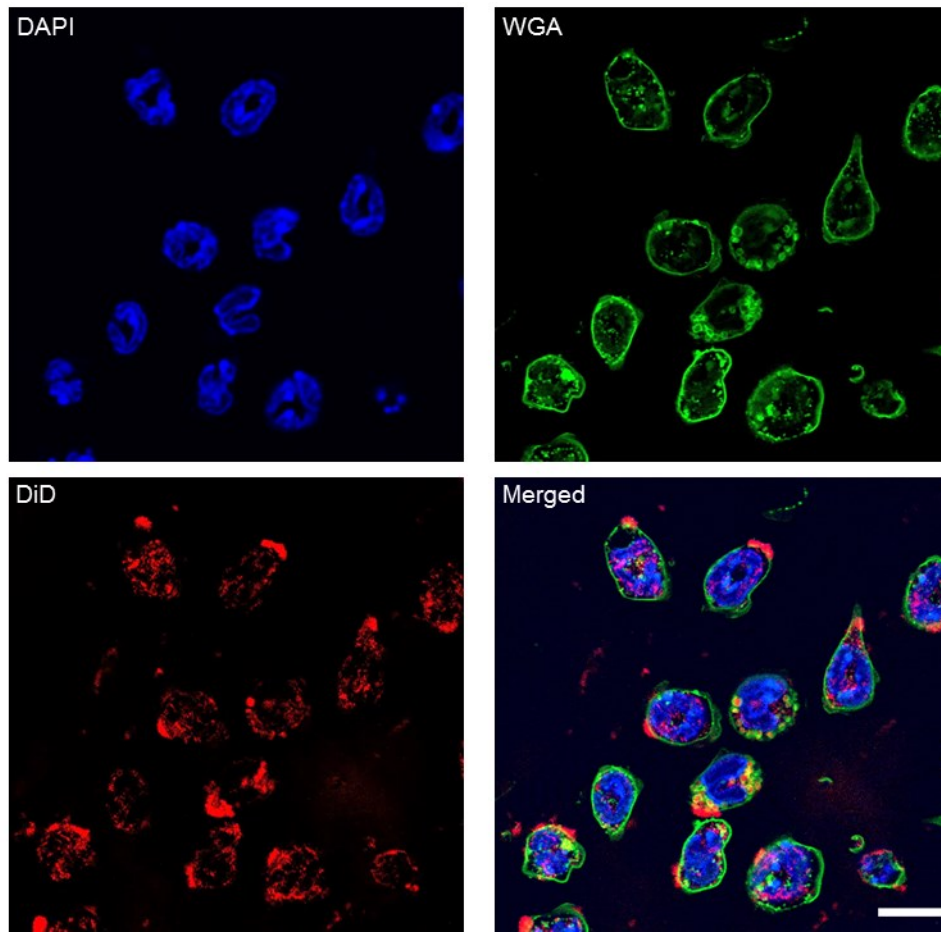


**Figure 2.19** CLSM representative images of MTX-liposome/neutrophils. The nuclei of neutrophils were stained with DAPI, the membranes of neutrophils were stained with WGA and the liposomes were labelled with DiD. The merged image is the overlay of three individual images. Scale bar: 10  $\mu\text{m}$ .

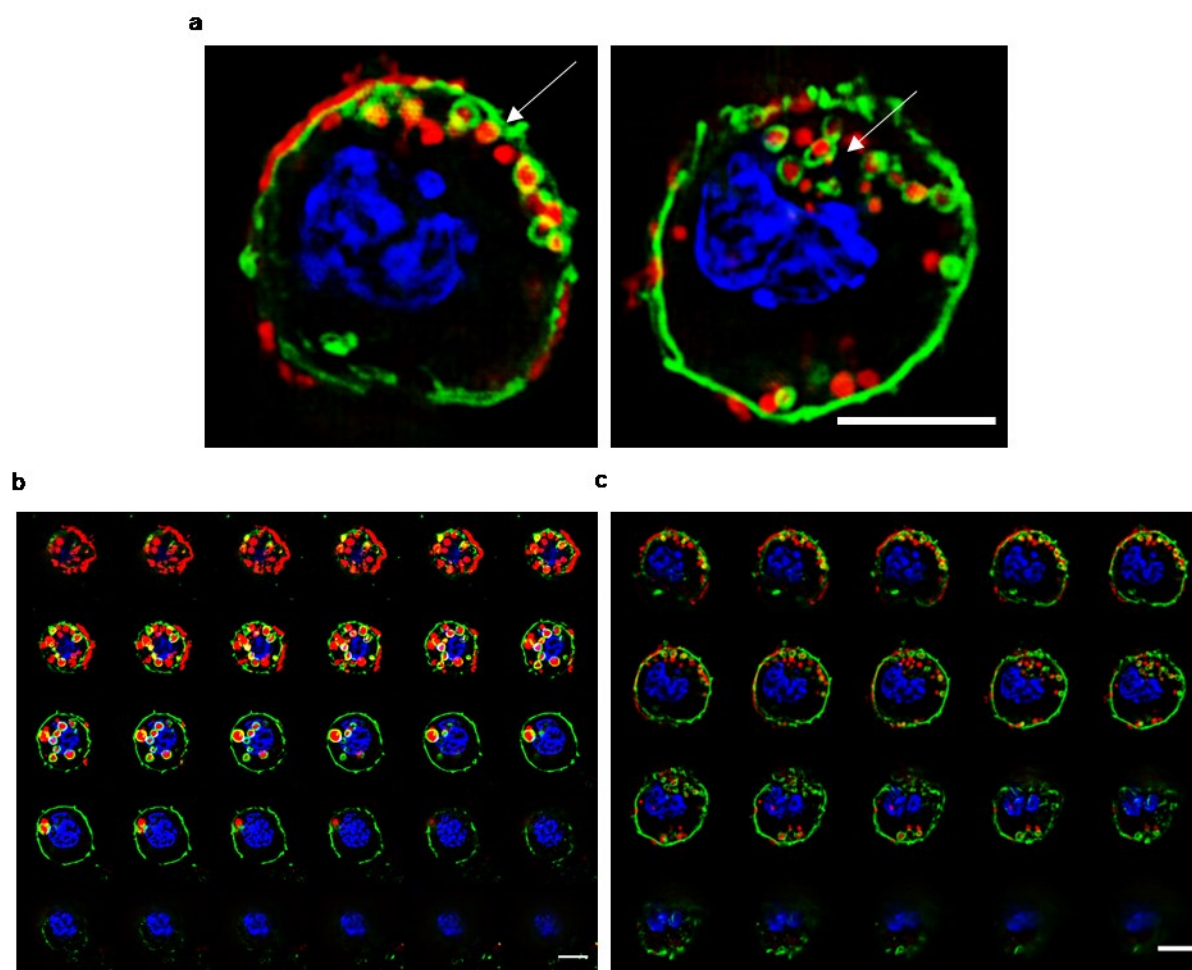


**Figure 2.20** Fluorescence representative images of a single MTX-liposome/neutrophil. *a*, Super resolution images (3D-SIM) showing the location of MTX-liposomes on/in a single neutrophil. Full image series in *c*. *b* and *c*, 3D-SIM showing the location of MTX-liposomes on/in a single neutrophil at different *z* positions. Scale bars: 5  $\mu\text{m}$ . 3D-SIM images were acquired and analysed with the assistance of Dr. Charles W. Winter (Imperial College London).

In the context of medical applications, the most important aspect is the final achieved drug loading per cell. This allows calculating the necessary cell number to be injected to reach a certain drug level. To quantitatively determine the total amount of MTX loaded in the neutrophils, a methotrexate ELISA kit was used after sonication of MTX-liposome/neutrophils to release MTX. The MTX-liposome/neutrophils reached the highest loading capacity of 0.2  $\mu\text{g}$  per  $10^6$  cells when incubated at the highest loading concentration (Figure 2.21d), which is the maximum loading capacity found for MTX-liposome onto neutrophils without affecting neutrophil viability and chemotaxis. Based on published studies, a dose of free MTX from 0.75  $\text{mg kg}^{-1}$  to 1  $\text{mg kg}^{-1}$  is used to suppress inflammation in mice,<sup>289</sup> but adverse effects such as myelosuppression and interstitial pneumonitis are also appendant.<sup>290</sup> When MTX is

combined with biomaterials and cell-based immunotherapy,<sup>291</sup> a lower dose down to 0.1 mg kg<sup>-1</sup> has been reported as sufficient for different diseases such as peritonitis,<sup>292</sup> MI and rheumatoid arthritis.<sup>293</sup> Compared with these reported effective doses for anti-inflammation applications in mice, the loaded amount of MTX within neutrophils used in this study is within this range and justifies its use in the following *in vitro* cell studies and *in vivo* mouse studies.

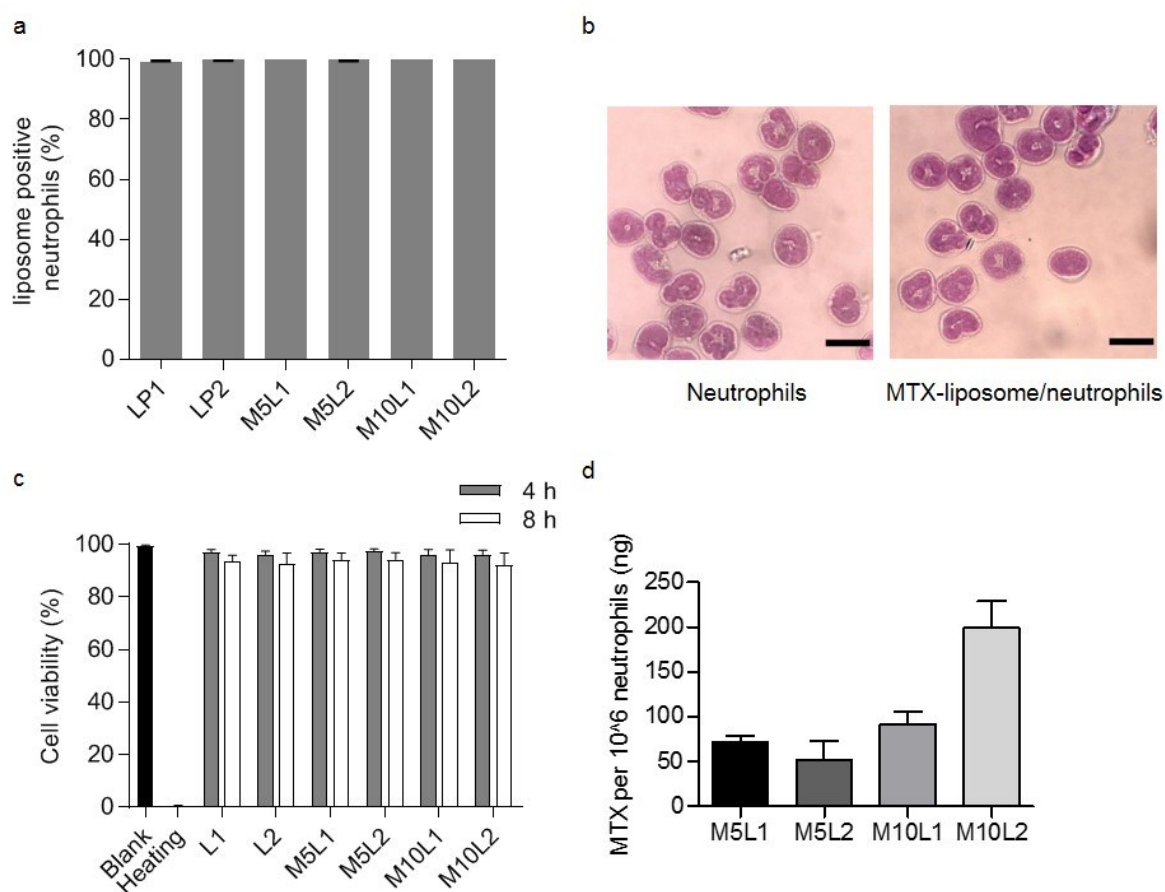


**Figure 2.21 Neutrophil uptake and viability for MTX-loaded liposomes and subsequent loading amount of MTX with neutrophils.** *a*, Flow cytometry analysis of MTX-liposome/neutrophils. Isolated neutrophils were incubated with MTX loaded liposomes at different lipid concentrations for 1 h (mean  $\pm$  s.d.,  $N = 3$ ). *b*, Morphological images (representative) of neutrophils with/without loading with MTX-liposomes stained with Giemsa-Wright stain. Images were recorded under bright field, 100X. Scale bar: 10  $\mu$ m. *c*, Isolated neutrophils were incubated with blank liposomes and MTX-liposomes at different lipid concentrations. Zombie Green cell viability kit was used to measure neutrophil viability by flow cytometry. Neutrophils heated at 70  $^{\circ}$ C for 10 min were used as the negative control (dead cells) (mean  $\pm$  s.d.,  $N = 3$ ). *d*, Quantity of MTX loaded in neutrophils after incubation with MTX-liposomes at different concentrations for 1 h. The cell pellet was collected by centrifugation and the MTX amount was measured by ELISA after rupturing the cells and liposomes by sonication (mean  $\pm$  s.d.,  $N = 3$ ).

### 2.3.6. Physiological functions of neutrophils after loading with MTX-liposomes

After characterisation and confirmation of the successful and efficient loading of neutrophils with MTX-liposomes, the physiological functions of loaded neutrophils were tested to ensure that loaded neutrophils can perform their physiological functions normally. Three physiological functions of neutrophils were tested before and after loading with blank liposomes and MTX loaded liposomes as described in section 2.3.2.

Similarly, CD11b protein expression, superoxide generation ability and cell migration behaviour were assessed. The CD11b expression level of neutrophils and MTX-liposome/neutrophils significantly increased with increasing fMLP concentration (Figure 2.22a) and no significant differences were detected between blank neutrophils, blank liposome/neutrophils and MTX-liposome/neutrophils. This result indicates that after loading with blank liposomes and MTX-liposomes, neutrophils still responded to an inflammation signal and expressed CD11b protein, which is necessary for adhesion and migration, similarly to blank neutrophils.

The superoxide generation capability of neutrophils and liposome-loaded neutrophils was also measured using dihydroethidium. After treatment with fMLP, an increase of superoxide generation in blank neutrophils was detected (Figure 2.22b). After loading with blank liposomes and MTX-liposomes, there was a similar increasing trend of superoxide generation in neutrophils. No significant differences were observed in the superoxide amount produced between blank neutrophils and liposome-loaded neutrophils after fMLP treatment.



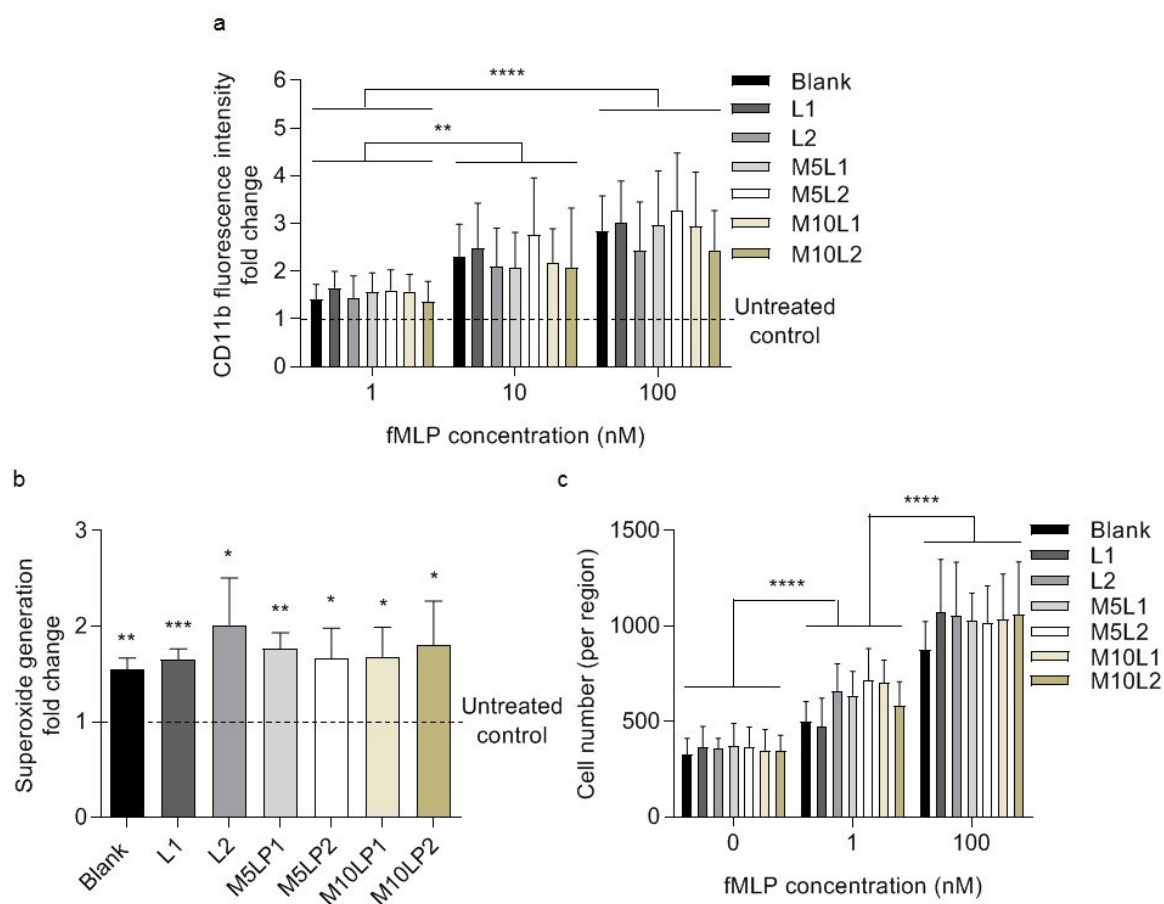


**Figure 2.22 Physiological functions of neutrophils after loading with MTX-liposomes. a,** Change in the CD11b expression of liposome loaded neutrophils after treatment with fMLP at different concentrations. Neutrophils were loaded with blank liposomes and MTX-liposomes at different concentrations and then stained with PE anti-mouse CD11b antibody (mean  $\pm$  s.d.,  $N = 3$ ).  $**P < 0.01$ ,  $****P < 0.0001$ , two-way ANOVA, Bonferroni post hoc test. **b,** Change in the superoxide generation of liposome loaded neutrophils with and without fMLP treatment. The superoxide level of cells was detected using dihydroethidium and compared to untreated control (mean  $\pm$  s.d.,  $N = 3$ ).  $*P < 0.05$ ,  $**P < 0.01$ ,  $***P < 0.001$ , unpaired two-tailed Student's  $t$  test. **c,** Quantity of migrated neutrophils on the bottom side of the membrane (mean  $\pm$  s.d.,  $N = 3$ ).  $****P < 0.0001$ , two-way ANOVA, Bonferroni post hoc test.

Furthermore, the active migration ability of loaded neutrophils was determined using a transwell migration assay. More neutrophils migrated through the pores of the transwell membrane (images were taken at the lower side of the membrane to count number of migrated cells) in the medium containing fMLP (Figure 2.22c, Figure 2.23), which indicates that neutrophils were activated by supplied fMLP and migrated towards the higher fMLP concentration area. After loading with blank liposomes and MTX-liposomes, there was a similar number of neutrophils migrating to the lower side of the membrane. Importantly,



from confocal images of migrated neutrophils, the signal from DiD labelled MTX-liposomes was still observed in migrated neutrophils (Figure 2.24), which shows that neutrophils responded to the inflammation signal, migrated and carried MTX-liposomes across the membrane following the chemokine gradient.

Neutrophils have been used as the cell carrier to deliver liposomes to brain tumours.<sup>239</sup> Anti-cancer drug paclitaxel (PTX) was encapsulated into liposomes and the physiological functions of neutrophils were evaluated *in vitro* after loading with PTX-liposomes. Neutrophils exhibited the same physiological activities including the migration capacity and chemotactic function after liposome loading compared with untreated neutrophils. However, neutrophils containing PTX fully lost these activities. This suggests that PTX was compartmentalised by liposomes to not influence the physiological activities of neutrophils. In this study, the composition of liposomes was optimised to retain MTX inside liposomes to avoid premature exposure of neutrophils to the drug, thus neutrophils can still perform their physiological functions after MTX-liposome loading.

In conclusion, after loading with MTX-liposomes, neutrophils maintained their physiological functions, which indicates that they can respond to inflammation signals in the blood and migrate to the inflammatory site, at the same time carrying their loaded cargoes. These results also correspond to the previous experiments when testing with blank liposomes (liposome composition: DOPC, 18:0 TAP, and cholesterol), which confirms that MTX was successfully compartmentalised to not affect the neutrophil's functions. This is key because premature drug release could inhibit the carrier neutrophils from transporting the cargo to the desired place.

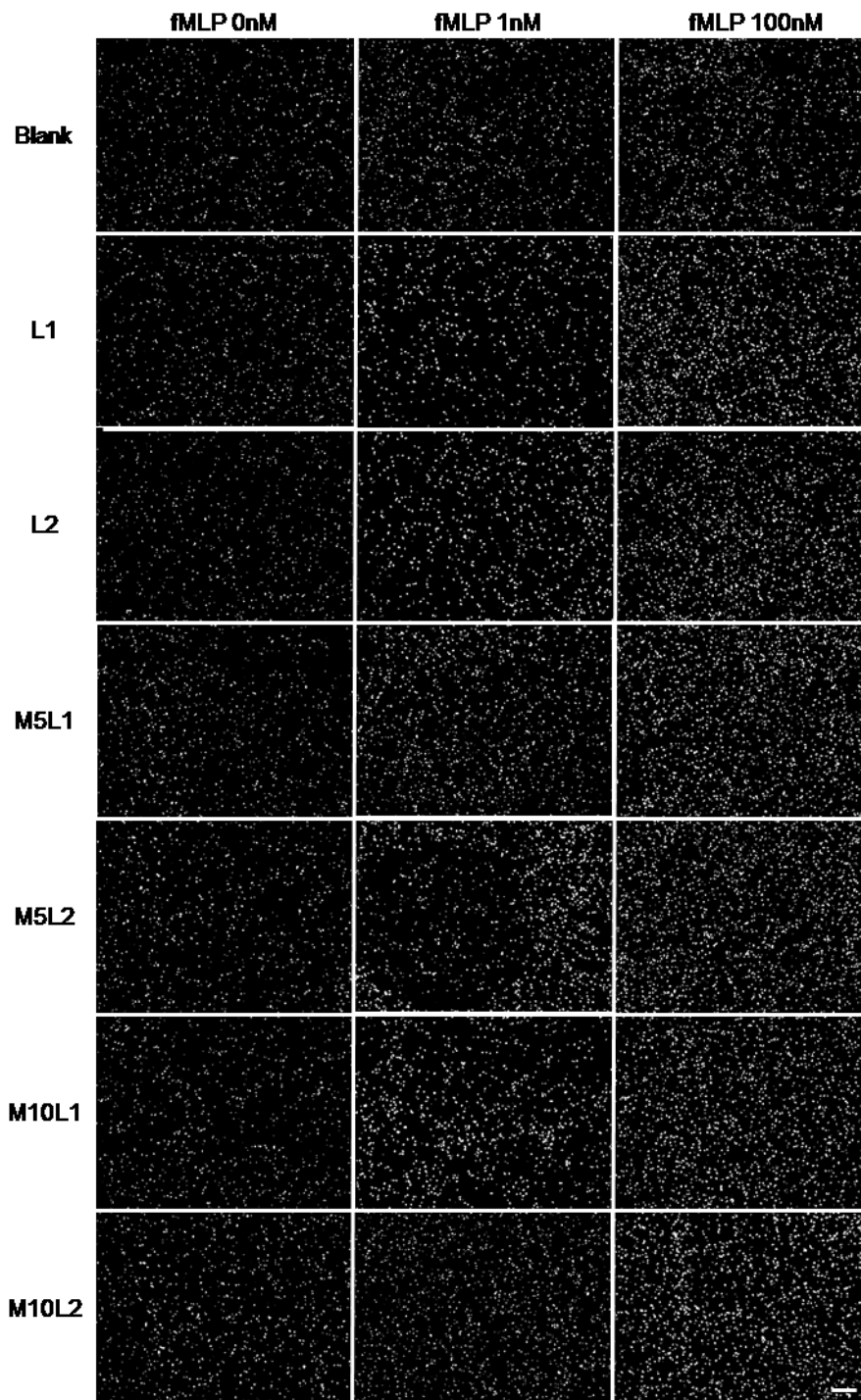


**Figure 2.23** Representative images of neutrophils at the bottom side of the transwell membrane after the migration test. Neutrophils were incubated with blank liposomes or MTX-liposomes at different lipid concentrations. Formulated MTX-liposome/neutrophils were deposited in the upper chamber of the transwell and activated by fMLP in the lower chamber. MTX-liposome/neutrophils migrated through the pores of the membrane. Membranes were taken out and the cells on the upper side were removed. The nuclei of neutrophils at the bottom side of the membrane were stained with DAPI and imaged by fluorescence microscopy (DAPI channel). Scale bar: 100  $\mu\text{m}$ .

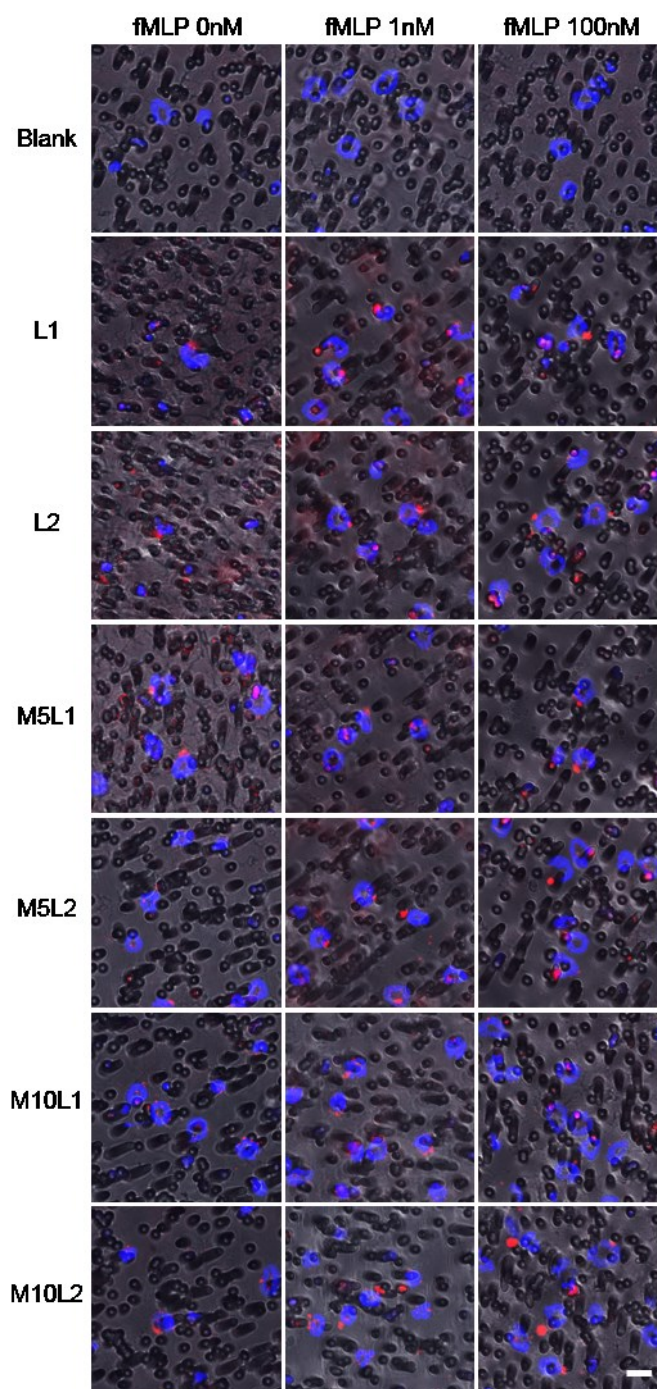


**Figure 2.24** CLSM representative images of MTX-liposome/neutrophils on the transwell membrane. Formulated MTX-liposome/neutrophils (liposomes were labelled with DiD) or controls were put in the upper chamber of the transwell to measure the cell migration ability. The membranes were cut out and put in an ibidi plate and imaged using CLSM. Pores of the membrane (dark grey) were traversed by the liposome-loaded neutrophils. Scale bars: 5  $\mu\text{m}$ .

### 2.3.7. Inflammation-responsive transfer of MTX-liposomes from neutrophils to macrophages

After testing the physiological functions of neutrophils and confirming that after loading with MTX-liposomes, the neutrophils maintained their adhesion and migration abilities responding to inflammatory signals, the release of loaded MTX-liposomes from carrier neutrophils in the medium containing PMA was determined. In this medium, neutrophils will rupture to form NETs causing MTX-liposome release.

Similarly to the experiments above using blank liposomes, FCS was employed to measure the released DiD labelled MTX-liposomes in the cell medium. After 8 h incubation, a much higher raw fluorescence intensity was detected in supernatants of MTX-liposome/neutrophils incubated in the cell medium containing PMA compared to samples from the basal medium without any supplement of PMA (Figure 2.25a). The corresponding autocorrelation curves and calculated hydrodynamic diameters indicate that MTX-liposomes were released from neutrophils (Figure 2.25b). The difference in particle counts compared between control groups and PMA treated groups demonstrates that the inflammatory environment (with PMA) caused NETs formation resulting in a large increase of MTX-liposome release to the medium (Figure 2.25c). Furthermore, the signal per liposome (CPP in kHz) and diameter ( $D_h$ ) revealed that there were no significant differences detectable between the original liposomes and the released MTX-liposomes. Partial aggregation of liposomes was also found in some autocorrelation curves, some outliers in the CPP and size plots (Figure 2.25d and e), which is due to the positively charged surface of MTX-liposomes. Furthermore, the amount of MTX in the released particle solution after incubation of loaded neutrophils in the presence of PMA was quantified by ELISA. 96% of loaded MTX was detected in the supernatant of MTX-liposomes loaded neutrophils after incubation in the presence of PMA for 8 h (Figure 2.26). The MTX release results are in good agreement with previous reported study; PTX-liposome loaded neutrophils showed a burst release of PTX at 4 h timepoint in the presence of PMA and achieved about 94% of PTX release after 8 h.<sup>239</sup>

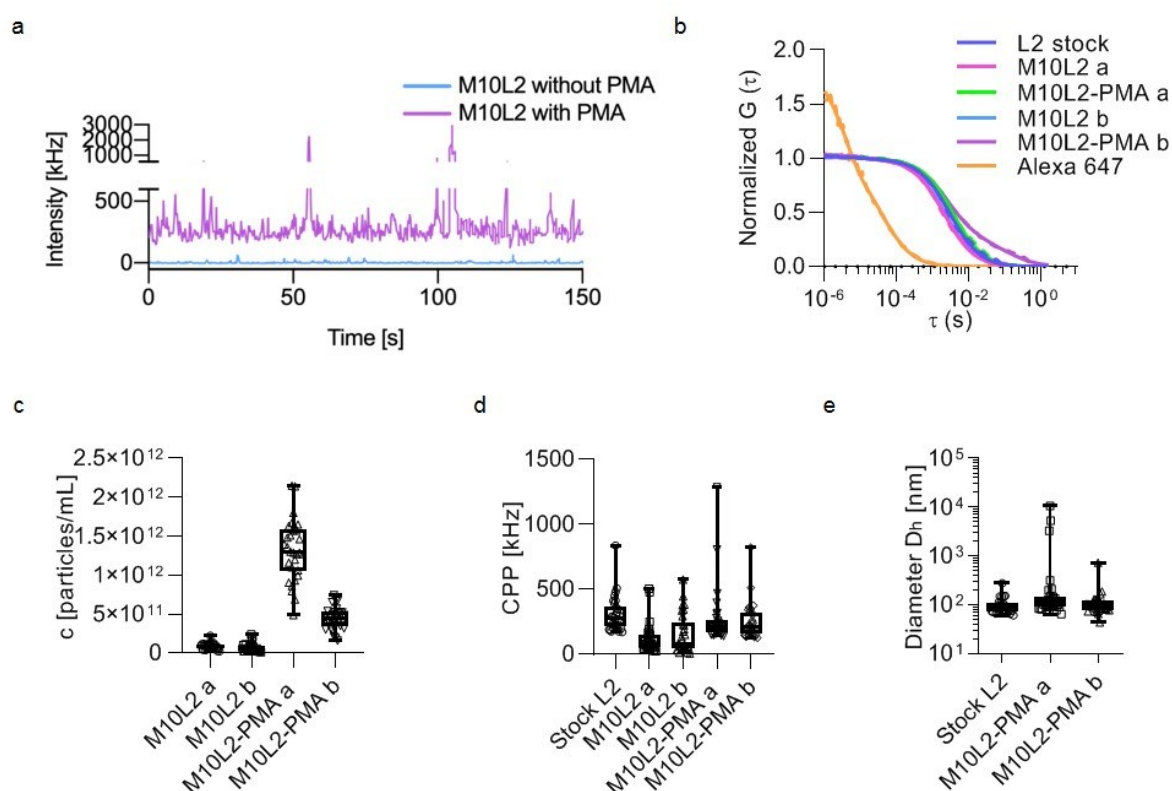


**Figure 2.25 Stimulated release of MTX-liposomes (DiD labelled) from neutrophils after treatment with PMA detected by FCS.** *a*, Raw fluorescence intensity traces recorded for samples collected after incubation of MTX-liposomes/neutrophils with and without stimulated release (+/- PMA). *b*, Average autocorrelation curves from FCS measurements ( $n = 30$  independent measurements, 5 s each). *c*, Amount of released MTX-liposomes given in particles per mL, signal (counts) per particle (CPP) and hydrodynamic diameter ( $D_h$ ) of liposomes was calculated from the fit parameters obtained in *b*. Centre line, the median; box limits, upper and lower quartiles; whiskers, minimum and maximum values ( $n = 30$  measurements per sample, two repeats were shown as *a* and *b*). Stock L2 and Alex 647 results are reused from Figure 2.13. Dr. Adrian Najer performed FCS experiments and FCS data analysis. (Imperial College London).

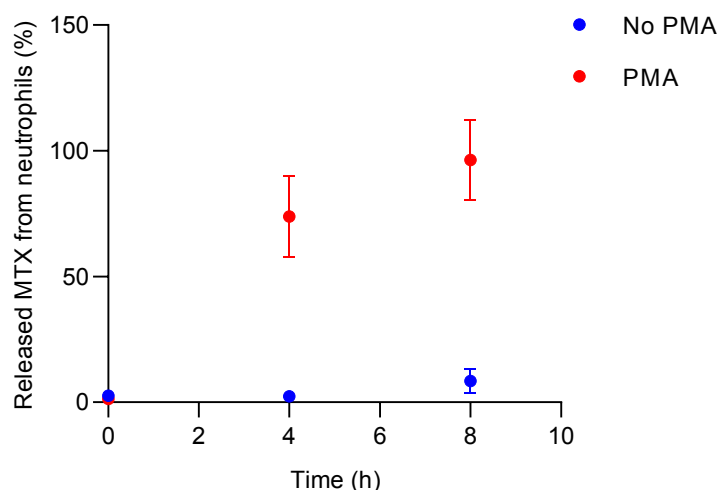


**Figure 2.26 Percentage of released MTX from neutrophils.** *Formulated MTX-liposome/neutrophils were incubated with and without the inflammatory stimuli (+/- PMA). The supernatants were collected at different time points and released MTX in the supernatants was quantified by ELISA. n = 3.*

After demonstrating that neutrophils can release loaded MTX-liposomes in an inflammatory condition, the re-uptake of the released MTX-liposomes by macrophages was tested. MTX-liposomes/neutrophils were co-cultured with macrophages for 8 h in the basal medium and in the presence of PMA. After removal of neutrophils, macrophages were measured using flow cytometry. Nearly 82% of macrophages had phagocytosed MTX-liposomes (Figure 2.27), which indicates that neutrophils had undergone rupture stimulated by PMA to release loaded MTX-liposomes and successfully transported them to target macrophages.

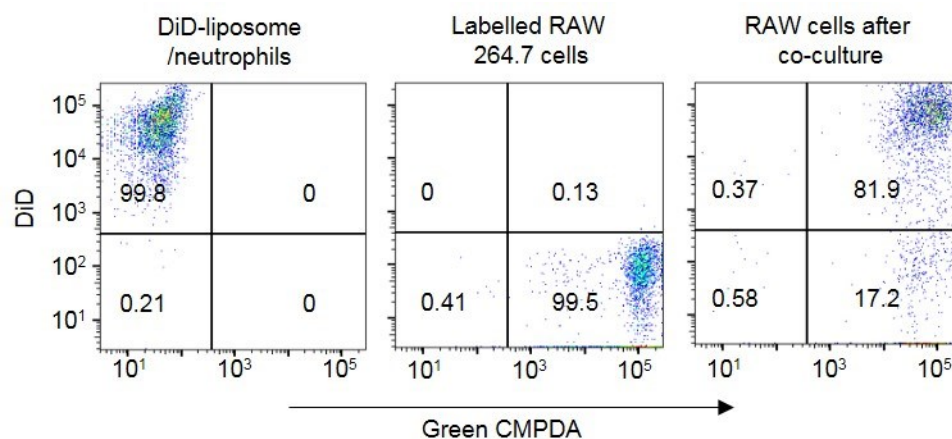


**Figure 2.27** Flow cytometry analysis of macrophages after co-culture with MTX-liposome/neutrophils (liposomes were labelled with DiD). Macrophages were co-cultured with MTX-liposome/neutrophils in the medium containing PMA for 8 h. Green CMPDA channel shows macrophage labelling and DiD channel represents MTX-liposome labelling.

The final mechanism involved in the described delivery strategy is the drug effect on the target cells eventually. Low concentrations of MTX ( $\sim 350 \mu\text{g mL}^{-1}$ ) are known to suppress TNF- $\alpha$  expression in cells and also inhibit folic acid synthesis, which slows down cell proliferation.<sup>110,294</sup> Thus, the TNF- $\alpha$  expression level and cell proliferation of macrophages (RAW 264.7) were assessed after co-culturing with MTX-liposome/neutrophils and treatment with different inflammatory cytokines. LPS and PMA were supplied to mimic an inflammatory environment. A dramatically increased expression of TNF- $\alpha$  gene in macrophages was detected after supplying LPS and PMA in the culture medium, which indicates that macrophages were stimulated by LPS and PMA towards a pro-inflammatory phenotype as reported by published studies (Figure 2.28).<sup>295</sup> After treatment with different amounts of MTX-liposomes and free MTX using equivalent drug concentrations, no significant decrease of TNF- $\alpha$  expression in macrophages was detected. This could be due to the short treatment time (only treated for 6 h) with MTX-liposomes and free MTX. The treatment cannot be prolonged because after a 6 h timepoint the expression of TNF- $\alpha$  drops down spontaneously in macrophages.<sup>295</sup> Therefore, another readout was tested that can show the effect of MTX-liposomes on macrophages when delivered via neutrophils.

To test the effect on the proliferation of macrophages, MTX-liposome/neutrophils were co-cultured with macrophages for 24 h to ensure sufficient time for MTX to be released from neutrophils and interact with macrophages. The results show that macrophages cultured with inflammatory cytokines only (PMA and/or LPS) tended to grow 1.5-time faster compared to cells grown in the basal medium (Figure 2.29). In contrast, after applying MTX-liposome/neutrophils to macrophages in an inflammatory environment, the cell growth ability of the macrophages was reduced to a similar level seen when directly treated with free MTX using equivalent drug concentrations. Encouragingly, the observed reduction in cell growth rate using the neutrophil-mediated delivery system confirms that neutrophils can deliver sufficient amounts of drug to have the desired effect on target cells.

In conclusion, all the *in vitro* data suggests that the composition of liposomes was optimised with the proper size and zeta potential to be taken up by neutrophils efficiently and retain MTX inside liposomes with minimum exposure to neutrophils. Neutrophils remained viable and retained their physiological properties to allow for migration towards sources of inflammatory signals. Next, inflammation triggered release of drug-loaded liposomes from neutrophils and subsequent delivery to target cells where the drug exerts its function was achieved.



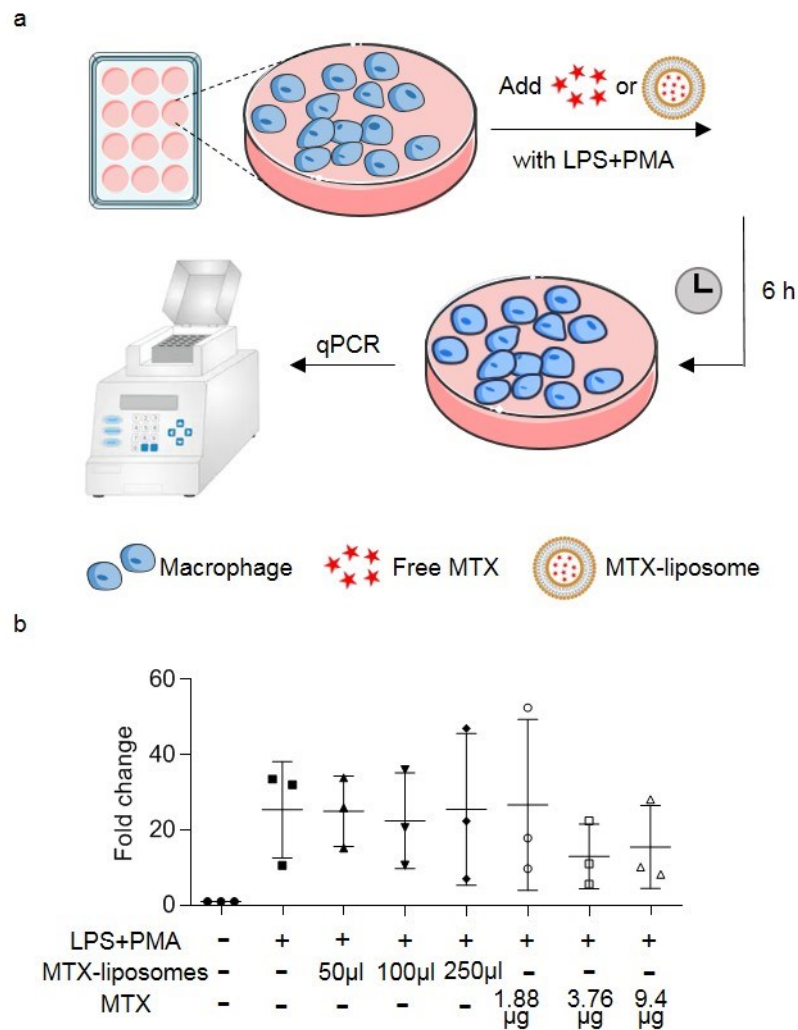


**Figure 2.28 TNF- $\alpha$  inhibition effect of MTX-liposome on co-cultured macrophages (RAW 264.7 cells).** **a**, Schematic illustration of the measurement procedure. Macrophages were first seeded in a 12-well plate in advance. Different concentrations of MTX-liposomes and the equivalent amount of free MTX were added and incubated for 6 h with supplement of LPS and PMA in the culture medium. Macrophages were then collected and lysed to run qPCR for measuring TNF- $\alpha$  gene expression. **b**, Fold changes of TNF- $\alpha$  gene expression in macrophages after treating with MTX-liposomes and the equivalent amount of MTX (mean  $\pm$  s.d.,  $N = 3$ ).

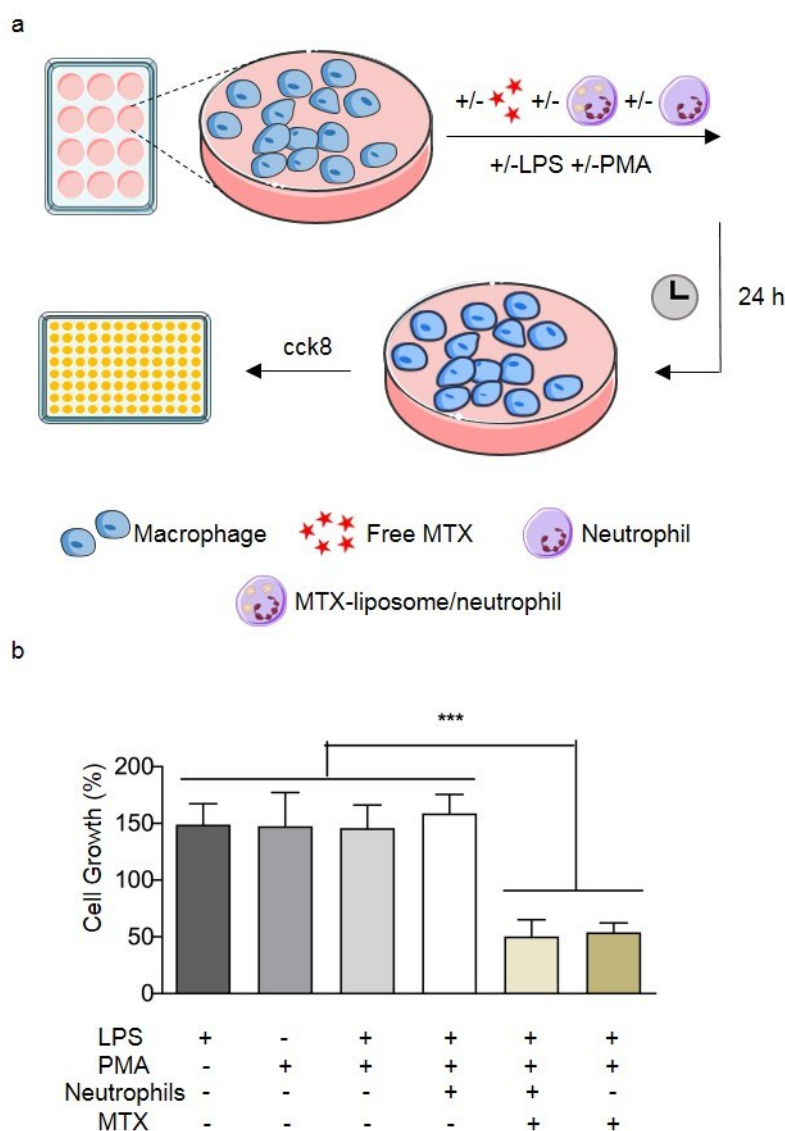


**Figure 2.29 Anti-proliferation effect of MTX-liposome on co-cultured macrophages (RAW 264.7 cells) when transported *via* neutrophils.** **a**, Schematic illustration of the measurement procedure. Macrophages were first seeded in a 12-well plate in advance. MTX-liposome/neutrophils and the equivalent amount of free MTX were added and incubated for 24 h with supplement of LPS and PMA in the culture medium. Macrophage viability was measured using Cell Counting Kit 8. **b**, Proliferation of macrophages after treatment with inflammatory cytokines and co-culture with MTX-liposome/neutrophils was compared to basal medium (mean  $\pm$  s.d.,  $N = 3$ ). \*\*\* $P < 0.001$ , one-way ANOVA, Bonferroni post hoc test.

## 2.4. Conclusions

A neutrophil mediated drug delivery system that takes advantage of the physiological functions of neutrophils to respond to inflammatory stimuli was developed and

demonstrated. Furthermore, this system actively delivers anti-inflammatory drug loaded liposomes to target cells *in vitro*.

Neutrophils were isolated from mouse bone marrow using a negative selection method and obtained near 97% purity. Methotrexate-loaded liposomes (MTX-liposomes) were formulated with optimised particle size ( $111 \pm 46\text{nm}$ ) and zeta potential ( $+26 \pm 7\text{mV}$ ) using a film-hydration method. MTX was successfully retained inside liposomes by increasing the cholesterol percentage in the liposome composition to finally trap more than 90% of MTX inside liposomes within the timeframe needed for neutrophil-loading and delivery. However, in a complex environment mimicking the inflammatory site, 85% of MTX was released after 52 h incubation in 90% FBS (v/v), suggesting efficient release of MTX from liposomes after MTX-liposomes are released from neutrophils at the inflammatory site. Successful neutrophil loading with MTX-liposomes was achieved by simply incubating neutrophils with MTX-liposomes *ex vivo* for 1 h. Typically, more than 95% of the neutrophils contained MTX-liposomes, while maintaining viability. The location of liposomes on/in neutrophils was observed using high resolution fluorescence microscopy, showing consistent loading at the membrane and inside of neutrophils.

The physiological functions of neutrophils after loading with MTX-liposomes were determined using different methods. After MTX-liposome loading, the neutrophils retained their functions showcased by the expression of CD11b protein, migration and generation of superoxide in response to the inflammatory factor fMLP. These results represent the neutrophil's important functions of adherence, migration and killing in an inflammatory environment. Upon transferring neutrophils to an inflammatory environment induced by PMA, successful neutrophil activation and release of NETs were observed by confocal microscopy and simultaneous release of the loaded MTX-liposomes was detected by FCS and quantified by ELISA. To further evaluate trafficking of the drug from neutrophils to target cells, MTX-liposome/neutrophils were co-cultured with macrophages (RAW 264.7). After 24h co-culture in the medium containing PMA, 82% of macrophages phagocytosed liposomes released from neutrophils and their proliferation was suppressed 3 fold compared to untreated macrophages.

Overall, the developed neutrophil-mediated drug delivery system, MTX-liposome loaded neutrophils, can load sufficient anti-inflammatory drug MTX *via* cationic liposomes with

preservation of physiological functions of neutrophils to allow their response to inflammatory signals. Furthermore, MTX-liposome loaded neutrophils can exert biological effects on target cells. More importantly, this neutrophil based delivery system offers the versatility to load different types of nanoparticles *e.g.* stimuli-responsive micelles or polymersomes that can allow encapsulation of various drug doses, other drugs and additionally incorporate triggered release in the target cells.

As discussed in the introduction, liposomes are a good nanocarrier to realise rapid drug release from neutrophils to mitigate inflammation promptly for the treatment of acute inflammation. In case of treating chronic inflammation, macrophages are a good cell carrier involved from the early stages of inflammation to the late tissue remodelling stage. Nanoparticles with higher stability, such as polymersomes and polymer micelles, are suitable nanocarriers to be incorporated inside macrophages to maintain nanoparticle integrity and realise sustained drug release. The formulation and optimisation of macrophage-mediated drug delivery systems with different types of nanoparticles will be investigated in the next chapter.

## Chapter 3

# Cellular interactions of different types of nanoparticles with macrophages

## 3. Cellular interactions of different types of nanoparticles with macrophages

### 3.1. Introduction

Macrophages play an important role in the innate immune response to inflammation after tissue injury.<sup>296</sup> When compared to neutrophils that are recruited to the site of inflammation in the very early stage of inflammation, macrophages are implicated in the inflammatory response throughout,<sup>236</sup> starting from the early stage of inflammation to the late tissue resolution and remodelling phase.<sup>45</sup> Furthermore, during different stages of the inflammatory response, macrophages can polarise into different phenotypes to fulfil various tasks following exposure to chemotactic factors. In the early stages of inflammation, macrophages are polarised to a pro-inflammatory phenotype (M1 macrophages), which are responsible for producing a large number of inflammatory cytokines and mediators to amplify inflammation.<sup>47,48</sup> In contrast, during the late stages of inflammation and the resolution/remodelling phase, M1 macrophages transform to and/or are replaced by macrophages of a reparative phenotype (M2 macrophages), which play key roles in facilitating extracellular matrix (ECM) deposition and tissue regeneration.<sup>51,297</sup>

Similar to neutrophils, the phagocytotic nature of macrophages has been exploited to employ them as a carrier cell for the delivery of drugs or drug encapsulated nanoparticles to inflammatory sites. Their attractiveness as a drug delivery system is further heightened by their natural ability to migrate to and infiltrate inflammatory sites as well as their innate avoidance of recognition by the immune system.<sup>296,298</sup> For example, there was found significant accumulation of tumour-associated macrophages in cancer-related inflammation.<sup>299</sup> This has led to several studies demonstrating that macrophages (primary macrophages or macrophage cell lines such as RAW 264.7 cells) loaded with anti-cancer drugs or drug encapsulated nanoparticles can be used to efficiently deliver anti-cancer drugs to tumour sites.<sup>300–302</sup> In parallel, macrophage-mediated drug delivery systems have also been applied for the treatment of diseases with associated inflammation such as Parkinson's disease (PD) and rheumatoid arthritis (RA).<sup>244,303,304</sup>

In the context of drug delivery for anti-inflammation therapy, macrophages need to load sufficient quantities of therapeutic agents and preserve their physiological functions after

loading to successfully deliver loaded drugs or drug encapsulated nanoparticles to the desired site and resolve inflammation. Most importantly, it has previously been found that macrophages can polarise into their M1 or M2 phenotypes upon activation by nanoparticles.<sup>305</sup> Therefore, it is important to study phenotypic shifts of macrophages induced by loading with nanoparticles to ensure that the loaded macrophages do not exhibit an unfavourable phenotype, which could amplify inflammation after administration.

The work presented in this chapter aims at designing and formulating different types of nanoparticles for their application in macrophage-mediated drug delivery for the treatment of inflammatory diseases. It is hypothesised that different types of nanoparticles including organic nanoparticles and inorganic nanoparticles with positive and negative surface charges can result in different cellular responses of macrophages after loading *via* phagocytosis. Cell viability, physiological functions and macrophage phenotypes (pro- or anti-inflammatory phenotype) will be affected after loading with different types of nanoparticles. To demonstrate the hypothesis, a small library of different nanocarriers from liposomes, polymer micelles, polymersomes to mesoporous silica nanoparticles (MSNs) were chosen for the study. These chosen nanoparticles have their own advantages and disadvantages as drug carriers. Liposomes can encapsulate both hydrophilic and hydrophobic drugs and have high biocompatibility. Many liposomal formulations are currently on the market for medical use. However, they have limited physical and chemical stability and low versatility compared to polymer-based nanoparticles. The issue of drug leakage is another limitation of liposomes. In contrast, polymer-based nanostructures such as polymersomes and micelles can be fine-tuned in terms of stability and permeability using the diversity of polymer chemistry, which also allows easy surface functionalisation. The main disadvantages are: polymers are not molecularly defined structures and polymer synthesis usually has a big batch-to-batch variation, which currently prevents many polymeric nanoparticle systems to be translated to the clinic. MSNs have tailorable mesoporous structure, high surface area, tuneable geometry and low polydispersity while their slow degradation properties hinder their entry to the clinic. The nanoparticles in this chapter were chosen by considering the long-term migration timescales of macrophages towards inflammatory sites and the potential of using macrophages to deliver drugs for tissue regeneration in the late stages of inflammation. This is why apart from liposomes that have also been used for neutrophil-mediated delivery

(chapter 2), other nanoparticles with higher stability were tested in this chapter to help maintaining nanoparticle integrity inside macrophages. This will ensure in the future that the drug can be retained inside nanoparticles whilst aiming for sustained drug release from the hybrid system.

Organic nanoparticles were further functionalised with a neutral or positively charged surface. A positively charged nanoparticle surface can promote interactions with the macrophage membrane and achieve high loading efficiencies. In contrast, a neutrally charged surface coating such as with poly(ethylene glycol) (PEG) or poly(2-methyl-2-oxazoline) (PMOXA) can greatly enhance nanoparticle stability after being released from macrophages at the desired site as PEG units can form a hydrating layer by absorbing water molecules to prevent/delay protein absorption.<sup>218</sup> Thus, these two different surface functionalisation strategies were considered herein for designing the nanoparticle component of the delivery system. As previously reported, nanoparticle surface charge impacts cell uptake, intracellular trafficking and cytotoxicity of nanoparticles;<sup>256,306</sup> as such, this parameter was evaluated in this study. RAW 264.7 cells, a commonly used model of mouse macrophages, were employed to explore macrophage cellular responses to nanoparticles. Various nanoparticle concentrations were tested with macrophages (RAW 264.7 cells), aiming at selecting nanoparticles with high macrophage uptake efficiencies, which is important in determining the overall loading capacity of the drug. Macrophage viability was also quantified to reveal varying degrees of cytocompatibility of these nanoparticles. Subsequently, the migration ability of macrophages, a function that dominates the movement of macrophages to the inflammatory site, was investigated after loading with different types of nanoparticles. Finally, macrophage phenotypes were investigated after loading with different types of nanoparticles in order to evaluate whether the nanoparticles employed in this study could cause a shift of macrophages to a pro-inflammatory M1 phenotype. All these are important considerations for the development of macrophage-mediated drug delivery systems.

## 3.2. Materials and methods

### 3.2.1. Materials

1,2-dioleoyl-sn-glycero-3-phosphocholine (DOPC) and 1,2-stearoyl-3-trimethylammonium-propane (DSTAP) were purchased from Avanti Polar Lipids. 1,2-distearoyl-sn-glycero-3-



phosphoethanolamine-N-(azido(poly(ethylene glycol)-2000) (DSPE-PEG 2000), cholesterol, poly(D,L-lactide)-block-poly(acrylic acid) (PDLLA (9 kDa)-PAA (9 kDa)), (2-Aminoethyl)trimethylammonium chloride hydrochloride (ATA), 1-ethyl-3-(3-dimethylaminopropyl)carbodiimide (EDC), poly(ethylene glycol)-poly( $\epsilon$ -caprolactone) (PEG-PCL), cetrimonium chloride (CTAC), triethanolamine (TEA), tetraethyl orthosilicate (TEOS), hydrochloric acid 37% (HCl), N-hydroxysuccinimide (NHS), 3-triethoxysilylpropylamine (APTES), 1,1'-dioctadecyl-3,3',3'-tetramethylindodicarbocyanine, 4-chlorobenzenesulfonate salt (DiD), sucrose, 2-(N-Morpholino)ethanesulfonic acid hydrate (MES), Spectra-Por Float-a-Lyzer G2, 2-[4-(aminoiminomethyl)phenyl]-1H-indole-6-carboximidamide hydrochloride (DAPI), cell counting kit-8, fluorescein isothiocyanate (FITC) were purchased from Sigma Aldrich. poly(2-methyl-2-oxazoline)-block-poly(dimethylsiloxane)-block-poly(2-methyl-2-oxazoline) (PMOXA-PDMS-PMOXA) (MOXA(500)-DMS(4800)-MOXA(500)) and poly(dimethylsiloxane)-block-poly(acrylic acid) (PDMS-PAA) were purchased from Polymer Source.  $\alpha$ -methoxy- $\omega$ -carboxylic acid poly(ethylene glycol) (PEG-MW 2000 Dalton) (MeO-PEG-COOH 2000) was purchased from Iris BIOTECH GMBH. PD-10 desalting columns, PD minitrap desalting columns and PD miditrap desalting columns were purchased from GE Healthcare. 2-well cell culture inserts were purchased from ibidi. APC anti-CD86, PE anti-CD86 and CD16/CD32 antibody were purchased from ThermoFisher.

### 3.2.2. Nanoparticle preparation and characterisation

*Cationic liposomes:* DOPC, DSTAP and cholesterol (w:w:w = 76:14:10) were dissolved in chloroform and the organic solvent was subsequently removed *via* vacuum rotary evaporation at 65 °C for 2 h. The resulting lipid film was hydrated with PBS at room temperature at a final lipid concentration of 8 mg mL<sup>-1</sup>. Finally, the liposome dispersion was gradually extruded through a 200 nm polycarbonate membrane (Whatman® Nucleopore Track-Etched™ membranes) for 19 times and through a 100 nm polycarbonate membrane for 31 times.

*PEG-liposomes:* DOPC, DSPE-PEG 2000 and cholesterol (w:w:w = 69:3:8) were dissolved in chloroform and the organic solvent was removed *via* vacuum rotary evaporation at 65 °C for 2 h. The resulting lipid film was hydrated with PBS at room temperature at a final lipid concentration of 8 mg mL<sup>-1</sup>. Finally, the liposome dispersion was gradually extruded through

a 200 nm polycarbonate membrane (Whatman® Nucleopore Track-Etched™ membranes) for 19 times and through a 100 nm polycarbonate membrane 31 times.

*Cationic micelles:* PDLLA-PAA was dissolved in tetrahydrofuran (THF) ( $100 \text{ mg mL}^{-1}$ ).  $100 \mu\text{L}$  of PDLLA-PAA solution was then injected into 1 mL buffer (0.5 M MES and 0.25 M NaCl, pH = 6) under stirring to form micelles. THF was subsequently evaporated by open flask stirring and blowing nitrogen on top of the solution. ATA (1.5 eq, 17.5 mg) was added to the obtained micelle dispersion and mixed, followed by adding coupling reagent EDC (0.5 eq, 6.6 mg) every hour over 8 h. After reaction, cationic micelles were purified using sequential size exclusion chromatography with PBS.

*PEG-micelles:* PEG-PCL was dissolved in THF ( $20 \text{ mg mL}^{-1}$ ).  $300 \mu\text{L}$  of PEG-PCL solution was then added dropwise into 3 mL of PBS under stirring (150 rpm). THF was evaporated by open flask stirring and blowing nitrogen on top of the solution.

*Cationic polymersomes:* PMOXA–PDMS–PMOXA and PDMS-PAA were dissolved in ethanol respectively ( $8 \text{ mg mL}^{-1}$ ).  $750 \mu\text{L}$  of PMOXA–PDMS–PMOXA and  $250 \mu\text{L}$  of PDMS-PAA were mixed and organic solvent was removed *via* vacuum rotary evaporation at  $40 \text{ }^\circ\text{C}$  for 1 h. The resulting polymer film was hydrated with PBS at room temperature at a final polymer concentration of  $2 \text{ mg mL}^{-1}$  and stirred for 2 d. Then, the polymersome dispersion was gradually extruded through a 200 nm polycarbonate membrane (Whatman® Nucleopore Track-Etched™ membranes) for 19 times and through a 100 nm polycarbonate membrane for 31 times. A PD-10 desalting column was used to change the buffer from PBS to modification buffer (0.1 M MES and 0.05 M NaCl, pH = 6). ATA (1.5 eq, 10.7 mg) was added to the obtained polymersome dispersion and mixed, followed by adding coupling reagent EDC (0.5 eq, 3.7 mg) every hour over 8 h. After reaction, formed cationic polymersomes were purified using sequential size exclusion chromatography (PD-10 desalting columns) with PBS.

*PMOXA-Polymersomes:* PMOXA–PDMS–PMOXA was dissolved in ethanol ( $8 \text{ mg mL}^{-1}$ ). 1 mL of PMOXA–PDMS–PMOXA was added into a round bottom flask and solvent was removed *via* vacuum rotary evaporation at  $40 \text{ }^\circ\text{C}$  for 1 h. The resulting polymer film was hydrated with PBS at room temperature at a final polymer concentration of  $2 \text{ mg mL}^{-1}$  and stirred for 2 d. The polymersome dispersion was gradually extruded through a 200 nm polycarbonate membrane (Whatman® Nucleopore Track-Etched™ membranes) for 19 times and through a 100 nm

polycarbonate membrane 31 times. The polymersome sample was further purified using the PD-10 desalting column. Amicon ultra centrifugal filters (100 kDa) were used to concentrate the polymersome sample.

To label liposomes, micelles and polymersomes for confocal microscopy and flow cytometry analysis, DiD (0.1% wt) was added to the lipid or polymer solutions in organic solvent prior to particle formation.

*PEG-mesoporous silica nanoparticles (PEG-MSNs)*: 2 g CTAC and 0.02 g TEA were mixed in 20 mL distilled water at 95 °C. Then, 1.5 mL TEOS was added dropwise to the mixture under vigorous stirring (600 rpm), followed by 1 h stirring until white precipitates formed. The precipitates were centrifuged and washed with ethanol and then dried at 50 °C. The white powder was refluxed for 3 h at 60 °C in a mixture of 37% aqueous HCl and methanol (1:100); afterwards, the products (MSNs) were collected by centrifugation at 10000 rpm for 10 min, washed with methanol and dried at 50 °C. To prepare organoamine-grated MSNs, 500 mg of the dry MSNs was stirred with 3.68 mg APTES in 250 mL of toluene at 80 °C for 6h. The mixture was centrifuged at 10000 rpm and the supernatant was discarded. The white powder was washed twice with ethanol and dried in vacuum. To functionalise PEG on the surface of MSNs, the obtained MSNs were dispersed in buffer (phosphate buffer 10 mM pH7) at a concentration of 5 mg mL<sup>-1</sup>. 50 mg MeO-PEG-COOH 2000, 50 mg EDC and 20 mg NHS were added and kept stirring overnight. The products of PEG coated MSNs were collected by centrifugation, washed with PBS and dried at 50 °C. To label the PEG coated MSNs, 1 mg FITC and 22 µL APTES were mixed in 1 mL ethanol under stirring for 2 h in the dark. 50 µL of the mixture solution was added into 25 mL MSNs dispersion (2 mg mL<sup>-1</sup>), followed with 24 h stirring at 60 °C. FITC labelled PEG-MSNs were collected by centrifugation after washing with ethanol three times.

The size of nanoparticles was measured by Dynamic Light Scattering (DLS) using a Zetasizer Nano ZS (Malvern). For all the DLS measurements, samples were placed in disposable micro cuvettes and the scattering angle was set at 173°. Each measurement consisted of 15 runs which were repeated in triplicate at 25 °C. The measurements were averaged and recorded (number mean values). The nanoparticle surface zeta potentials were also measured using a Zetasizer Nano ZS (Malvern). For all the measurements, the sample was mixed with 300 mM sucrose at a volume ratio of 5:95 v:v (sample to sucrose solution) and the mixture was placed

in disposable cuvettes. Each measurement consisted of 15 runs which were repeated in triplicate at 25 °C.

### 3.2.3. Uptake of nanoparticles by RAW 264.7 cells

#### *Flow cytometry analysis*

RAW 264.7 cells were cultured in high glucose DMEM medium with 10% fetal bovine serum (v/v) and 1% penicillin-streptomycin (v/v). Raw 264.7 cells were seeded in a 24-well plate ( $5 \times 10^5$  cells well<sup>-1</sup>) and incubated overnight. Fluorescent dye labelled nanoparticles were added to the cells at different concentrations and incubated for 2 h, followed by washing with PBS three times to remove free nanoparticles. Cells were detached from the bottom by pipetting and then centrifuged at 350 g for 5 min to obtain the cell pellet. Paraformaldehyde (PFA) (4 % v/v) was added for 15 min at room temperature to fix the cells, followed by centrifugation and washing with PBS. 500 µL of PBS was added to resuspend the cells and the samples were measured by flow cytometry. To detect the DiD signal, the samples were excited at 640 nm with a 670/14 emission filter. Ten thousand events were recorded for each sample and the data was analysed by FlowJo (TreeStar) software.

#### *Microscopy analysis*

RAW 264.7 cells were placed into an ibidi 8-well plate (treated bottom) at a density of  $10^5$  cells well<sup>-1</sup> and cultured overnight to allow for cell attachment. Fluorescent dye labelled nanoparticles were then added at different concentrations and incubated for 2 h. This process was followed by washing with cold PBS three times and fixed with 4% PFA for 15 min at room temperature. DAPI ( $100 \text{ ng mL}^{-1}$ ) was added and incubated for 15 min at room temperature to stain the cell nuclei. Confocal Laser Scanning Microscopy (CLSM) was used to image the samples.

### 3.2.4. Cell viability

To determine the viability of RAW 264.7 cells after treating with different types of nanoparticles, cells were seeded in a 96-well plate at a density of  $5 \times 10^4$  cells well<sup>-1</sup> and incubated overnight. Different concentrations of nanoparticle samples (mix with growth medium) were added into each well and incubated for 4 h and 8 h respectively. The cells were then washed three times with cold PBS and the viability of cells was measured using Cell

Counting Kit-8. The absorbance of each well was measured at 450 nm using a microplate reader (SpectraMax M5, molecular devices).

### 3.2.5. Cell migration assay

2-well cell culture inserts were placed into a 24-well plate. 70  $\mu\text{L}$  of a RAW 264.7 cell suspension ( $7 \times 10^5$  cells  $\text{mL}^{-1}$ ) was added into each well of the insert and incubated overnight. After cell attachment, the inserts were gently removed using a sterile tweezer and the created physical gaps in the cell monolayer were recorded using microscopy under bright field (OLYMPUS IX71). Nanoparticles were then added to each well of the plate and incubated for 2 h, followed by washing with cold PBS three times to remove free nanoparticles. The cells were cultured in growth medium (10% v/v FBS) for another 48 h to allow for migration. Cell migration into the gap was recorded using microscopy under bright field and the cell-covered area was quantified using ImageJ.

### 3.2.6. Identification of RAW 264.7 cell phenotype

RAW 264.7 cells were seeded in a 24-well plate ( $4 \times 10^5$  cells per well) and incubated overnight. Different types of nanoparticles were added into each well and incubated for 2 h, followed by washing with cold PBS three times to remove free nanoparticles. After additional incubation for 24 h, the cells were harvested by washing with PBS and pipetting to detach from the bottom. Harvested cells from each well were centrifuged, resuspended and incubated with CD16/CD32 antibody in blocking solution (10% FBS in a PBS solution) for 15 min on ice. The cells were then stained with a mixture of monoclonal fluorochrome-conjugated antibodies in blocking solution for 30 min on ice, in which APC anti-CD86 ( $0.2 \mu\text{g} \mu\text{L}^{-1}$ ) was used for measuring the pro-inflammatory phenotype (M1-like) and PE anti-CD206 ( $0.2 \mu\text{g} \mu\text{L}^{-1}$ ) was used for measuring the anti-inflammatory phenotype (M2-like). Then, the cells were fixed with 4% PFA (v/v) and resuspended in 500  $\mu\text{L}$  of PBS. The fluorescence intensity was measured using flow cytometry. To detect the APC and PE signal, the samples were excited at 640nm with a 670/15 nm emission filter and 561 nm with a 582/15 nm emission filter. RAW 264.7 cells activated with IFN $\gamma$  ( $20 \text{ ng mL}^{-1}$ ) and lipopolysaccharide (LPS)( $100 \text{ ng mL}^{-1}$ ) for 18 h were used as the M1 macrophage control, and IL-4 ( $20 \text{ ng mL}^{-1}$ ) for 18 h as the M2 macrophage control.

### 3.2.7. Statistics

All the statistical analyses were conducted in GraphPad 8.0 (Prism). All the statistical tests were specified in the figure legends. Shapiro-Wilk test was used to assess normality and thus determine the statistical test. 'n' refers to technical replicates; 'N' refers to biological replicates.

## 3.3. Results and discussion

Various types of nanoparticles are being investigated for applications in the fields of gene and drug delivery, imaging and diagnostics (see chapter 1 section 1.3). Although many types of nanoparticles have reached the preclinical phase, only few protein-based, lipid-based, and polymer-based nanoparticles have thus far been clinically approved for drug delivery.<sup>307</sup> In this chapter, three types of soft nanoparticles including liposomes, micelles, and polymersomes were formulated, wherein each type of nanoparticles was equipped with a neutral or positively charged surface. Apart from organic nanoparticles, mesoporous silica nanoparticles (MSNs), a type of inorganic nanoparticles that are currently investigated in pre-clinic studies,<sup>180</sup> were also chosen as they have a large surface area and pore volume to achieve high drug loadings. RAW 264.7 cells (macrophages), a widely used mouse macrophage cell line, were chosen as model macrophages to study cellular responses after loading with formulated nanoparticles. Cell uptake and viability after incubation with different nanoparticles were first determined to reveal nanoparticle loading efficiencies and compatibility with macrophages, which sets the basis for loading the maximum quantity of nanoparticles into the macrophages without adversely affecting cell viability. Furthermore, the migratory behaviour of macrophages after loading with these nanoparticles was evaluated using a cell migration assay. Lastly, macrophage phenotypic shifts after nanoparticle loading were studied to showcase potential immune responses generated from the chosen nanomaterials (Figure 3.1).

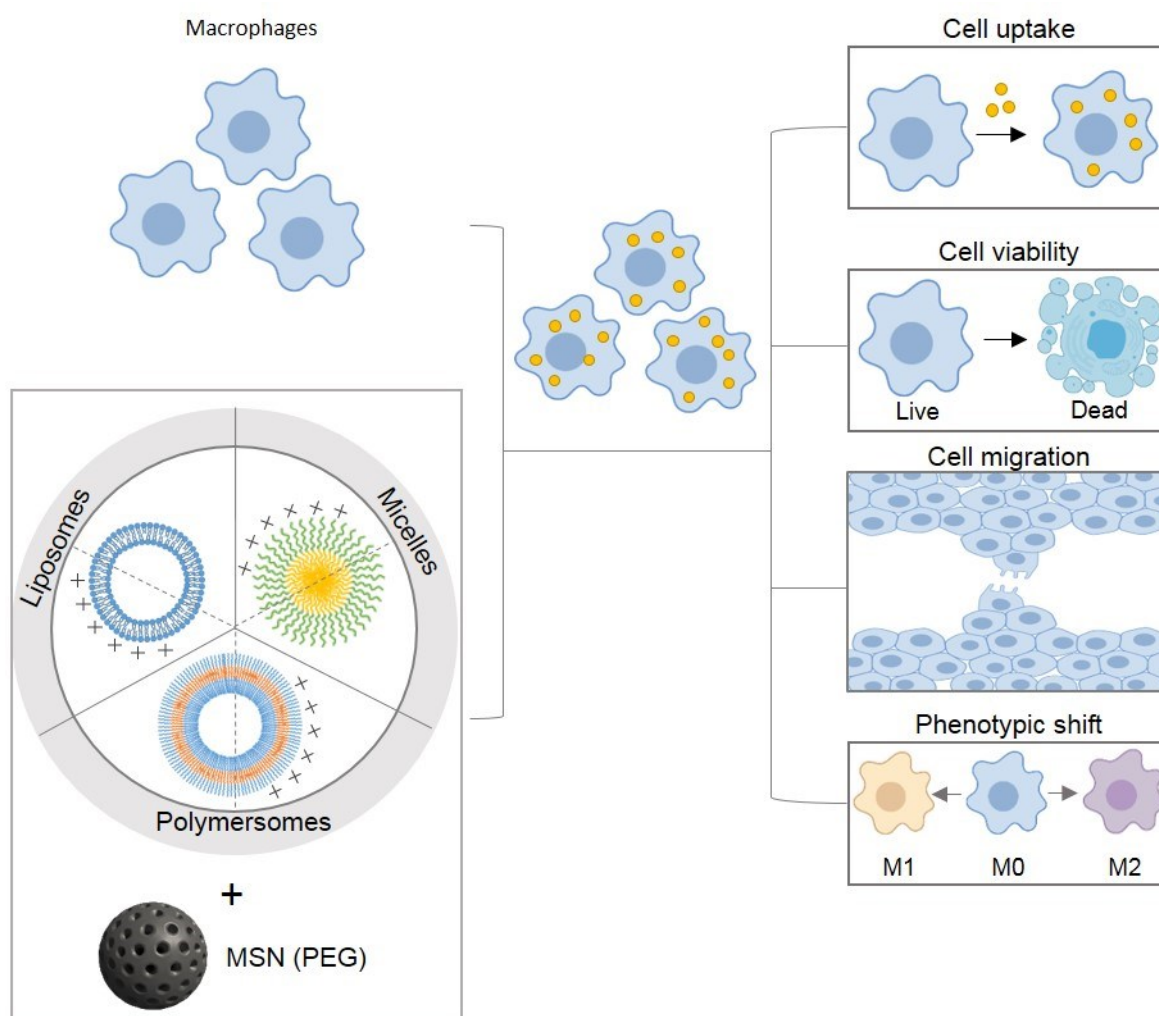


**Figure 3.1 Schematic illustration of different types of nanoparticles loaded into macrophages and evaluation of cellular responses.** *Liposomes, micelles and polymersomes with positively or neutrally charged surfaces and PEG functionalised MSNs were prepared and incubated with RAW 264.7 cells (macrophages). After macrophages were loaded with these nanoparticles, different cellular responses including cell uptake, cell viability, cell migratory behaviour and phenotypic shifts were investigated.*

### 3.3.1. Preparation and characterisation of nanoparticle loaded macrophages

Liposomes were prepared using the thin-film hydration method and extruded to obtain a size of about 100 nm. A lipid composition of DOPC, DSTAP and cholesterol was used to make cationic liposomes as this composition has demonstrated satisfactory liposome loading efficiency and cytocompatibility when formulating the liposome-neutrophil delivery system (see Chapter 2, Section 2.3.1). To prepare PEG coated liposomes, DSTAP was replaced by a PEGylated lipid, DSPE-PEG in the composition. DLS was used to confirm the size of cationic liposomes and PEG-liposomes of about 100 nm (Figure 3.2a). The zeta potential was

measured using a Zeta sizer. As expected, with the cationic lipid DSTAP in the liposome, the zeta potential of the formulated cationic liposomes shifted to positive values of about +28 mV, compared to the neutral PEG-liposomes that revealed a neutral zeta potential of about +3.0 mV (Figure 3.2a).

Micelles were prepared using a nano-precipitation method. To prepare cationic micelles, poly(D,L-lactide)-block-poly(acrylic acid) (PDLLA-PAA) micelles were first prepared and positive charges (quaternary ammonium) on the micelle surface were subsequently introduced by reacting the primary amine from (2-Aminoethyl)trimethylammonium chloride hydrochloride (ATA) with the carboxylic acid residues of the outer PAA block of the micelles in the presence of EDC. Functionalised cationic micelles had a size of about 40 nm and a zeta potential of +36 mV. PEG-micelles were formed using the same nano-precipitation method by injecting a THF solution of PEG-PCL into PBS under stirring (250 rpm), obtaining micelles with a size of about 68 nm and a neutral zeta potential of -5 mV (Figure 3.2b).

Polymersomes were prepared using a thin-film hydration method and the size was controlled by extrusion. The triblock copolymer poly(2-methyl-2-oxazoline)-block-poly(dimethylsiloxane)-block-poly(2-methyl-2-oxazoline) (PMOXA-PDMS-PMOXA) was used to form neutrally charged polymersomes as PMOXA has previously been used as an alternative to PEG by protecting nanoparticle surfaces from protein absorption.<sup>308</sup> PMOXA-polymersomes had a size around 130 nm and a near neutral zeta potential of +7 mV. Similar to cationic micelles, polymersomes (a mixture of PMOXA-PDMS-PMOXA and PDMS-PAA) with a carboxylic acid containing polymer (PAA) were first prepared and positive charges were then introduced using ATA and EDC coupling reaction. Figure 3.2c showed that cationic polymersomes were successfully obtained with a size around 144 nm and a zeta potential around +21 mV.

MSNs with uniform pore size were first synthesised by a sol-gel process, using CTAC as a structure-directing agent.<sup>196</sup> Surface PEGylation of MSNs was achieved via EDC/NHS coupling reaction. The resulting PEG-MSNs had a size of about 101 nm and a zeta potential around -7 mV (Figure 3.2d).



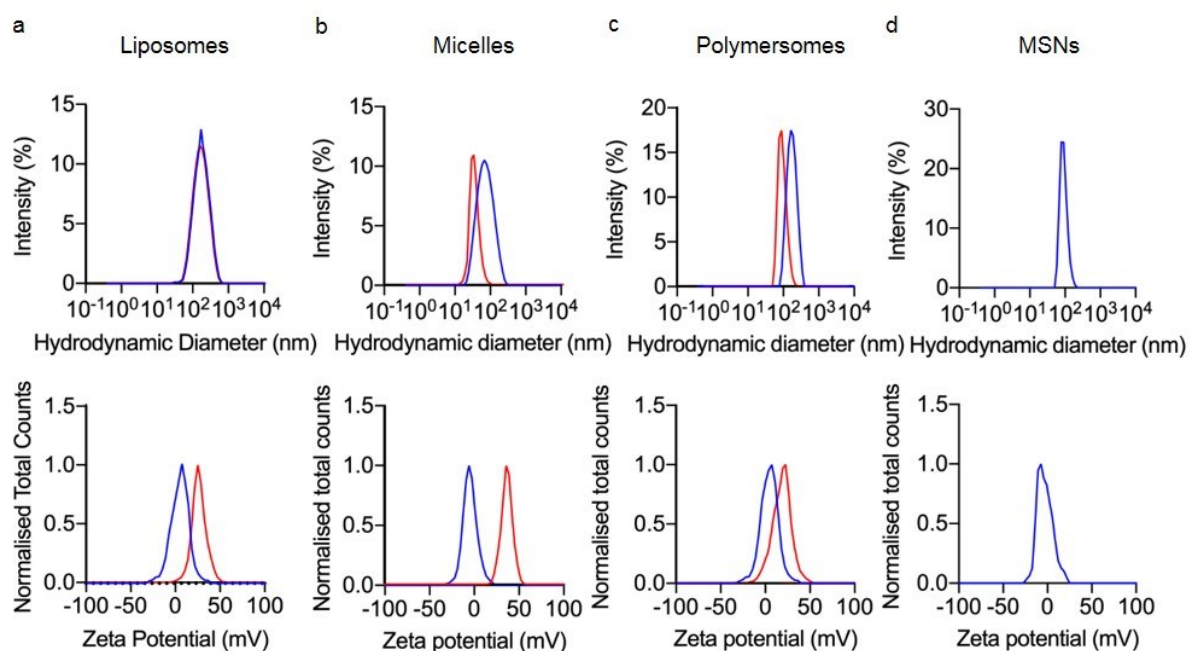


**Figure 3.2 Characterisation of different types of nanoparticles.** *a*, Particle-size measure by dynamic light scattering (DLS) and zeta potential distribution of cationic liposomes (red) and PEG-liposomes (blue). *b*, Particle-size measured by DLS and zeta potential distribution of cationic micelles (red) and PEG-micelles (blue). *c*, Particle-size measured by DLS and zeta potential distribution of cationic polymersomes (red) and PMOXA-polymersomes (blue). *d*, Particle-size measured by DLS and zeta potential distribution of PEG-MSNs.

After preparation and characterisation of the nanoparticle library, a simple loading protocol was used to load these nanoparticles into macrophages. Macrophages were incubated with formulated nanoparticles for 2 h and excess nanoparticles were subsequently washed away by centrifugation/resuspension steps. Nanoparticle uptake efficiency for macrophages was measured using flow cytometry (liposomes, micelles and polymersomes were labelled with 1,1'-dioctadecyl-3,3,3',3'-tetramethylindodicarbocyanine, 4-chlorobenzenesulfonate salt (DiD)) and PEG-MSNs were labelled with fluorescein isothiocyanate (FITC)). All the formulated liposomes, micelles and polymersomes were readily taken up by macrophages with more than 90% of the cells being positive for macrophages upon incubation for 2 h at all concentrations tested (Figure 3.3), which is likely due to the phagocytotic nature of macrophages. However, in the case of PEG-MSNs, the percentage of PEG-MSN positive macrophages dramatically increased from 18 % to 88 % with increasing silica concentrations during incubation. Furthermore, the mean fluorescence intensity of macrophages was measured after loading organic nanoparticles (DiD labelled) and the mean values for each

type of nanoparticles are shown in Figure 3.3c. This parameter can be used to compare uptake efficiencies of the neutral versus positively charged nanoparticles. Since size, hence particle concentrations are different between the different types of nanoparticles, direct comparisons between the particles are less informative. As expected, the mean fluorescence intensities of macrophages after uptake of cationic liposomes and polymersomes were significantly higher than in the case of neutral liposomes and polymersomes, indicating each macrophage phagocytosed more liposomes and polymersomes with a positively charged surface. This is expected as a positively charged nanoparticle surface can facilitate interactions with the negatively charged macrophage membrane, resulting in higher nanoparticle loading quantities. Further, PEG and PMOXA coating can increase surface hydrophilicity, which in turn inhibits cell uptake. In contrast, macrophages had significantly lower mean fluorescence intensities after uptake of cationic micelles than those neutral micelles. This may be due to the high cytotoxicity of the cationic micelles (Figure 3.6) that could have impaired the macrophage phagocytosis function. Even at the lowest polymer concentrations, cationic micelles were shown to change the morphology of the cells (Figure 3.4).

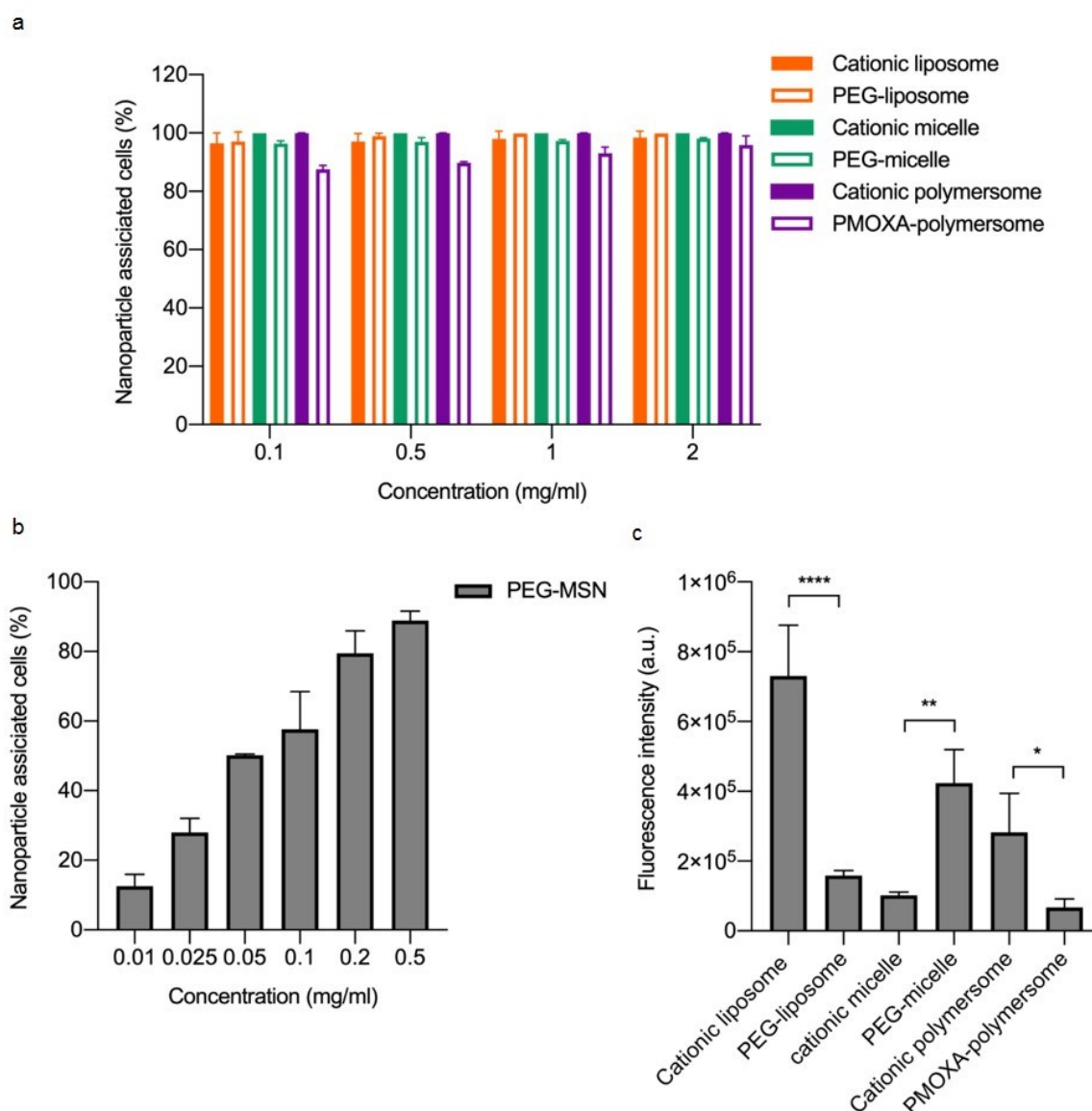


**Figure 3.3 Nanoparticle loading into macrophages.** **a**, Flow cytometry analysis of macrophages after loading with DiD-labelled cationic liposomes, PEG-liposomes, cationic micelles, PEG-micelles, cationic polymersomes and PMOXA-polymersomes. **b**, Flow cytometry analysis of macrophages after loading with FITC-labelled PEG-MSNs. Macrophages were incubated with different types of nanoparticles at different concentrations for 2 h and washed before measuring by flow cytometry. Data shown as mean  $\pm$  s.d.,  $N = 3$ . **c**, Mean fluorescence intensity of macrophages after loading with DiD labelled nanoparticles (incubate at 2 mg/mL) measured by flow cytometry. Data shown as mean  $\pm$  s.d.,  $N = 3$ . \*\*\*\* $P < 0.0001$ , \*\* $P < 0.01$ , \* $P < 0.05$ , one-way ANOVA, Bonferroni post hoc test.

Co-localisation of nanoparticles with macrophages was shown by CLSM images (Figure 3.4), which correlates well with the flow cytometry data confirming that most cells had taken up all the nanoparticles during the 2 h loading procedure when using a high nanoparticle concentration during incubation. Furthermore, the CLSM images and 3D structural

illumination microscopy (3D SIM) images (only the sample of cationic liposome loaded macrophages was shown) (Figure 3.5) indicate that the nanoparticles were present inside the macrophages except for the cationic micelles which tended to be absorbed to the cell membrane. Another possible explanation for observing the DiD signal on the cell membrane after loading cationic micelles is that the cell membrane incorporated some DiD from the cationic micelles. DiD is not an ideal label for micelles; it is usually used for membraneous structures such as liposomes/polymersomes but was used herein to keep the cargo consistent between the different particle types. Moreover, after cationic micelle loading, the morphology of the cell nuclei and membranes were different from the other nanoparticle loaded macrophages; the nucleus size was smaller. One potential reason could be that cationic micelles were toxic and disrupted the cell membrane at the tested concentration. In general, the location of nanoparticles on or inside macrophages is not a major concern for the herein described type of cell-based delivery as long as loaded nanoparticles can be successfully transported and released from the macrophages at the site of disease. Since cell-loading would happen *ex vivo*, protein fouling on positively charged nanoparticles, potential aggregation and non-specific delivery is a much smaller concern in this case compared to nanoparticles used directly by intravenous injection.

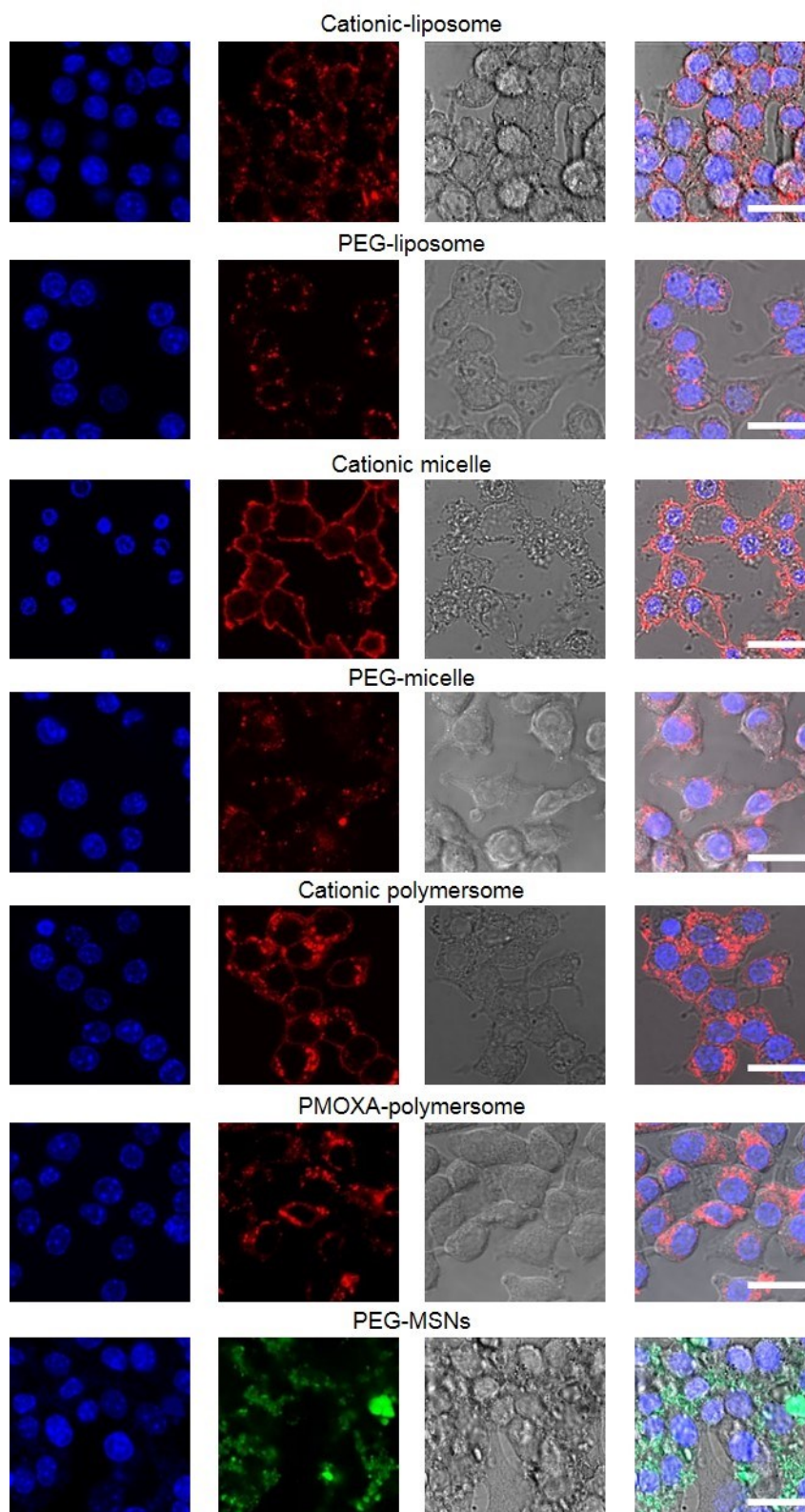


**Figure 3.4 Co-localisation of nanoparticles with macrophages using CLSM.** CLSM representative images of nanoparticle loaded macrophages (DiD was used to label the hydrophobic region of liposomes, micelles and polymersomes (red), FITC was used to label the surface of MSNs (green), DAPI was used to stain the cell nuclei (blue)). Scale bars: 20  $\mu\text{m}$ .

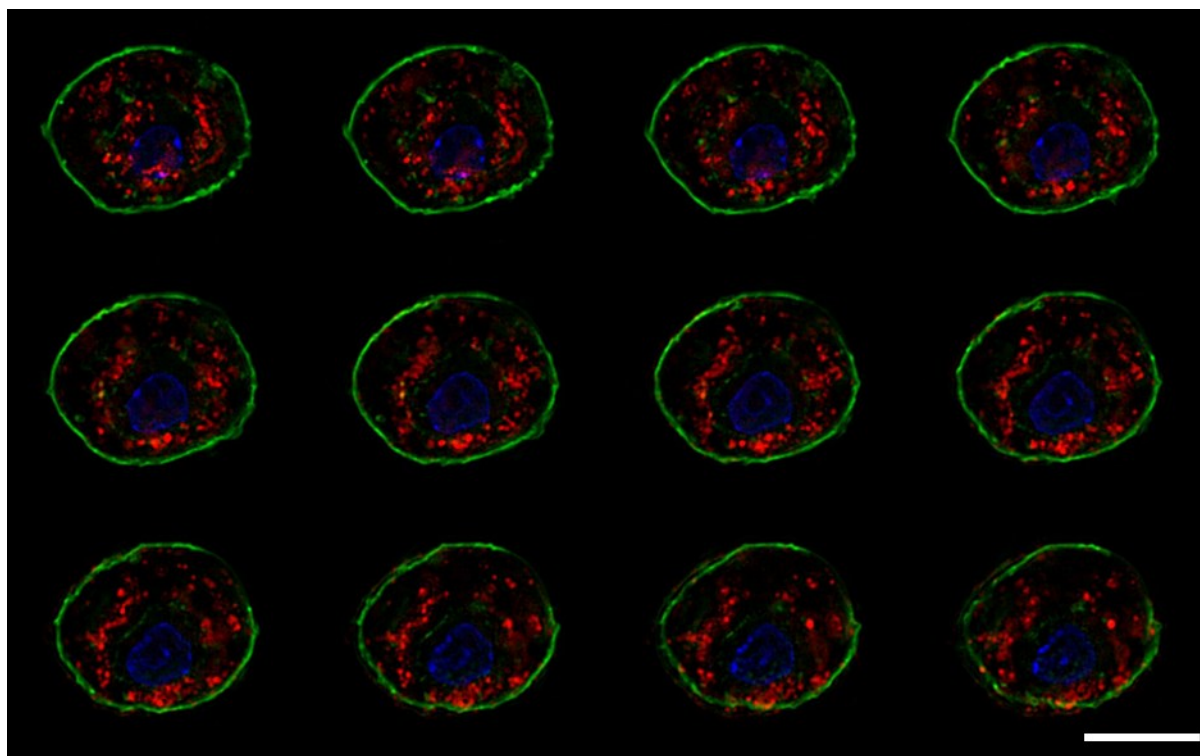


**Figure 3.5 Super resolution representative images (SIM) of cationic liposome loaded macrophages.** Images showing the location of MTX-liposomes (red) on/in a single macrophage at different  $z$  positions. Scale bar:  $10\ \mu\text{m}$ .

The most important parameter is the cell viability after loading with nanoparticles, which determines the highest nanoparticle-macrophage ratio that can be tolerated to achieve maximum nanoparticle loading capacity. Macrophage viability was tested after loading with different concentrations of each type of nanoparticle for 4 and 8 h incubation (Figure 3.6). In the case of organic nanoparticles with a neutrally charged surface, more than 80% of macrophages were alive at the highest concentrations tested ( $2\ \text{mg mL}^{-1}$ ) after 8 h incubation (Figure 3.6b). Cationic liposomes also showed high cytocompatibility with more than 80% of live macrophages after 8 h incubation at all the tested lipid concentrations. However, cationic micelles and polymersomes exhibited high cytotoxicity at high polymer concentrations for both 4 and 8 h incubation times; only 29% and 35% of macrophages were alive after 8 h incubation at the highest polymer concentration. It has previously been reported that positively charged nanoparticles can induce cytotoxicity by causing damage to the cell either directly or by detachment of absorbed polymers.<sup>256</sup> In the case of cationic micelles and polymersomes, a single polymer chain can be modified with multiple cationic charges by EDC coupling resulting in a high localised cationic charge density that can damage macrophages



during incubation. In contrast, a single cationic lipid molecule presents only a single cationic charge, which could account for their lower cytotoxicity compared to the polymeric cations. If needed, the micelles and polymersomes could later be optimised by reducing the equivalents of ATA used during the modification process, which will reduce the density of positive charges and should hence reduce cytotoxicity. PEG-MSNs also presented some cytotoxicity at the highest silica concentration after 8 h incubation (Figure 3.6c), where the highest macrophage uptake efficiency was seen (Figure 3.3b). Additionally, when comparing the different concentrations of organic nanoparticles used for cell phagocytosis, macrophages were cultured with PEG-MSNs at much lower silica concentrations but still revealed cytotoxicity at the highest silica concentration. It further suggests a higher cytotoxicity of PEG-MSNs compared to organic nanoparticles. Overall, the cell uptake and viability results showed that all the neutrally charged organic nanoparticles and cationic liposomes had high cell uptake efficiencies and cytocompatibilities. Cationic micelles and polymersomes were also taken up efficiently by macrophages but were toxic when incubating at high polymer concentrations. In terms of nanoparticle loading quantities per cell, cationic liposomes and polymersomes had significantly higher numbers of nanoparticles taken up by macrophages compared to neutral liposomes and polymersomes, whereas cationic micelles adversely affected phagocytosis in macrophages because of their high cytotoxicity. PEG-MSNs had high cell uptake efficiencies only when incubating at high silica concentrations, however, the cytotoxicity also increased significantly at these concentrations. Therefore, the best loading efficiencies without affecting cell viability was achieved with cationic liposomes, cationic polymersomes and neutral micelles.

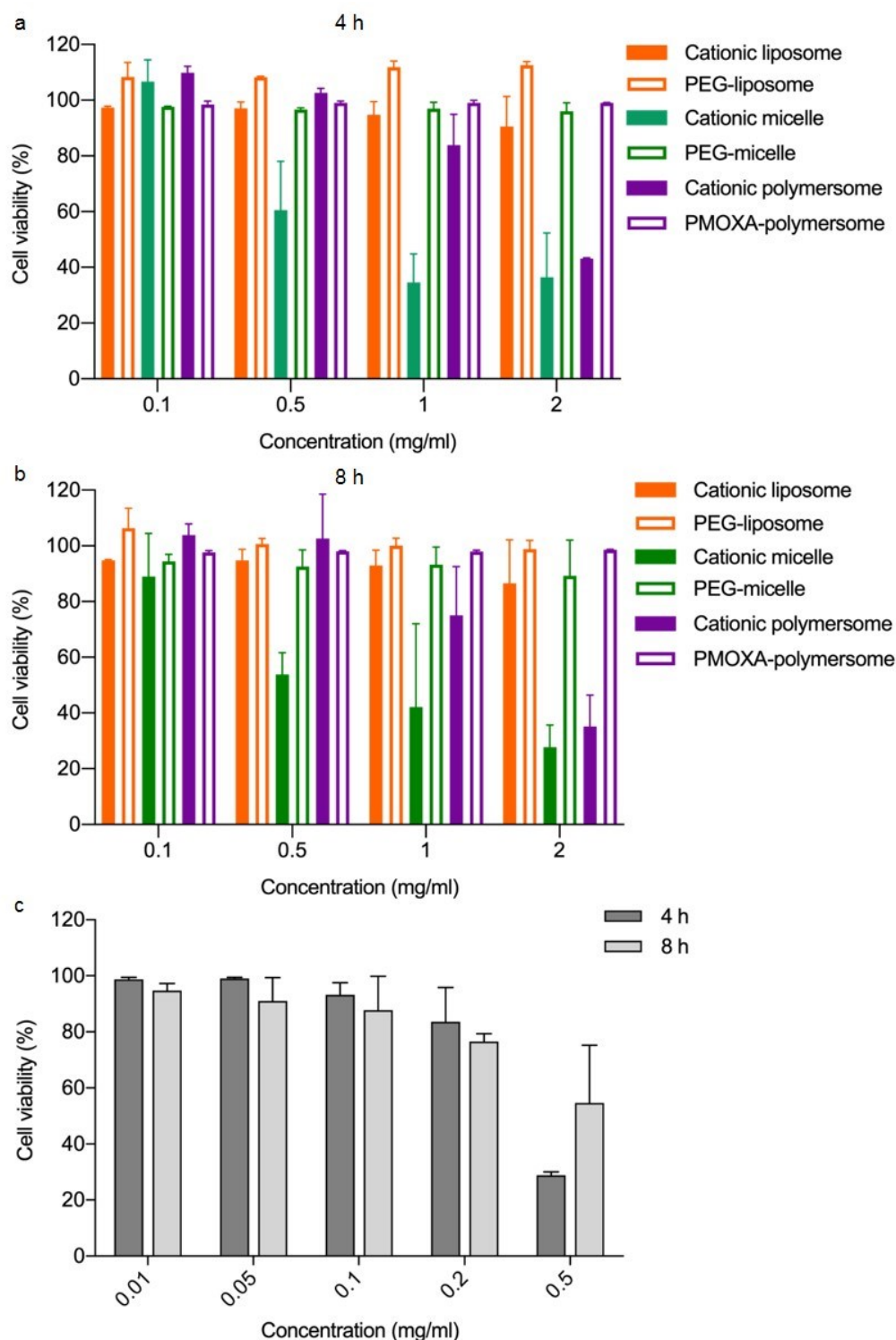


**Figure 3.6** Cytocompatibility of nanoparticles to macrophages after incubation for 4 h and 8 h. Macrophages were incubated with different types of nanoparticles at different concentrations for 4 and 8 h, respectively. Cell counting kit-8 was used to measure macrophage viability. **a** showing cytocompatibility of liposomes, micelles and polymersomes to macrophages after incubation for 4 h. **b** showing cytocompatibility of liposomes, micelles and polymersomes to macrophages after incubation for 8 h. **c** showing cytocompatibility of PEG-MSNs to macrophages after incubation for 4 and 8 h. Data shown as mean  $\pm$  s.d.,  $N = 3$ .



### 3.3.2. Physiological functions of macrophages after loading with different nanoparticles

After confirmation of nanoparticle uptake by macrophages, two key functions of macrophages including cellular migration and cell phenotype were investigated after nanoparticle loading. This is crucial because retaining the migration function of native macrophages after loading with nanoparticles ensures that the macrophages would potentially still be able to migrate to the inflammatory site after intravenous administration *in vivo*. Polarisation of macrophages after loading with nanoparticles is particularly important in the context of anti-inflammation therapy since macrophages that polarise to a pro-inflammatory M1 phenotype after loading with nanoparticles could potentially act to amplify inflammation rather than reduce it.

Firstly, the migration ability of nanoparticle loaded macrophages was conducted using a cell migration assay, wherein a well-defined physical gap of 500  $\mu\text{m}$  within the cell monolayer was generated by using a removable insert. Macrophages were then incubated with different nanoparticles at the highest concentration shown to allow more than 80% cell viability (Figure 3.6) to avoid the influence of dead cells. 48 h after nanoparticle loading, the remaining gap was recorded using a microscope under bright field and the change in the cell-covered area was quantified using ImageJ. Similar to native macrophages, macrophages after loading with organic nanoparticles migrated to close the gap, indicating retention of their native migration function (Figure 3.7a). This suggests that after loading with organic nanoparticles, macrophages still have the ability to move to the site of inflammation upon *i.v.* injection. However, PEG-MSN loaded macrophages migrated very slowly with a large gap remaining after 48 h incubation post loading. This effect is clearly seen in Figure 3.7b which demonstrates that PEG-MSN loaded macrophages had much lower cell migration per hour compared to all the organic nanoparticles and blank macrophages, suggesting that PEG-MSNs inhibited the innate migratory function of macrophages.

Interactions of MSNs with cells can be affected by many parameters including synthesis routes, particle shapes, pore sizes, surface functionalisation, mesoporosity and crystallinity.<sup>309</sup> Slight changes of one or various parameters can greatly influence cellular responses upon MSN exposure to cells. Different sizes of MSNs from 30 nm to 270 nm were synthesised by Mou and co-workers and incubated with Hela cells.<sup>310</sup> MSNs with a size of 50

nm showed a higher cell uptake efficiency than those with bigger sizes.<sup>310</sup> In another report, HeLa cells were found to endocytose MSNs more efficiently with a positively charged surface.<sup>311</sup> These results indicate that decreasing the size of MSNs or modifying the MSN surface with positive charges can potentially enhance macrophage cellular uptake. However, in a recent study, both small (80 nm) and large (500 nm) MSNs were found to possess weakened cell migration behaviour, which is possibly caused by strong interactions between these MSNs and nucleotides.<sup>312</sup> A potential strategy to solve this issue is to modify the surface of MSNs with functional groups to decrease the affinity of MSNs to nucleotides.

According to previous results, PEG-MSNs did not have a high cell uptake efficiency when incubating at a biocompatible silica concentration. The migration ability of macrophages was also inhibited after loading with PEG-MSNs. Nevertheless, all the organic nanoparticles can achieve high cell uptake efficiencies without impairing cell viability and migration ability. Therefore, PEG-MSNs were deemed not a suitable nanocarrier for macrophage loading and delivery and were therefore excluded in subsequent studies.

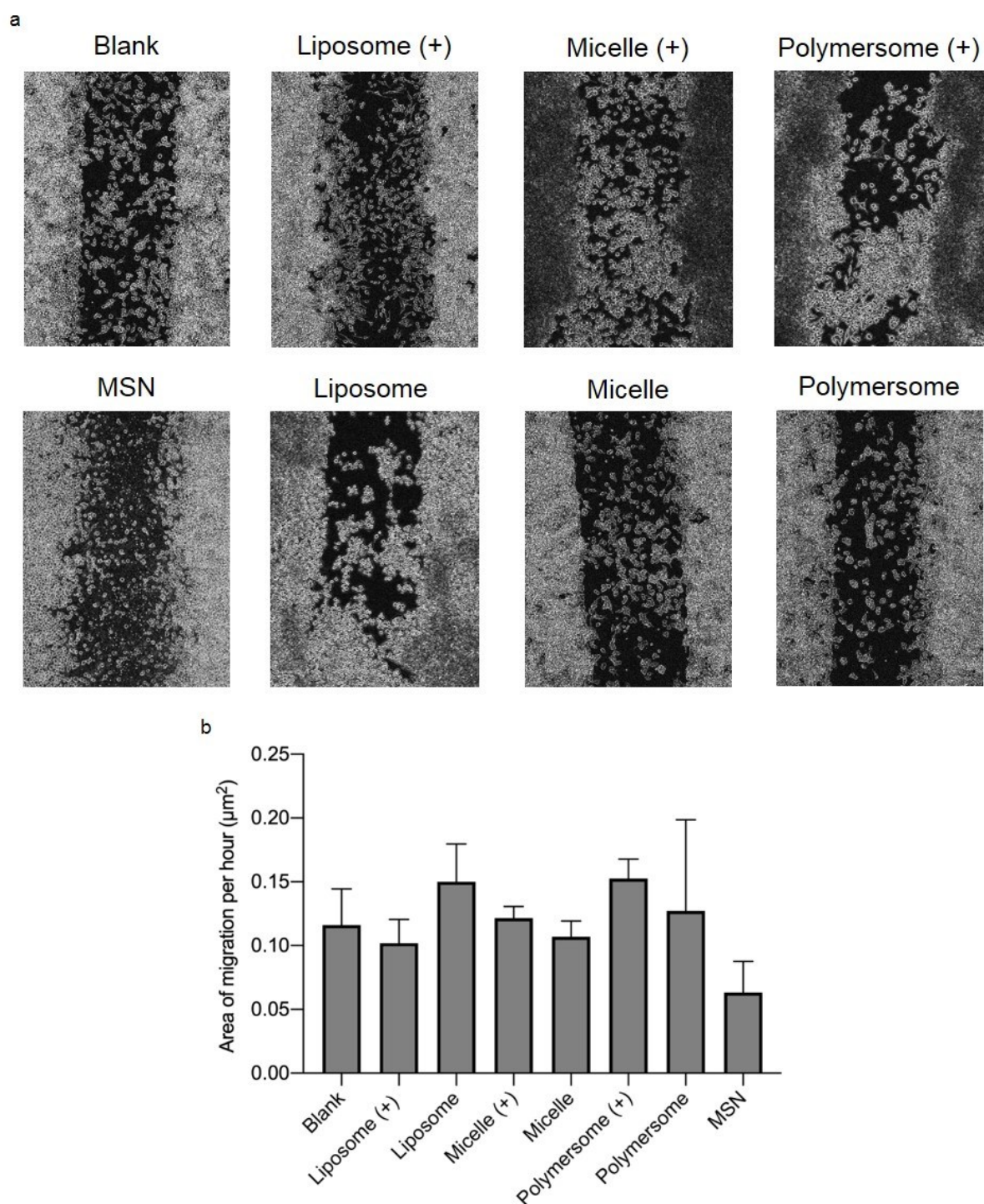


**Figure 3.7** Effect of different types of nanoparticles on migration of macrophages. **a**, Light microscope representative images of gap closure of untreated macrophages and nanoparticle loaded macrophages. Macrophages incubated with different types of nanoparticles displayed closing of the physical gap after 48 h (representative pictures from 3 repeated experiments). Scale bar = 100 nm. **b**, Area of macrophage migration per hour after loading with different types of nanoparticles. ImageJ was used to quantify the cell-covered area at 48 h post loading. Data shown as mean  $\pm$  s.d.,  $N = 3$ .

Macrophage phenotypic shift is an important criteria to consider in a macrophage-delivery system because macrophage polarisation towards a M1 phenotype after loading with nanoparticles could exacerbate inflammation at the disease site upon reinjection, whilst phenotypic shift to a M2 phenotype could assist with cell proliferation and tissue regeneration, favouring the treatment of inflammatory diseases. As such, macrophage phenotypic shifts after loading with organic nanoparticles were also investigated. As positive controls, lipopolysaccharide/interferon- $\gamma$  (LPS/IFN $\gamma$ ) was used to derive M1 macrophages and interleukin 4 (IL-4) was used to promote M2 macrophage polarisation. As expected, the M1/M2 ratio of macrophages treated with LPS/IFN $\gamma$  was significantly increased after 18 h incubation, which suggests that macrophages were almost completely polarised to a pro-inflammatory M1 phenotype. All the organic nanoparticle treated macrophages were found to stay at a low M1/M2 ratio comparable to the untreated macrophages (Figure 3.8), which suggests that these nanoparticles did not cause a pro-inflammatory effect in macrophages. However, macrophages stimulated by IL-4 did not generate a significant decrease in the M1/M2 ratio as measured by flow cytometry (Figure 3.8). Others have previously observed the same problem wherein CD86/CD206 expression was not significantly affected by IL-4 stimulation of RAW 264.7 cells measured by flow cytometry.<sup>313</sup> Nonetheless, no shift towards M1 was detected, indicating no unwanted effects of organic nanoparticle loading on the macrophage phenotype. When comparing between different nanoparticle-treated macrophages, the M1/M2 ratio was slightly shifted, but no significant difference to untreated macrophages was detected. This suggests that different nanomaterials and surface modifications of nanoparticles such as targeting ligand and peptide conjugation could potentially polarise macrophages, hence phenotypic shifts of macrophages need to be checked carefully after loading new nanoparticles into macrophages.

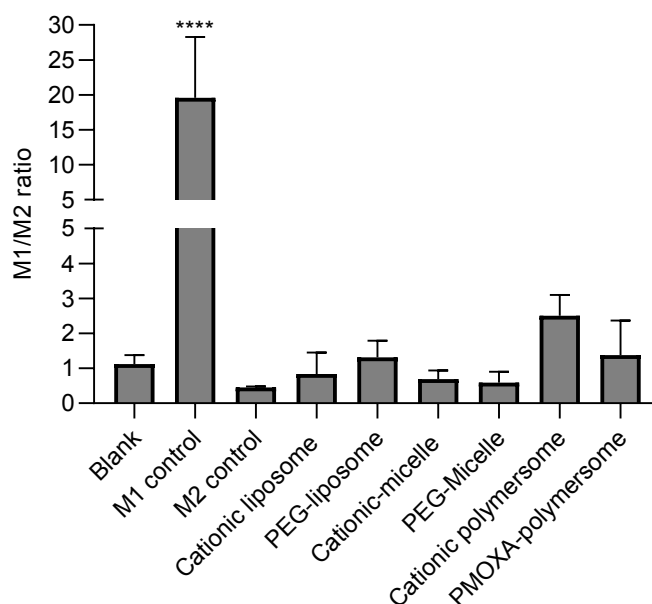


**Figure 3.8 Polarisation of macrophages after loading with different types of nanoparticles.** Macrophages were incubated with different types of nanoparticles for 2 h and free nanoparticles were washed away. After an extra incubation of 24 h, macrophages were harvested and stained with APC anti-CD86 for measuring the pro-inflammatory phenotype (M1-like) and PE anti-CD206 ( $0.2 \mu\text{g } \mu\text{L}^{-1}$ ) for measuring the anti-inflammatory phenotype (M2-like). The fluorescent intensity was measured using flow cytometry. Data shown as mean  $\pm$  s.d.,  $N = 3$ . \*\*\*\* $P < 0.0001$ , one-way ANOVA, Bonferroni post hoc test.

Many studies have employed macrophages as a cell carrier and tested their drug delivery efficiencies *in vitro* and *in vivo*. RAW 264.7 cells were loaded with doxorubicin (DOX)-silica capsules *via* internalisation without affecting cell viability and migration ability.<sup>265</sup> After quantifying the release of pro- and anti-inflammatory cytokines from RAW 264.7 cells, DOX-silica capsule loading was found to polarise RAW 264.7 cells towards the pro-inflammatory M1 phenotype. The formulated hybrids were intravenously injected to mice bearing subcutaneously inoculated U87MG tumours and achieved efficient suppression of tumour growth. In this study, macrophage polarisation to M1 phenotype after loading with DOX-silica capsules was not an issue since it is an anti-cancer therapy, however, extra M1-like macrophage injection may exacerbate inflammation, which would potentially complicate the treatment of inflammatory diseases. Liposomes were also used as the nanocarrier to encapsulate DOX and macrophages efficiently delivered DOX-liposomes to tumour sites in mice with subcutaneous tumours.<sup>245</sup> In these two studies, silica capsules and liposomes played an important role to preserve the cytotoxicity of DOX against tumour cells and to not

affect biological activities of macrophages. In this study, apart from PEG-MSNs and liposomes, polymersomes and micelles with higher stability were also tested and they can further minimise premature exposure of macrophages to the drug.

Macrophage-mediated drug delivery strategy has also been explored to deliver drug encapsulated nanoparticles across the blood brain barrier (BBB) to brain tissue. As macrophages can infiltrate into human immunodeficiency virus (HIV) infected brain tissue, they were used to deliver nanoformulated antiretroviral drug to HIV-1 infected brain regions.<sup>314</sup> Indinavir nanoparticles were loaded into bone marrow derived macrophages (BMDMs) and formulated hybrids were *i.v.* injected to mice with HIV-1 encephalitis. BMDMs showed continuous indinavir release for 14 d and resulted in reduced viral replication. The sustained release of indinavir to the HIV-1 infected regions can help limiting neural damage. Another study used BMDMs to deliver antioxidant enzymes across the BBB to target neuro-inflammation.<sup>244</sup> The antioxidant enzyme was packaged into a block copolymer to form nanoenzymes and then loaded into macrophages. The release of active enzymes from BMDMs sustained up to 7 d *in vitro*. Furthermore, upon *i.v.* injection in 1-methyl-4-phenyl-1,2,3,6-tetrahydropyridine (MPTP) intoxicated mice, the nanoenzyme-BMDM treatment decreased expression levels of neuroinflammation markers CD11b and GFAP and increased the numbers of surviving dopaminergic neurons, indicating a neuro-protective effect achieved by this system. In this study, it is important to note that in addition to the macrophage-guided delivery across the BBB, the long term drug release property (up to 7 d) is a key advantage of the nanoenzyme-BMDM delivery system; to protect neuro-tissue from degeneration by aiding tissue repair usually requires drug delivery systems having sustained drug release properties. These two studies suggest the advantage of macrophage-mediated drug delivery systems with sustained drug release properties for aiding tissue repair.

These and other studies highlight the great promise of using macrophages to deliver drug encapsulated nanoparticles to inflamed tissue. One of the most important components of the macrophage mediated delivery system is the nanocarrier, which determines the drug loading capacity and the release profiles from macrophages.<sup>303,315</sup> Nanocarriers are also used to maintain drug integrity inside macrophages and compartmentalise the drug to not affect macrophage biological activity. Moreover, nanocarrier loading may influence the state of macrophages. In this chapter, different types of nanoparticles were formulated and tested

based on these considerations. Liposomes, micelles, polymersomes and MSNs chosen in this chapter have different stabilities and surface functionalities, resulting in different loading efficiencies and cellular responses of macrophages. Macrophage recruitment to inflammatory sites takes longer than for neutrophils and they do not have a rapid drug release mechanism like neutrophils (NETs formation). As such, nanoparticles with higher chemical and physical stability may be more suitable for loading into macrophages to protect the drug from destruction and to avoid premature drug activity. This is the main reason of testing other nanoparticles apart from liposomes that have been used for neutrophil-mediated delivery. Furthermore, macrophages participating in different stages of inflammation also give more potential applications. In addition to use a macrophage-mediated drug delivery strategy to mitigate inflammation, promoting tissue regeneration is another application prospect, which could be achieved by injecting loaded macrophages in the late inflammation/tissue remodelling stage. In this case, a macrophage-mediated delivery system with controlled drug release is required and nanoparticles with higher stability can fulfil this task; for example, the polymersomes and micelles tested in this chapter can be suitable candidates. Phenotypic shifts of macrophages after nanoparticle loading need to be checked for anti-inflammation and tissue repair applications as polarisation towards M1 macrophages is harmful for both applications. The initial exploration of the different nanoparticle types loaded into macrophages discussed in this chapter sets the basis for future optimisation of macrophage-based delivery for these types of applications.

### 3.4. Conclusions

The effect of different types of nanoparticles on cellular responses of macrophages was investigated in this chapter in order to set the basis for developing macrophage-mediated nanoparticle delivery similar to the neutrophil-based strategy described in the previous chapter. Four types of nanoparticles including liposomes, micelles, polymersomes and MSNs were studied, in which liposomes, micelles and polymersomes were further functionalised with a neutral and positive charge on the surface to study the biological effects of surface charge. This will later allow to pick the most suitable nanocarrier for macrophage-mediated delivery that demands more stable nanocarriers due to the longer timescales of this type of delivery (days for macrophages versus hours for neutrophils).

All the nanoparticles were optimised with a size ranging from 40 nm to 144 nm. Nanoparticles were coated with PEG or PMOXA to obtain a neutrally charged surface; for liposomes, micelles and polymersomes, an ammonium moiety was introduced to form a positively charged surface. When incubated with RAW 264.7 macrophages, positively and neutrally charged liposomes, micelles and polymersomes all showed high cell uptake efficiencies with more than 80% of macrophages containing nanoparticles at each concentration tested. In contrast, the cell uptake efficiency of PEG-MSNs showed a strong dose dependence with up to 88% uptake at the highest silica concentration, where high cytotoxicity was detected. Regarding the effect of surface charge on nanoparticle loading quantities per macrophage, macrophages took up higher numbers of liposomes and polymersomes with a positively charged surface than those with a neutral surface. In contrast, cationic micelles were loaded less efficiently inside macrophages compared to neutral micelles due to their cytotoxicity. Neutrally charged liposomes, micelles, polymersomes and cationic liposomes were also found to be cytocompatible with macrophages for all the tested concentrations, whereas PEG-MSNs, cationic micelles and cationic polymersomes exhibited high cytotoxicity at higher loading concentrations, causing more than 50% of dead cells at the highest concentration after 8 h incubation. The migratory behaviour of macrophages after loading with different types of nanoparticles was determined using a cell migration assay. All the organic nanoparticles did not have detrimental effects on macrophage migration, whereas PEG-MSNs strongly inhibited the migration ability of macrophages rendering them unsuitable as a nanocarrier for formulating a macrophage-mediated delivery system. To further determine whether macrophages exhibit an unfavourable phenotype after nanoparticle loading, macrophage phenotypic shifts were evaluated. All the positively and neutrally charged liposomes, micelles, and polymersomes did not polarise macrophages to a M1 phenotype, which indicates that these nanoparticles had no pro-inflammatory effects on macrophages.

Overall, among all the tested nanoparticles, cationic liposomes, PEG-liposomes, cationic polymersomes, PEG-polymersomes and PEG micelles were revealed as suitable nanoparticles for subsequent development of macrophage-based drug delivery systems because they exhibited high cell uptake efficiencies, cytocompatibility and they did not cause unwanted effects on cell migration and phenotypic shifts. Furthermore, considering the long-term timescales of macrophage-mediated drug delivery (days rather than hours) and potential



applications of promoting tissue regeneration, polymersomes and micelles may be more suitable nanocarriers than liposomes as they can be engineered to possess higher stability to help maintaining nanoparticle integrity inside macrophages for a prolonged time, retaining the drug inside the nanoparticles, whilst achieving sustained drug release from the hybrid system.

Compared with neutrophils, macrophage-mediated drug delivery systems have long-term delivery properties and a less defined release mechanism for loaded cargoes. Hence, the developed neutrophil-mediated delivery system (MTX-liposome/neutrophils) of the previous Chapter 2 will be further validated *in vivo* in mouse models of inflammation to achieve rapid inflammation mitigation in the early stages of inflammation in the next chapter.

## Chapter 4

*In vivo* validation of the neutrophil-mediated drug delivery system for the treatment of inflammatory diseases

## 4. *In vivo* validation of the neutrophil-mediated drug delivery system for the treatment of inflammatory diseases

### 4.1. Introduction

Inflammation is implicated in the pathogenesis of many diseases such as cardiovascular diseases (*e.g.* stroke, MI) and autoimmune diseases (*e.g.* rheumatoid arthritis), where unchecked acute and/or chronic inflammation can cause extensive tissue damage.<sup>267</sup> At the tissue level, acute inflammation triggers immune cell infiltration and release of pro-inflammatory cytokines including tumour necrosis factor- $\alpha$  (TNF- $\alpha$ ), interleukin-1 (IL-1), and interleukin-6 (IL-6), which lead to tissue damage and hemodynamic changes.<sup>2</sup> If acute inflammation cannot be resolved immediately, it may become chronic resulting in irreversible tissue injury and loss of tissue function.

Cardiovascular disease is a major cause of death and disability worldwide with 37% of heart failures attributable to acute myocardial infarction (MI), which occurs when blood flow to the heart is suddenly blocked. Clinical outcomes in patients following MI can be improved surgically by primary percutaneous coronary intervention (PPCI) which restore blood flow through occluded vessels.<sup>316</sup> However, rapid myocardial reperfusion in itself leads to severe cardiomyocyte death and further myocardial injury.<sup>82</sup> The inflammatory response following acute MI plays an important role in inducing ischemia-reperfusion injury (IRI),<sup>317,318</sup> as such, inflammation is a crucial therapeutic target for the treatment of myocardial IRI. However, using anti-inflammatory drugs to mitigate inflammation for the treatment myocardial IRI can cause severe side effects (see Chapter 1 section 1.1.2). Although nanoparticle based delivery systems have been explored to target these drugs to the injured heart, their efficient local delivery remains challenging. Moreover, only one inflammation pathway is usually sensed by nanoparticle-based drug delivery systems, which is hard to manage the dynamic balance of pro- and anti-inflammation.<sup>225</sup> Immune cell-mediated drug delivery, which leverages the inherent functions of immune cells to sense and respond to dynamic inflammatory signals, is a promising alternative strategy to solve these problems.

The results in chapter 2 have demonstrated the successful development of a neutrophil-mediated drug delivery system that can be loaded with sufficient amounts of the anti-

inflammatory drug methotrexate (MTX) *via* cationic liposomes, whilst maintaining the physiological functions of neutrophils to allow response to inflammatory signals. After co-culture of MTX-liposome-loaded neutrophils with macrophages, successful transport of liposomes from neutrophils to macrophages was achieved and resulted in the inhibited proliferation of macrophages in culture. Thus, the migration ability of liposome-loaded neutrophils to inflammatory sites as well as the resulting anti-inflammation treatment effect were further investigated *in vivo* using a general tissue injury mouse model and a clinically relevant inflammatory disease mouse model of IRI.

Lipopolysaccharide (LPS), a known activator of toll-like receptor 4 (TLR4) that induces secretion of pro-inflammatory cytokines, is commonly injected locally or intravenously to induce acute local or systemic inflammation, respectively.<sup>319,320</sup> Several pro-inflammatory cytokines such as TNF- $\alpha$ , IL-6, and IL-1 are up-regulated upon LPS injection.<sup>321</sup> As such, LPS-induced tissue injury in the quadriceps muscle of mice (LPS-injury skeletal muscle model) was used in this chapter and represents general tissue injury induced by inflammation. Secondly, IRI in the heart (myocardial IRI model), the leading cause of adverse cardiovascular outcomes and heart failure, is a good model to represent clinically relevant inflammation-associated diseases in specific organs, which is why this delivery system was further studied in a mouse model of myocardial IRI.

The work presented in this chapter will evaluate the potential to utilise the MTX-liposome/neutrophil delivery system to mitigate inflammation in the LPS-injury skeletal muscle model and the myocardial IRI model. It is hypothesised that liposome loaded neutrophils can migrate to the inflamed muscle and the ischemic heart following intravenous injection. After loading the system with MTX, MTX-liposome/neutrophils can reduce inflammatory cytokines in the LPS injected muscle and improve cardiac function of the ischemic heart after treatment. To demonstrate the hypothesis, initially, the migratory behaviour of loaded neutrophils to the injured quadriceps and heart was evaluated by flow cytometry and Fluorescent Molecular Tomography (FMT), respectively. Then, this delivery system was loaded with MTX and injected intravenously to investigate the downregulation of inflammatory cytokine levels in the LPS-injury skeletal muscle model. Further, the improvement of cardiac function in the myocardial IRI model upon injection of the developed

MTX-loaded delivery system was studied. These two mouse models provided relevant data regarding the anti-inflammatory effects of the MTX-liposome/neutrophil delivery system after migration and release of the loaded drug at the inflammatory sites. Furthermore, it showcases the versatility of this system to be applicable in the treatment of different inflammatory diseases.

## 4.2. Materials and methods

### 4.2.1. Animals

LPS-injury skeletal muscle model: All animals were handled in accordance with the UK Home Office Animals Scientific Procedures Act 1986 and with an internal ethics board and UK government approved project (P63FE629C) and personal license (IC37CBB8F) from Dr. Anna Blakney. Food and water were supplied *ad libitum*. Female BALB/c mice (Charles River, UK) 6-8 weeks (treatment mice) or 10-12 weeks (donor mice) of age were placed into groups (n = 5) and housed in a fully acclimatised room.

Myocardial IRI model: All animals were handled in accordance with the UK Home Office Animals Scientific Procedures Act 1986 and with an internal ethics board and UK government approved project (PD359F318) and personal license (I6D2D5295) from Dr. Mohamed Bellahcene. Food and water were supplied *ad libitum*. Female CD1 mice (Charles River, UK) 4-5 weeks (treatment mice) or 8-10 weeks (donor mice) of age were placed into groups (n = 5) and housed in a fully acclimatised room.

### 4.2.2. LPS-injury skeletal muscle model and flow cytometry

LPS-biotin/streptavidin particles were prepared by complexing biotinylated LPS elementary bodies (LPS Biotin-EB, Invivogen, France) with streptavidin from *Streptomyces avidinii* (Sigma, UK) at a ratio of 1:4 biotin:streptavidin (w/w) in PBS. Mice were injected intramuscularly in the right quadriceps with 50 µg of particles (10 µg LPS Biotin EB, 40 µg streptavidin) in 50 µL, while the left quadriceps was not injected to serve as an internal control.

To explore the migration of injected neutrophils to the inflamed quadriceps in the right leg, 24 h after LPS injection, isolated neutrophils from donor mice (labelled with VivoTrack 680) were intravenously injected to LPS injected mice ( $4 \times 10^6$  per mouse). 1 h, 2 h, and 4 h post *i.v.* injection, 0.5 mL of the blood was collected from the tail vein for each mouse. Mice were

then sacrificed and quadriceps from both legs were taken out. Blood samples were mixed with red blood cell lysis buffer (Sigma, UK) to lyse most of red blood cells before the staining step. Quadriceps were digested using 2 mL of Dulbecco's Modified Eagle's Medium supplemented with 1 mg mL<sup>-1</sup> collagenase P (Sigma, UK) and 5 mg mL<sup>-1</sup> dispase II (Sigma, UK) for 30 min and passed through the cell strainer to obtain a single cell suspension. The cell suspensions of quadriceps samples and blood samples were then stained with Fixable Aqua Dead cell stain (Thermo Fisher, UK) diluted 1:400 for 20 min and neutrophil surface markers PE anti-mouse CD11b (250 ng mL<sup>-1</sup>) and Alexa 488 anti-mouse Ly6G/Ly6C (250 ng mL<sup>-1</sup>) (Biolegend) for 30 min. Cells were fixed with 3% PFA (v/v) and measured using flow cytometry.

To determine the migration of neutrophils after loading with liposomes, formulated liposome/neutrophils (liposomes were labelled with DiI and neutrophils were labelled with VivoTrack 680) were intravenously injected to LPS-injected mice 24 h after LPS injection. 1 h post *i.v.* injection, mice were sacrificed and quadriceps from both legs were taken out. A single cell suspension was obtained as described above and then stained with Aqua Dead cell stain and neutrophil surface markers PerCP anti-mouse CD11b (250 ng mL<sup>-1</sup>) and Alexa 488 anti-mouse Ly6G/Ly6C (250 ng mL<sup>-1</sup>). Cells were fixed with 1.5% PFA and measured using flow cytometry.

Dr. Anna Blakney performed LPS injection, *i.v.* injection, muscle and blood collection (Department of Infectious Diseases, Imperial College London).

#### 4.2.3. ELISA (Luminex) assay

To demonstrate the anti-inflammation treatment effect of the MTX-liposome/neutrophil system, MTX was loaded into liposomes (10 mg mL<sup>-1</sup> MTX was used during liposome formation) and MTX-liposome/neutrophils were formulated as described above (chapter 2 section 2.2.3). 24 h after LPS injection, formulated MTX-liposome/neutrophils were intravenously injected (10<sup>7</sup> neutrophils per mouse) to LPS injected mice. Free MTX (of 2 µg of MTX per mouse), MTX-liposomes (an equivalent amount of 2 µg of MTX per mouse) and blank neutrophils (10<sup>7</sup> neutrophils per mouse) were also *i.v.* injected to LPS injected mice as control groups and model mice without any treatment as the untreated control group. An extra 24 h after neutrophil *i.v.* injection, mice from 5 groups were sacrificed and the quadriceps from left healthy legs and right LPS injected legs were taken out. All the quadriceps

were weighed and lysed in Cell Lysis Buffer 2 (R&D Systems) for 30 min at 37 °C. The supernatant was collected after centrifugation. Three different inflammatory cytokines IL-1  $\alpha$ , TNF-  $\alpha$  and IL-6 in the supernatant were quantified using Magnetic Luminex Assay (R&D Systems). Briefly, each muscle was weighed and lysed using two times weight/volume of the lysis buffer for 30 min at room temperature. The samples were then centrifuged and the supernatants were analysed using the customised Mouse Magnetic Luminex Assay. The plate was read on a Luminex analyser.

#### 4.2.4. Quadriceps histology

Quadriceps were collected at 2 d, 4 d, and 7 d after LPS injection, and non-injected quadriceps were also collected as the control. All the quadriceps were fixed in 10% formalin (v/v PBS) for 24 h at room temperature and then transferred to 70% ethanol (v/v PBS) to dehydrate before wax embedding. One quadriceps was embedded in one block and 4 slices (5  $\mu$ m thick) were collected evenly throughout the whole quadriceps. All the sections were mounted on glass slides for staining. Slides were stained with H&E to identify cell infiltration. Stained slides were imaged using widefield microscopy (Zeiss Axio Observer). The specimen collection and staining were performed by Miss Lorraine Lawrence from the National Heart & Lung Institute at Imperial College London.

#### 4.2.5. Myocardial ischemia-reperfusion injury (IRI) model

Female CD-1 mice (4-5 weeks old) were anaesthetized with 4% isoflurane and then maintained at 2% in 100% O<sub>2</sub>. Mice received 0.024 mg buprenorphine subcutaneously (1.1 mg kg<sup>-1</sup>; Vetergesic, Alstoe Animal Health, UK), and were placed on a supine position, and intubated and ventilated with a tidal volume of 250  $\mu$ L and a respiratory rate of 150 breaths min<sup>-1</sup> (Hugo-Sachs MiniVent type 845; Harvard Apparatus Ltd., Kent, UK). The chest was shaved and a skin disinfectant was applied. A film dressing was placed over the chest to prevent fur entering the wound. After a left thoracotomy in the fourth intercostal space, the pericardium was removed, a 6-0 polyethylene suture was used to ensnare the left anterior descending (LAD) and tied against a polythene tubing for 60 min (LAD ischaemia) after which the ligating suture was loosened to allow reperfusion. The ligature was consistently positioned ~1mm below the atrio-ventricular junction. At the end of surgery mice were given 0.5 mL saline by subcutaneous injection to counter dehydration and allowed to recover in a

heated chamber for 20 min, then moved to a normal holding cage with supplemental heat for a few hours and mashed food at floor level. Adequate post-operative care was provided. Electrocardiogram (ECG), heart rate and body temperature were monitored throughout surgery. Consistency of the surgical IRI model was ensured by application of pre-defined surgical exclusion criteria: clear ST segment elevation on the ECG and distinct blanching of the myocardium after LAD ligation are primary criteria used to confirm the occurrence of myocardial infarction.

Dr. Mohamed Bellahcene performed myocardial IRI surgery, *i.v* injection and organ collection (National Heart and Lung Institute, Imperial College London).

#### 4.2.6. Fluorescence Molecular Tomography

To determine the biodistribution of injected neutrophils in mice with myocardial IRI, 24 h after reperfusion, neutrophils were isolated from donor mice, labelled with VivoTrack 680 and intravenously injected to mice with myocardial IRI ( $3.36 \times 10^6$  neutrophils per mouse) and healthy mice. 1 h and 2 h post intravenous injection, mice were sacrificed and the hearts were flushed with PBS and taken out. Kidney, spleen, lung and liver were harvested as well for *ex vivo* imaging. Five same organs from non-injected healthy mice were also harvested as the control. A part of each organ was imaged using Fluorescence Molecular Tomography (FMT4000, PerkinElmer) under channel 680nm, OsteoSense 680 to detect the VivoTrack 680 signal from the injected neutrophils.

To investigate the biodistribution of liposome loaded neutrophils in mice with myocardial IRI, 24 h after reperfusion, formulated liposome/neutrophils (liposomes were labelled with DiD (composition of POPC, DSTAP and cholesterol)) were intravenously injected to mice with myocardial IRI ( $5.6 \times 10^6$  neutrophils per mouse) and healthy mice. 1 h post *i.v.* injection, mice were sacrificed and the hearts were flushed with PBS and taken out. Kidney, spleen, lung and liver were harvested for *ex vivo* imaging. Five same organs from non-injected healthy mice were also harvested as the control. All the organs were imaged using Fluorescence Molecular Tomography (FMT4000, PerkinElmer) under channel 630nm, Vivo Tag-S 645 conjugate to detect the DiD signal from the liposomes. The collected fluorescence data were reconstructed by FMT 4000 system software (TrueQuant v3.0, PerkinElmer) for the quantification of fluorescence signals in different organs.



#### 4.2.7. Cardiac functional assessment

MTX was loaded into liposomes (10 mg mL<sup>-1</sup> MTX was used during liposome formation) and MTX-liposome/neutrophils were formulated as described in Chapter 2 section 2.2.5. 24 h after myocardial IRI surgery, two-dimensional (2D) echocardiography was performed to each mouse to confirm the initial heart damage. Meanwhile, formulated MTX-liposome/neutrophils were intravenously injected (10<sup>7</sup> neutrophils per mouse) to mice with myocardial IRI, non-injected IRI mice served as the control group. 4 weeks after the MTX-liposome/neutrophil treatment, cardiac functions were measured using 2D echocardiography and pressure–volume (PV) loop. Mice were then sacrificed and the hearts were taken out for histology analysis.

##### *2D echocardiography*

2D echocardiography was performed using a Vevo 770 system, mice were kept under light anaesthesia (~1.5-2% isoflurane) during recording after 5% isoflurane induction. Care was taken to avoid compression of thoracic cage which might otherwise distort ventricular geometry or induce bradycardia. All images were digitally recorded. Subsequent independent detailed off-line analysis is also blinded to genotype and performed using a Vevo software. All variables were obtained from short-axis images at mid-papillary level from left parasternal window and this approach is well-published/validated with respect to robustness and reproducibility in recent studies.<sup>322</sup> As recommended in consensus guidelines, all measurements were determined from at least 3 consecutive cardiac cycles, avoiding breath-associated artefacts. Analysis was performed from satisfactory images and acceptable heart rate range (all heart rates should fall within the recommended range of 400-650 beats min<sup>-1</sup> to be suitable for analysis).

##### *PV loops*

Animals were intubated and maintained under general anaesthesia: standard induction (4% isoflurane, 0.5 mL min<sup>-1</sup> O<sub>2</sub>) and maintenance dosage (2.5% isoflurane, 0.5 mL min<sup>-1</sup> O<sub>2</sub>), achieving deep anaesthesia without severe anaesthetic-induced cardiac functional depression. Intubated animals were placed on a supine position, and ventilated with a tidal volume of 250 µL and a respiratory rate of 150 breaths min<sup>-1</sup> (Hugo-SachsMiniVent type 845; Harvard Apparatus Ltd., Kent, UK). A PV catheter was inserted into the right carotid artery

through a small incision in the terminally anaesthetised animals. The catheter was carefully guided through the artery down to the aortic arch where central aortic pressure can be measured. PV loops were obtained by carefully pushing the PV probe at the end of the catheter across the aortic valve until it reached the LV cavity. Ventilation was briefly stopped (5 seconds) during data acquisition to avoid influence from ventilation of the lungs on the PV signals. The acquisition protocol consists of measurements of baseline cardiac function, inferior caval vein occlusions to record load-independent parameters. After that the inferior caval vein was occluded for a short time (5 seconds) to record load-independent parameters in the PV plane. Data were analysed using Labchart version 7 Pro software (ADInstruments, UK) including the module for PV loop analysis.

Dr. Mohamed Bellahcene performed the 2D echocardiography and PV loop assessments and data analysis (National Heart and Lung Institute, Imperial College London).

#### *Heart histology*

Mice were sacrificed 4 weeks after the treatment. Hearts were perfused with cold PBS, excised, cleaned to remove the blood and fixed in 10% formalin (v/v in PBS) for 24 h at room temperature. Imaging of a whole heart was carried out using NIKON D750. Three representative images were recorded for each heart from ventral, dorsal, and lateral view. Hearts were then transferred from 10% formalin to 70% ethanol (v/v PBS) to dehydrate before wax embedding. One heart was embedded in one block and was sliced transversally from the apex up towards the LAD ligation knot. Slices were 5  $\mu\text{m}$  thick with an interval of 250  $\mu\text{m}$ . All the sections were mounted on glass slides for staining. Slides were stained with Sirius red to identify collagen deposition. Stained slides were imaged using widefield microscopy (Zeiss Axio Observer). The specimen collection and staining were performed by Miss Lorraine Lawrence (National Heart and Lung Institute, Imperial College London).

#### *Collagen deposition analysis*

ImageJ was used to quantify the collagen area of images obtained using widefield microscopy through a macro, which is designed by Mr Stephen Rothery from the FILM Facility at Imperial College London. The macro allowed the quantification of the collagen-rich area (red) and the whole tissue area (collagen-rich area + healthy myocardium area (yellow)). The collagen percentage was calculated as the ratio of the collagen-rich area to the whole tissue area.

#### 4.2.8. Statistics

All the statistical analyses were conducted in GraphPad 8.0 (Prism). All the statistical tests were specified in the figure legends. Shapiro-Wilk test was used to assess normality and thus determine the statistical test. For non-normal distributions, the left healthy leg and right inflamed leg from the same mouse were preselected as a pair to analyse. 'n' refers to the number of animals used for the experiment.

### 4.3. Results and discussions

In this chapter, two different mouse models, the LPS-injury skeletal muscle model and the myocardial IRI model were employed in order to demonstrate the migration behaviour of liposome loaded neutrophils and a subsequent treatment effect after intravenous injection of MTX-liposome loaded neutrophils *in vivo* (Figure 4.1). The first model is an artificial inflammation model wherein LPS is injected intramuscularly to the mouse quadriceps to induce local inflammation. The population of loaded neutrophils in the quadriceps after injection was analysed using flow cytometry and the desired anti-inflammatory effect was determined by quantifying key inflammatory cytokine levels in the quadriceps. The second model represents a clinically relevant disease model of myocardial IRI following acute MI, which was aiming to study the neutrophil-mediated delivery to the injured heart. The migration ability of loaded neutrophils was investigated using FMT. The resulting cardiac functional improvement after the MTX-liposome/neutrophil treatment was evaluated using 2D echocardiography and PV-loop assessment.

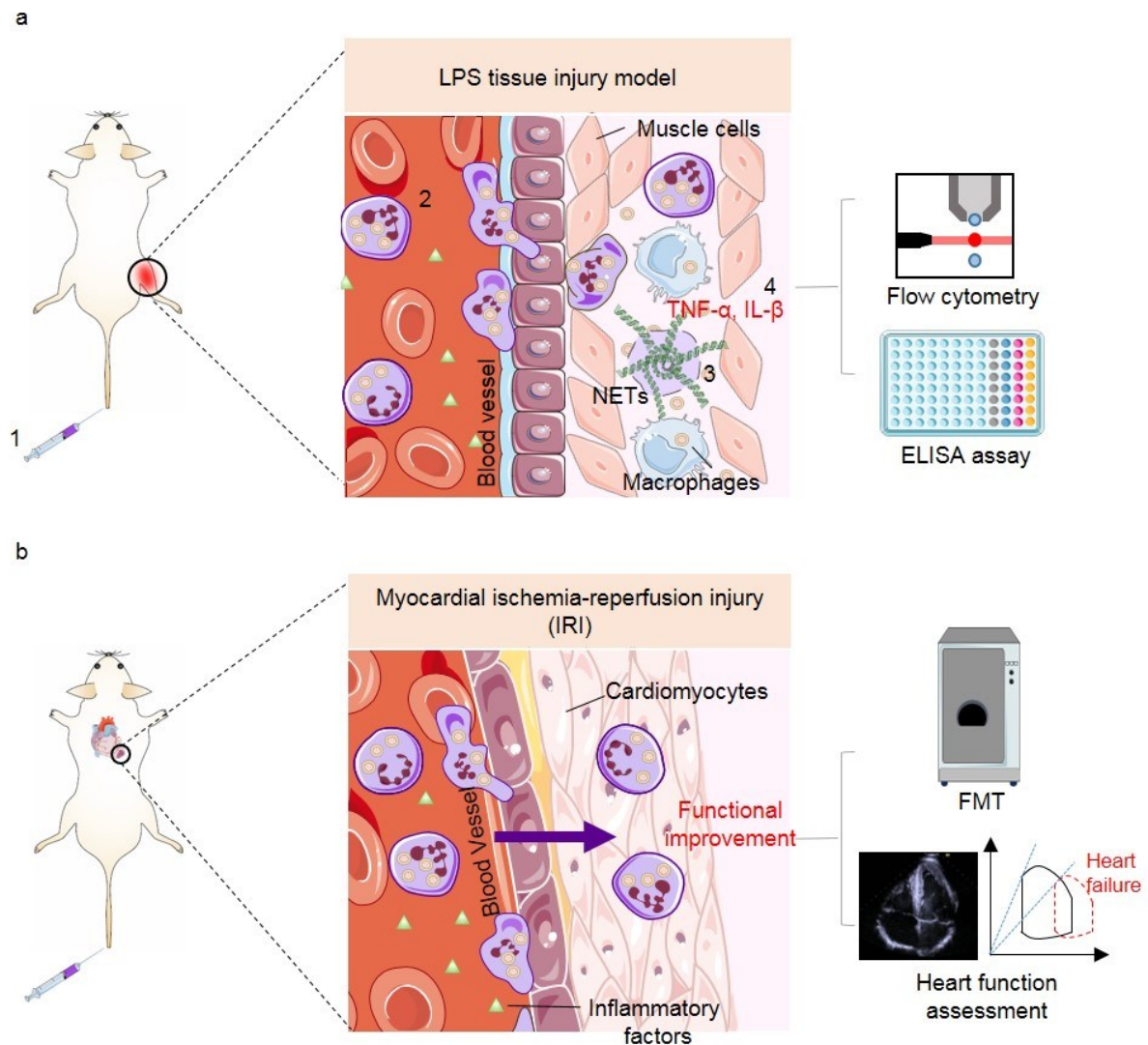


**Figure 4.1** Schematic illustration of two different mouse models used to determine the migration behaviour of loaded neutrophils and the treatment effect after intravenous injection of MTX-liposome/neutrophils. **a**, Schematic shows the anti-inflammation effect of the MTX-liposome loaded neutrophil delivery system in an LPS-injury skeletal muscle model. After intravenous injection (1), MTX-liposome/neutrophils respond to inflammatory signals in the bloodstream, migrating to the inflamed quadriceps (2) and then being activated by concentrated chemoattractants in the inflamed quadriceps to release neutrophil extracellular traps (NETs). MTX-liposomes are concomitantly released and taken up by other cells such as macrophages and monocytes in the inflamed quadriceps (3). Simultaneously, MTX suppresses the release of TNF- $\alpha$  and IL-6 from these cells (4). The migration behaviour of loaded neutrophils is analysed by flow cytometry and cytokine levels in the quadriceps are quantified by ELISA. **b**, Schematic shows the migration of the neutrophil mediated delivery system in a myocardial ischemia-reperfusion injury (IRI) model. Liposome loaded neutrophils are guided by inflammatory factors, migrating across blood vessels and accumulating in the injured heart, which is imaged by FMT. Furthermore, cardiac function is evaluated to determine the treatment effect of MTX-liposome/neutrophils in the mice with myocardial IRI. The graphics were adapted from the Servier Medical Art website.

#### 4.3.1. *In vivo* migration of liposome/neutrophils to inflamed skeletal muscle

LPS is the major component in the outer membrane of Gram-negative bacteria. LPS can activate TLR4 to promote the secretion of pro-inflammatory cytokines and has been used to induce acute inflammation in tissues in many studies; for example, an intratracheal injection of LPS caused acute lung injury in mice,<sup>323</sup> whilst 10 µg of LPS intramuscular injection can induce acute inflammation in the calf muscle of mice.<sup>324</sup> Therefore, the artificial inflammation model was first employed wherein LPS was intramuscularly injected to the right quadriceps of each mouse to induce acute inflammation. In order to precisely analyse the arrival of *ex vivo* loaded and reinjected neutrophils in the inflamed quadriceps, specific neutrophil and liposome markers were used for detailed flow cytometry analysis.

As previously reported, 24 h after LPS injection, the highest inflammatory gene expression was detected in the LPS-injected quadriceps, suggesting efficient recruitment of immune cells to the inflammatory site within the timeframe of 24 h up to 7 d.<sup>325</sup> Thus, quadriceps with LPS injection were collected after 2, 4, and 7 d and stained with Haematoxylin and Eosin (H&E) to visualise the accumulation of cells in the injured tissue (Figure 4.2), which are presumably immune cells because of the induced injury in the LPS-injected quadriceps. Compared to the healthy quadriceps, high numbers of immune cells infiltrated the LPS-injected quadriceps for all the timepoints, which agrees with the previous study confirming that the inflammatory response induced by LPS injection in the muscle was sustained up to 7 d.<sup>325</sup>

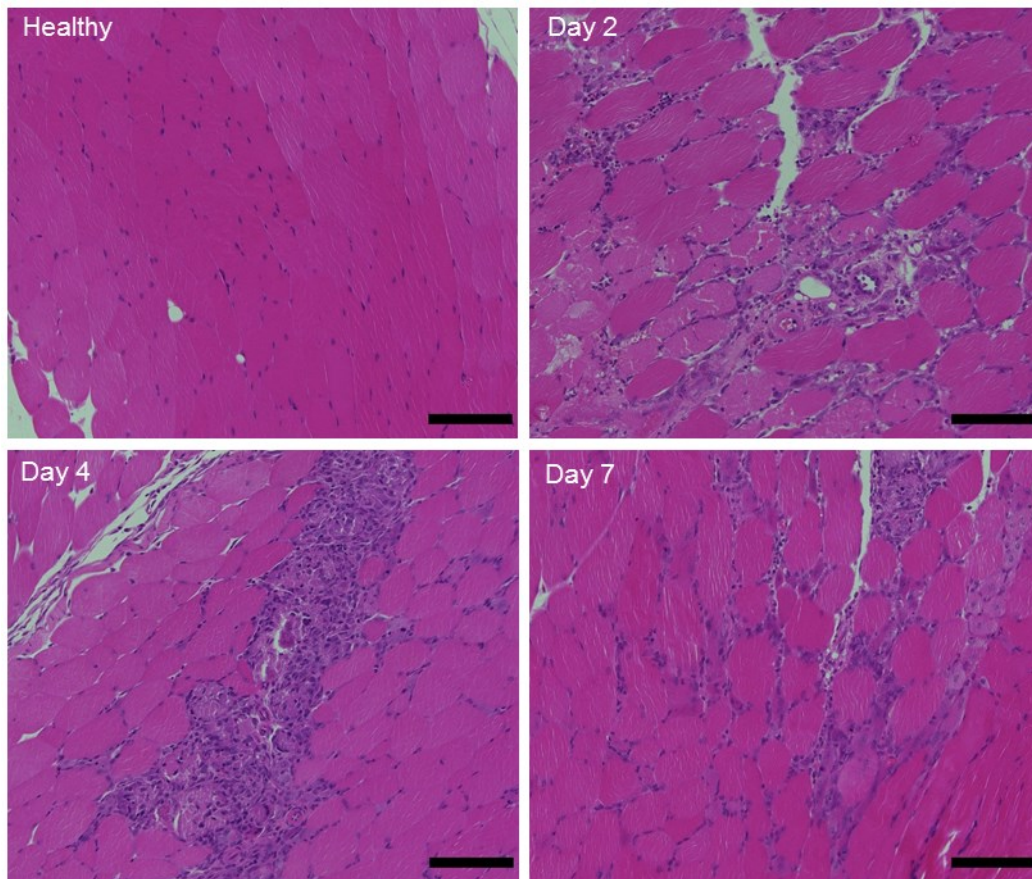


**Figure 4.2 H&E staining of healthy quadriceps and LPS-injected quadriceps after different timepoints.** *The extracellular matrix and cytoplasm were stained in pink, cell nuclei were stained in blue. Scale bars = 100  $\mu$ m. The specimen collection and staining were performed by Miss Lorraine Lawrence (National Heart and Lung Institute, Imperial College London).*

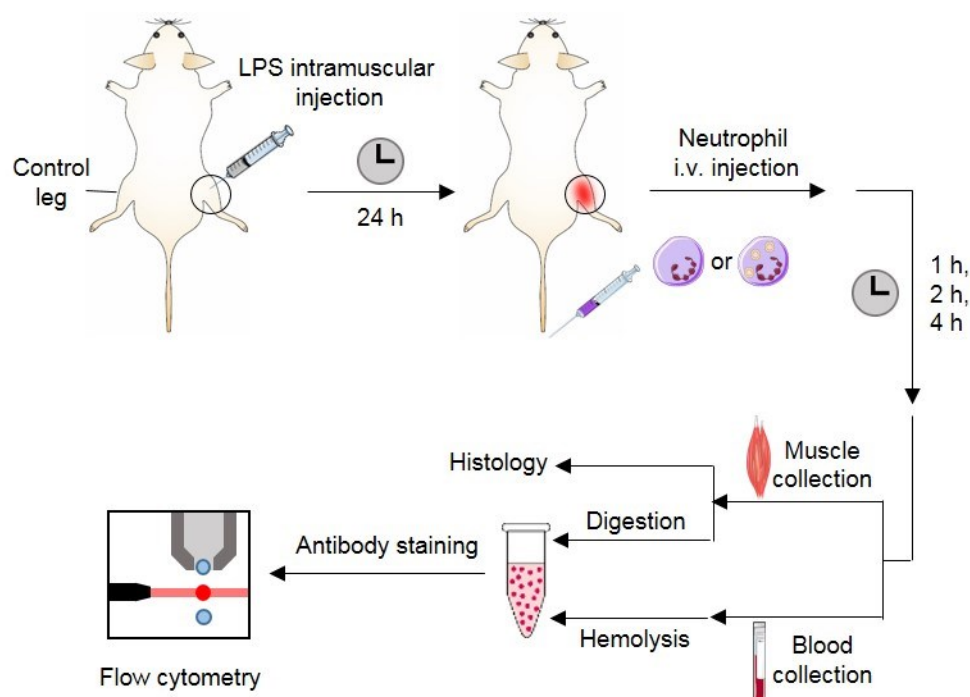


**Figure 4.3 Schematic illustration of sample preparation process of quadriceps and blood collected after LPS injection.** *Blood and quadriceps were collected after i.v. injection of neutrophils or liposome/neutrophils (liposomes were labelled with DiI, neutrophils were labelled with VivoTrack 680). For blood samples, lysis buffer was used to lyse red blood cells prior to staining. The quadriceps was digested using collagenase to obtain a single cell suspension. The cell suspension of the blood or quadriceps sample was stained with neutrophil surface makers to identify neutrophils. Flow cytometry was used to quantify different neutrophil populations. The quadriceps with or without LPS injection was also sliced and stained with H&E.*

Due to the highest inflammatory gene expression at 24 h after LPS injection,<sup>325</sup> isolated neutrophils labelled with VivoTrack 680 were injected intravenously at the peak of immune cell recruitment, 24 h post LPS injection. Quadriceps from both legs were collected at 1 h timepoint and processed to generate single cell suspensions that were analysed using flow cytometry to identify infiltrating neutrophils (Figure 4.3). Neutrophils accumulated in the LPS-injected quadriceps and accounted for 2.7% of total cells whereas only 0.03% of neutrophils were present in the healthy quadriceps (Figure 4.4, Figure 4.5a). This indicates that the intramuscular injection of LPS caused a local inflammation response in the right quadriceps

that resulted in neutrophil recruitment. Within the total neutrophil population in the LPS-injected quadriceps, 23% of neutrophils were positive for VivoTrack 680 (Figure 4.4, Figure 4.5b), which confirms that injected neutrophils migrated to the inflamed tissue. In total, 0.6% of the total cell population collected from the LPS-injected quadriceps were injected neutrophils, which was expected as a large number of muscle cells and stroma cells are present in the quadriceps.



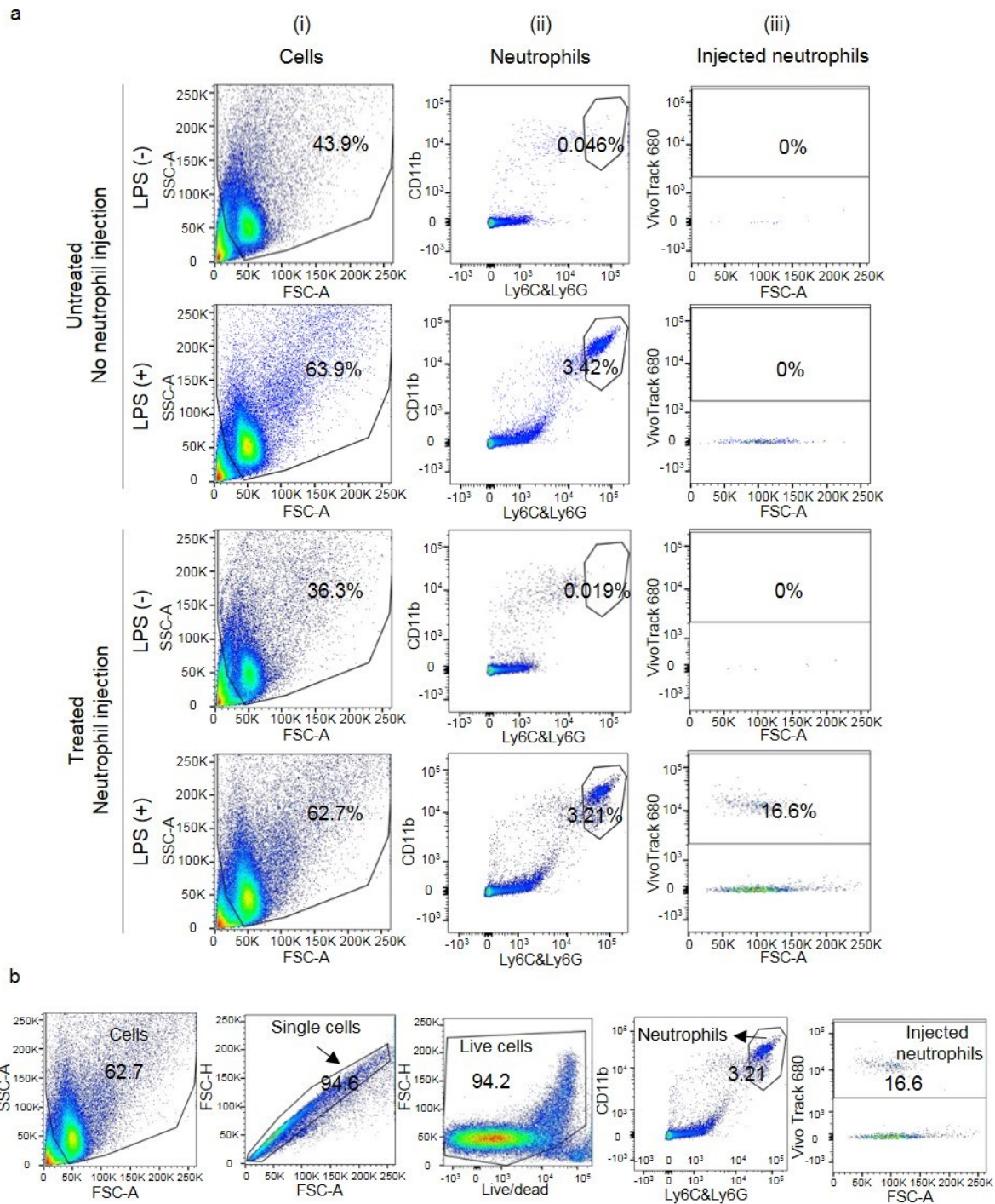


**Figure 4.4** Flow cytometry analysis of quadriceps with or without neutrophil injection (labelled with VivoTrack 680). **a**, (i) Forward scatter vs side scatter plot for total counted events; gate excludes cell doublets. (ii) PE anti-mouse CD11b and APC anti-mouse Ly6C/Ly6G plots for neutrophils. Gate shows the double positive population of neutrophils. (iii) Gate shows the VivoTrack 680 positive population of injection neutrophils compared to the total neutrophil population. For all the leg samples, the gating area was chosen based on the quadriceps samples from untreated mice. **b**, An example of the gating strategy.

To further study the time course of neutrophil migration, quadriceps were collected at 2 h and 4 h timepoints after neutrophil injection. In agreement with a previous study describing an inflammation response of up to 7 d after LPS injection,<sup>325</sup> endogenous neutrophils were identified at each time point in the LPS-injected quadriceps while there were only negligible numbers of neutrophils present in the healthy quadriceps (Figure 4.5a). Injected neutrophils were detected in the LPS-injected quadriceps 1 h and 2 h after injection but no injected neutrophils were detected after 4 h (Figure 4.5b). Thus, most of the injected labelled neutrophils were recruited to the inflamed quadriceps within 2 h after injection. Blood samples collected at each timepoint were also analysed by flow cytometry. The results mirrored the results from muscle samples. Injected neutrophils were detected at the 1h and 2 h timepoints (Figure 4.6). This indicates that injected neutrophil were circulating in the blood up to 2 h after injection.

Neutrophil recruitment from bone marrow, liver and spleen and transmigration into tissue usually takes 2-16 h.<sup>26</sup> In this study, injected neutrophils were shown in the inflamed quadriceps within 2 h after injection and disappeared after 4 h. Firstly, when injecting isolated neutrophils directly into the bloodstream at the peak of inflammation, the recruitment process may happen faster and transmigration of adherent neutrophils only takes 2-15 min,<sup>3</sup> which can explain why a shorter timeframe of neutrophil recruitment was seen in this study. Secondly, some injected neutrophils might just transiently adhere to the vessel walls. However, the muscle is full of tiny capillaries and these capillaries are in direct contact with myocytes, thus the released liposomes from neutrophils can still access the inflamed tissue.

A similar neutrophil-mediated delivery strategy was previously successfully applied to enhance the delivery of the cytotoxic agent paclitaxel to brain tumours.<sup>242</sup> However, in this study, the highest accumulation of *ex vivo* loaded and reinjected neutrophils was observed in the brain at 8 h post injection and the recruitment of neutrophils to the brain sustained up to 24 h, which is much longer than the time course of neutrophil migration identified in this study. These differences may have arisen due to differences in inflammation triggered from glioma surgical resection in the brain (being less intense) compared to LPS injection. More severe inflammation in case of the LPS model may facilitate faster neutrophil recruitment to the inflammatory site. Additionally, the blood-brain barrier may slow down the neutrophil migration. Furthermore, rather than identifying neutrophils based on cell surface markers,

Xue *et al.* used a fluorescent dye for tracking the neutrophil membrane. The fluorescence signal in the brain might be ruptured neutrophil debris retained in the brain rather than intact neutrophils. In this study (Figure 4.5), whole neutrophils arriving at the inflamed tissue were identified through the combination of a fluorescent membrane tag and surface markers to identify injected intact neutrophils that arrived at the target tissue by using flow cytometry.

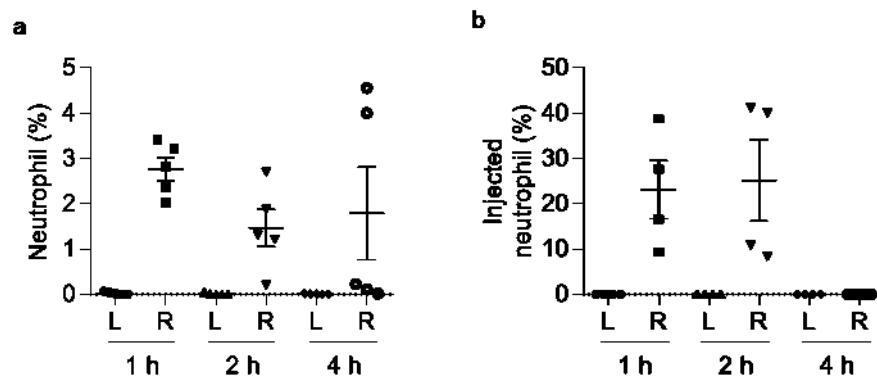


**Figure 4.5** Quantification of endogenous neutrophils and injected neutrophils in healthy quadriceps and LPS-injected quadriceps after neutrophil injection. **a**, Neutrophil percentage of overall cell population in healthy quadriceps (L) and LPS-injected quadriceps (R) at 1 h, 2 h and 4 h post neutrophil injection. Data shown as the mean  $\pm$  s.e.m.,  $n = 5$ . **b**, Percentage of injected neutrophils within total neutrophil population in healthy quadriceps (L) and LPS-injected quadriceps (R) at 1 h, 2 h and 4 h post neutrophil injection. Data shown as the mean  $\pm$  s.e.m.,  $n = 4$ .

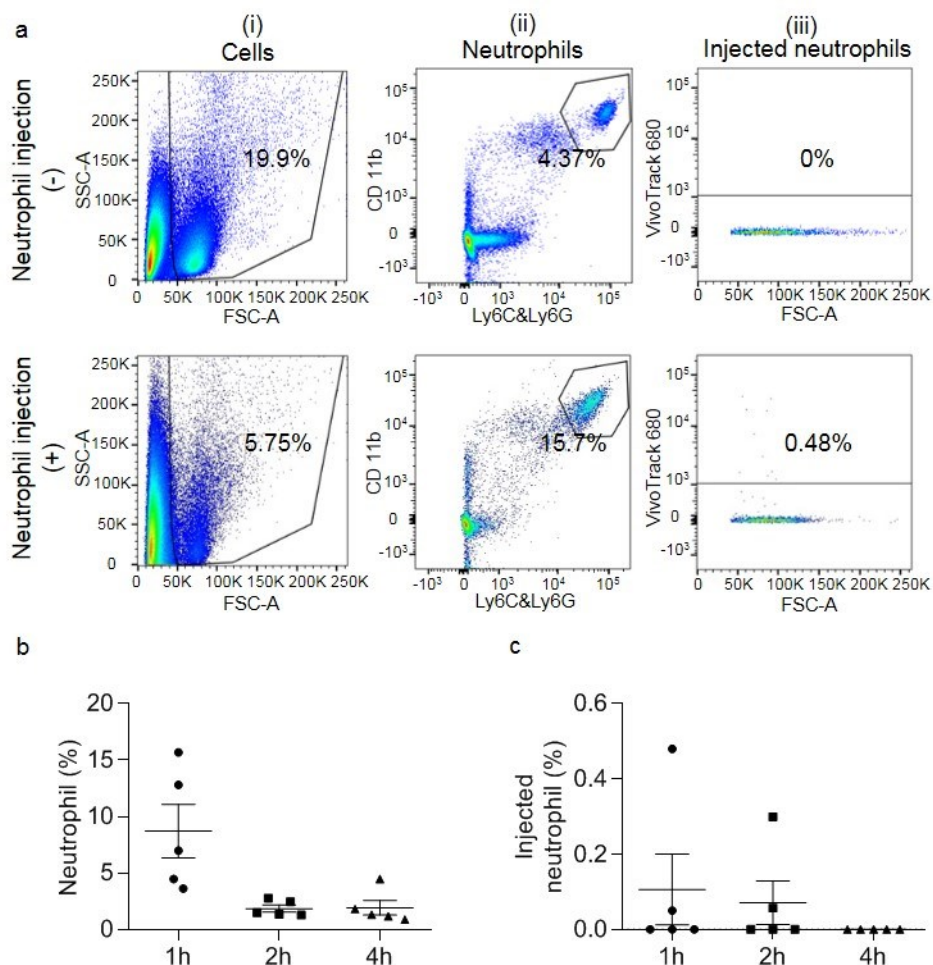


**Figure 4.6 Quantification of endogenous neutrophils and injected neutrophils in the blood after neutrophil injection.** **a**, Flow cytometry analysis of blood after injection of ex vivo isolated neutrophils (neutrophils were labelled with VivoTrack 680). Blood was collected from the tail vein and resuspended in red blood cell lysis buffer to remove most of red blood cells before the staining step. (i) Forward scatter vs side scatter plot for total counted events; gate excludes cell doublets and red blood cells. (ii) PE anti-mouse CD11b and APC anti-mouse Ly6C/Ly6G plots for neutrophils. Gate shows the double positive population of neutrophils. (iii) Gate shows the in VivoTrack 680 positive population of injection neutrophils compared to the total neutrophil population. For all the blood samples, the gating area was chosen based on the blood samples from non-injected mice. **b**, Overall neutrophil percentage in the blood at 1 h, 2 h and 4 h post neutrophil injection. Data shown as the mean  $\pm$  s.e.m.,  $n = 5$ . **c**, Percentage of injected neutrophils within total neutrophil population in the blood at 1 h, 2 h and 4 h post neutrophil injection. Data shown as the mean  $\pm$  s.e.m.,  $n = 5$ .

After confirming that injected neutrophils can migrate to the inflamed quadriceps after neutrophil injection, isolated VivoTrack 680 labelled neutrophils were loaded with DiI labelled liposomes as described above to test if these neutrophils can also carry particles to the inflamed muscles. Flow cytometry results showed that more than 98% of the injected

neutrophil population still contained DiL-labelled liposomes in the LPS-injected quadriceps, whilst none were found in the healthy quadriceps (Figure 4.7). This suggests that liposome loaded neutrophils retain their ability to migrate to inflamed tissue *in vivo* and carry liposomes for subsequent delivery to target cells.

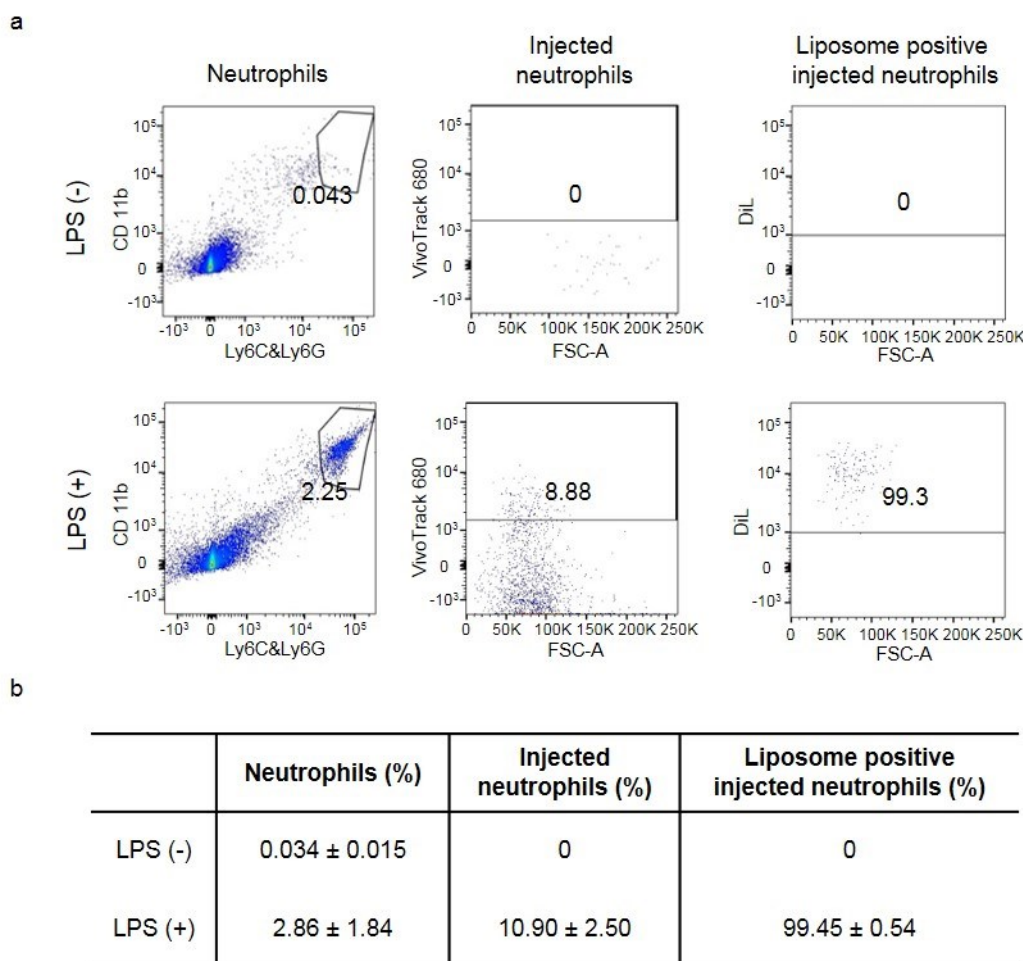


**Figure 4.7 Quantification of liposome loaded neutrophils in healthy quadriceps and LPS-injected quadriceps after injection.** *a*, Flow cytometry analysis of quadriceps after injection of liposome loaded neutrophils (liposomes were labelled with DiL; neutrophils were labelled with VivoTrack 680). *b*, From left to right: Overall neutrophil percentage in the quadriceps at 1 h post neutrophil injection. Percentage of injected neutrophils within total neutrophil population in the quadriceps at 1 h post neutrophil injection. Percentage of liposome positive neutrophils within injected neutrophil population in the quadriceps at 1 h post neutrophil injection. Data shown as the mean ± s.e.m.,  $n = 4$ .

These results have demonstrated that *ex vivo* isolated neutrophils can respond to inflammatory signals in the blood and migrate to the inflamed muscle in the LPS-injury skeletal muscle model within 2 h after neutrophil injection. After loading with liposomes,



neutrophils can also carry liposomes to the inflamed muscle while there were no liposome-loaded neutrophils arriving in the healthy quadriceps. It confirms that injected neutrophils can locally deliver loaded nanocarriers to the site of inflammation.

#### 4.3.2. *In vivo* migration of liposome/neutrophils to the IRI heart

To determine the versatility of the liposome/neutrophil delivery system that migrates to inflammatory sites, this system was further applied to a myocardial IRI model. Healthy mice and mice with myocardial IRI were *i.v.* injected with isolated neutrophils (labelled with VivoTrack 680) after 24 h reperfusion. Non-injected healthy mice served as another control group. The heart (perfused with PBS to remove non-infiltrated neutrophils), kidney, spleen, liver and lung were harvested from all the mice at 1 h and 2 h timepoints after neutrophil injection, followed by Fluorescence Molecular Tomography (FMT) scanning to determine the VivoTrack 680 signal from the injected neutrophils in each organ (Figure 4.8).

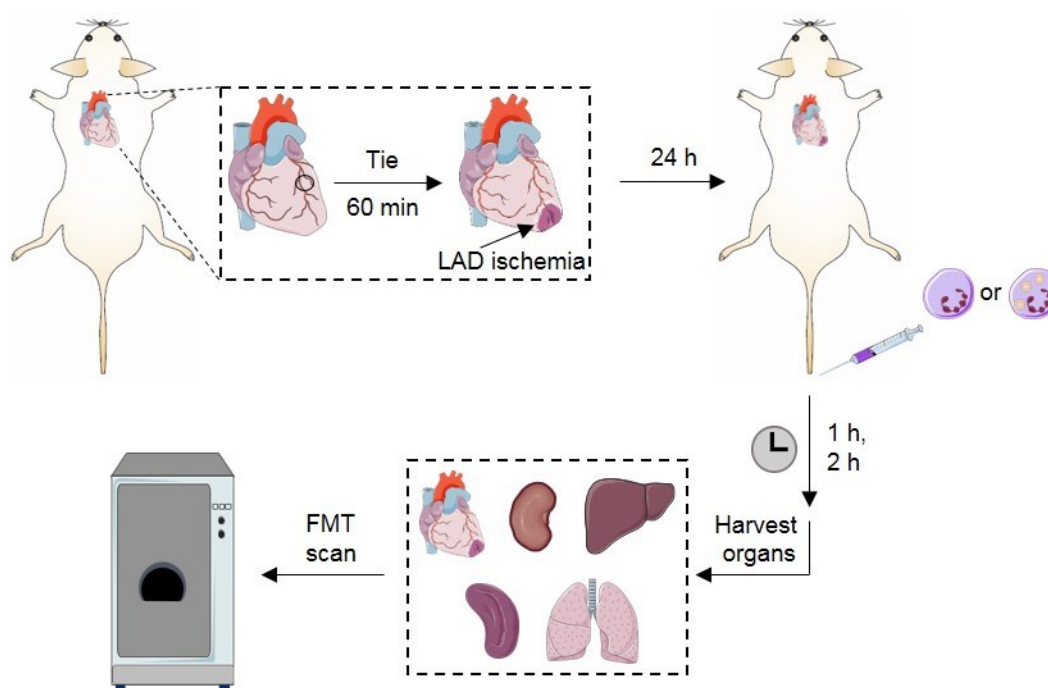


**Figure 4.8 Schematic illustration of myocardial IRI surgery, the following treatment and sample analysis process in the myocardial IRI mouse model.** LAD was ligated for 60 min to induce a transient MI, after which the ligating suture was loosened to allow reperfusion. Ex vivo isolated neutrophils (labelled with VivoTrack 680) and liposome loaded neutrophils (liposomes were labelled with DiD) were injected intravenously after 24 h reperfusion. Heart (perfused with PBS), liver, spleen, lung and kidney were harvested for FMT scanning at 1 h and 2 h post injection.

In this model, 1 h and 2 h timepoints were chosen to study the migration behaviour of injected neutrophils based on the migratory behaviour of neutrophils observed in the LPS-injury skeletal muscle model (Figure 4.5). After VivoTrack 680 labelled neutrophils were *i.v.* injected to mice with myocardial IRI and healthy mice, the VivoTrack 680 signal from injected neutrophils was only clearly detected in the IRI hearts at 1 h and 2 h timepoints (Figure 4.9a, Figure 4.10a), while the signal in the healthy hearts was comparable to the blank control hearts. To quantitatively compare the dye signal in the hearts, the collected fluorescence images were reconstructed by the FMT 4000 system software to yield total fluorescence signals of the organs. The quantitative data confirms that at both timepoints the amount of the VivoTrack 680 dye from injected neutrophils was significantly higher in the IRI hearts compared to the healthy hearts. There was no difference found between the healthy hearts from the injected mice and the control mice (Figure 4.9b, Figure 4.10b). This result reveals that injected neutrophils only migrated and accumulated in the injured hearts due to the inflammatory environment found in myocardial IRI. The biodistribution of injected neutrophils in other organs was also detected and quantified by FMT scanning and 3D reconstruction analysis. Some VivoTrack 680 signal was also detected in all other tested organs in mice with myocardial IRI, mainly in the liver and spleen (Figure 4.9c, Figure 4.10c). This might be due to systemic inflammation after acute MI,<sup>326</sup> which induced the migration of neutrophils to other inflamed organs, or it caused premature NET formation in the blood with neutrophil debris ending up in the mononuclear phagocyte system of the liver and spleen. This finding is in good agreement with a previous study that also observed the distribution of *ex vivo* isolated neutrophils in other organs after intravenous injection.<sup>242</sup> They also found the majority of neutrophils ending up in liver and spleen when tested in surgically treated glioma-bearing mice.

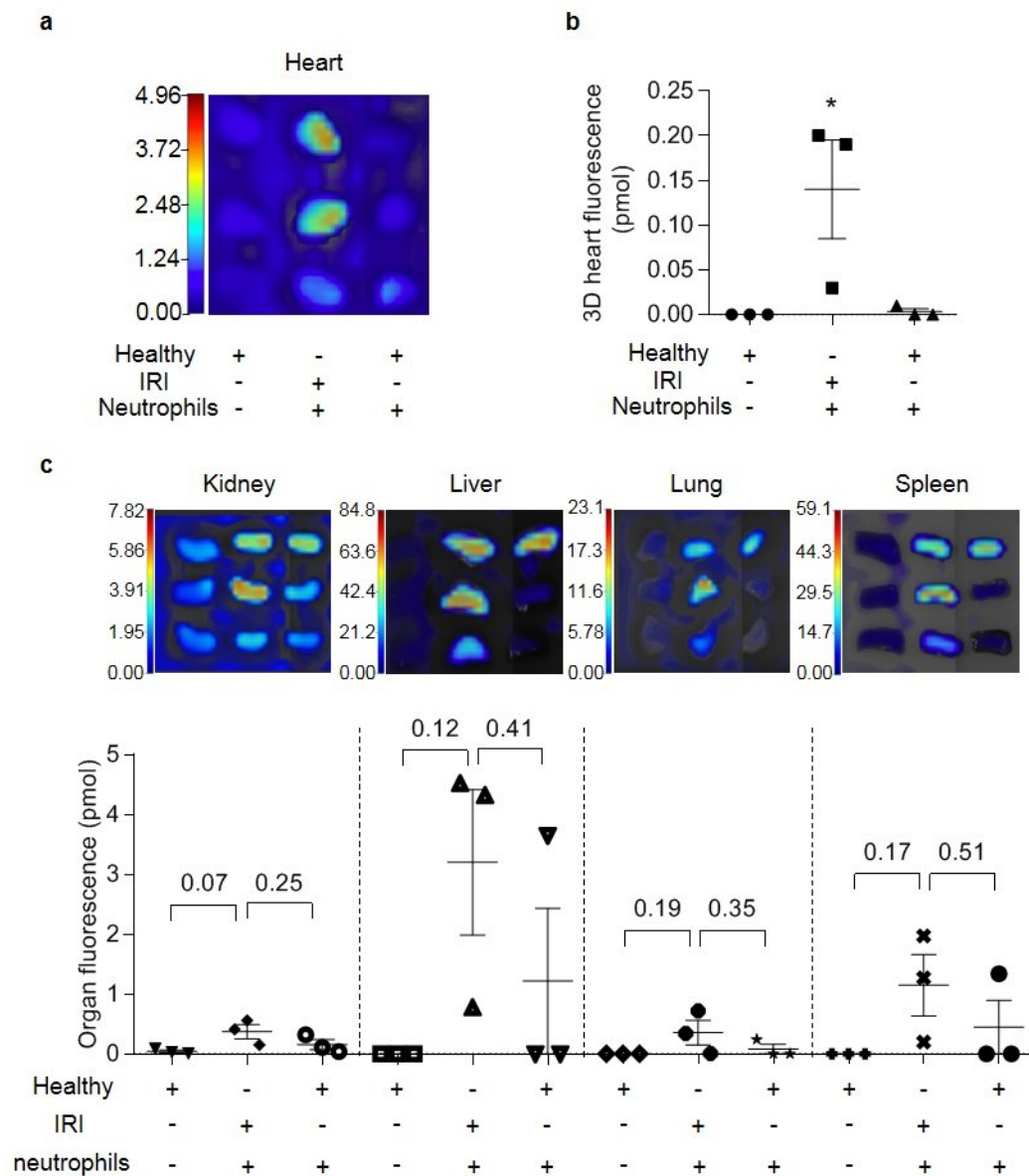


**Figure 4.9** *In vivo* accumulation of neutrophils (labelled with VivoTrack 680) in the heart after myocardial IRI surgery and biodistribution in other organs at 1 h post neutrophil injection. **a**, Fluorescence image of hearts from mice after different treatments. **b**, Total amount of VivoTrack 680 dye in hearts (pmol, mean  $\pm$  s.e.m.). \* $P < 0.05$ , one way ANOVA, Bonferroni post hoc test,  $n = 3$ . **c**, *In vivo* biodistribution of injected neutrophils in kidney, liver, lung and spleen (from left to right). Top row: fluorescence images of different organs from mice. Bottom row: Total amount of VivoTrack 680 dye in different organs (pmol, mean  $\pm$  s.e.m.). One way ANOVA, Bonferroni post hoc test,  $n = 3$ .



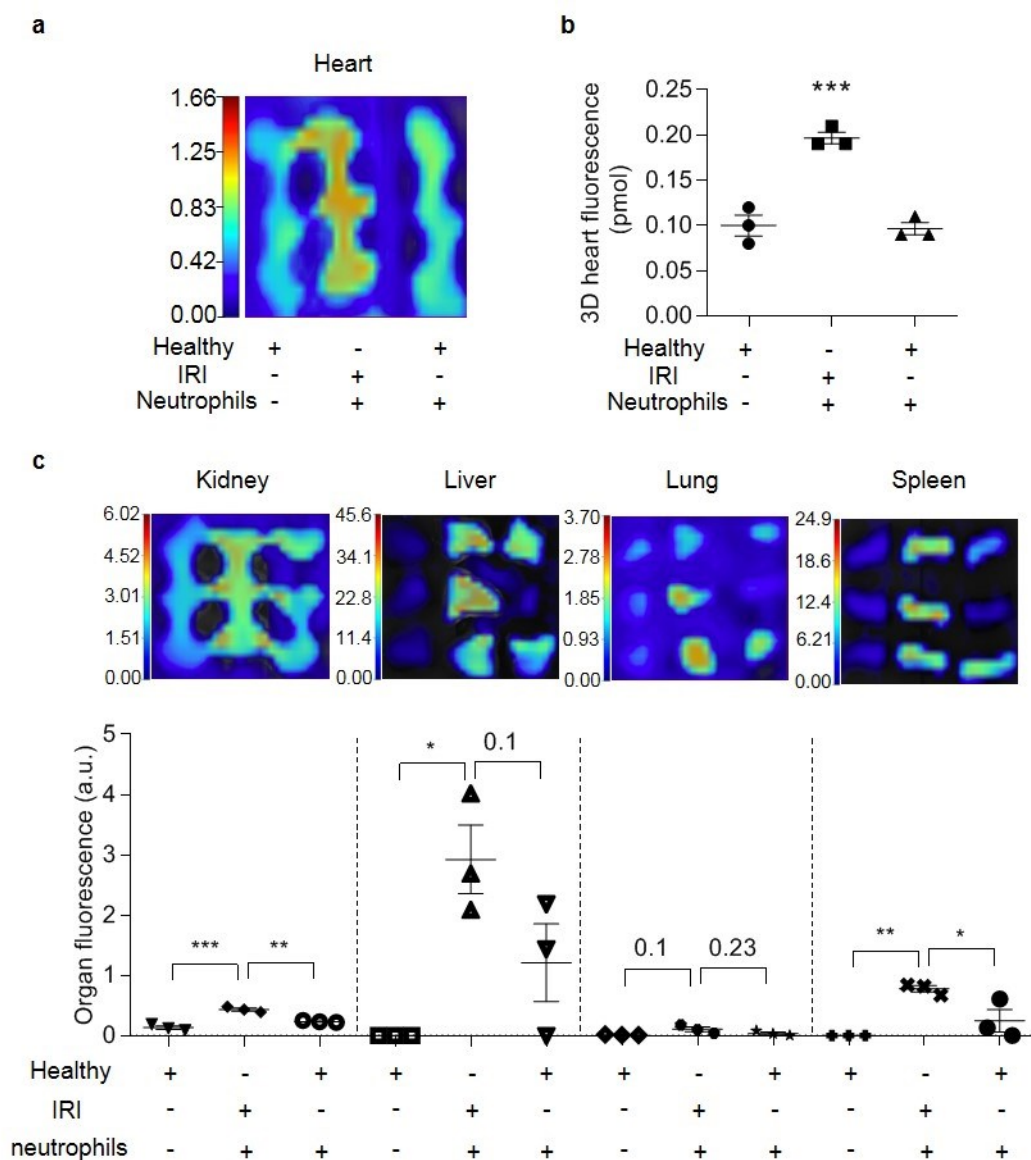


**Figure 4.10** *In vivo* accumulation of neutrophils (labelled with VivoTrack 680) in the heart after myocardial IRI surgery and biodistribution in other organs at 2 h post neutrophil injection. **a**, Fluorescence image of hearts from mice after different treatments. **b**, Total amount of VivoTrack 680 dye in hearts (pmol, mean  $\pm$  s.e.m.). \*\*\* $P < 0.001$ , one way ANOVA, Bonferroni post hoc test,  $n = 3$ . **c**, *In vivo* biodistribution of injected neutrophils in kidney, liver, lung and spleen (from left to right). Top row: fluorescence images of different organs from mice. Bottom row: total amount of *in vivo* track 680 dye in different organs (pmol, mean  $\pm$  s.e.m.). \* $P < 0.05$ , \*\* $P < 0.01$ , \*\*\* $P < 0.001$ , one way ANOVA, Bonferroni post hoc test,  $n = 3$ .

Furthermore, the ability of neutrophils to carry liposomes to the injured hearts was investigated. This sets the basis to achieve specific delivery of drug loaded liposomes to the injured heart using neutrophils. To explore the *in vivo* migration of liposome/neutrophils to the injured hearts after myocardial IRI surgery and the distribution in the other organs,

liposomes (labelled with DiD) loaded neutrophils were injected and organs were collected at 1 h post injection. The IRI hearts showed significantly higher DiD fluorescence signal from liposomes than the other two groups (Figure 4.11a and b), which reveals accumulation of liposomes in the injured hearts by using the neutrophil-mediated strategy. Similar to the previous neutrophil migration results (Figure 4.9, Figure 4.10), DiD signal also appeared in the other organs (Figure 4.11c), which can be explained as above by systemic inflammation and premature NETs formation.

To put the data in context to the nanomedicine field it is worth referring back to delivery efficiencies typically achieved when injecting nanocarriers without any cellular component. In general, the delivery efficiency of nanoparticle-based drug delivery systems is very low and the mean and median delivery efficiencies are 2.24% and 0.76% of the injected dose, respectively (this is a meta-analysis of nanoparticle delivery to tumours).<sup>269</sup> Because of different biological barriers encountered by these delivery systems before arriving at the desired site, most of the injected dose will be cleared by the mononuclear phagocyte system and the particles end up in the liver and spleen. In this study, most of the liposomes were detected in the liver and spleen, which agrees with many published studies. However, the biodistribution results suggest that even in a complicated mouse model of IRI following acute MI, injection of *ex vivo* loaded neutrophils can be employed as a delivery strategy to transport significant numbers of liposomes to the injured hearts by exploiting the intrinsic functions of neutrophils migrating to the inflammatory site. Thus, it is promising to use this system to deliver anti-inflammatory drugs to the site of inflammation and improve anti-inflammatory therapies.

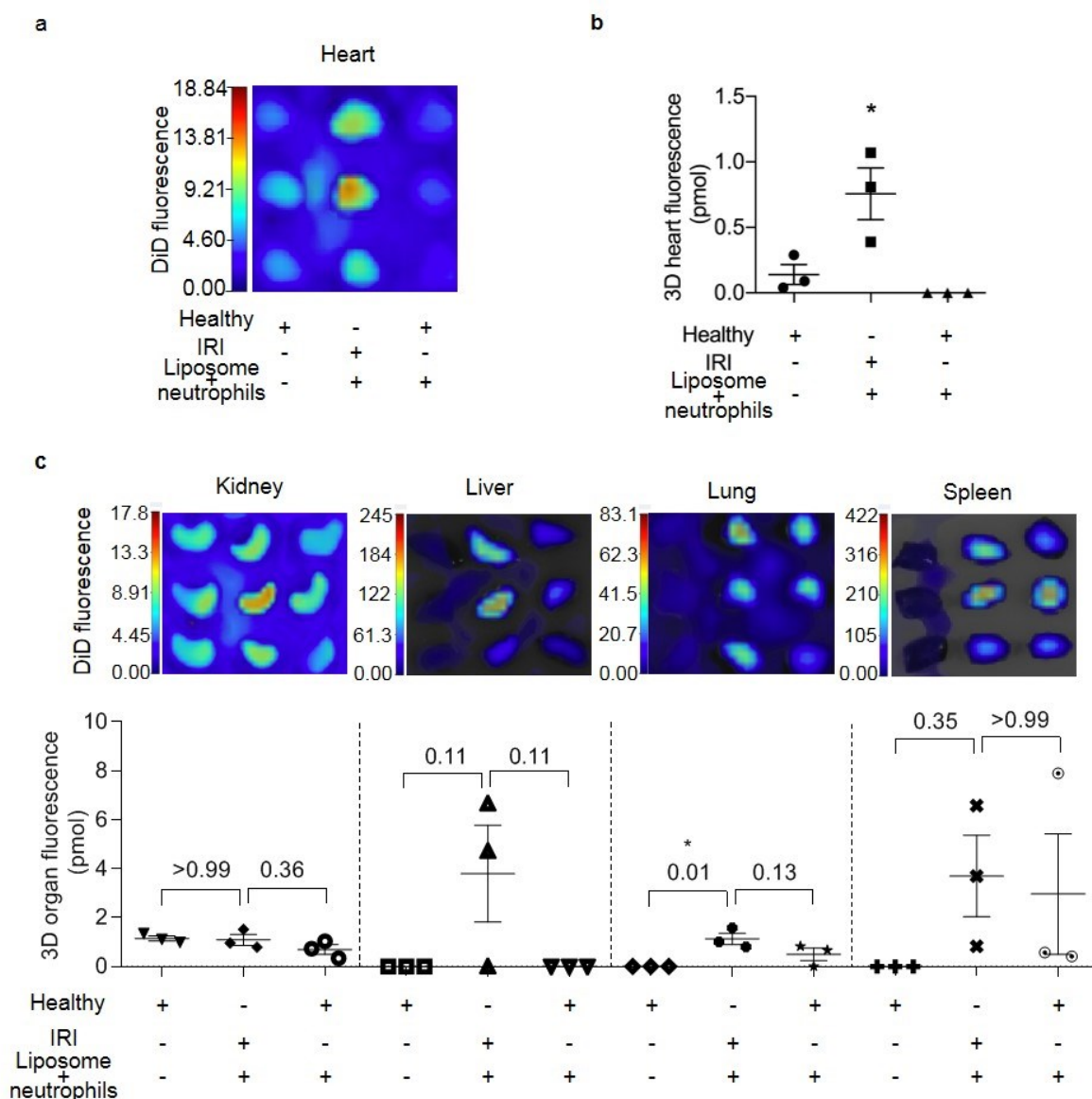


**Figure 4.11** *In vivo* accumulation of liposome/neutrophils in the heart after myocardial IRI surgery and biodistribution in other organs at 1 h post injection. **a**, Fluorescence image of hearts from mice at 1 h post liposome/neutrophil injection (liposomes were labelled with DiD). **b**, Total amount of the DiD dye in hearts (pmol, mean  $\pm$  s.e.m.). \* $P < 0.05$ , one way ANOVA, one way anova, Bonferroni post hoc test,  $n = 3$ . **c**, *In vivo* biodistribution of DiD labelled liposomes (1 h post liposome/neutrophil injection) in kidney, liver, lung and spleen (from left to right). Top row: fluorescence images of different organs from mice. Bottom row: total amount of the DiD dye present in the different organs (pmol, mean  $\pm$  s.e.m.). \* $P < 0.05$ , one way ANOVA, Bonferroni post hoc test,  $n = 3$ .

Overall, these results have demonstrated that *ex vivo* isolated neutrophils can migrate to the injured sites in response to inflammatory signals in the blood after *i.v.* injection. For this

purpose, two different mouse models were employed representing a localised inflammation in tissue (LPS-injury skeletal muscle model) and an inflammatory heart disease with clinical relevance (myocardial IRI model). Most importantly, after loading neutrophils with liposomes, they carried the loaded liposomes to inflammatory sites in both models, which suggests this delivery system has the promise of increasing drug action through localised delivery; this was tested in the following two subchapters.

#### 4.3.3. *In vivo* anti-inflammatory treatment *via* neutrophil-mediated delivery in the LPS-injury skeletal muscle model

Since previous results demonstrated that liposome loaded neutrophils can migrate and deliver their cargo to inflamed tissue, the anti-inflammation treatment effect of the hybrid system MTX-liposome/neutrophils was explored using the LPS-injury skeletal muscle model. In this model, the LPS injected quadriceps was defined as the inflammation site while the non-injected quadriceps was used as the internal control for each mouse. In this experiment, three inflammatory cytokines IL-6, IL-1 $\alpha$  and TNF- $\alpha$ , which are responsible for regulating inflammation, were measured (Figure 4.12), because MTX used to treat inflammatory diseases alters their expression levels in different cell types.<sup>294,109</sup> For example, MTX loaded nanocapsules were shown to significantly reduce the cytokine levels of IL-6 and TNF- $\alpha$  in mononuclear cells obtained from RA synovial fluid.<sup>327</sup> In a patient study, the IL-1 $\alpha$  and TNF- $\alpha$  expression in the inflamed synovial tissue was decreased after treating with MTX in patients with psoriatic arthritis.<sup>328</sup> On the other hand, animal models of LPS-induced inflammation have been used in many studies to test the efficacy of developed drug delivery systems. Chu *et al.* formulated denatured albumin nanoparticles loaded with a NF- $\kappa$ B inhibitor TPCA-1. These TPCA-1 loaded nanoparticles can target activated neutrophils in the bloodstream which will then be transported by neutrophils into inflamed alveoli of mice with LPS-injected lung inflammation. A significant reduction of IL-6 and TNF- $\alpha$  expression in the bronchoalveolar lavage fluid was detected after treatment.<sup>237</sup> Another study used LPS-induced sepsis model to test the anti-inflammatory activity of curcumin loaded solid lipid nanoparticles. After intraperitoneal injection of curcumin loaded solid lipid nanoparticles, the expression of serum pro-inflammatory cytokines IL-6, IL-1 $\beta$  and TNF- $\alpha$  was significantly decreased compared to free curcumin injection.<sup>329</sup> Thus, LPS-induced skeletal muscle injury employed in this study is a good model to test the anti-inflammatory activity of MTX-liposome/neutrophils.

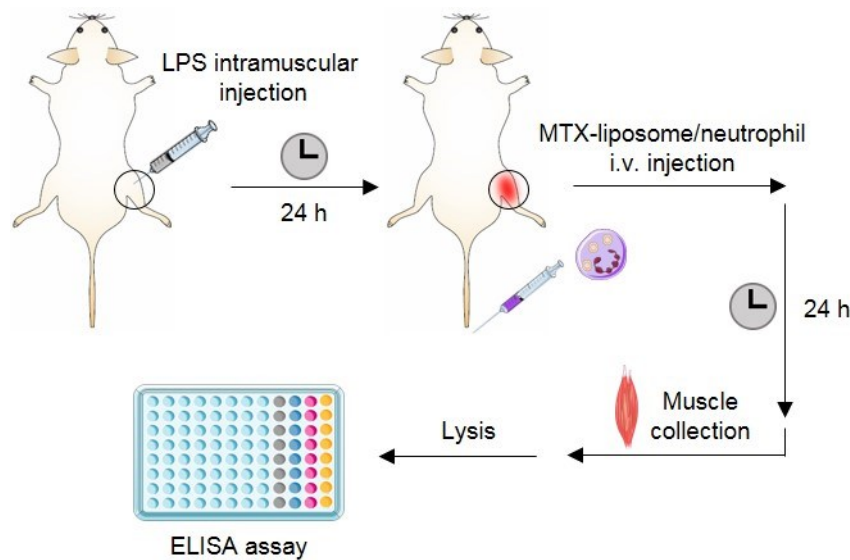


**Figure 4.12 Schematic illustration of the anti-inflammation treatment *via* neutrophil-mediated delivery in the LPS-injury skeletal muscle model.** *MTX-liposome/neutrophils were i.v. injected to the model mice at 24 h post LPS intramuscular injection. After 24 h, quadriceps from both legs were collected and lysed in Eppendorf tubes. Different inflammatory cytokine levels (TNF- $\alpha$ , IL-6, IL-1 $\alpha$ ) were measured using an ELISA assay.*

Inflammatory cytokines IL-6, IL-1 $\alpha$  and TNF- $\alpha$  were first measured in untreated control mice, comparing the healthy quadriceps and the LPS-injected quadriceps to test whether these cytokine levels were increased in the injured muscle after LPS injection. As expected, IL-6 and TNF- $\alpha$  levels increased significantly in the LPS-injected quadriceps compared to the healthy quadriceps while IL-1 $\alpha$  remained at baseline levels (Figure 4.13 Untreated Group). Thus, IL-6 and TNF- $\alpha$  were subsequently used as indicators of inflammation in the subsequent treatment study.

$10^6$  neutrophils loaded with MTX-liposomes were then injected into LPS-treated mice, which corresponds to an amount of 2  $\mu$ g of MTX per mouse. This dose was previously found to be sufficient to mitigate inflammation.<sup>330,331</sup> Blank neutrophils, an equivalent amount of MTX loaded liposomes and free MTX were *i.v.* injected to LPS injected mice to serve as control groups. After 24 h, quadriceps from both legs were collected, processed and cytokine levels (IL-6 and TNF- $\alpha$ ) were measured using a commercial cytokine ELISA test (Magnetic Luminex Kit). MTX-liposome/neutrophils treatment reduced IL-6 levels in the LPS-injected quadriceps to levels comparable to those in the healthy quadriceps while levels in control groups stayed

elevated (Figure 4.13a). An equivalent amount of MTX injection did not down-regulate IL-6 levels in the LPS-injected quadriceps. MTX-liposomes themselves did also not have any beneficial effect; these mice still had significantly higher IL-6 levels in the LPS-injected quadriceps compared to the healthy quadriceps. This is likely due to the positive charge on the liposome surface which resulted in rapid clearance of the MTX-liposomes from the bloodstream after *i.v.* injection<sup>332</sup> and failure to reach the target site. When MTX-liposomes are loaded into neutrophils, they are protected and carried to the inflamed muscle and locally release MTX-liposomes to mitigate inflammation. These results further confirmed that injected neutrophils infiltrated the inflamed quadriceps and released loaded MTX-liposomes resulting in the desired anti-inflammation effects, while free MTX and MTX-liposomes did not have any beneficial effect because they were not able to infiltrate tissue without the carrier neutrophils. Comparing the fold change of IL-6 in the LPS-injected versus non-injected quadriceps between the control and various treatment groups, only MTX-liposome/neutrophil treatment had significantly lowered the levels of IL-6 in the inflamed quadriceps compared to the untreated control group (Figure 4.14), suggesting the benefit of the neutrophil-based drug delivery. The TNF- $\alpha$  levels were also significantly increased in the LPS-injected leg of all the control groups, but not in the MTX/liposome-neutrophil group, which further confirms that only the MTX-liposome/neutrophil treatment resulted in beneficial effects (Figure 4.13b). However, the TNF- $\alpha$  levels did not increase as high as the IL-6 levels after LPS injection, indicating that TNF- $\alpha$  is not an ideal marker in this model.

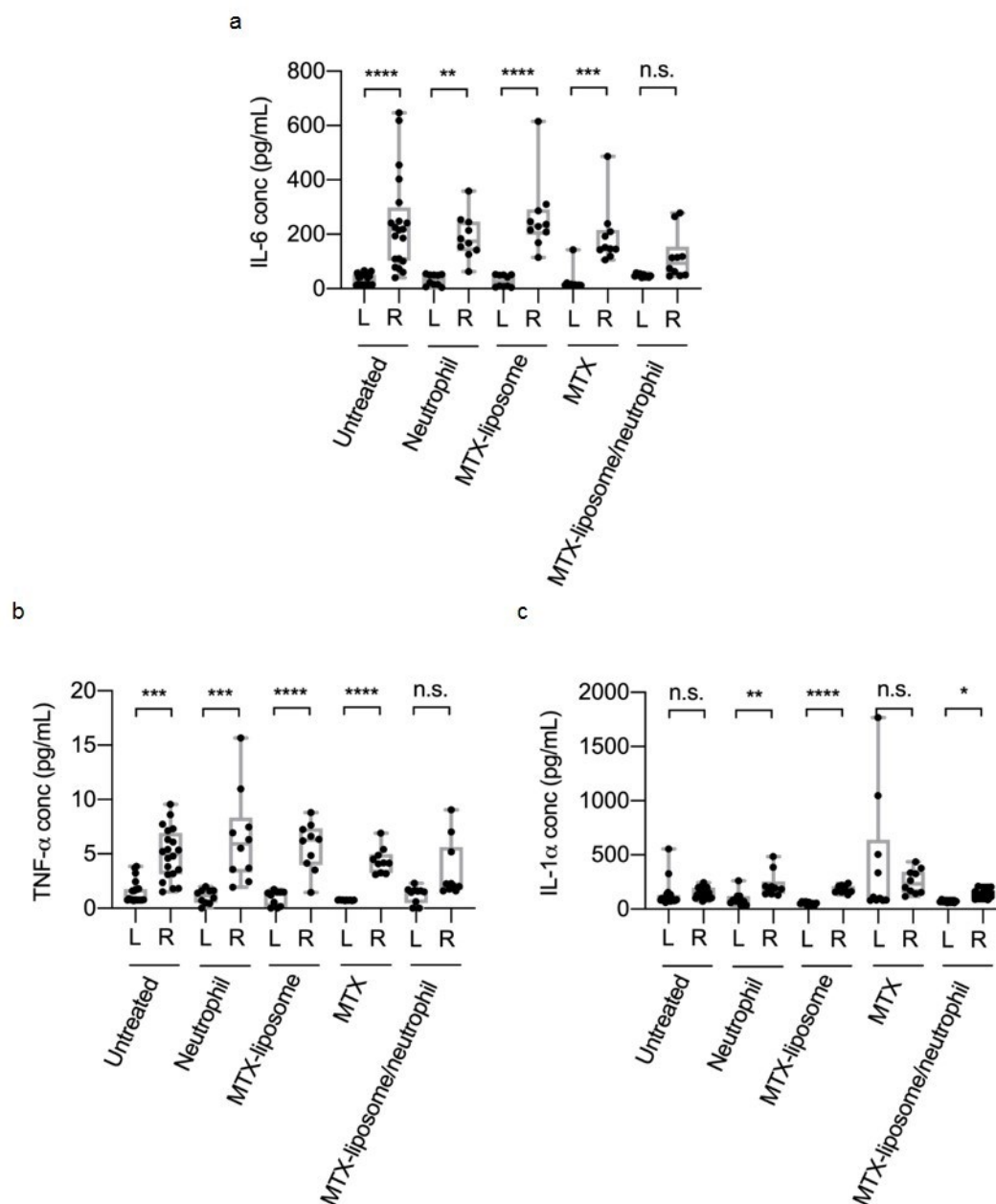


**Figure 4.13** Inflammatory cytokine levels in healthy quadriceps and LPS-injected quadriceps after different treatments measured by ELISA assay. **a**, IL-6 levels **b**, TNF- $\alpha$  levels and **c**, IL- $\alpha$  levels in the healthy quadriceps and the LPS-injected quadriceps after different treatments. Centre line, the median; box limits, upper and lower quartiles; whiskers, minimum and maximum values. \* $P < 0.05$ , \*\* $P < 0.01$ , \*\*\* $P < 0.001$ , \*\*\*\* $P < 0.0001$ , Kruskal-Wallis, Corrected Dunn's post hoc test.  $n = 20$  in the untreated group,  $n = 10$  in other treated groups.

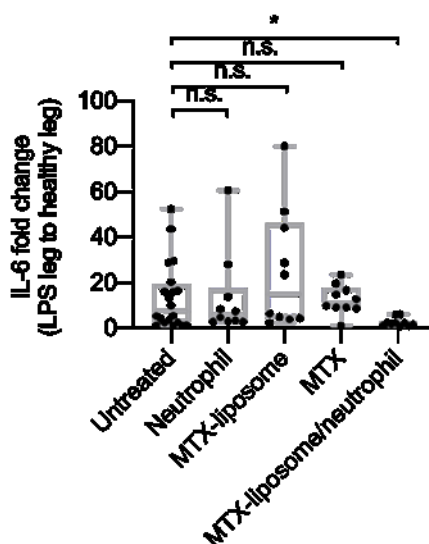


**Figure 4.14 IL-6 levels in inflamed versus healthy quadriceps after different treatments.** Fold-change of IL-6 expression level in LPS injected versus non-injected quadriceps. Centre line, the median; box limits, upper and lower quartiles; whiskers, minimum and maximum values,  $n = 20$  in the untreated group,  $n = 10$  in other treated groups. \* $P < 0.05$ , \*\* $P < 0.01$ , Kruskal-Wallis, Corrected Dunn's post hoc test.

Significant reduction of the cytokines IL-6 and TNF- $\alpha$  achieved with the MTX-liposome/neutrophil delivery system is a promising steppingstone to realise a new type of treatment for inflammatory diseases. Suppression of pro-inflammatory cytokine levels in inflamed tissue has already been shown by others to be essential in treating inflammatory diseases. In a study reported by *Bartlett et al*, thermosensitive nanoparticles formulated by 2-acrylamido-2-methyl-1-propanesulfonic acid and poly(N-isopropylacrylamide) were used to load anti-inflammatory cell-penetrating peptides (CPPs) *via* electrostatic interactions.<sup>333</sup> The passive loading of the CPPs can easily be controlled by tuning particle swelling at different temperatures. The anti-inflammatory CPP loaded nanoparticles were then intra-articularly injected to an inflamed cartilage plug and a significant reduction of IL-6 production was observed after 6 d. These results indicate that IL-6 is a potential target for the treatment of osteoarthritis. In another study of MI, a DNA enzyme deoxyribozyme that can silence TNF- $\alpha$  expression in cells was functionalised on the surface of gold nanoparticles.<sup>334</sup> The gold nanoparticles were shown to help deoxyribozyme escape from endosomes to achieve efficient silencing. After injecting the deoxyribozyme loaded gold nanoparticles directly into the ischemia area of the MI heart, the level of TNF- $\alpha$  mRNA was significantly reduced in the LV. Reduced cellular infiltration and cell death in the MI heart shown by



immunohistochemistry also confirmed the anti-inflammatory effect of the deoxyribozyme loaded gold nanoparticles. Furthermore, TNF- $\alpha$  silencing improved ejection fraction (EF) and fractional shortening (FS) of the MI heart 3 d after injection. Thus, suppression of TNF- $\alpha$  expression is an effective treatment for MI. These findings support that TNF- $\alpha$  and IL-6 play a vital role in the pathological processes of many inflammatory diseases, and suppression of these two pro-inflammatory cytokine levels in the inflamed tissue is an effective approach to treat inflammatory diseases.

Liposomes have also been used as drug carriers to target inflamed tissue by conjugating targeting molecules to the liposome surface. Koning *et al.* reported that arginine–glycine–aspartic acid (RGD) conjugated liposomes can target angiogenic vascular endothelial cells at the site of inflammation by binding to  $\alpha\beta 3$  integrins expressed on the cell surface.<sup>169</sup> After loading liposomes with dexamethasone phosphate and *i.v.* injection to rats with adjuvant-induced arthritis, disease development was significantly delayed and lower arthritis severity was detected after treatment.<sup>169</sup> In another study, HAP-1 (SFHQFARATLAS), a peptide with high specificity for fibroblast-like synoviocytes, was conjugated to PEGylated liposomes to target the inflamed joint of arthritis rats.<sup>335</sup> A significant reduction in joint swelling and inflammatory cell infiltration was observed in the inflamed joint after *i.v.* injection of prednisolone phosphate loaded HAP-1-liposomes. These studies demonstrated targeted liposome delivery systems for the treatment of inflammatory diseases. In this study, instead of using chemical engineering to conjugate targeting molecules on the liposome surface to achieve active targeting, neutrophils were employed as the cell carrier to transport MTX-liposomes to the inflamed tissue by leveraging intrinsic functions of neutrophils that migrate to the inflammatory site. The neutrophil-mediated drug delivery system is also flexible; it allows to load different types of nanoparticles into neutrophils and different types of anti-inflammatory drugs loaded inside the nanoparticles. Moreover, considering several sensors and feedback pathways involved in the dynamic process of inflammation, neutrophils can respond to various inflammation pathways. However, simpler liposome-based drug delivery systems usually only sense and target one inflammation pathway, which may result in a suppressed host defence or induce compensatory pro-inflammatory responses *via* other pathways.

Taken together, the *in vivo* migration and treatment studies of the neutrophil-mediated MTX-liposome delivery system in the LPS-injury skeletal muscle model demonstrated that loaded neutrophils can migrate to inflamed target tissue *in vivo*. Upon arrival in the inflamed tissue, neutrophils release the drug-loaded liposomes causing the intended anti-inflammatory treatment effect. Not all of the liposomes delivered *via* neutrophils end up in the target tissue (Figure 4.11), but the treatment results showing significant reduction of inflammatory cytokines in the inflamed muscle only *via* neutrophil-based delivery, suggests that even a low delivery efficiency can significantly improve anti-inflammatory therapies using the cell-based delivery system compared to free drug or drug-loaded liposomes.

#### 4.3.4. *In vivo* improvement of cardiac function *via* neutrophil-mediated delivery in the myocardial IRI model

Given the anti-inflammatory treatment effect of the MTX-liposome/neutrophil system demonstrated in the LPS-injury skeletal muscle model, the myocardial IRI model was subsequently employed to further investigate the versatility of neutrophil mediated delivery. Myocardial IRI is the leading cause of death and disability in the world. Compared to the LPS-injury skeletal muscle model, the myocardial IRI model is an inflammatory disease model with longer disease progression period and higher relevance to human diseases, with functional readouts to further test the delivery efficacy of the liposome/neutrophil system. MTX used in this study has also previously been reported to reduce cardiovascular morbidity and mortality in patients with autoimmune diseases and cardiovascular diseases (low dose from 7.5 to 15 mg weekly).<sup>336,337</sup> In experimental models, MTX treatment reduced the infarct size and improved cardiac function of the hearts with IRI.<sup>338</sup> For example, MTX encapsulated lipid core nanoparticles realised a 40% improvement of systolic functions and a significant reduction of cardiac dilation in a rat model of MI after intraperitoneal administration.<sup>168</sup> However, the use of MTX for the treatment of cardiovascular diseases is limited by its potential severe side effects (see Chapter 1 section 1.1.2) and invasive administration routes. In most animal studies, effective MTX treatments are usually seen using intraperitoneal or intramyocardial injection,<sup>168,339</sup> which is difficult to achieve in patients. Thus, myocardial IRI model is a valid model to investigate MTX delivery efficacy using the neutrophil-mediated delivery system via a simple *i.v.* injection.

To this end, the transient MI surgery was performed on mice to induce IRI, followed by *i.v.* injection of MTX-liposome/neutrophils after 24 h reperfusion (Figure 4.15). The mice with myocardial IRI without treatment served as the control group. Due to the time-consuming nature of these experiments and the requirement of high *n* numbers, free MTX and MTX-liposomes were not tested in this model. However, in the LPS-injury mouse model (chapter 4 section 4.3.3) the results showed that these two control groups did not achieve down-regulation of inflammation at an equivalent dose (2  $\mu$ g MTX) compared to the MTX-liposome/neutrophils, which was the only group achieving a therapeutic effect. 2D Echocardiography was performed 24 h after surgery to record the initial heart damage after the surgery and it was subsequently used to assess cardiac function after treatment. 4 weeks after treatment, two different assessment methods, 2D echocardiography and PV loop were applied to measure cardiac function in the mice of the two groups. Hearts were then collected for histology to determine fibrotic tissue using Sirius red staining.

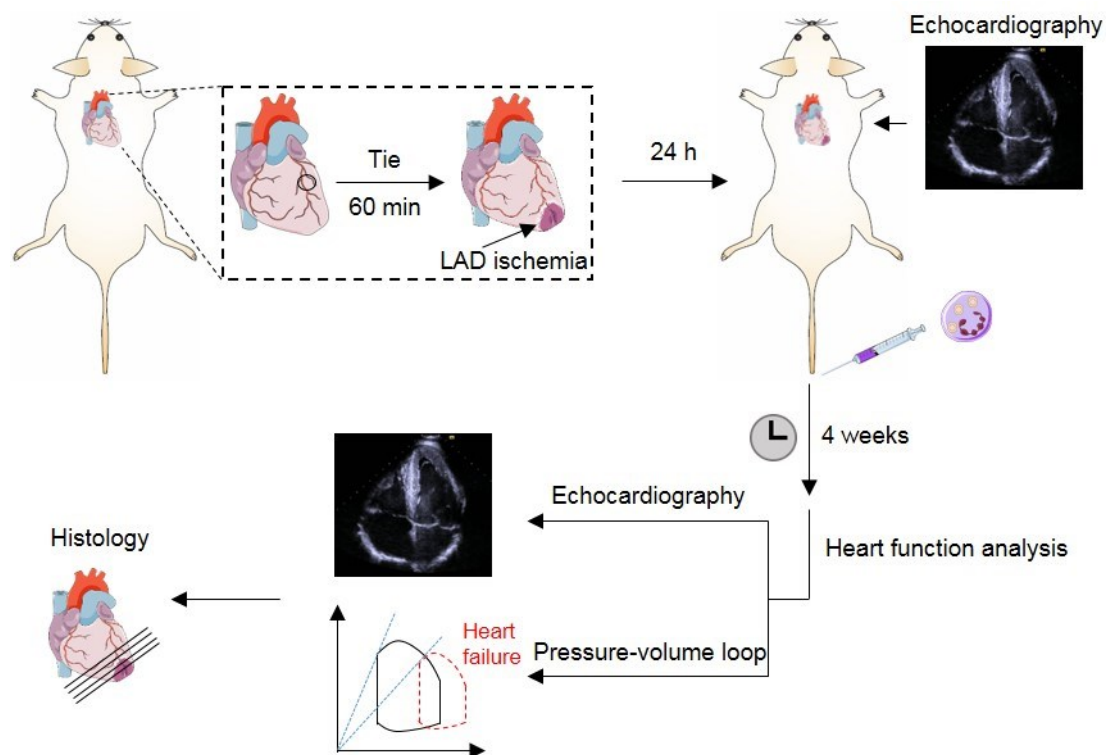


**Figure 4.15 Schematic illustration of myocardial IRI surgery and subsequent treatment.** LAD was ligated for 60 min to induce transient MI, after which the ligating suture was loosened to allow for reperfusion. MTX-liposome/neutrophils were injected intravenously after 24 h reperfusion and cardiac function was measured using 2D echocardiography. After 4 weeks, cardiac function was measured again using two different methods, 2D echocardiography and PV loop. Hearts were collected for histology analysis. The graphics of hearts were adapted

from the Servier Medical Art website. The echocardiography image was adapted from PeaceHealth.

#### 4.3.4.1 Histology of injured hearts

Collagen formation plays an important role in the pathogenesis of different cardiac diseases. One of the most widely used approaches to visualise collagen is to stain histological tissue with Sirius red.<sup>340</sup> All the hearts were imaged in dorsal, lateral and ventral view before embedding for the histology assessment. As shown in Figure 4.16, the infarct area can be identified as a whitened area in the LV wall below the ligation. However, some hearts from either group did not show obvious infarct areas. IRI is induced by transient MI, which is milder compared to permanent MI injury that can cause a large infarct area. As such, it was not easy to identify the infarct area in every IRI heart.

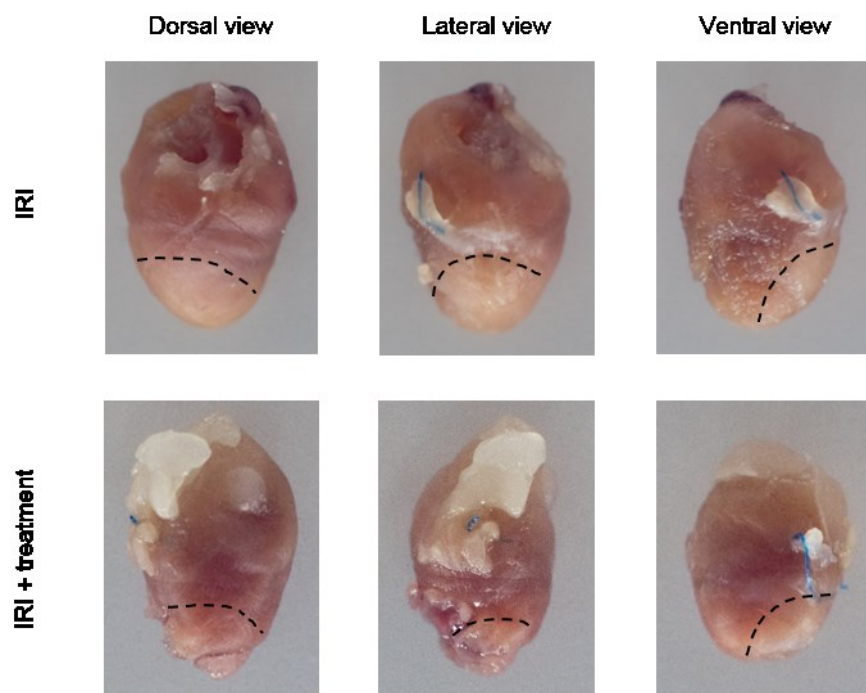


**Figure 4.16** Images of IRI hearts with/without the treatment after PFA fixation. Representative images in dorsal, lateral and ventral view of the IRI hearts with/without the MTX-liposome/neutrophil treatment 4 weeks post treatment.

Upon cardiac cell death, dead cardiomyocytes are replaced by collagen, which is also called reparative fibrosis process.<sup>341</sup> To maintain good cardiac function, it is important to reduce fibrosis with minimum collagen deposition after myocardial IRI. To determine collagen

deposition in the IRI hearts after the MTX-liposome/neutrophil treatment, all the hearts were embedded, sliced and stained with Sirius red to visualise the collagenous areas that will be stained in red. To accurately quantify the collagen percentage for each heart, sections from apex to the level of LAD ligation were collected to represent the severity of cardiac fibrosis. Figure 4.17 and Figure 4.18 show representative brightfield images of 6 serial sections of the hearts from the IRI group and the IRI + treatment group respectively. Within each group, the size of the collagen areas varied a lot between different hearts; for example, in the IRI group, collagen areas in different levels of the heart from mouse 2 were much larger than those areas in the heart of mouse 3. There were no significant differences observed from the images between the IRI group and the IRI + treatment group due to this large variation. ImageJ was then used to quantify the collagen percentage at each level of each heart by calculating the ratio of the collagen area to the whole tissue area to show the extent of fibrosis. In this case, only 3 sections from level 4 to level 6 of each heart were selected for quantification due to a lot of broken sections from level 1 to level 3. In Figure 4.19, no significant difference was found for each level between the IRI group and the IRI + treatment group, suggesting that the MTX-liposome/neutrophil treatment was not able to minimise cardiac tissue death. Next, echocardiography and PV loop analysis is discussed to explore whether the MTX-liposome/neutrophil treatment can improve cardiac function of the IRI heart.

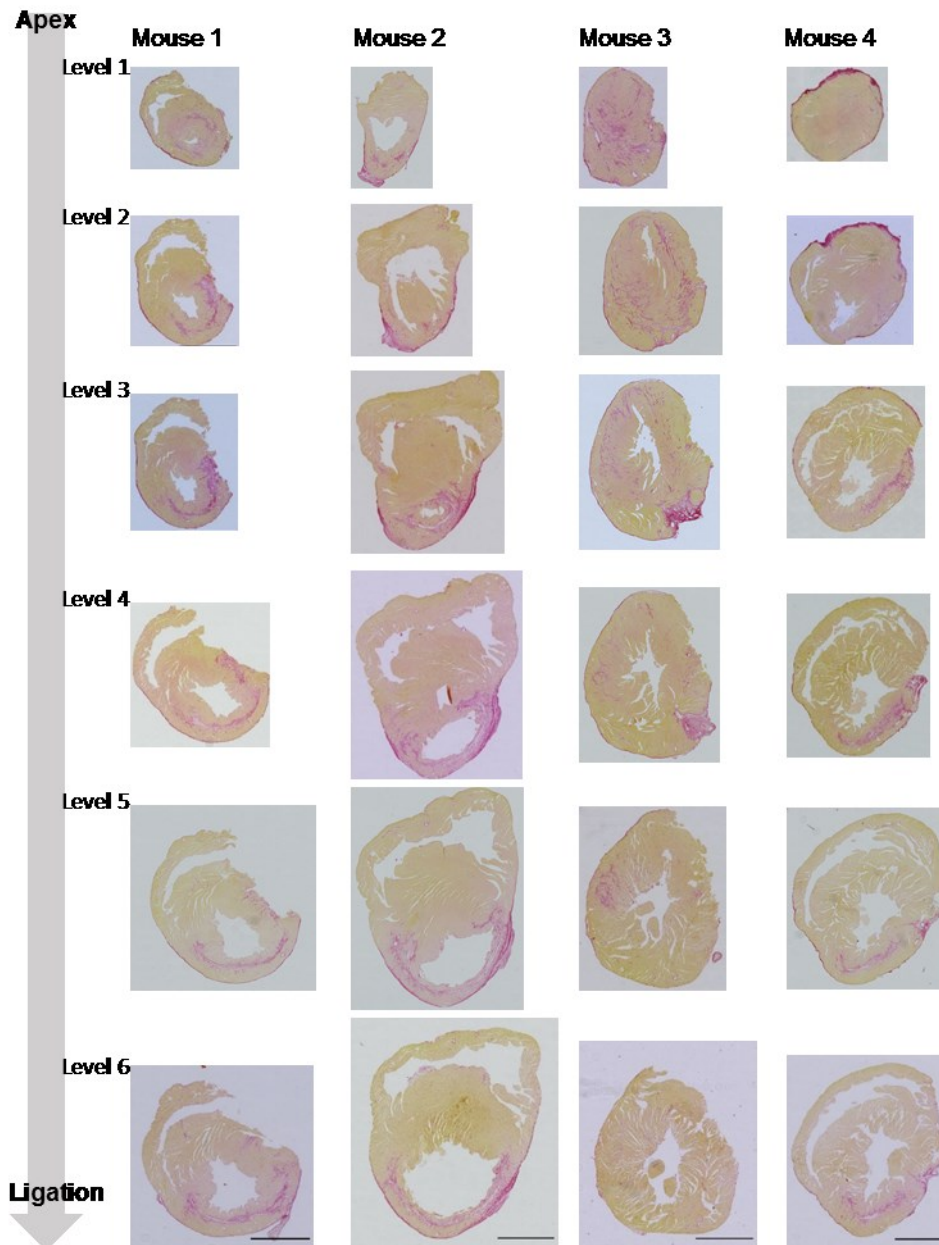


**Figure 4.17** Representative brightfield images of Sirius red stained slices from the IRI group. Serial transversal sections of the cardiac tissue sliced from Apex to the LAD ligation of the heart. Sirius red staining; yellow shows cardiac tissue, red shows collagen. Scale bars = 1mm. The specimen collection and staining were performed by Miss Lorraine Lawrence (National Heart and Lung Institute, Imperial College London).

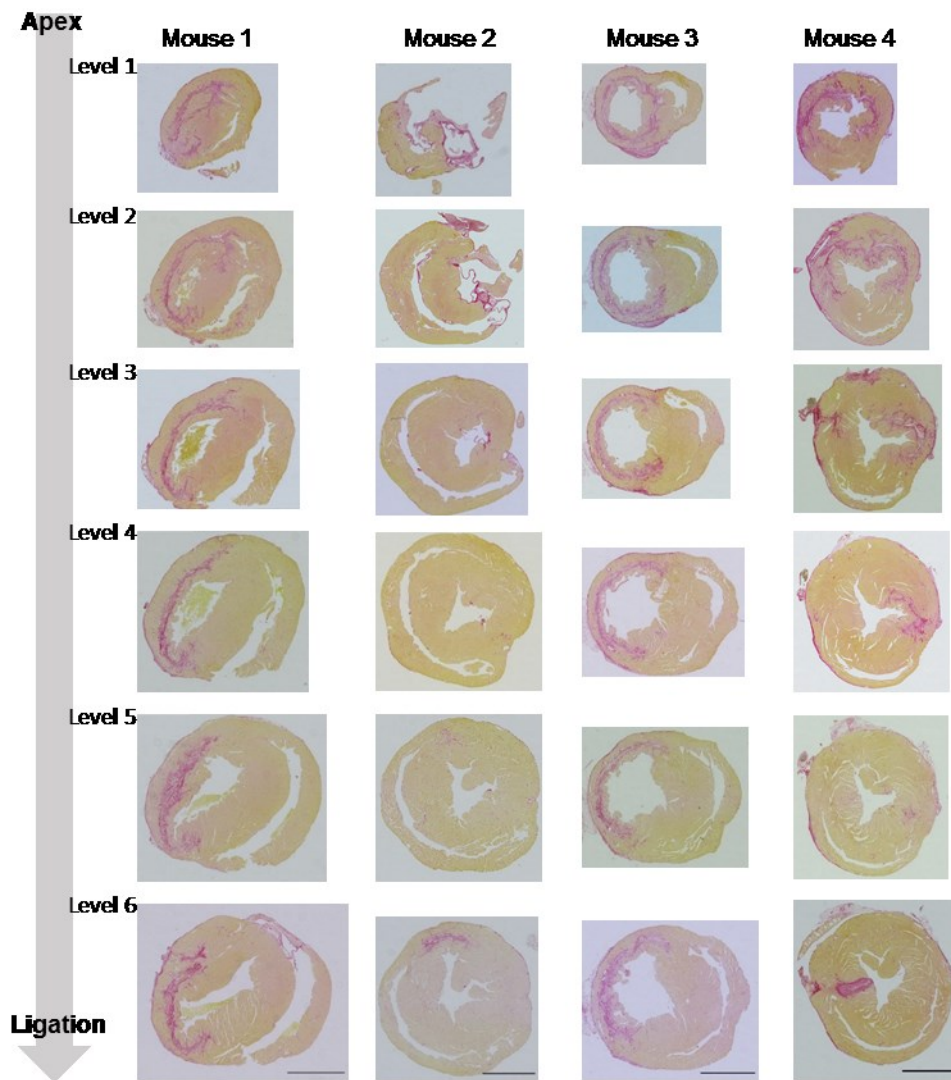


**Figure 4.18** Representative brightfield images of Sirius red stained slices from the IRI + treatment group. Serial transversal sections of the cardiac tissue sliced from Apex to the LAD ligation of the heart. Sirius red staining; yellow shows cardiac tissue, red shows collagen. Scale bars = 1mm. The specimen collection and staining were performed by Miss Lorraine Lawrence (National Heart and Lung Institute, Imperial College London).



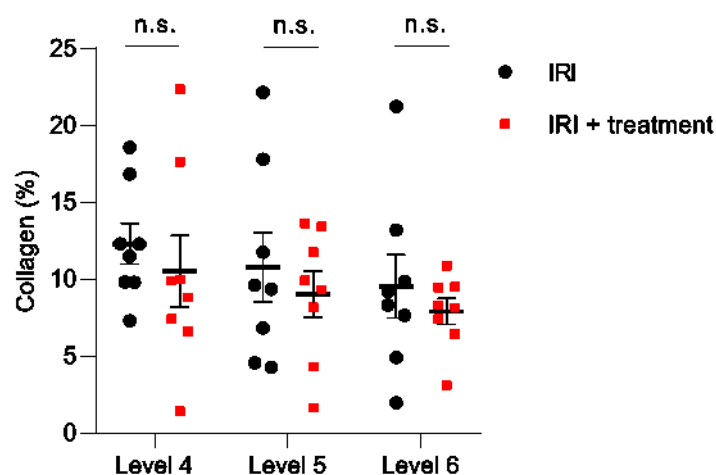


**Figure 4.19 Quantification of collagen deposition in histological slices at different levels.** Collagen percentage (%) following myocardial IRI with/without the treatment 4 weeks post treatment (representative images shown in Figure 4.26 and Figure 4.27). Data are presented as mean  $\pm$  s.e.m.,  $n = 8$ . Two-way ANOVA, Bonferroni multiple comparison test.

#### 4.3.4.2 Echocardiography analysis

Echocardiography is a widely used assessment in cardiology to measure load-dependent parameters of cardiac structure and function. It uses sound waves to create real-time images of the heart, which can be used to quantify the heart structure (*e.g.* chamber size and wall thickness) and estimate heart function (*e.g.* cardiac output and ejection fraction). The biggest advantage of echocardiography is that it is a non-invasive assessment, thus allowing multiple measurements at different timepoints during a study. In this study, echocardiography was first applied after 24 h reperfusion (pre-treatment timepoint) to ensure initial cardiac damage caused by the transient MI surgery, and was applied again at 4 weeks (4 weeks timepoint) after MTX-liposome/neutrophil injection to determine whether the treatment improved cardiac structure and function.

Firstly, no differences were found in body weight between the IRI group and the IRI + treatment group at both timepoints (Figure 4.20a), which indicates that all the mice had similar morphometric characteristics when hemodynamics were measured. To determine whether the IRI surgery was successful, ejection fraction (EF) was recorded 24 h after surgery. EF is one of the most common indices of cardiac contractility used in cardiac studies; it measures how much blood inside the left ventricle (LV) is squeezed out at each contraction.



The normal EF of a healthy heart is usually above 55%,<sup>342</sup> while reduced EF (50% or less) was observed after 24 h reperfusion (pre-treatment timepoint) in mice from both groups (Figure 4.20b), indicating successful cardiac damage in all the mice after the transient MI surgery. 4 weeks post treatment, the change in EF was not significantly different between the IRI group and the IRI + treatment group (Figure 4.20c) while a slight increase can be seen in the IRI + treatment group, which suggests that MTX-liposome/neutrophil injection might increase the pumping efficiency of the IRI heart. However, with the current group size it is hard to conclude the beneficial effect. Hence, more mice are needed for further validation. Another index of muscular contractility, fractional shortening (FS) measures the percentage change in LV diameter during systole. Comparing the change in FS between both groups, the treatment significantly improved FS of the IRI hearts after 4 weeks (Figure 4.20d), indicating improved cardiac contractility of the injured hearts after injection of MTX-liposome/neutrophils. Thus, EF and FS results suggest the improved ability of the IRI heart to squeeze more blood at systole after the MTX-liposome/neutrophil treatment.

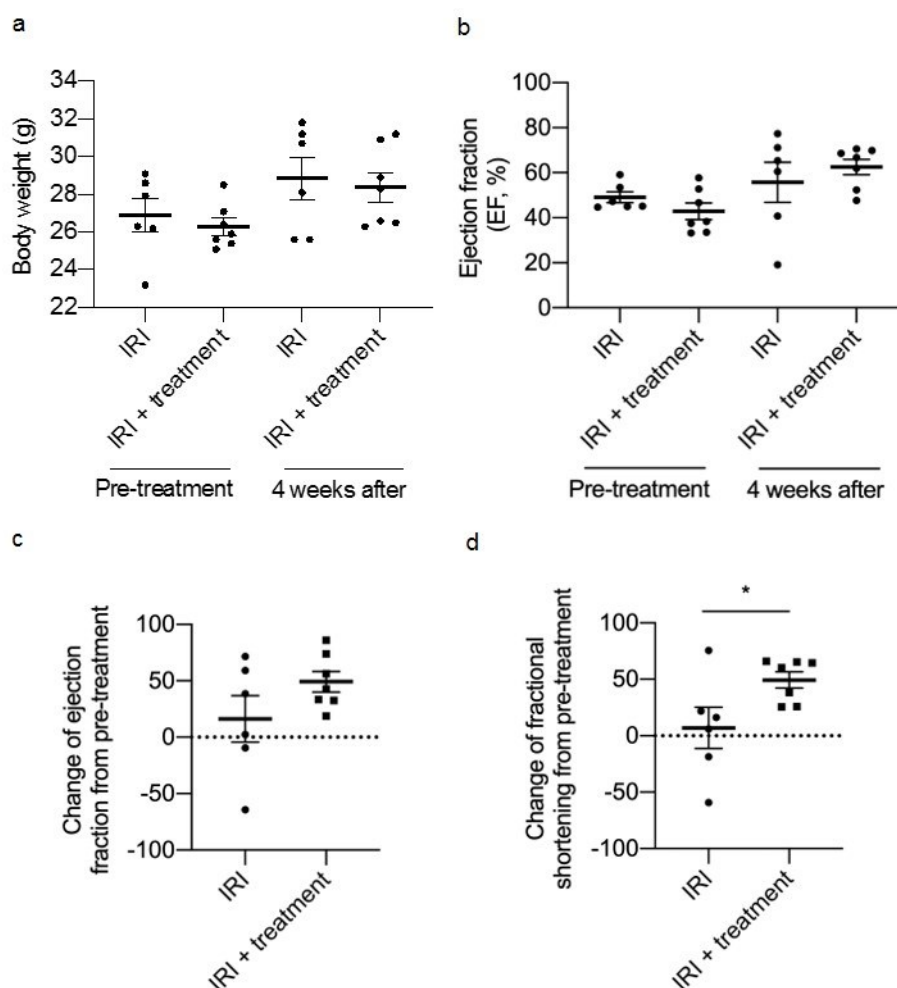


**Figure 4.20** Graphic representation of body weight and muscular contractility related parameters. **a**, Body weight (g). **b**, Ejection fraction (%). **c**, Percentage change in ejection fraction (EF) at the 4 weeks timepoint compared with the pre-treatment timepoint. **d**, Percentage change in fractional shortening (FS) at the 4 weeks timepoint compared with the pre-treatment timepoint. Data shown as mean  $\pm$  s.e.m., \* $P < 0.05$ , unpaired Student's *t*-test,  $n = 7$ .

Furthermore, systolic and diastolic parameters related to heart dimensions were measured using echocardiography: (1) LV posterior wall, (2) LV anterior wall, (3) LV volume, and (4) LV intraventricular cavity. There were no significant differences in the changes of all the dimension related parameters in both groups (Figure 4.21). The change of LV mass was also similar in both groups (Figure 4.22a). These results suggest that the MTX-liposome/neutrophil treatment did not alter the heart structure.

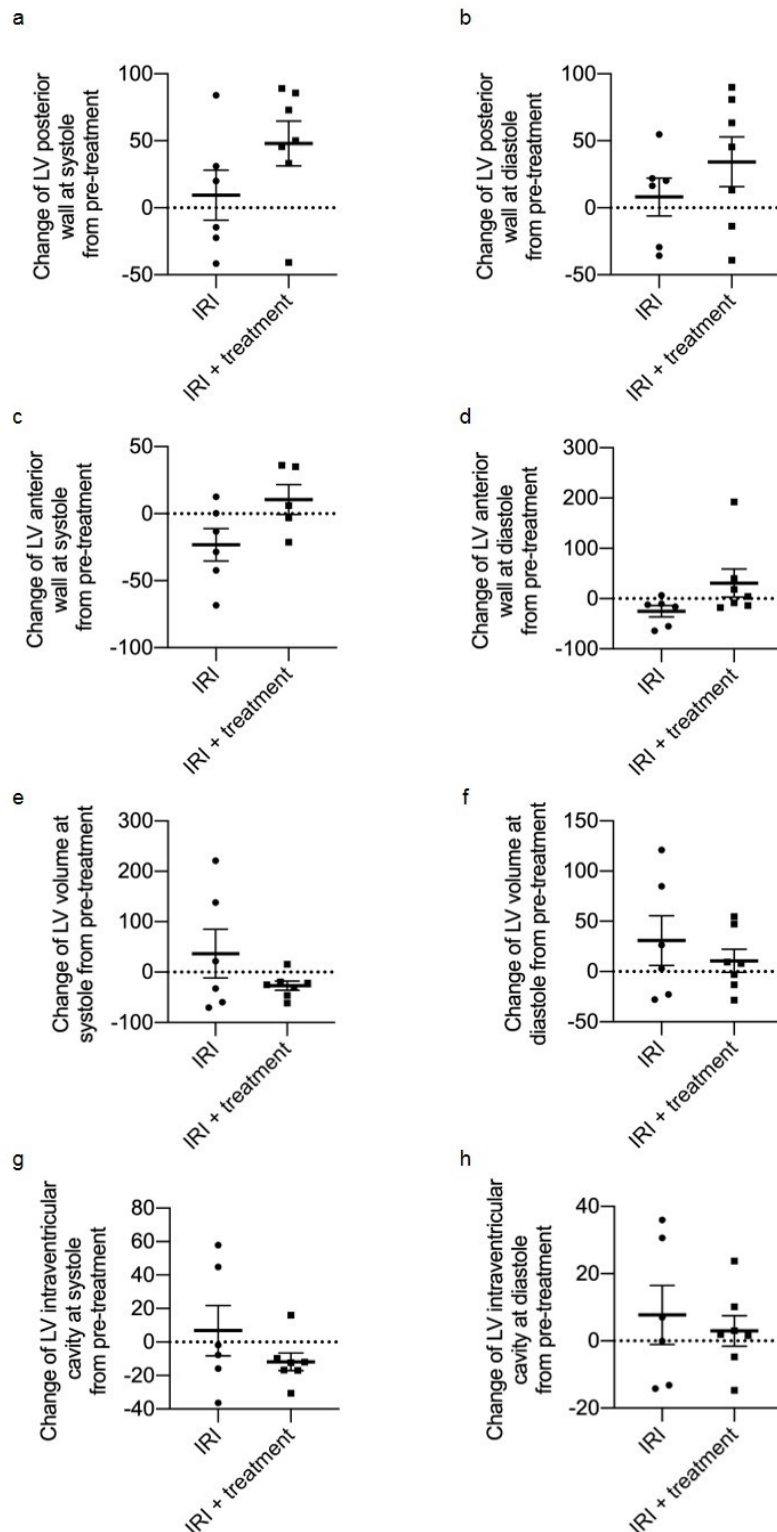


**Figure 4.21** Graphic representation of heart dimension related parameters. Percentage change in **a**, LV posterior wall at systole; **b**, LV posterior wall at diastole; **c**, LV volume at systole; **d**, LV volume at diastole; **e**, LV intraventricular at systole; **f**, LV intraventricular at diastole at the 4 weeks timepoint compared with the pre-treatment timepoint. Data shown as mean  $\pm$  s.e.m., \* $P < 0.05$ , unpaired Student's *t*-test,  $n = 7$ .

There were also no significant differences observed in heart rate, cardiac output (the measurement of the volume of blood being pumped by the heart per minute) and stroke volume (the measurement of the volume of blood squeezed out from each ventricle) in both groups (Figure 4.22b-d), which agrees with EF showing that the MTX-liposome/neutrophil treatment did not significantly improve the pumping efficiency of the injured hearts.

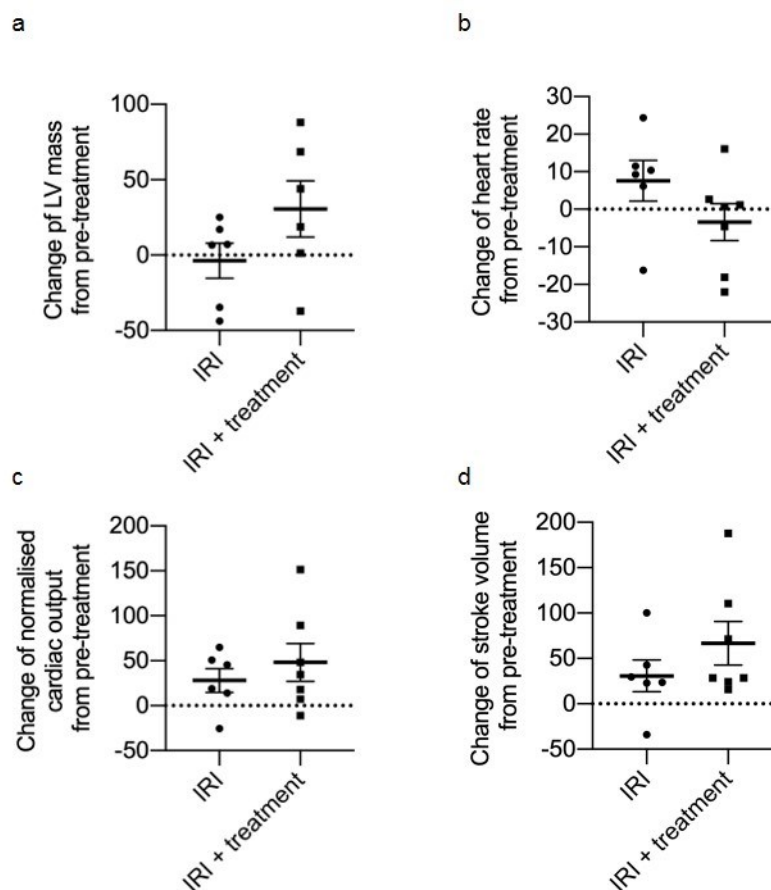


**Figure 4.22** Graphic representation of LV mass, heart rate, normalised cardiac output, and stroke volume. Percentage change in **a**, LV mass; **b**, Heart rate; **c**, Cardiac output normalised to body weight; **d**, Stroke volume at the 4 weeks timepoint compared with the pre-treatment timepoint. Data shown as mean  $\pm$  s.e.m., \* $P < 0.05$ , unpaired Student's *t*-test,  $n = 7$ .

Table 4-1 summarises all the cardiac parameters measured by 2D echocardiography in the IRI group and the IRI + treatment group at pre-treatment timepoint and 4 weeks timepoint.

Echocardiographic parameters	IRI		IRI + MTX-liposome/neutrophils	
	Pre-treatment (n = 6)	4 weeks (n = 7)	Pre-treatment (n = 6)	4 weeks (n = 7)
Ejection fraction (%)	49 ± 2	56 ± 9	43 ± 4	63 ± 3
Fractional shortening (%)	27 ± 1	29 ± 5	23 ± 2	35 ± 2
Stroke volume (mL)	31 ± 3	39 ± 4	28 ± 3	44 ± 3
LVAW;d (mm)	1.0 ± 0.1	0.7 ± 0.1	0.7 ± 0.1	0.8 ± 0.1
LVAW;s (mm)	1.4 ± 0.2	1.1 ± 0.2	1.0 ± 0.1	1.1 ± 0.1
LVID;d (mm)	3.9 ± 0.2	4.2 ± 0.2	4.0 ± 0.1	4.1 ± 0.2
LVID;s (mm)	2.9 ± 0.1	3.0 ± 0.4	3.1 ± 0.1	2.7 ± 0.2
LVPW;d (mm)	1.0 ± 0.1	1.0 ± 0.1	0.8 ± 0.1	1.0 ± 0.1
LVPW;s (mm)	1.2 ± 0.1	1.3 ± 0.2	0.9 ± 0.1	1.3 ± 0.1
LV Vol;d (μL)	64 ± 7	79 ± 11	66 ± 4	72 ± 7
LV Vol;s (μL)	33 ± 4	39 ± 13	38 ± 3	28 ± 5
LV mass corrected (mg)	134 ± 26	114 ± 9	91 ± 10	110 ± 9
Normalised cardiac output	0.6 ± 0.1	0.7 ± 0.1	0.5 ± 0.1	0.7 ± 0.1
Heart rate (bmp)	494 ± 30	526 ± 21	475 ± 40	450 ± 27

**Table 4-1 Cardiac parameters assessed through 2D echocardiography.** Summary of all cardiac structure and function parameters for two experimental group. Data shown as mean ± s.e.m. LVAW;d: left ventricle anterior wall at diastole; LVAW;s: left ventricle anterior wall at systole; LVID;d: left ventricle intraventricular wall at diastole; LVID;s: left ventricle intraventricular wall at systole; LVPW;d: left ventricle posterior wall at diastole; LVPW;s: left ventricle posterior wall at systole; LV Vol;d : left ventricle volume at diastole; LV Vol;s : left ventricle volume at systole. Dr. Mohamed Bellahcene performed echocardiography and data analysis (National Heart and Lung Institute, Imperial College London).

To summarise, 2D echocardiography results show that the MTX-liposome/neutrophil treatment significantly improved FS of the injured hearts after 4 weeks. However, the heart structure and pumping ability were not altered by the treatment.

#### 4.3.4.3 Pressure-volume loop analysis

Pressure-volume loop (PV loop) is the gold standard method to assess direct cardiac function, which uses a pressure-measuring catheter inserted into the ventricle to provide a real-time volume and micromanometer pressure signal. The major advantage of PV loop measurements is that it quantifies absolute volumes directly and enables the measurement of LV performance under load-independent conditions. In contrast, non-invasive methods

such as echocardiography rely on motion parameters that can be affected by loading conditions and result in the lack of specificity to the ventricle.<sup>343</sup> Thus, PV loop measurements have higher sensitivity compared to echocardiography. However, an important limitation of PV measurements is their invasive nature and mice must be sacrificed after the measurements.

In this study, PV loops were generated in mice at 4 weeks post MTX-liposome/neutrophil injection to assess different parameters of cardiac function. Mice with myocardial IRI without treatment served as the control group. All the comparisons were made between the two groups at the 4 weeks timepoint. Firstly, no significant differences were observed in body weight (Figure 4.20a) and tibia length (Figure 4.23) when comparing the IRI group and the IRI + treatment group, which indicates that all the mice had similar morphometric characteristics when hemodynamics were measured.

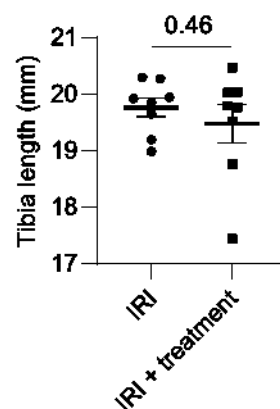


**Figure 4.23** Graphic representation of Tibia length (mm). Data shown as mean  $\pm$  s.e.m., unpaired Student's *t* test,  $n = 8$ .

Secondly, EF was shown to be slightly improved in the IRI + treatment group compared to the IRI group (Figure 4.24a). Particularly, the mean EF in the IRI group was below 50% after 4 weeks, which is still below the normal level of a healthy heart. Whereas in the IRI + treatment group, the mean EF was increased to 60% at 4 weeks after MTX-liposome/neutrophil injection, within the normal LV EF ranging from 55% to 70%. When comparing with other studies that obtained similar mean EF (about 60%) after the MTX-nanoparticle treatment, the MTX dose used in this study is 10 times lower.<sup>168</sup> There was already some indication that EF could be

improved in the MTX/liposome neutrophil treatment group from the echocardiography data (Figure 4.20c); this trend was confirmed with the PV loop data, however, due to the small number of animals in each group ( $n = 8$ ) and the large variation between individual animals, no statistically significant conclusions can be drawn at the moment. Continuation of these experiments is warranted given the promising trends observed. Usually, similar studies in IRI mice were conducted with group sizes of  $n > 12$ .

In general, reduced EF following myocardial IRI can be due to inadequate heart rate, excessive arterial load, insufficient chamber filling (diastolic functions), depressed systolic functions and cardiac tissue death. Therefore, any post-myocardial IRI treatment that can improve EF could potentially act through one or several of these pathways. An increase in the mean EF was observed after the treatment while heart rates were similar between both groups, which indicates that the MTX-liposome/neutrophil treatment did not improve EF through heart rate modulation (Figure 4.24b).

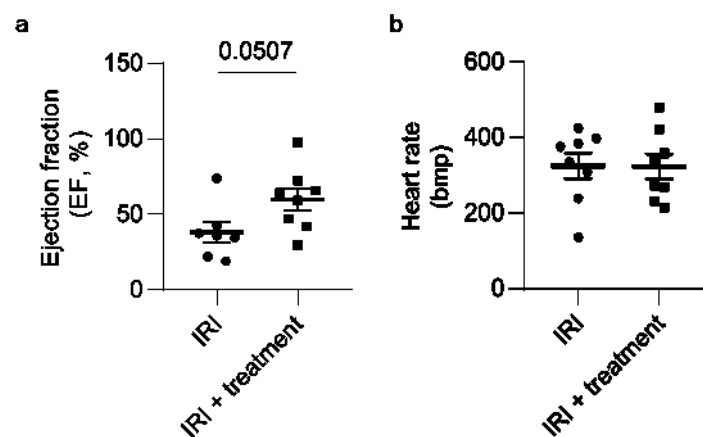


**Figure 4.24** Graphic representation of ejection fraction (EF in %) and heart rate (bpm). Data shown as mean  $\pm$  s.e.m., unpaired Student's *t* test.  $n = 8$ .

Next, arterial load related parameters including end-systolic volume, arterial elastance and mean arterial pressure were determined. End-systolic volume measures the volume of blood in the ventricle at the end of contraction. Figure 4.25a shows that the volume of blood present in the heart after contraction tends to be lower in mice from the IRI + treatment group, which suggests that during each cardiac contraction more blood was ejected from the heart in mice with myocardial IRI after the treatment. This result also agrees with improved EF, showing

increased pumping efficiency after the MTX-liposome/neutrophil treatment. Arterial elastance is defined as the ratio of pulse pressure variation and stroke volume variation and is an index of vascular resistance, providing a valid measurement of arterial load. Arterial elastance tends to be lower in the IRI + treatment group than the IRI group, which suggests a reduced vascular resistance in those treated mice compared to the untreated mice (Figure 4.25b). Mean arterial pressure is directly related to diastolic arterial pressure (DAP) and systolic arterial pressure (SAP), which is calculated as  $DAP + 1/3(SAP - DAP)$ . A slight decrease was also detected in the mean arterial pressure in the IRI + treatment group indicating reduced vascular tone, which agrees with reduced arterial elastance (Figure 4.25c, d, e). These findings suggest that improved EF might have resulted from reduced arterial load.

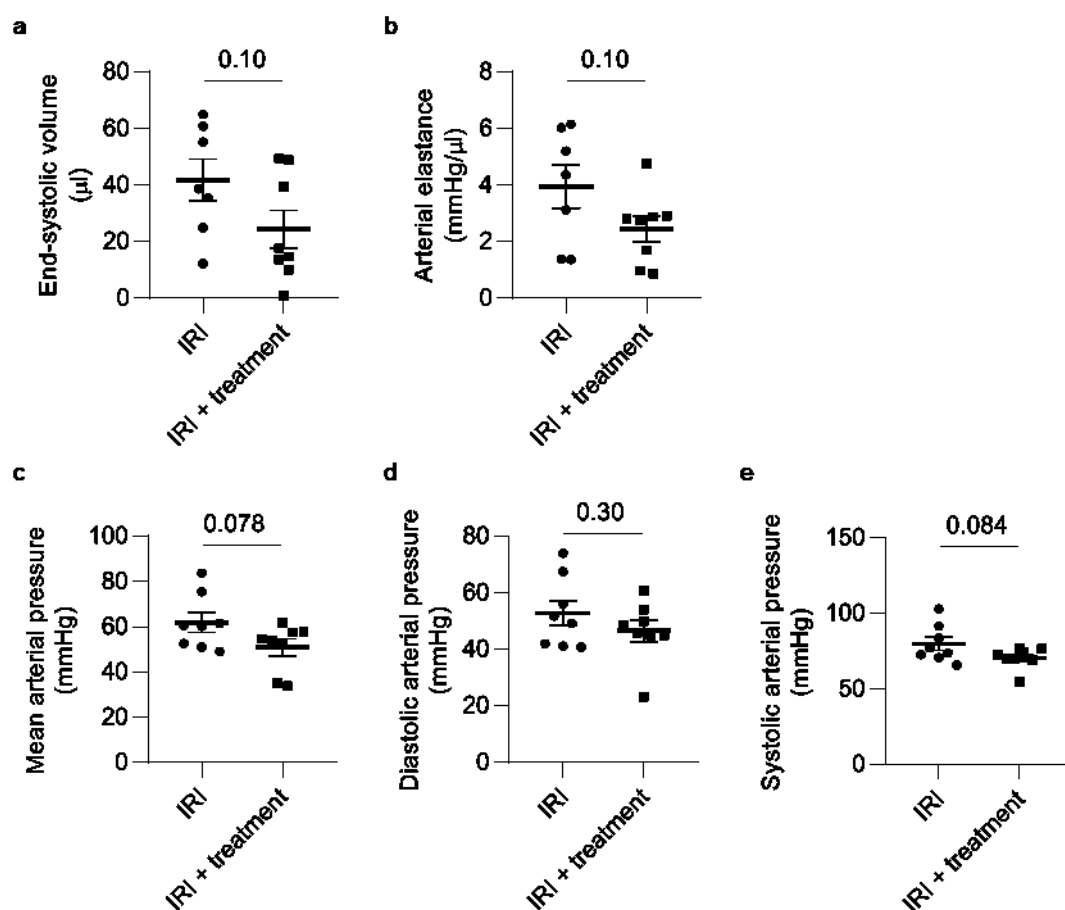


**Figure 4.25** Graphic representation of arterial load related parameters. **a**, End-systolic volume ( $\mu\text{L}$ ). **b**, Arterial elastance ( $\text{mmHg}/\mu\text{L}$ ). **c**, Mean arterial pressure ( $\text{mmHg}$ ). **d**, Diastolic arterial pressure ( $\text{mmHg}$ ). **e**, Systolic arterial pressure ( $\text{mmHg}$ ). Data shown as mean  $\pm$  s.e.m., unpaired Student's *t* test.  $n = 8$ .



Furthermore, diastolic function related parameters including end-diastolic volume,  $dP/dt$  min, LV end-diastolic pressure and Tau were measured to investigate whether increased EF is a result of improved diastolic functions. End-diastolic volume measures the volume of blood present in the heart at diastole, which was comparable between the two groups. It suggests that the MTX-liposome/neutrophil treatment did not modify chamber filling (Figure 4.26a). This conclusion is further confirmed by more diastolic function related parameters (Figure 4.26b, c and d).  $dP/dt$  min represents the minimum rate of pressure change in the ventricle, which was not different between the two groups. LV end-diastolic pressure measures the blood volume in the LV at the end of diastole, which was also similar in both groups. Time constant of LV relaxation during isovolumic diastole, Tau, indicates the rate of LV relaxation and was the same in the two groups as well. These results suggest that diastolic functions of the injured hearts were not altered by the MTX-liposome/neutrophil treatment.

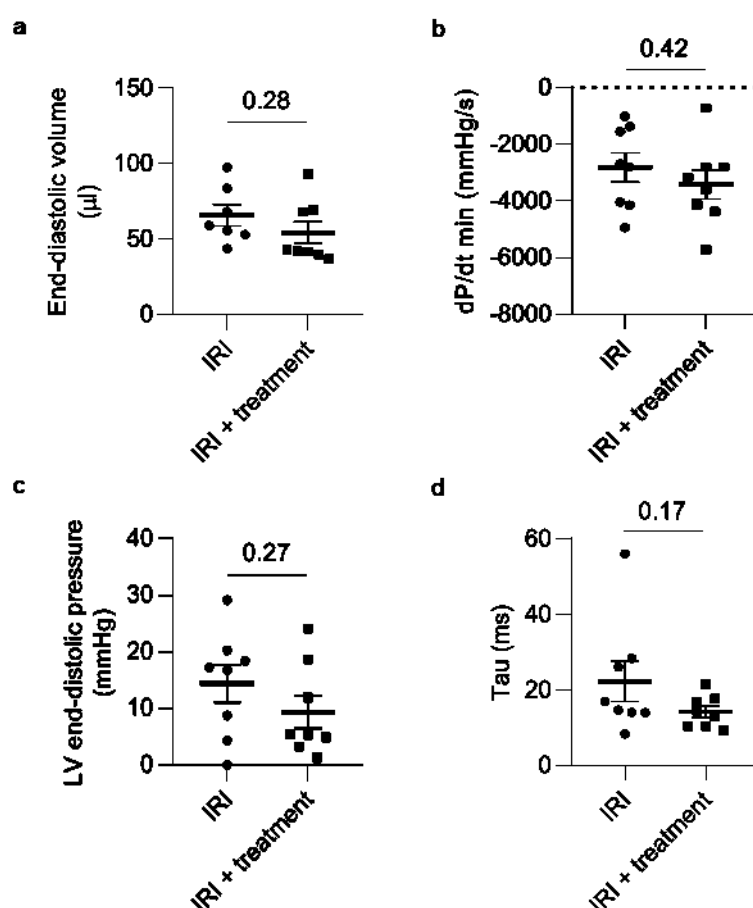


**Figure 4.26** Graphic representation of diastolic function related parameters. **a**, End-diastolic volume ( $\mu$ L). **b**,  $dP/dt$  min (mmHg/s). **c**, LV end-diastolic pressure (mmHg). **d**, Tau (ms). Data shown as mean  $\pm$  s.e.m., unpaired Student's *t* test.  $n = 8$ .

The systolic functions were also not improved by the MTX-liposome/neutrophil treatment as LV systolic pressure and dP/dt max were the same in both groups (Figure 4.27). dP/dt max represents the maximum rate of pressure change in the ventricle. These results confirm that there was no change in the systolic functions, indicating that the MTX-liposome/neutrophil treatment did not improve EF through enhanced systolic functions.

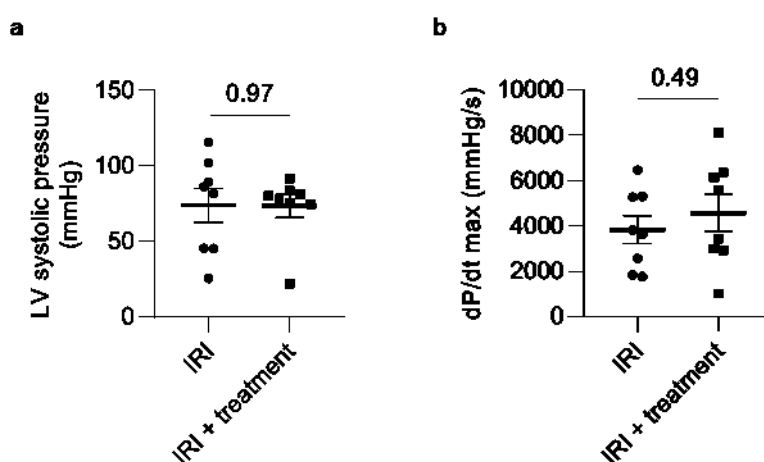


**Figure 4.27** Graphic representation of systolic function related parameters. *a*, LV systolic pressure (mmHg). *b*, dP/dt max (mmHg/s). Data shown as mean  $\pm$  s.e.m., unpaired Student's *t* test.  $n = 8$ .

Finally, EF is a load-dependent parameter. A big advantage of PV loop measurements is that in addition to all the load-dependent parameters discussed above, it is also possible to measure some load-independent parameters of systolic and diastolic functions including Ees, Eed, Ea/Ees and preload-recrutable stroke work. Ees represents the end-systolic elastance, which provides an index of myocardial contractility, while Eed represents end-diastolic elastance, which is an index of ventricular stiffness. The ratio of Ea/Ees represents the interplay between cardiac function and arterial system, which expresses the global cardiovascular efficiency. Preload-recrutable stroke work is determined as the relationship between stroke work and end-diastolic volume, which shows the severity of contractile dysfunction. All these four load-independent parameters were not changed after the MTX-liposome/neutrophil treatment, indicating that the treatment did not improve the systolic

and diastolic functions, which confirms the conclusions drawn from the load-dependent parameters (Figure 4.28).

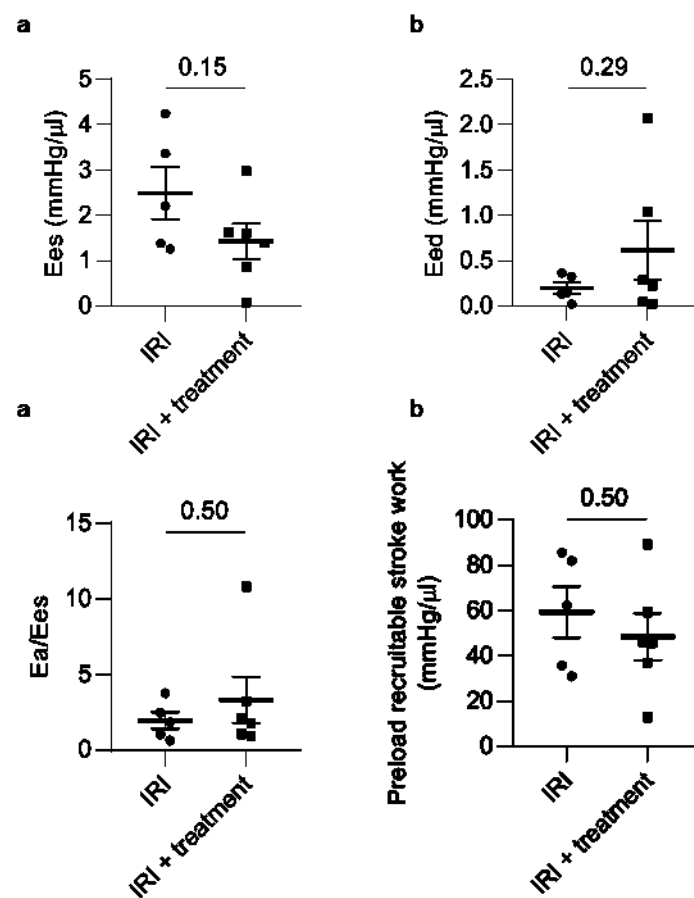


**Figure 4.28** Graphic representation of load-independent parameters. *a*, Ees (mmHg/ $\mu$ L). *b*, Eed (mmHg/ $\mu$ L). *c*, Ea/Ees. *d*, Preload-recruitable stroke work (mmHg/ $\mu$ L). Data shown as mean  $\pm$  s.e.m., unpaired Student's *t* test. *n* = 8.

A summary of all the cardiac parameters measured by PV loop assessment in the IRI group and the IRI + treatment group at 4 weeks timepoint are shown in Table 4-2.

PV loop parameters	IRI	IRI + treatment
	n = 5-8	n = 6-8
Tibia length (mm)	20 ± 0.2	19 ± 0.3
Ejection fraction (%)	38 ± 7	60 ± 7
Heart rate (bmp)	325 ± 34	324 ± 33
End-systolic volume (µL)	42 ± 7	24 ± 7
Arterial elastance (mmHg/µL)	4.0 ± 0.8	2.5 ± 0.4
Mean arterial pressure (mmHg)	62 ± 4	51 ± 4
End-diastolic volume (µL)	66 ± 7	54 ± 7
dP/dt min (mmHg/s)	-2813 ± 513	-3410 ± 514
LV end-diastolic pressure (mmHg)	14 ± 3	9 ± 3
Tau (ms)	22 ± 5	14 ± 2
LV systolic pressure (mmHg)	74 ± 11	74 ± 8
dP/dt max (mmHg/s)	3837 ± 613	4573 ± 828
Ees (mmHg/µL)	2.5 ± 0.6	1.4 ± 0.4
Eed (mmHg/µL)	0.2 ± 0.1	0.6 ± 0.3
Ea/Ees	1.9 ± 0.6	3.3 ± 1.5
Preload-recruitable stroke work (mmHg/µL)	59 ± 11	48 ± 10

**Table 4-2 Cardiac functions assessed through PV loop measurements.** Summary of all cardiac function parameters for the two experimental groups. Data shown as mean ± s.e.m. Dr. Mohamed Bellahcene performed PV loop measurements and data analysis (National Heart and Lung Institute, Imperial College London).

Overall, PV loop analysis suggests that the MTX-liposome/neutrophil treatment post myocardial IRI tends to improve EF *via* reducing arterial load (pressure), not through increasing heart rate and improving diastolic and systolic functions. A further possible pathway is that the treatment could have possibly improved EF by reducing cardiac tissue death, which has been discussed in section 4.3.4.1 showing no reduced cardiac tissue death after the treatment.

In most of the cardiac function parameters, only a slight increase or decrease was detected by echocardiography or PV loop measurements. The validity of the conclusions has to be verified by repeating the experiments using more mice in each group; there are usually at least 12 mice per group used for this model.<sup>168,344</sup> Therefore, big differences are not expected

in these parameters and the large variation between animals hinders drawing definite conclusions with the current group size. Another possible reason for not observing significant differences in most of the cardiac function parameters is that the injected dose of MTX (2  $\mu$ g per mouse) may not be sufficient to reduce cardiac damage in the myocardial IRI model. In this case, three strategies can be considered in the future to address this issue: 1), injecting a higher number of MTX-liposome/neutrophils; 2) using another nanocarrier that has higher stability and longer drug retention times than liposomes (*e.g.* polymersomes) to achieve a higher capacity of drug loading without affecting neutrophil viability and chemotaxis; 3) using another drug with better efficacy for cardio-protection. Nevertheless, in this study, the successful delivery of liposomes to the inflamed muscle and injured heart was achieved using the carrier neutrophils. Further, a significant reduction of inflammatory cytokines in the inflamed muscle (LPS-injury skeletal muscle model, see chapter 4 section 4.3.3) was only obtained *via* neutrophil-based delivery, suggesting that the neutrophil-based drug delivery system can improve anti-inflammatory efficiency compared to free drug or drug-loaded liposomes.

Several studies in the literature have also used the myocardial IRI model to determine the delivery efficacy of particle-mediated delivery systems to deliver anti-inflammatory drugs or cardio-protective drugs to the injured heart. Seshadri *et al.* reported a type of polyketal microparticles to deliver Cu/Zn superoxide dismutase (SOD1) to rat myocardium.<sup>339</sup> The formulated SOD1 loaded microparticles significantly down-regulated the superoxide level in macrophages, which is usually overproduced after myocardial IRI and results in a rapid death of cardiomyocytes and cardiac dysfunction. After intramyocardial injection, the SOD1 loaded microparticles significantly reduced early cardiomyocyte death and improved FS in the IRI heart. However, the process of intramyocardial injection is invasive as it requires incision to reach the myocardium in order to deliver the drug, which causes extra myocardial injury and is hard to translate to the clinic. Thus, many studies focused on developing targeted drug delivery systems that can be administrated in a non-invasive way. The passive targeting approach mainly relies on the increased microvascular permeability in the injured heart. Galagudza *et al.* reported that silica nanoparticles with a size between 6 nm to 13 nm can accumulate in the rat IRI heart after intravenous injection.<sup>345</sup> Moreover, after absorbing a cardio-protective agent adenosine on the particle surface, there was a further reduction of

infarct size observed compared to adenosine injection alone. The main disadvantages of this system are the slow biodegradation of silica nanoparticles. Another study investigated in detail the effect of nanoparticle size on the *in vivo* biodistribution in a mouse model of myocardial IRI.<sup>346</sup> Micelles with a size around 15 nm and liposomes with a size around 100 nm were both shown to accumulate in the IRI heart while no nanoparticles were observed in the healthy heart after intravenous injection. Interestingly, these two types of nanoparticles were found in different areas of the IRI heart, wherein liposomes were detected absorbing more to vessels, cardiomyocytes, and immune cells, micelles were only found adjacent to cardiomyocytes. This study suggests that micelles and liposomes are suitable nanocarriers for passive drug delivery to the injured heart. While liposomes and micelles were functionalised with PEG to increase blood circulation time, accumulation of these nanoparticles in the injured heart can only last for 3 h after administration. In this study, cationic liposomes, which did not accumulate in the inflamed tissue when using alone, can be carried by neutrophils to the inflamed muscle and injured heart and successfully mitigate inflammation (Figure 4.13).

Additionally, active targeting approaches have shown beneficial targeting effects and positive treatment outcomes in myocardial IRI models. By attaching anti-myosin antibodies to the surface of ATP-loaded liposomes, a further improvement of systolic and diastolic functions in the IRI heart was achieved compared to non-functionalised ATP-loaded liposomes.<sup>347</sup> In a rat model of MI, the targeting molecule anti-P-selectin was conjugated to vascular endothelial growth factor (VEGF) encapsulated liposomes to selectively target the surface of dysfunctional endothelium. A significant increase in FS and improved systolic functions were observed in the MI heart after *i.v.* injection of targeted VEGF encapsulated liposomes whereas non-targeted VEGF encapsulated liposomes failed to improve any cardiac functions.<sup>348</sup> These findings suggest that chemically conjugating targeting molecules to the nanoparticle surface can achieve better targetability upon systemic administration. However, this strategy sometimes requires complex chemical reactions and could lead to non-homogenous surface ligand density.<sup>349</sup>

In this study, instead of relying on chemical engineering to conjugate receptor targeting molecules on the nanocarrier surface to achieve active targeting, an immune cell-mediated drug delivery system was employed. The inherent properties of neutrophils were leveraged to realise local delivery of nanoparticles to the injured heart in a non-invasive way. After

intravenous injection, *ex vivo* isolated neutrophils successfully delivered loaded liposomes to the IRI heart. When loading this system with MTX, a significant improvement of FS was observed in the IRI heart measured by echocardiography at 4 weeks after MTX-liposome/neutrophil injection. EF was also shown to be slightly increased when assessed by PV loop measurements. These results support the idea that neutrophils can be an ideal cell carrier to deliver nanoparticles to the site of inflammation and achieve positive outcomes in the treatment of inflammatory diseases when loaded with anti-inflammatory therapeutics. More importantly, considering the specific challenges for anti-inflammation therapy discussed in section 1.3.6, neutrophils have their inherent properties to respond to a few sensors and feedback pathways involved in the dynamic inflammation process. The amount and timeframe of neutrophil recruitment to the site of inflammation is determined by the severity of inflammation, thus allowing to deliver different amounts of the drug to alter the balance of pro- and anti- inflammation. In contrast, nanoparticle-based drug delivery systems usually sense and target one inflammation pathway, which may result in a suppressed host defence or induce a compensatory pro-inflammation response *via* other pathways.<sup>225</sup>

## 4.4 Conclusions

The work presented in this chapter demonstrated the treatment effects of the MTX-liposome/neutrophil system in two different mouse models of inflammation. The LPS-injury skeletal muscle model represents acute inflammation in the tissue, whilst the myocardial IRI model is a human-disease (MI) relevant model of inflammation associated with organ diseases.

LPS was injected intramuscularly to induce damage in the quadriceps of mice. Isolated neutrophils were injected intravenously to these LPS-injected mice. The injected neutrophils were detected only in the LPS-injected quadriceps at 1 h and 2 h post neutrophil injection. Meanwhile, the injected neutrophils were also only observed in the blood at 1 h and 2 h timepoints but disappeared at the 4 h timepoint. These results suggest that isolated and reinjected neutrophils can respond to inflammatory signals in the blood and migrate to the inflamed muscle within 2 h after injection. After loading the neutrophils with liposomes *ex vivo*, liposome-positive injected neutrophils were detected and co-localised in the LPS-injected quadriceps while there were no liposome-loaded neutrophils arriving in the healthy

quadriceps, demonstrating that neutrophils can also carry liposomes to the inflamed muscle. Subsequently, the migration behaviour of neutrophils and liposome loaded neutrophils was investigated in the myocardial IRI model. Upon *i.v.* injection, the accumulation of injected neutrophils was seen in the IRI hearts. After loading neutrophils with liposomes, the signal of liposomes was also detected in the IRI hearts, which indicates that *ex vivo* loaded neutrophils can carry liposomes to the injured hearts. These results showcase that the neutrophil-mediated delivery system is able to respond to inflammatory signals and carry loaded liposomes to the site of inflammation.

MTX was then loaded into liposomes and the formulated MTX-liposome/neutrophils were injected intravenously to evaluate the anti-inflammatory treatment effects in these two inflammation models. In the LPS-injury skeletal muscle model, the MTX-liposome/neutrophil treatment successfully reduced the inflammatory cytokine levels of TNF- $\alpha$  and IL-6 in the inflamed muscle to comparable levels of the healthy quadriceps. In the myocardial IRI model, two different assessment methods were employed to measure cardiac function. FS was significantly improved after the treatment of MTX-liposome/neutrophils measured by echocardiography, and a slight increase of EF was also seen from PV loop analysis. Furthermore, by analysing other parameters such as heart rate, systolic and diastolic functions and collagen deposition, arterial load reduction was revealed as the possible pathway that resulted in slightly improved EF shown by PV loop analysis.

Overall, the developed neutrophil-mediated drug delivery system, liposome loaded neutrophils, can respond to inflammatory signals in the blood and carry loaded liposomes to the site of inflammation *in vivo*. Furthermore, after encapsulating MTX, a potent immune-suppressive drug, MTX-liposome/neutrophils can significantly reduce inflammatory cytokine levels of TNF- $\alpha$  and IL-6 in the inflamed muscle in the LPS-injury skeletal muscle model. In the myocardial IRI model, the MTX-liposome/neutrophil treatment significantly improved FS measured by echocardiography and slightly increased EF as shown by PV loop measurements. These findings suggest versatility of the neutrophil-mediated delivery system; it allows to transport drug loaded nanocarriers to the inflammatory site to locally deliver anti-inflammatory drugs to promote tissue regeneration in various inflammatory diseases.



# Chapter 5

## Conclusions and future work

## 5. Conclusions and future work

### 5.1. Conclusions

Controlling inflammation is the first step to treat inflammatory diseases and the prerequisite for tissue regeneration. Systemic administration of anti-inflammatory drugs is challenging due to poor bioavailability and bio-stability of the drugs, deleterious off-target effects and obstacles of biological barriers, which usually result in insufficient drug quantities accumulating at the disease site and undesired toxicity in other organs. Development of drug delivery systems to target anti-inflammatory drugs to the site of inflammation in a non-invasive way is a promising but demanding task. Of particular importance is the ability of the developed drug delivery system to rapidly respond to various inflammatory signals and release the loaded drugs to the inflamed tissue. This thesis aimed to address this need through the development of immune cell-mediated drug delivery systems that leverage key functionalities of nanoparticles and immune cells. Nanoparticles were used to achieve sufficient drug loading, controllable release and shield the drug from the carrier immune cells whilst immune cells were exploited for inflammation responsiveness and active local delivery. The goal here is to provide a universal strategy for the localised and non-invasive delivery of anti-inflammatory therapeutics to remote inflammatory sites. This research consisted of the formulation, optimisation, characterisation and application of neutrophil and macrophage mediated drug delivery systems combined with different types of nanoparticles and using various *in vitro* and *in vivo* models. The investigations offer further prospects of using different immune cells and nanoparticles to deliver various therapeutics or their combinations at different stages of inflammation, opening up new opportunities for innovative treatments of inflammatory diseases.

#### 5.1.1. *In vitro* development of immune cell-mediated drug delivery systems

A neutrophil-mediated drug delivery system was developed to deliver an anti-inflammatory agent encapsulated in a nanocarrier to inflamed tissue. Liposomes, biocompatible nanocarriers that can encapsulate both hydrophilic and hydrophobic drugs, were chosen for this study. Methotrexate (MTX), a potent immunosuppressive agent used to treat inflammatory and autoimmune diseases, was encapsulated in liposomes (MTX-liposome). By tuning the membrane fluidity of liposomes, sufficient MTX encapsulation with appropriate

drug retention times and nearly complete release in a complex biological environment was achieved. A simple one-step protocol was optimised to accomplish ideal loading of MTX-liposomes into neutrophils *ex vivo* without adversely affecting cell viability. Furthermore, loaded neutrophils retained their key functions of adhesion and migration towards sources of inflammatory signals. A big focus was put on precisely deciphering the liposome loading/release mechanism and the ability of neutrophils to transport the drug-loaded nanocarrier *in vitro* to downregulate inflammation. For this purpose, fluorescence correlation spectroscopy (FCS) was employed to characterise and quantify the integrity of released nanocarriers in the complex culture environment. The quantities of MTX loaded in the neutrophil-liposome hybrid system and stimulated release from neutrophils *via* triggering neutrophil extracellular traps (NETs) formation in an inflammatory environment were further confirmed by ELISA. Subsequent transport of MTX-liposomes from neutrophils to target cells was demonstrated *in vitro* using a co-culture method with macrophages. The intended biological effects were achieved in the target macrophages using the hybrid delivery system. These results suggest an optimised delivery system amenable to loading a sufficient amount of MTX. Neutrophils remained viable and retained their physiological properties of adhesion and migration to allow their movement towards sources of inflammatory signals. Further, inflammation-triggered release of drug-loaded liposomes from the neutrophils and subsequent liposome delivery to target cells was achieved.

In parallel, macrophages were also investigated as an alternative cell carrier to load nanoparticles. A nanoparticle library was screened for evaluating nanoparticle suitability for the development of macrophage-mediated drug delivery systems. Due to the longer timescales of this type of delivery, nanoparticles with better stability were chosen in this chapter in order to retain and protect the encapsulated drug from being released inside macrophages. Four different types of nanoparticles that are currently in clinical studies or have already been clinically approved for drug delivery were chosen, including liposomes, micelles, polymersomes and mesoporous silica nanoparticles (MSNs). The surface charge of organic nanoparticles was further varied to study the charge effect on cellular responses. All the organic nanoparticles had high macrophage uptake efficiencies at all the tested concentrations regardless of a neutral or positively charge surface. In terms of the effect of surface charge on nanoparticle loading quantities per macrophages, cationic liposomes and

polymersomes had significantly higher numbers inside macrophages than neutral ones whereas cationic micelles were found to impair macrophages phagocytosis ability. In contrast, MSNs showed a strong dose-dependent cell uptake efficiency with higher uptake for increasing silica concentrations. Neutral and cationic liposomes, micelles and polymersomes revealed high cytocompatibility when loaded into macrophages whereas cationic micelles and polymersomes have high cytotoxicity at high polymer concentrations because of their excessive cations. Decreased cell viability was detected at the highest silica concentration for PEG-MSNs. Furthermore, the migration function of macrophages, which determines the ability of macrophages to move towards the site of inflammation, was investigated after loading with different types of nanoparticles. All the organic nanoparticles did not impair the macrophage migratory behaviour, whereas PEG-MSNs inhibited the cell migration ability. Importantly, all the organic nanoparticles did not significantly polarise macrophages to a pro-inflammatory M1 phenotype, which suggests suitability of these types of nanocarriers for anti-inflammation therapies. Considering the long-term delivery timescales of macrophage-mediated drug delivery and potential applications of promoting tissue repair, apart from liposomes that have been used for neutrophil-mediated delivery, other nanoparticles with higher stability tested in this chapter can help maintaining nanoparticle integrity inside macrophages, keeping the drug retained inside nanoparticles whilst achieving sustained drug release from the hybrid system.

### 5.1.2. *In vivo* anti-inflammation treatments

Inflammation is an important therapeutic target for the treatment of many diseases including cardiovascular disease, autoimmunity, and cancer. Based on the results obtained from the above *in vitro* studies, the neutrophil-mediated drug delivery system, MTX-liposome loaded neutrophils, was chosen to study the anti-inflammation efficiency *in vivo*. The reasons being the advantages of a well-defined release mechanism and the rapid recruitment of neutrophils in the early stages of inflammation. Two mouse models of inflammation were employed to evaluate the neutrophil-mediated strategy, namely a lipopolysaccharides (LPS)-injury skeletal muscle model and a myocardial ischemia reperfusion injury (IRI) model. The former represents general tissue injury caused by inflammation and the latter represents an inflammation associated organ disease with a longer disease progression timeline and high relevance to human diseases. The migratory behaviour of injected neutrophils was first

investigated in these two mouse inflammation models. Neutrophils were detected in the LPS-injected quadriceps 1 h and 2 h after injection and disappeared at the 4h timepoint, indicating that injected neutrophils were recruited to the site of inflammation within 2 h after injection. When neutrophils were loaded with liposomes, injected neutrophils and liposomes were both detected in the LPS-injected quadriceps and co-localised well, whilst none were found in the healthy control quadriceps. This suggests the ability of neutrophils to carry loaded nanocarriers to the inflammatory site. In the myocardial IRI mouse model, the same migratory behaviour of injected neutrophils was observed, as demonstrated by the detection of injected neutrophils and liposome loaded neutrophils in the IRI heart after intravenous injection. These results indicate the versatility of the liposome-neutrophil hybrid system delivering loaded nanocarriers to various inflammatory sites (inflamed muscle and injured hearts).

The anti-inflammation treatment efficiency of the MTX-liposome loaded neutrophil system was further evaluated in these two mouse models. In the LPS-injury skeletal muscle model, only MTX-liposome loaded neutrophils significantly reduced the inflammatory cytokine levels of TNF- $\alpha$  and IL-6 in the LPS-injected quadriceps to comparable levels as measured in the healthy quadriceps. Neither free MTX nor MTX-liposome injections caused a decrease in the cytokine levels using the same dose. In the myocardial IRI model, the anti-inflammation treatment *via* the neutrophil system was further showcased by investigating the improvement of cardiac function using two different assessment methods, echocardiography and pressure-volume (PV) loop analysis. The MTX-liposome loaded neutrophils significantly improved fractional shortening of the IRI heart measured by echocardiography and a slight increase of ejection fraction was also seen when analysed by PV loop measurements, which are promising first steps, but it needs to be investigated in more detail with larger animal groups in the future.

These results reveal the potential of immune cell-mediated drug delivery as a universal strategy to deliver combinations of different types of nanoparticles and various therapeutic agents to inflammatory sites, mitigating inflammation and promoting tissue regeneration for the treatment of inflammatory diseases.

## 5.2. Future work

In this thesis, two different mouse inflammation models were employed to demonstrate the anti-inflammatory efficacy of MTX-liposome loaded neutrophils. As mentioned in Chapter 4, only a slight increase or decrease was detected in most of the cardiac parameters measured by echocardiography and PV loop analysis. Thus, to verify the validity of the conclusions, more mice should be tested in each group, ideally reaching  $n = 12$  as previously used in other studies using this model. Other possible strategies can be considered to improve the treatment efficacy: (1) increasing the injected MTX dose by injecting more neutrophils; however, injecting a large number of neutrophils might cause inflammation; (2) choosing another nanocarrier with longer drug retention times to increase the MTX loading capacity; thus, injecting the same number of neutrophils but loaded with a higher MTX dose; (3) using another drug or drug combinations with better efficacy for cardio-protection such as dexrazoxane. Regarding the nanoparticle optimisation for macrophage-mediated drug delivery systems shown in Chapter 3, it is interesting to further encapsulate regenerative drugs into organic nanoparticles to be loaded in macrophages. Injection of the hybrids in the late resolution/remodelling stage could be used to promote tissue regeneration after injury. Brynskikh *et al.* developed a macrophage-mediated delivery system with sustained catalase release properties. Catalase was packaged into a complex forming nanoparticles (nanoenzymes) to help loading catalase into macrophages and prevent catalase from degradation. Active catalase was slowly released from the hybrids over 5-7 d. Significant amounts of catalase were detected in the brain after *i.v.* injection to mice with PD and the nanoenzyme-macrophage system exhibited neuron-protective effects by increasing the number of surviving dopaminergic neurons.<sup>244</sup> This study gives a great promise to use organic nanoparticles optimised in chapter 3 to encapsulate regenerative drugs and realise sustained drug release from macrophages after nanoparticle loading for tissue repair.

## 5.3. Perspectives

This thesis developed immune cell-mediated drug delivery systems *in vitro* for the treatment of inflammatory diseases and validated the subsequent anti-inflammation treatment effect *in vivo*. The technologies presented here provide a universal strategy to design immune cell-mediated drug delivery systems with properties of sufficient drug loading capacity,

inflammation responsiveness and stimulated nanocarrier release in inflammatory environments, finally achieving local and non-invasive delivery of drugs to inflammatory sites.

The system design can be further tailored to meet therapeutic requirements in different stages of inflammation. Different immune cells can be chosen as cell carriers to meet the purpose of delivering drugs at different stages of inflammation. Neutrophils, which have mainly been used in this thesis, are one of the first leukocytes to be recruited to inflamed tissues. As neutrophils are only present in the early stages of inflammation and due to their ability to form NETs when highly activated in inflamed tissue, they are attractive cell carriers for drug delivery in the early inflammation stages. A crucial therapeutic target is the mitigation of inflammation in this phase; anti-inflammatory agents such as MTX, dexamethasone (DEX), glucocorticoids can be considered.<sup>108</sup> In terms of the choice of nanocarriers, apart from liposomes used in this thesis, nanoparticles with higher membrane stability or possessing stimuli-responsive properties may be utilised to increase the drug loading capacity of the system to improve treatment outcomes. Neutrophil-mediated drug delivery also has some limitations. Neutrophils start apoptosis quickly after isolation, thus, nanoparticle-neutrophil hybrids has to be formulated and reinjected as soon as possible. Injection of excessive neutrophils could potentially cause extra inflammation. Some hybrids can also be activated in the blood to form NETs, resulting in reduced drug delivery efficiencies. These need to be considered when choosing neutrophils as the cell carrier.

On the other hand, macrophages remain present much longer at the site of inflammation than neutrophils, starting from the early inflammation stage to the tissue remodelling/resolution phase. Moreover, unlike neutrophils' short lifespan after isolation, isolated macrophages can be cultured *ex vivo*, which enables various nanoparticle loading strategies onto/into macrophages; for example, loading macrophages with nanoparticles *via* covalent conjugation can generate a strong binding between macrophages and nanoparticles, avoiding the possible detachment of nanoparticles from the cells before they arrive at the target site. In this case, different nanoparticle release profiles from macrophages can be achieved by introducing stimuli-responsive linkers between nanoparticles and macrophages. Phenotypic shifts of macrophages after nanoparticle loading is another key parameter to be checked after formulating the system. Macrophage polarisation towards a M1 pro-inflammatory phenotype may exacerbate inflammation after administration, having a

deleterious effect on anti-inflammation therapy. However, a shift to the M2 reparative phenotype after loading may favour tissue regeneration. In this thesis, the M1 and M2 surface markers were measured using flow cytometry. However, the M2 surface marker CD206 did not respond well. An alternative method should be employed; for example, using qRT-PCR to measure M2 specific markers such as arginase, CD206 and IL-10. It is important to note that the timeline of macrophage migration to the site of inflammation and payload release may take up to 2 weeks. As such, macrophages are not an ideal cell carrier for rapid mitigation of inflammation. In contrast, in the context of tissue regeneration, new tissue formation usually takes a long period and the long term migration and payload release properties of macrophage-mediated delivery systems could benefit this purpose. However, it is a considerable nanoengineering challenge to keep the drug encapsulated and protected from the carrier macrophages for a long time, whilst achieving controlled release over time and subsequent uptake and action in the target cells. Other immune cells such as T cells and dendritic cells involved in inflammation responses can also be considered as alternative cell carriers.

In terms of anti-inflammation therapy, apart from the inflammation models used in this thesis, it is worth applying immune cell-mediated drug delivery systems to other inflammation associated diseases, especially inflammation associated brain diseases such as Parkinson's disease (PD) and Alzheimer's disease (AD). It is particularly challenging to achieve active delivery of drugs to the brain as the blood brain barrier (BBB) prevents most of the drugs and drug loaded nanoparticles from being taken up by the brain. By leveraging the intrinsic functions of immune cells migrating across the BBB, it is promising to accomplish active drug delivery to the inflamed brain tissue *via* immune cell-hitchhiking. In this case, neutrophils and macrophages can be attractive cell carriers to deliver anti-inflammatory or neuro-protective drugs to the brain. One example is using macrophages to deliver catalase to the inflamed brain tissue in a mouse model of PD (see the discussions above).<sup>244</sup> In the case of using neutrophils as a cell carrier, Xue *et al.* developed a liposome-neutrophil delivery system to efficiently deliver paclitaxel to a tumour site in the brain.<sup>239</sup> These studies suggest the possibilities of using the immune cell-hitchhiking strategy to target drugs to the brain tissue upon systemic administration for the treatment of inflammation associated brain diseases. Anti-inflammatory drugs such as MTX and DEX, and anti-neuro degeneration drugs such as



dopamine and glial cell line-derived neurotrophic factor can be used for the treatment of PD and AD.<sup>350,351</sup> Dual drug delivery is also possible by exploiting differential recruitment of different immune cell populations over time. For example, neutrophils can be utilised to deliver immune-modulating drugs shortly after tissue injury and macrophages loaded with regenerative drugs can later be injected to enhance regeneration.

It is envisioned that the framework presented here further encourages the combinations of immune cells, nanomaterials, and drugs to form a new type of hybrid material that leverages key functionalities of each component with the potential of various biomedical applications.

# References

1. Medzhitov, R. Inflammation 2010: New adventures of an old flame. *Cell* **140**, 771–776 (2010).
2. Rankin, J. A. Biological mediators of acute inflammation. *AACN Clin. Issues* **15**, 3–17 (2004).
3. Ley, K., Laudanna, C., Cybulsky, M. I. & Nourshargh, S. Getting to the site of inflammation: The leukocyte adhesion cascade updated. *Nat. Rev. Immunol.* **7**, 678–689 (2007).
4. Forbes, S. J. & Rosenthal, N. Preparing the ground for tissue regeneration: From mechanism to therapy. *Nat. Med.* **20**, 857–869 (2014).
5. Eming, S. A., Krieg, T. & Davidson, J. M. Inflammation in wound repair: Molecular and cellular mechanisms. *J. Invest. Dermatol.* **127**, 514–525 (2007).
6. Cicchese, J. M. *et al.* Dynamic balance of pro- and anti-inflammatory signals controls disease and limits pathology. *Immunol. Rev.* **285**, 147–167 (2018).
7. Medzhitov, R. Origin and physiological roles of inflammation. *Nature* **454**, 428–435 (2008).
8. Dostert, C. *et al.* Innate immune activation through Nalp3 inflammasome sensing of asbestos and silica. *Science* **320**, 674–7 (2008).
9. Parke, D. V. & Parke, A. L. Chemical-induced inflammation and inflammatory diseases. *Int. J. Occup. Med. Environ. Health* **9**, 211–217 (1996).
10. Guo, C., Hou, Z. & Zeng, Z. The development of allergic inflammation. *Nature* **454**, 445–454 (2013).
11. Cross, A. S. What is a virulence factor? *Crit. Care* **12**, 196 (2008).
12. Casadevall, A. & Pirofski, L. A. Virulence factors and their mechanisms of action: The view from a damage-response framework. *J. Water Health* **7**, 2–18 (2009).
13. Moran, A. P., Prendergast, M. M. & Appelmelk, B. J. Molecular mimicry of host structures by bacterial lipopolysaccharides and its contribution to disease. *FEMS Immunol. Med. Microbiol.* **16**, 105–115 (1996).
14. Rock, K. L. & Kono, H. The inflammatory response to cell death. *Annu. Rev. Pathol. Mech. Dis.* **3**, 99–126 (2008).
15. Bianchi, M. E. DAMPs, PAMPs and alarmins: all we need to know about danger. *J. Leukoc. Biol.* **81**, 1–5 (2007).
16. Mariathasan, S. *et al.* Cryopyrin activates the inflammasome in response to toxins and ATP. *Nature* **440**, 228–232 (2006).
17. Park, J. S. *et al.* High mobility group box 1 protein interacts with multiple Toll-like receptors. *Am. J. Physiol. Physiol.* **290**, C917–C924 (2006).
18. Hofmann, M. A. *et al.* RAGE mediates a novel proinflammatory axis: A central cell surface receptor for S100/calgranulin polypeptides. *Cell* **97**, 889–901 (1999).
19. Seth R, Justin P, F. E. & Stephen E, and R. M. Recognition of Commensal Microflora by Toll-Like Receptors Is Required for Intestinal Homeostasis. *J. Torrey Bot. Soc.* **130**, 147 (2003).
20. Pull, S. L., Doherty, J. M., Mills, J. C., Gordon, J. I. & Stappenbeck, T. S. Activated macrophages are an adaptive element of the colonic epithelial progenitor niche necessary for regenerative responses to injury. *Proc. Natl. Acad. Sci. U. S. A.* **102**, 99–

- 104 (2005).
21. Pober, J. S. & Sessa, W. C. Evolving functions of endothelial cells in inflammation. *Nat. Rev. Immunol.* **7**, 803–815 (2007).
  22. Martinon, F., Pétrilli, V., Mayor, A., Tardivel, A. & Tschopp, J. Gout-associated uric acid crystals activate the NALP3 inflammasome. *Nature* **440**, 237–241 (2006).
  23. Flier, J. S., Underhill, L. H., Brownlee, M., Cerami, A. & Vlassara, H. Advanced Glycosylation End Products in Tissue and the Biochemical Basis of Diabetic Complications. *N. Engl. J. Med.* **318**, 1315–1321 (1988).
  24. Yan, S. F. *et al.* The biology of RAGE and its ligands: Uncovering mechanisms at the heart of diabetes and its complications. *Curr. Diab. Rep.* **7**, 146–153 (2007).
  25. Berliner, J. A. & Heinecke, J. W. The role of oxidized lipoproteins in atherogenesis. *Free Radical Biology and Medicine* **20**, 707–727 (1996).
  26. Kolaczowska, E. & Kubes, P. Neutrophil recruitment and function in health and inflammation. *Nat. Rev. Immunol.* **13**, 159–175 (2013).
  27. Summers, C. *et al.* Neutrophil kinetics in health and disease. *Trends Immunol.* **31**, 318–324 (2010).
  28. Kulidjian, A. A., Inman, R. & Issekutz, T. B. Rodent models of lymphocyte migration. *Semin. Immunol.* **11**, 85–93 (1999).
  29. Anderson, D. C., Miller, L. J., Schmalstieg, F. C., Rothlein, R. & Springer, T. A. Contributions of the Mac-1 glycoprotein family to adherence-dependent granulocyte functions: structure-function assessments employing subunit-specific monoclonal antibodies. *J. Immunol.* **137**, 15–27 (1986).
  30. Foxman, E. F., Campbell, J. J. & Butcher, E. C. Multistep navigation and the combinatorial control of leukocyte chemotaxis. *J. Cell Biol.* **139**, 1349–1360 (1997).
  31. Yipp, B. G. & Kubes, P. Antibodies against neutrophil LY6G do not inhibit leukocyte recruitment in mice in vivo. *Blood* **121**, 241–242 (2013).
  32. Ruszczak, Z. Effect of collagen matrices on dermal wound healing. *Adv. Drug Deliv. Rev.* **55**, 1595–1611 (2003).
  33. Borregaard, N. Neutrophils, from Marrow to Microbes. *Immunity* **33**, 657–670 (2010).
  34. Häger, M., Cowland, J. B. & Borregaard, N. Neutrophil granules in health and disease. *J. Intern. Med.* **268**, 25–34 (2010).
  35. Brinkmann, V. Neutrophil Extracellular Traps Kill Bacteria. *Science (80-. )*. **303**, 1532–1535 (2004).
  36. Yipp, B. G. *et al.* Infection-induced NETosis is a dynamic process involving neutrophil multitasking in vivo. *Nat. Med.* **18**, 1386–1393 (2012).
  37. Megens, R. T. A. *et al.* Presence of luminal neutrophil extracellular traps in atherosclerosis. *Thromb. Haemost.* **107**, 597–598 (2012).
  38. von Brühl, M. L. *et al.* Monocytes, neutrophils, and platelets cooperate to initiate and propagate venous thrombosis in mice in vivo. *J. Exp. Med.* **209**, 819–835 (2012).
  39. Knight, J. S. & Kaplan, M. J. Lupus neutrophils: ‘NET’ gain in understanding lupus pathogenesis. *Curr. Opin. Rheumatol.* **24**, 441–450 (2012).
  40. Demers, M. *et al.* Cancers predispose neutrophils to release extracellular DNA traps that contribute to cancer-associated thrombosis. *Proc. Natl. Acad. Sci. U. S. A.* **109**, 13076–13081 (2012).
  41. Mathias, J. R. *et al.* Resolution of inflammation by retrograde chemotaxis of neutrophils in transgenic zebrafish. *J. Leukoc. Biol.* **80**, 1281–1288 (2006).
  42. Woodfin, A. *et al.* The junctional adhesion molecule JAM-C regulates polarized

- transendothelial migration of neutrophils in vivo. *Nat. Immunol.* **12**, 761–769 (2011).
43. Buckley, C. D. *et al.* Identification of a phenotypically and functionally distinct population of long-lived neutrophils in a model of reverse endothelial migration. *J. Leukoc. Biol.* **79**, 303–311 (2006).
  44. Issekutz, A. C., Chuluyan, H. E. & Lopes, N. CD11/CD18-independent transendothelial migration of human polymorphonuclear leukocytes and monocytes: Involvement of distinct and unique mechanisms. *J. Leukoc. Biol.* **57**, 553–561 (1995).
  45. Koh, T. J. & DiPietro, L. A. Inflammation and wound healing: the role of the macrophage. *Expert Rev. Mol. Med.* **13**, 1–12 (2011).
  46. Badiu, D., Vasile, M. & Teren, O. Regulation of wound healing by growth factors and cytokines. *Wound Heal. Process. Phases Promot.* **83**, 73–93 (2011).
  47. Hume, D. A. The many alternative faces of macrophage activation. *Front. Immunol.* **6**, 209–212 (2015).
  48. Barrientos, S., Stojadinovic, O., Golinko, M. S., Brem, H. & Tomic-Canic, M. Growth factors and cytokines in wound healing. *Wound Repair Regen.* **16**, 585–601 (2008).
  49. Wetzler, C., Kampfer, H., Stallmeyer, B., Pfeilschifter, J. & Frank, S. Large and sustained induction of chemokines during impaired wound healing in the genetically diabetic mouse: Prolonged persistence of neutrophils and macrophages during the late phase of repair. *J. Invest. Dermatol.* **115**, 245–253 (2000).
  50. Rappolee, D., Mark, D., Banda, M. & Werb, Z. Wound macrophages express TGF- $\alpha$  and other growth factors in vivo: analysis by mRNA phenotyping. *Science (80- )*. **241**, 708–712 (1988).
  51. DiPietro, L. A. & Polverini, P. J. Role of the macrophage in the positive and negative regulation of wound neovascularization. *Behring Inst. Mitt.* 238–247 (1993).
  52. Bellingan, G. J., Caldwell, H., Howie, S. E., Dransfield, I. & Haslett, C. In vivo fate of the inflammatory macrophage during the resolution of inflammation: inflammatory macrophages do not die locally, but emigrate to the draining lymph nodes. *J. Immunol.* **157**, 2577–85 (1996).
  53. Theoharides, T. C. *et al.* Mast cells and inflammation. *Biochim. Biophys. Acta - Mol. Basis Dis.* **1822**, 21–33 (2012).
  54. Schwartz, L. B. Mediators of human mast cells and human mast cell subsets. *Ann. Allergy* **58**, 226–237 (1987).
  55. Dvorak, A. M. New Aspects of Mast Cell Biology. *Int. Arch. Allergy Immunol.* **114**, 1–9 (1997).
  56. McLeod, J. J. A., Baker, B. & Ryan, J. J. Mast cell production and response to IL-4 and IL-13. *Cytokine* **75**, 57–61 (2015).
  57. Elsworth, B. *et al.* PTEX is an essential nexus for protein export in malaria parasites. *Nature* **511**, 587–91 (2014).
  58. Skokos, D. *et al.* Mast Cell-Dependent B and T Lymphocyte Activation Is Mediated by the Secretion of Immunologically Active Exosomes. *J. Immunol.* **166**, 868–876 (2001).
  59. Meltzer, E. O. *et al.* Rhinosinusitis: Establishing definitions for clinical research and patient care. *J. Allergy Clin. Immunol.* **114**, 155–212 (2004).
  60. Hamann, A. & Syrbe, U. T-cell trafficking into sites of inflammation. *Rheumatology* **39**, 696–699 (2000).
  61. Cope, A. P. Studies of T-cell activation in chronic inflammation. *Arthritis Res.* **4**, S197–S211 (2002).
  62. Gutcher, I. & Becher, B. APC-derived cytokines and T cell polarization in autoimmune

- inflammation. *J. Clin. Invest.* **117**, 1119–1127 (2007).
63. Masopust, D., Vezys, V., Marzo, A. L. & Lefrançois, L. Preferential localization of effector memory cells in nonlymphoid tissue. *J. Immunol.* **192**, 845–849 (2014).
  64. Abbas, A. K. *et al.* Regulatory T cells: Recommendations to simplify the nomenclature. *Nat. Immunol.* **14**, 307–308 (2013).
  65. Wencker, M. *et al.* Innate-like T cells straddle innate and adaptive immunity by altering antigen-receptor responsiveness. *Nat. Immunol.* **15**, 80–87 (2014).
  66. Dadi, S. *et al.* Cancer Immunosurveillance by Tissue-Resident Innate Lymphoid Cells and Innate-like T Cells. *Cell* **164**, 365–377 (2016).
  67. Glyn-Jones, S. *et al.* Osteoarthritis. *Lancet* **386**, 376–387 (2015).
  68. Heinegård, D. & Saxne, T. The role of the cartilage matrix in osteoarthritis. *Nat. Rev. Rheumatol.* **7**, 50–56 (2011).
  69. Sutton, K. M., Grauer, J. N., Biswas, D. & Bible, J. E. Articular cartilage and osteoarthritis. *AAOS Compr. Orthop. Rev.* **2** **1**, 93–104 (2018).
  70. Vilá, S. Inflammation in osteoarthritis. *P. R. Health Sci. J.* **36**, 123–129 (2017).
  71. McInnes, I. B. & Schett, G. The pathogenesis of rheumatoid arthritis. *N. Engl. J. Med.* **365**, 2205–2219 (2011).
  72. Sweeney, S. E. & Firestein, G. S. Rheumatoid arthritis: Regulation of synovial inflammation. *Int. J. Biochem. Cell Biol.* **36**, 372–378 (2004).
  73. Willenbacher, R. F. Inflammatory bowel disease. *Semin. Gastrointest. Dis.* **7**, 94–104 (1996).
  74. Moldoveanu, A. C., Diculescu, M. & Braticevici, C. F. ierbintean. Cytokines in inflammatory bowel disease. *Rom. J. Intern. Med.* **53**, 118–127 (2015).
  75. Frangogiannis, N. G., Smith, C. W. & Entman, M. L. The inflammatory response in myocardial infarction. *Cardiovasc. Res.* **53**, 31–47 (2002).
  76. Lowenstein, C. J. Myocardial reperfusion injury. *N. Engl. J. Med.* **357**, 2409 (2007).
  77. Zografos, T. A. & Katritsis, D. G. Cyclosporine before PCI in Acute Myocardial Infarction. *N. Engl. J. Med.* **374**, 88–90 (2016).
  78. Sangiuliano, B., Pérez, N. M., Moreira, D. F. & Belizário, J. E. Cell death-associated molecular-pattern molecules: Inflammatory signaling and control. *Mediators Inflamm.* **2014**, (2014).
  79. Oka, T. *et al.* Erratum: Mitochondrial DNA that escapes from autophagy causes inflammation and heart failure. *Nature* **490**, 292 (2012).
  80. Mangold, A. *et al.* Neutrophil extracellular traps and monocyte subsets at the culprit lesion site of myocardial infarction patients. *Sci. Rep.* **9**, 1–10 (2019).
  81. Zhao, Z. Q. *et al.* Reperfusion induces myocardial apoptotic cell death. *Cardiovasc. Res.* **45**, 651–660 (2000).
  82. Zhao, Z. Q. *et al.* Progressively developed myocardial apoptotic cell death during late phase of reperfusion. *Apoptosis* **6**, 279–290 (2001).
  83. Ong, S. B. *et al.* Inflammation following acute myocardial infarction: Multiple players, dynamic roles, and novel therapeutic opportunities. *Pharmacol. Ther.* **186**, 73–87 (2018).
  84. Dobaczewski, M., Xia, Y., Bujak, M., Gonzalez-Quesada, C. & Frangogiannis, N. G. CCR5 signaling suppresses inflammation and reduces adverse remodeling of the infarcted heart, mediating recruitment of regulatory T cells. *Am. J. Pathol.* **176**, 2177–2187 (2010).
  85. Shinde, A. V. & Frangogiannis, N. G. Fibroblasts in myocardial infarction: A role in

- inflammation and repair. *J. Mol. Cell. Cardiol.* **70**, 74–82 (2014).
86. Brenner, C., Galluzzi, L., Kepp, O. & Kroemer, G. Decoding cell death signals in liver inflammation. *J. Hepatol.* **59**, 583–594 (2013).
  87. Leitão, H. S. *et al.* Hepatic fibrosis, inflammation, and steatosis: Influence on the MR viscoelastic and diffusion parameters in patients with chronic liver disease. *Radiology* **283**, 98–107 (2017).
  88. Ramadori, G., Moriconi, F., Malik, I. & Dudas, J. Physiology and pathophysiology of liver inflammation, damage and repair. *J. Physiol. Pharmacol.* **59**, 107–117 (2008).
  89. Pawlotsky, J. M. Pathophysiology of hepatitis C virus infection and related liver disease. *Trends Microbiol.* **12**, 96–102 (2004).
  90. Gao, B. *et al.* Innate immunity in alcoholic liver disease. *Am. J. Physiol. Liver Physiol.* **300**, G516–G525 (2011).
  91. Brenner, D. A. *et al.* Non-alcoholic steatohepatitis-induced fibrosis: Toll-like receptors, reactive oxygen species and Jun N-terminal kinase. *Hepatol. Res.* **41**, 683–686 (2011).
  92. Maher, J. J. DAMPs ramp up drug toxicity. *J. Clin. Invest.* **119**, 246–249 (2009).
  93. Poltorak, A. Defective LPS Signaling in C3H/HeJ and C57BL/10ScCr Mice: Mutations in Tlr4 Gene. *Science (80-. )*. **282**, 2085–2088 (1998).
  94. Szabo, G., Mandrekar, P. & Dolganiuc, A. Innate Immune Response and Hepatic Inflammation. *Semin. Liver Dis.* **27**, 339–350 (2007).
  95. Brusselle, G. & Bracke, K. Targeting immune pathways for therapy in asthma and chronic obstructive pulmonary disease. *Ann. Am. Thorac. Soc.* **11**, S322–S328 (2014).
  96. Leitch, A. E., Duffin, R., Haslett, C. & Rossi, A. G. Relevance of granulocyte apoptosis to resolution of inflammation at the respiratory mucosa. *Mucosal Immunol.* **1**, 350–363 (2008).
  97. Willemsse, B. W. M., Postma, D. S., Timens, W. & ten Hacken, N. H. T. The impact of smoking cessation on respiratory symptoms, lung function, airway hyperresponsiveness and inflammation. *Eur. Respir. J.* **23**, 464–476 (2004).
  98. Niewoehner, D. E. Cigarette smoking, lung inflammation, and the development of emphysema. *J. Lab. Clin. Med.* **111**, 15–27 (1988).
  99. Hernandez, T. & Mayadas, T. N. The Changing landscape of renal inflammation. *Trends Mol. Med.* **22**, 151–163 (2016).
  100. Stenvinkel, P. Chronic kidney disease: A public health priority and harbinger of premature cardiovascular disease. *J. Intern. Med.* **268**, 456–467 (2010).
  101. Sanz, A. B. *et al.* NF- $\kappa$ B in renal inflammation. *J. Am. Soc. Nephrol.* **21**, 1254–1262 (2010).
  102. Poveda, J. *et al.* NF $\kappa$ Biz protein downregulation in acute kidney injury: Modulation of inflammation and survival in tubular cells. *Biochim. Biophys. Acta - Mol. Basis Dis.* **1862**, 635–646 (2016).
  103. Vezzani, A. & Granata, T. Brain inflammation in epilepsy: Experimental and clinical evidence. *Epilepsia* **46**, 1724–1743 (2005).
  104. Liu, B. & Hong, J. S. Role of microglia in inflammation-mediated neurodegenerative diseases: Mechanisms and strategies for therapeutic intervention. *J. Pharmacol. Exp. Ther.* **304**, 1–7 (2003).
  105. Nakada, Y. *et al.* Hypoxia induces heart regeneration in adult mice. *Nature* **541**, 222–227 (2017).
  106. Banjara, M. & Ghosh, C. Sterile neuroinflammation and strategies for therapeutic intervention. *Int. J. Inflamm.* **2017**, 1–20 (2017).
  107. Manabe, I. Chronic inflammation links cardiovascular, metabolic and renal diseases.

- Circ. J.* **75**, 2739–2748 (2011).
108. Dinarello, C. A. Anti-inflammatory Agents: Present and Future. *Cell* **140**, 935–950 (2010).
  109. Tian, H. & Cronstein, B. N. Understanding the mechanisms of action of methotrexate: Implications for the treatment of rheumatoid arthritis. *Bull. NYU Hosp. Jt. Dis.* **65**, 168–173 (2007).
  110. Chan, E. S. L. & Cronstein, B. N. Molecular action of methotrexate in inflammatory diseases. *Arthritis Res.* **4**, 266–273 (2002).
  111. Riksen, N. P., Smits, P. & Rongen, G. A. The nonspecific anti-inflammatory therapy with methotrexate for patients with chronic heart failure. *Am. Hear. journal.* **151**, 62–68 (2006).
  112. Papich, M. G. Dexamethasone. in *Saunders Handbook of Veterinary Drugs (Fourth Edition)* (ed. Papich, M. G.) 217–219 (W.B. Saunders, 2016). doi:<https://doi.org/10.1016/B978-0-323-24485-5.00195-9>
  113. Liu, C. & Liu, K. Cardiac outcome prevention effectiveness of glucocorticoids in acute decompensated heart failure: COPE-ADHF study. *J. Cardiovasc. Pharmacol.* **63**, 333–338 (2014).
  114. Willoughby, D. A., Moore, A. R. & Colville-Nash, P. R. COX-1, COX-2, and COX-3 and the future treatment of chronic inflammatory disease. *Lancet* **355**, 646–648 (2000).
  115. Stevenson, D. D. Aspirin and NSAID sensitivity. *Immunol. Allergy Clin. North Am.* **24**, 491–505 (2004).
  116. Hawkey, C. J. COX-2 inhibitors. *Lancet* **353**, 307–314 (1999).
  117. Di Rosa, M., Calignano, A., Carnuccio, R., Ialenti, A. & Sautebin, L. Multiple control of inflammation by glucocorticoids. *Agents Actions* **17**, 284–289 (1986).
  118. Tuckermann, J. P., Kleiman, A., McPherson, K. G. & Reichardt, H. M. Molecular mechanisms of glucocorticoids in the control of inflammation and lymphocyte apoptosis. *Crit. Rev. Clin. Lab. Sci.* **42**, 71–104 (2005).
  119. Masters, S. L., Simon, A., Aksentijevich, I. & Kastner, D. L. Horror autoinflammaticus: The molecular pathophysiology of autoinflammatory disease. *Annu. Rev. Immunol.* **27**, 621–668 (2009).
  120. Drenth, J. P. H. *et al.* Mutations in the gene encoding mevalonate kinase cause hyper-IgD and periodic fever syndrome. *Nat. Genet.* **22**, 178–181 (1999).
  121. Emsley, H. C. A. *et al.* A randomised phase II study of interleukin-1 receptor antagonist in acute stroke patients. *J. Neurol. Neurosurg. Psychiatry* **76**, 1366–1372 (2005).
  122. Fleischmann, R. M. *et al.* Anakinra, a recombinant human interleukin-1 receptor antagonist (r-metHuIL-1ra), in patients with rheumatoid arthritis: A large, international, multicenter, placebo-controlled trial. *Arthritis Rheum.* **48**, 927–934 (2003).
  123. Abbate, A. *et al.* Interleukin-1 Blockade With Anakinra to Prevent Adverse Cardiac Remodeling After Acute Myocardial Infarction. *Am. J. Cardiol.* **105**, 1371–1377 (2010).
  124. Lachmann, H. J. *et al.* Use of canakinumab in the cryopyrin-associated periodic syndrome. *N. Engl. J. Med.* **360**, 2416–2425 (2009).
  125. Serhan, C. N. & Chiang, N. Endogenous pro-resolving and anti-inflammatory lipid mediators: A new pharmacologic genus. *Br. J. Pharmacol.* **153**, S200–S215 (2008).
  126. Jin, Y. *et al.* Anti-angiogenesis effect of the novel anti-inflammatory and pro-resolving lipid mediators. *Investig. Ophthalmol. Vis. Sci.* **50**, 4743–4752 (2009).
  127. Chiang, N., Dalli, J., Colas, R. A. & Serhan, C. N. Identification of resolvin D2 receptor mediating resolution of infections and organ protection. *J. Exp. Med.* **212**, 1203–1217

- (2015).
128. Krishnamoorthy, S. *et al.* Resolvin D1 binds human phagocytes with evidence for proresolving receptors. *Proc. Natl. Acad. Sci. U. S. A.* **107**, 1660–1665 (2010).
  129. Sulciner, M. L. *et al.* Resolvins suppress tumor growth and enhance cancer therapy. *J. Exp. Med.* **215**, 115–140 (2018).
  130. Arita, M. *et al.* Resolvin E1, an endogenous lipid mediator derived from omega-3 eicosapentaenoic acid, protects against 2,4,6-trinitrobenzene sulfonic acid-induced colitis. *Proc. Natl. Acad. Sci. U. S. A.* **102**, 7671–7676 (2005).
  131. Choudhary, C. *et al.* Lysine Acetylation Targets Protein Complexes and Co-Regulates Major Cellular Functions. *Science (80-. ).* **325**, 834–840 (2009).
  132. Marks, P. A. *et al.* Histone deacetylases and cancer: Causes and therapies. *Nat. Rev. Cancer* **1**, 194–202 (2001).
  133. Patil, V. *et al.* Antimalarial and antileishmanial activities of histone deacetylase inhibitors with triazole-linked cap group. *Bioorganic Med. Chem.* **18**, 415–425 (2010).
  134. Serhan, C. N. & Levy, B. D. Resolvins in inflammation: Emergence of the pro-resolving superfamily of mediators. *J. Clin. Invest.* **128**, 2657–2669 (2018).
  135. Huang, N., Katz, J. P., Martin, D. R. & Wu, G. D. Inhibition of IL-8 gene expression in Caco-2 cells by compounds which induce histone hyperacetylation. *Cytokine* **9**, 27–36 (1997).
  136. Diakos, C. *et al.* Novel mode of interference with nuclear factor of activated T-cells regulation in T-cells by the bacterial metabolite n-butyrate. *J. Biol. Chem.* **277**, 24243–24251 (2002).
  137. Leoni, F. *et al.* The antitumor histone deacetylase inhibitor suberoylanilide hydroxamic acid exhibits antiinflammatory properties via suppression of cytokines. *Proc. Natl. Acad. Sci. U. S. A.* **99**, 2995–3000 (2002).
  138. Vojinovic, J., Dinarello, C. A., Damjanov, N. & Oldoni, T. Safety and efficacy of oral ITF 2357 in patients with active systemic onset juvenile idiopathic arthritis (SOJIA)-Results of a phase II, open label, international, Multicentre clinical trial. in *Arthritis and Rheumatism* **58**, S943–S943 (WILEY-BLACKWELL COMMERCE PLACE, 350 MAIN ST, MALDEN 02148, MA USA, 2008).
  139. Badri, W. *et al.* Encapsulation of NSAIDs for inflammation management: Overview, progress, challenges and prospects. *Int. J. Pharm.* **515**, 757–773 (2016).
  140. Vonkeman, H. E. & van de Laar, M. A. F. J. Nonsteroidal Anti-Inflammatory Drugs: Adverse Effects and Their Prevention. *Semin. Arthritis Rheum.* **39**, 294–312 (2010).
  141. Pardridge, W. M. Drug transport across the blood-brain barrier. *J. Cereb. Blood Flow Metab.* **32**, 1959–1972 (2012).
  142. Major, E. O. Progressive multifocal leukoencephalopathy in patients on immunomodulatory therapies. *Annu. Rev. Med.* **61**, 35–47 (2010).
  143. Braun, J. & Rau, R. An update on methotrexate. *Curr. Opin. Rheumatol.* **21**, 216–223 (2009).
  144. Halvorsen, P. *et al.* The effect of dexamethasone on side effects after coronary revascularization procedures. *Anesth. Analg.* **96**, 1578–1583 (2003).
  145. L Zhang, FX Gu, JM Chan, AZ Wang, R. L. and O. F. Therapeutic, Nanoparticles in Medicine: Applications and Developments. *Educ. Policy Anal. Arch.* **8**, 761–769 (2007).
  146. Danhier, F. *et al.* Paclitaxel-loaded PEGylated PLGA-based nanoparticles: In vitro and in vivo evaluation. *J. Control. Release* **133**, 11–17 (2009).
  147. Schiffelers, R. M. *et al.* Cancer siRNA therapy by tumor selective delivery with ligand-



- targeted sterically stabilized nanoparticle. *Nucleic Acids Res.* **32**, e149–e149 (2004).
148. JATZKEWITZ, H. Incorporation of physiologically-active substances into a colloidal blood plasma substitute. I. Incorporation of mescaline peptide into polyvinylpyrrolidone. *Hoppe. Seylers. Z. Physiol. Chem.* **297**, 149–56 (1954).
  149. Bangham, A. D. & Horne, R. W. Negative staining of phospholipids and their structural modification by surface-active agents as observed in the electron microscope. *J. Mol. Biol.* **8**, 660–668 (1964).
  150. Banik, B. L., Fattahi, P. & Brown, J. L. Polymeric nanoparticles: The future of nanomedicine. *Wiley Interdiscip. Rev. Nanomedicine Nanobiotechnology* **8**, 271–299 (2016).
  151. Maeda, H. Tumor-selective delivery of macromolecular drugs via the EPR effect: Background and future prospects. *Bioconjug. Chem.* **21**, 797–802 (2010).
  152. Petros, R. A. & Desimone, J. M. Strategies in the design of nanoparticles for therapeutic applications. *Nat. Rev. Drug Discov.* **9**, 615–627 (2010).
  153. US Government. U S Food and Drug Administration Web Page. (2016).
  154. Cho, K., Wang, X., Nie, S., Chen, Z. & Shin, D. M. Therapeutic nanoparticles for drug delivery in cancer. *Clin. Cancer Res.* **14**, 1310–1316 (2008).
  155. Liong, M. *et al.* Multifunctional inorganic nanoparticles for imaging, targeting, and drug delivery. *ACS Nano* **2**, 889–896 (2008).
  156. Bangham, A. D., Standish, M. M., Watkins, J. C. & Weissmann, G. The diffusion of ions from a phospholipid model membrane system. *Protoplasma* **63**, 183–187 (1967).
  157. Gregoriadis, G. & Ryman, B. E. Liposomes as carriers of enzymes or drugs: a new approach to the treatment of storage diseases. *Biochem. J.* **124**, 8–10 (1971).
  158. Gregoriadis, G. The Carrier Potential of Liposomes in Biology and Medicine. *N. Engl. J. Med.* **295**, 765–770 (1976).
  159. Gregoriadis, G. Drug entrapment in liposomes. *FEBS Lett.* **36**, 292–296 (1973).
  160. Bolotin, E. M. *et al.* Ammonium sulfate gradients for efficient and stable remote loading of amphipathic weak bases into liposomes and ligandoliposomes. *J. Liposome Res.* **4**, 455–479 (1994).
  161. Mayer, L. D. *et al.* Characterization of liposomal systems containing doxorubicin entrapped in response to pH gradients. *BBA - Biomembr.* **1025**, 143–151 (1990).
  162. Anwekar, H., Patel, S. & Singhai, a K. Liposome- as drug carriers. *Int. J. Pharm. Life Sci.* **2**, 945–951 (2011).
  163. Amselem, S., Gabizon, A. & Barenholz, Y. Optimization and upscaling of doxorubicin-containing liposomes for clinical use. *J. Pharm. Sci.* **79**, 1045–1052 (1990).
  164. Walsh, T. J. *et al.* Caspofungin versus liposomal amphotericin B for empirical antifungal therapy in patients with persistent fever and neutropenia. *N. Engl. J. Med.* **351**, 764–771 (2004).
  165. Korting, H. C., Zienicke, H., Schäfer-Korting, M. & Braun-Falco, O. Liposome encapsulation improves efficacy of betamethasone dipropionate in atopic eczema but not in psoriasis vulgaris. *Eur. J. Clin. Pharmacol.* **39**, 349–351 (1990).
  166. TREMBLAY, G. M., THÉRIEN, H.-M., ROCHELEAU, H. & CORMIER, Y. Liposomal dexamethasone effectiveness in the treatment of hypersensitivity pneumonitis in mice. *Eur. J. Clin. Invest.* **23**, 656–661 (1993).
  167. Camelo, S. *et al.* Drainage of fluorescent liposomes from the vitreous to cervical lymph nodes via conjunctival lymphatics. *Ophthalmic Res.* **40**, 145–150 (2008).
  168. Maranhão, R. C. *et al.* Methotrexate carried in lipid core nanoparticles reduces

- myocardial infarction size and improves cardiac function in rats. *Int. J. Nanomedicine* **12**, 3767–3784 (2017).
169. Koning, G. A. *et al.* Targeting of angiogenic endothelial cells at sites of inflammation by dexamethasone phosphate-containing RGD peptide liposomes inhibits experimental arthritis. *Arthritis Rheum.* **54**, 1198–1208 (2006).
170. Jubeh, T. T., Barenholz, Y. & Rubinstein, A. Differential adhesion of normal and inflamed rat colonic mucosa by charged liposomes. *Pharm. Res.* **21**, 447–453 (2004).
171. Hashida, N. *et al.* High-efficacy site-directed drug delivery system using sialyl-Lewis X conjugated liposome. *Exp. Eye Res.* **86**, 138–149 (2008).
172. Immordino, M. L., Dosio, F. & Cattel, L. Stealth liposomes: Review of the basic science, rationale, and clinical applications, existing and potential. *Int. J. Nanomedicine* **1**, 297–315 (2006).
173. Rao, J. P. & Geckeler, K. E. Polymer nanoparticles: Preparation techniques and size-control parameters. *Prog. Polym. Sci.* **36**, 887–913 (2011).
174. Torchilin, V. P. Multifunctional, stimuli-sensitive nanoparticulate systems for drug delivery. *Nat. Rev. Drug Discov.* **13**, 813–827 (2014).
175. Kataoka, K., Harada, A. & Nagasaki, Y. Block copolymer micelles for drug delivery: Design, characterization and biological significance. *Adv. Drug Deliv. Rev.* **64**, 37–48 (2012).
176. Discher, B. M. *et al.* Polymersomes: Tough vesicles made from diblock copolymers. *Science (80-. )*. **284**, 1143–1146 (1999).
177. Meng, F., Zhong, Z. & Feijen, J. Stimuli-responsive polymersomes for programmed drug delivery. *Biomacromolecules* **10**, 197–209 (2009).
178. Wang, B. L. *et al.* Treating acute cystitis with biodegradable micelle-encapsulated quercetin. *Int. J. Nanomedicine* **7**, 2239–2247 (2012).
179. Hammer, D. A. *et al.* Leuko-polymersomes. *Faraday Discuss.* **139**, 129–141 (2008).
180. Li, Z., Barnes, J. C., Bosoy, A., Stoddart, J. F. & Zink, J. I. Mesoporous silica nanoparticles in biomedical applications. *Chem. Soc. Rev.* **41**, 2590–2605 (2012).
181. Giljohann, D. A. *et al.* Gold nanoparticles for biology and medicine. *Angew. Chemie - Int. Ed.* **49**, 3280–3294 (2010).
182. Huang, H. C., Barua, S., Sharma, G., Dey, S. K. & Rege, K. Inorganic nanoparticles for cancer imaging and therapy. *J. Control. Release* **155**, 344–357 (2011).
183. Harper, B. W. *et al.* Advances in platinum chemotherapeutics. *Chem. - A Eur. J.* **16**, 7064–7077 (2010).
184. Feng, Q. L. *et al.* A mechanistic study of the antibacterial effect of silver ions on *Escherichia coli* and *Staphylococcus aureus*. *J. Biomed. Mater. Res.* **52**, 662–668 (2000).
185. McCarthy, J. R. & Weissleder, R. Multifunctional magnetic nanoparticles for targeted imaging and therapy. *Adv. Drug Deliv. Rev.* **60**, 1241–1251 (2008).
186. Yoon, H. Y. *et al.* Inorganic nanoparticles for image-guided therapy. *Bioconjug. Chem.* **28**, 124–134 (2017).
187. Kim, D., Jeong, Y. Y. & Jon, S. A drug-loaded aptamer - Gold nanoparticle bioconjugate for combined ct imaging and therapy of prostate cancer. *ACS Nano* **4**, 3689–3696 (2010).
188. Giljohann, D. A., Seferos, D. S., Prigodich, A. E., Patel, P. C. & Mirkin, C. A. Gene regulation with polyvalent siRNA-nanoparticle conjugates. *J. Am. Chem. Soc.* **131**, 2072–2073 (2009).
189. El-Sayed, I. H., Huang, X. & El-Sayed, M. A. Selective laser photo-thermal therapy of

- epithelial carcinoma using anti-EGFR antibody conjugated gold nanoparticles. *Cancer Lett.* **239**, 129–135 (2006).
190. Tkachenko, A. G. *et al.* Multifunctional gold nanoparticle-peptide complexes for nuclear targeting. *J. Am. Chem. Soc.* **125**, 4700–4701 (2003).
  191. Wang, F. *et al.* Doxorubicin-tethered responsive gold nanoparticles facilitate intracellular drug delivery for overcoming multidrug resistance in cancer cells. *ACS Nano* **5**, 3679–3692 (2011).
  192. Elsworth, B. *et al.* PTEX is an essential nexus for protein export in malaria parasites. *Nature* **511**, 587–91 (2014).
  193. Decuzzi, P. *et al.* Size and shape effects in the biodistribution of intravascularly injected particles. *J. Control. Release* **141**, 320–327 (2010).
  194. Khlebtsov, N. & Dykmana, L. Biodistribution and toxicity of engineered gold nanoparticles: A review of in vitro and in vivo studies. *Chem. Soc. Rev.* **40**, 1647–1671 (2011).
  195. Vallet-Regi, M., Rámila, A., Del Real, R. P. & Pérez-Pariente, J. A new property of MCM-41: Drug delivery system. *Chem. Mater.* **13**, 308–311 (2001).
  196. Tang, F., Li, L. & Chen, D. Mesoporous silica nanoparticles: Synthesis, biocompatibility and drug delivery. *Adv. Mater.* **24**, 1504–1534 (2012).
  197. Yiu, H. H. P., Botting, C. H., Botting, N. P. & Wright, P. A. Size selective protein adsorption on thiol-functionalised SBA-15 mesoporous molecular sieve. *Phys. Chem. Chem. Phys.* **3**, 2983–2985 (2001).
  198. Lee, C. H., Lo, L. W., Mou, C. Y. & Yang, C. S. Synthesis and characterization of positive-charge functionalized mesoporous silica nanoparticles for oral drug delivery of an anti-inflammatory drug. *Adv. Funct. Mater.* **18**, 3283–3292 (2008).
  199. Chen, J., Liu, M., Chen, C., Gong, H. & Gao, C. Synthesis and characterization of silica nanoparticles with well-defined thermoresponsive PNIPAM via a combination of RAFT and click chemistry. *ACS Appl. Mater. Interfaces* **3**, 3215–3223 (2011).
  200. Sood, A. & Panchagnula, R. Peroral route: An opportunity for protein and peptide drug delivery. *Chem. Rev.* **101**, 3275–3303 (2001).
  201. He, Q., Zhang, Z., Gao, F., Li, Y. & Shi, J. In vivo biodistribution and urinary excretion of mesoporous silica nanoparticles: Effects of particle size and PEGylation. *Small* **7**, 271–280 (2011).
  202. Anselmo, A. C. & Mitragotri, S. A Review of Clinical Translation of Inorganic Nanoparticles. *AAPS J.* **17**, 1041–1054 (2015).
  203. Boulant, S., Stanifer, M. & Lozach, P. Y. Dynamics of virus-receptor interactions in virus binding, signaling, and endocytosis. *Viruses* **7**, 2794–2815 (2015).
  204. Brown, W. L. *et al.* RNA bacteriophage capsid-mediated drug delivery and epitope presentation. *Intervirology* **45**, 371–380 (2002).
  205. Chatterji, A. *et al.* Chemical conjugation of heterologous proteins on the surface of cowpea mosaic virus. *Bioconjug. Chem.* **15**, 807–813 (2004).
  206. Lockney, D. M. *et al.* The red clover necrotic mosaic virus capsid as a multifunctional cell targeting plant viral nanoparticle. *Bioconjug. Chem.* **22**, 67–73 (2011).
  207. Brasch, M. *et al.* Encapsulation of phthalocyanine supramolecular stacks into virus-like particles. *J. Am. Chem. Soc.* **133**, 6878–6881 (2011).
  208. Brasch, M., Voets, I. K., Koay, M. S. T. & Cornelissen, J. J. L. M. Phototriggered cargo release from virus-like assemblies. *Faraday Discuss.* **166**, 47–57 (2013).
  209. Thanh, N. T. Magnetic Nanoparticles From Fabrication to Clinical Applications. *CRC*

- Press* **54**, 243–276 (2012).
210. Kottke, T. *et al.* Antiangiogenic cancer therapy combined with oncolytic virotherapy leads to regression of established tumors in mice. *Cancer Res.* **120**, 1551–1560 (2010).
  211. Steinmetz, N. F. *et al.* Intravital imaging of human prostate cancer using viral nanoparticles targeted to gastrin-releasing peptide receptors. *Small* **7**, 1664–1672 (2011).
  212. Suei, P. A., Varpness, Z., Gillitzer, E., Douglas, T. & Young, M. Targeting and photodynamic killing of a microbial pathogen using protein cage architectures functionalized with a photosensitizer. *Langmuir* **23**, 12280–12286 (2007).
  213. Oligino, T. *et al.* Intra-articular delivery of a herpes simplex virus IL-1Ra gene vector reduces inflammation in a rabbit model of arthritis. *Gene Ther.* **6**, 1713–1720 (1999).
  214. Green, N. K. *et al.* Extended plasma circulation time and decreased toxicity of polymer-coated adenovirus. *Gene Ther.* **11**, 1256–1263 (2004).
  215. Bachmann, M. F., Hengartner, H. & Zinkernagel, R. M. T helper cell-independent neutralizing B cell response against vesicular stomatitis virus: Role of antigen patterns in B cell induction. *Eur. J. Immunol.* **25**, 3445–3451 (1995).
  216. Etheridge, M. L. *et al.* The big picture on nanomedicine: The state of investigational and approved nanomedicine products. *Nanomedicine Nanotechnology, Biol. Med.* **9**, 1–14 (2013).
  217. Lundqvist, M. *et al.* Nanoparticle size and surface properties determine the protein corona with possible implications for biological impacts. *Proc. Natl. Acad. Sci. U. S. A.* **105**, 14265–14270 (2008).
  218. Amoozgar, Z. & Yeo, Y. Recent advances in stealth coating of nanoparticle drug delivery systems. *Wiley Interdiscip. Rev. Nanomedicine Nanobiotechnology* **4**, 219–233 (2012).
  219. Hamilton, A. *et al.* EORTC 10968: A phase I clinical and pharmacokinetic study of polyethylene glycol liposomal doxorubicin (Caelyx®, Doxil®) at a 6-week interval in patients with metastatic breast cancer. *Ann. Oncol.* **13**, 910–918 (2002).
  220. Dams, E. T. M. *et al.* Accelerated blood clearance and altered biodistribution of repeated injections of sterically stabilized liposomes. *J. Pharmacol. Exp. Ther.* **292**, 1071–1079 (2000).
  221. Laverman, P. *et al.* Factors affecting the accelerated blood clearance of polyethylene glycol-liposomes upon repeated injection. *J. Pharmacol. Exp. Ther.* **298**, 607–612 (2001).
  222. Blanco, E., Shen, H. & Ferrari, M. Principles of nanoparticle design for overcoming biological barriers to drug delivery. *Nat. Biotechnol.* **33**, 941–951 (2015).
  223. Golombek, S. K. *et al.* Tumor targeting via EPR: Strategies to enhance patient responses. *Adv. Drug Deliv. Rev.* **130**, 17–38 (2018).
  224. Saraiva, C. *et al.* Nanoparticle-mediated brain drug delivery: Overcoming blood-brain barrier to treat neurodegenerative diseases. *J. Control. Release* **235**, 34–47 (2016).
  225. Tabas, I. & Glass, C. K. Anti-inflammatory therapy in chronic disease: Challenges and opportunities. *Science (80-. )*. **339**, 166–172 (2013).
  226. Saxena, A., Russo, I. & Frangogiannis, N. G. Inflammation as a therapeutic target in myocardial infarction: Learning from past failures to meet future challenges. *Transl. Res.* **167**, 152–166 (2016).
  227. Hirlekar, R., Patel, P., Dand, N. & Kadam, V. Drug Loaded Erythrocytes: As Novel Drug Delivery System. *Curr. Pharm. Des.* **14**, 63–70 (2008).
  228. Ihler, G. M., Glew, R. H. & Schnure, F. W. Enzyme loading of erythrocytes. *Proc. Natl. Acad. Sci. U. S. A.* **70**, 2663–2666 (1973).

229. Rossi, L. *et al.* Erythrocyte-mediated delivery of dexamethasone in patients with chronic obstructive pulmonary disease. *Biotechnol. Appl. Biochem.* **33**, 85 (2001).
230. Muzykantov, V. R. Drug delivery by red blood cells: Vascular carriers designed by mother nature. *Expert Opin. Drug Deliv.* **7**, 403–427 (2010).
231. Biagiotti, S., Paoletti, M. F., Fraternali, A., Rossi, L. & Magnani, M. Drug delivery by red blood cells. *IUBMB Life* **63**, 621–631 (2011).
232. Pierigè, F., Serafini, S., Rossi, L. & Magnani, M. Cell-based drug delivery. *Adv. Drug Deliv. Rev.* **60**, 286–295 (2008).
233. Ravilla, S., Chandu, B. R., Nama, S. & Nagaveni, B. Erythrocytes as carrier for drugs, enzymes and peptides. *J. Appl. Pharm. Sci.* **2**, 166–176 (2012).
234. Mitragotri, S., Burke, P. A. & Langer, R. Overcoming the challenges in administering biopharmaceuticals: Formulation and delivery strategies. *Nat. Rev. Drug Discov.* **13**, 655–672 (2014).
235. Phillipson, M. & Kubes, P. The neutrophil in vascular inflammation. *Nat. Med.* **17**, 1381–1390 (2011).
236. Mantovani, A., Cassatella, M. A., Costantini, C. & Jaillon, S. Neutrophils in the activation and regulation of innate and adaptive immunity. *Nat. Rev. Immunol.* **11**, 519–531 (2011).
237. Chu, D., Gao, J. & Wang, Z. Neutrophil-Mediated Delivery of Therapeutic Nanoparticles across Blood Vessel Barrier for Treatment of Inflammation and Infection. *ACS Nano* **9**, 11800–11811 (2015).
238. Hou, J. *et al.* Accessing neuroinflammation sites: Monocyte/neutrophil-mediated drug delivery for cerebral ischemia. *Sci. Adv.* **5**, eaau8301 (2019).
239. Xue, J. *et al.* Neutrophil-mediated anticancer drug delivery for suppression of postoperative malignant glioma recurrence. *Nat. Nanotechnol.* **12**, 692–700 (2017).
240. Chu, D. *et al.* Nanoparticle Targeting of Neutrophils for Improved Cancer Immunotherapy. *Adv. Healthc. Mater.* **5**, 1088–1093 (2016).
241. Zhang, C. *et al.* Direct macromolecular drug delivery to cerebral ischemia area using neutrophil-mediated nanoparticles. *Theranostics* **7**, 3260–3275 (2017).
242. Luo, X. *et al.* Neutrophil-mediated delivery of pixantrone-loaded liposomes decorated with poly(Sialic acid)–octadecylamine conjugate for lung cancer treatment. *Drug Deliv.* **25**, 1200–1212 (2018).
243. Hu, L. *et al.* Neutrophil-Mediated Delivery of Dexamethasone Palmitate-Loaded Liposomes Decorated with a Sialic Acid Conjugate for Rheumatoid Arthritis Treatment. *Pharm. Res.* **36**, 97 (2019).
244. Brynskikh, A. M. *et al.* Macrophage delivery of therapeutic nanozymes in a murine model of Parkinsons disease. *Nanomedicine* **5**, 379–396 (2010).
245. Choi, J. *et al.* Use of macrophages to deliver therapeutic and imaging contrast agents to tumors. *Biomaterials* **33**, 4195–4203 (2012).
246. Haney, M. J. *et al.* Blood-borne macrophage-neural cell interactions hitchhike on endosome networks for cell-based nanozyme brain delivery. *Nanomedicine* **7**, 815–833 (2012).
247. Prisk, V. & Huard, J. Stem cells in tissue engineering. *Scaffolding Tissue Eng.* **414**, 531–544 (2005).
248. Levy, O. *et al.* mRNA-engineered mesenchymal stem cells for targeted delivery of interleukin-10 to sites of inflammation. *Blood* **122**, e23–e32 (2013).
249. Studeny, M. *et al.* Bone marrow-derived mesenchymal stem cells as vehicles for

- interferon- $\beta$  delivery into tumors. *Cancer Res.* **62**, 3603–3608 (2002).
250. Aboody, K. S. *et al.* Targeting of melanoma brain metastases using engineered neural stem/progenitor cells. *Neuro. Oncol.* **8**, 119–126 (2006).
251. Choi, M. R. *et al.* A cellular trojan horse for delivery of therapeutic nanoparticles into tumors. *Nano Lett.* **7**, 3759–3765 (2007).
252. Doshi, N. & Mitragotri, S. Macrophages recognize size and shape of their targets. *PLoS One* **5**, (2010).
253. Champion, J. A. & Mitragotri, S. Role of target geometry in phagocytosis. *Proc. Natl. Acad. Sci. U. S. A.* **103**, 4930–4934 (2006).
254. Beningo, K. A. & Wang, Y. L. Fc-receptor-mediated phagocytosis is regulated by mechanical properties of the target. *J. Cell Sci.* **115**, 849–856 (2002).
255. Fujiwara, M., Baldeschwieler, J. D. & Grubbs, R. H. Receptor-mediated endocytosis of poly( acrylic acid)-conjugated liposomes by macrophages. *Biochim. Biophys. Acta - Biomembr.* **1278**, 59–67 (1996).
256. Fröhlich, E. The role of surface charge in cellular uptake and cytotoxicity of medical nanoparticles. *Int. J. Nanomedicine* **7**, 5577–5591 (2012).
257. Weiss, L. & Zeigel, R. Cell surface negativity and the binding of positively charged particles. *J. Cell. Physiol.* **77**, 179–185 (1971).
258. Chambers, E. & Mitragotri, S. Prolonged circulation of large polymeric nanoparticles by non-covalent adsorption on erythrocytes. *J. Control. Release* **100**, 111–119 (2004).
259. Li, L. *et al.* Silica nanorattle–doxorubicin-anchored mesenchymal stem cells for tumor-tropic therapy. *ACS Nano* **5**, 7462–7470 (2011).
260. Polak, R. *et al.* Liposome-Loaded Cell Backpacks. *Adv. Healthc. Mater.* **4**, 2832–2841 (2015).
261. Cheng, H. *et al.* Nanoparticulate cellular patches for cell-mediated tumor-tropic delivery. *ACS Nano* **4**, 625–631 (2010).
262. Stephan, M. T., Moon, J. J., Um, S. H., Bersthteyn, A. & Irvine, D. J. Therapeutic cell engineering with surface-conjugated synthetic nanoparticles. *Nat. Med.* **16**, 1035–1041 (2010).
263. Lee, D. Y. *et al.* Optimization of monomethoxy-polyethylene glycol grafting on the pancreatic islet capsules. *J. Biomed. Mater. Res.* **62**, 372–377 (2002).
264. Zhao, Y. *et al.* Active Targeted Macrophage-mediated Delivery of Catalase to Affected Brain Regions in Models of Parkinson’s Disease. *J Nanomed Nanotechnol.* (2011). doi:10.4172/2157-7439.S4-003.Active
265. Zhang, W. *et al.* Nanoparticle-Laden Macrophages for Tumor-Tropic Drug Delivery. *Adv. Mater.* **30**, 1805557 (2018).
266. Xu, L., Zolotarskaya, O. Y., Yeudall, W. A. & Yang, H. Click hybridization of immune cells and polyamidoamine dendrimers. *Adv. Healthc. Mater.* **3**, 1430–1438 (2014).
267. Chen, L. *et al.* Inflammatory responses and inflammation-associated diseases in organs. *Oncotarget* **9**, 7204–7218 (2018).
268. Tenzer, S. *et al.* Rapid formation of plasma protein corona critically affects nanoparticle pathophysiology. *Nat. Nanotechnol.* **8**, 772–781 (2013).
269. Cheng, Y. H., He, C., Riviere, J. E., Monteiro-Riviere, N. A. & Lin, Z. Meta-Analysis of Nanoparticle Delivery to Tumors Using a Physiologically Based Pharmacokinetic Modeling and Simulation Approach. *ACS Nano* **14**, 3075–3095 (2020).
270. Moghimi, S. M., Hunter, A. C. & Murray, J. C. Long-circulating and target-specific nanoparticles: theory to practice. *Pharmacol. Rev.* **53**, 283–318 (2001).

271. Zhang, H. Thin-film hydration followed by extrusion method for liposome preparation. in *Methods in Molecular Biology* **1522**, 17–22 (Springer, 2017).
272. Baxa, U. Imaging of liposomes by transmission electron microscopy. in *Methods in Molecular Biology* **1682**, 73–88 (Springer, 2018).
273. Kapusta, P. & Gmbh, P. Absolute Diffusion Coefficients : Compilation of Reference Data for FCS Calibration. 0–1 (2010).
274. Müller, P., Schwille, P. & Weidemann, T. PyCorrFit-generic data evaluation for fluorescence correlation spectroscopy. *Bioinformatics* **30**, 2532–2533 (2014).
275. He, C., Hu, Y., Yin, L., Tang, C. & Yin, C. Effects of particle size and surface charge on cellular uptake and biodistribution of polymeric nanoparticles. *Biomaterials* **31**, 3657–3666 (2010).
276. Feng, D., Nagy, J. A., Pyne, K., Dvorak, H. F. & Dvorak, A. M. Neutrophils emigrate from venules by a transendothelial cell pathway in response to FMLP. *J. Exp. Med.* **187**, 903–915 (1998).
277. Nazarewicz, R. R., Bikineyeva, A. & Dikalov, S. I. Rapid and specific measurements of superoxide using fluorescence spectroscopy. *J. Biomol. Screen.* **18**, 498–503 (2013).
278. Winterbourn, C. C., Kettle, A. J. & Hampton, M. B. Reactive Oxygen Species and Neutrophil Function. *Annu. Rev. Biochem.* **85**, 765–792 (2016).
279. Paulsson, J. M., Jacobson, S. H. & Lundahl, J. Neutrophil activation during transmigration in vivo and in vitro. A translational study using the skin chamber model. *J. Immunol. Methods* **361**, 82–88 (2010).
280. Wilschut, J. & Hoekstra, D. Membrane fusion: from liposomes to biological membranes. *Trends Biochem. Sci.* **9**, 479–483 (1984).
281. Srisuk, P., Thongnopnua, P., Raktanonchai, U. & Kanokpanont, S. Physico-chemical characteristics of methotrexate-entrapped oleic acid-containing deformable liposomes for in vitro transepidermal delivery targeting psoriasis treatment. *Int. J. Pharm.* **427**, 426–434 (2012).
282. Eloy, J. O. *et al.* Liposomes as carriers of hydrophilic small molecule drugs: strategies to enhance encapsulation and delivery. *Colloids surfaces B Biointerfaces* **123**, 345–363 (2014).
283. Kraan, M. C. *et al.* Inhibition of neutrophil migration soon after initiation of treatment with leflunomide or methotrexate in patients with rheumatoid arthritis: Findings in a prospective, randomized, double-blind clinical trial in fifteen patients. *Arthritis Rheum.* **43**, 1488–1495 (2000).
284. Asako, H., Wolf, R. E. & Granger, D. N. Leukocyte adherence in rat mesenteric venules: Effects of adenosine and methotrexate. *Gastroenterology* **104**, 31–37 (1993).
285. Asako, H., Kubes, P., Baethge, B. A., Wolf, R. E. & Granger, D. N. Colchicine and methotrexate reduce leukocyte adherence and emigration in rat mesenteric venules. *Inflammation* **16**, 45–56 (1992).
286. McMullen, T. P. W., Lewis, R. N. A. H. & McElhaney, R. N. Cholesterol-phospholipid interactions, the liquid-ordered phase and lipid rafts in model and biological membranes. *Curr. Opin. Colloid Interface Sci.* **8**, 459–468 (2004).
287. Briuglia, M. L., Rotella, C., McFarlane, A. & Lamprou, D. A. Influence of cholesterol on liposome stability and on in vitro drug release. *Drug Deliv. Transl. Res.* **5**, 231–242 (2015).
288. CREAM, J. J. & POLE, D. S. The effect of methotrexate and hydroxyurea on neutrophil chemotaxis. *Br. J. Dermatol.* **102**, 557–563 (1980).

289. Cronstein, B. N., Naime, D. & Ostad, E. The antiinflammatory mechanism of methotrexate: Increased adenosine release at inflamed sites diminishes leukocyte accumulation in an in vivo model of inflammation. *J. Clin. Invest.* **92**, 2675–2682 (1993).
290. Choi, H. K., Hernán, M. A., Seeger, J. D., Robins, J. M. & Wolfe, F. Methotrexate and mortality in patients with rheumatoid arthritis: A prospective study. *Lancet* **359**, 1173–1177 (2002).
291. Park, J. E. *et al.* DC-Based Immunotherapy Combined with Low-Dose Methotrexate Effective in the Treatment of Advanced CIA in Mice. *J. Immunol. Res.* **2015**, (2015).
292. Montesinos, M. C., Desai, A. & Cronstein, B. N. Suppression of inflammation by low-dose methotrexate is mediated by adenosine A2A receptor but not A3 receptor activation in thioglycollate-induced peritonitis. *Arthritis Res. Ther.* **8**, 1–7 (2006).
293. To, H. *et al.* Methotrexate chronotherapy is effective against rheumatoid arthritis. *Chronobiol. Int.* **28**, 267–274 (2011).
294. Cronstein, B. N. The mechanism of action of methotrexate. *Rheum. Dis. Clin. North Am.* **23**, 739–755 (1997).
295. Han, S., Chen, Z., Han, P., Hu, Q. & Xiao, Y. Activation of Macrophages by Lipopolysaccharide for Assessing the Immunomodulatory Property of Biomaterials. *Tissue Eng. - Part A* **23**, 1100–1109 (2017).
296. Fujiwara, N. & Kobayashi, K. Macrophages in inflammation. *Curr. Drug Targets Inflamm. Allergy* **4**, 281–286 (2005).
297. Rappolee, D. A., Mark, D., Banda, M. J. & Werb, Z. Wound macrophages express TGF- $\alpha$  and other growth factors in vivo: analysis by mRNA phenotyping. *Science* **241**, 708–12 (1988).
298. Aderem, A. & Underhill, D. M. Mechanisms of phagocytosis in macrophages. *Annu. Rev. Immunol.* **17**, 593–623 (1999).
299. Sica, A., Allavena, P. & Mantovani, A. Cancer related inflammation: The macrophage connection. *Cancer Lett.* **267**, 204–215 (2008).
300. Choi, M. R. *et al.* Delivery of nanoparticles to brain metastases of breast cancer using a cellular Trojan horse. *Cancer Nanotechnol.* **3**, 47–54 (2012).
301. Muthana, M. *et al.* Use of macrophages to target therapeutic adenovirus to human prostate tumors. *Cancer Res.* **71**, 1805–1815 (2011).
302. Muthana, M. *et al.* Macrophage delivery of an oncolytic virus abolishes tumor regrowth and metastasis after chemotherapy or irradiation. *Cancer Res.* **73**, 490–495 (2013).
303. Biju, K. *et al.* Macrophage-mediated GDNF delivery protects against dopaminergic neurodegeneration: A therapeutic strategy for parkinson's disease. *Mol. Ther.* **18**, 1536–1544 (2010).
304. Chandrupatla, D. M. S. H., Molthoff, C. F. M., Lammertsma, A. A., van der Laken, C. J. & Jansen, G. The folate receptor  $\beta$  as a macrophage-mediated imaging and therapeutic target in rheumatoid arthritis. *Drug Deliv. Transl. Res.* **9**, 366–378 (2019).
305. Kodali, V. *et al.* Dysregulation of macrophage activation profiles by engineered nanoparticles. *ACS Nano* **7**, 6997–7010 (2013).
306. Yue, Z. G. *et al.* Surface charge affects cellular uptake and intracellular trafficking of chitosan-based nanoparticles. *Biomacromolecules* **12**, 2440–2446 (2011).
307. Anselmo, A. C. & Mitragotri, S. Nanoparticles in the clinic: An update. *Bioeng. Transl. Med.* **4**, e10143 (2019).
308. Konradi, R., Acikgoz, C. & Textor, M. Polyoxazolines for nonfouling surface coatings - A direct comparison to the gold standard PEG. *Macromol. Rapid Commun.* **33**, 1663–1676



- (2012).
309. Williams, D. F. On the mechanisms of biocompatibility. *Biomaterials* **29**, 2941–2953 (2008).
  310. Lu, F., Wu, S. H., Hung, Y. & Mou, C. Y. Size effect on cell uptake in well-suspended, uniform mesoporous silica nanoparticles. *Small* **5**, 1408–1413 (2009).
  311. Slowing, I., Trewyn, B. G. & Lin, V. S. Y. Effect of surface functionalization of MCM-41-type mesoporous silica nanoparticles on the endocytosis by human cancer cells. *J. Am. Chem. Soc.* **128**, 14792–14793 (2006).
  312. Zhang, Y., Hu, L., Yu, D. & Gao, C. Influence of silica particle internalization on adhesion and migration of human dermal fibroblasts. *Biomaterials* **31**, 8465–8474 (2010).
  313. He, X. T. *et al.* The effects of conditioned media generated by polarized macrophages on the cellular behaviours of bone marrow mesenchymal stem cells. *J. Cell. Mol. Med.* **22**, 1302–1315 (2018).
  314. Dou, H. *et al.* Macrophage Delivery of Nanoformulated Antiretroviral Drug to the Brain in a Murine Model of NeuroAIDS. *J. Immunol.* **183**, 661–669 (2009).
  315. Dou, H. *et al.* Development of a macrophage-based nanoparticle platform for antiretroviral drug delivery. *Blood* **108**, 2827–2835 (2006).
  316. Buja, L. M. Myocardial ischemia and reperfusion injury. *Cardiovasc. Pathol.* **14**, 170–175 (2005).
  317. Lowenstein, C. J. Myocardial reperfusion injury. *N. Engl. J. Med.* **357**, 2409; author reply 2409–10 (2007).
  318. Frangogiannis, N. G. The inflammatory response in myocardial injury, repair, and remodelling. *Nat. Rev. Cardiol.* **11**, 255–265 (2014).
  319. Doyle, A., Zhang, G., Fattah, E. A. A., Eissa, N. T. & Li, Y. Toll-like receptor 4 mediates lipopolysaccharide-induced muscle catabolism via coordinate activation of ubiquitin-proteasome and autophagy-lysosome pathways. *FASEB J.* **25**, 99–110 (2011).
  320. Juskewitch, J. E. *et al.* LPS-induced murine systemic inflammation is driven by parenchymal cell activation and exclusively predicted by early MCP-1 plasma levels. *Am. J. Pathol.* **180**, 32–40 (2012).
  321. Everhardt Queen, A., Moerdyk-Schauwecker, M., McKee, L. M., Leamy, L. J. & Huet, Y. M. Differential expression of inflammatory cytokines and stress genes in male and female mice in response to a lipopolysaccharide challenge. *PLoS One* **11**, (2016).
  322. Rudski, L. G. *et al.* Guidelines for the Echocardiographic Assessment of the Right Heart in Adults: A Report from the American Society of Echocardiography. Endorsed by the European Association of Echocardiography, a registered branch of the European Society of Cardiology, and . *J. Am. Soc. Echocardiogr.* **23**, 685–713 (2010).
  323. Liu, S. *et al.* Neutrophil extracellular traps are indirectly triggered by lipopolysaccharide and contribute to acute lung injury. *Sci. Rep.* **6**, (2016).
  324. Kitazawa, M., Trinh, D. N. & LaFerla, F. M. Inflammation induces tau pathology in inclusion body myositis model via glycogen synthase kinase-3 $\beta$ . *Ann. Neurol.* **64**, 15–24 (2008).
  325. McKay, P. F. *et al.* Identification of potential biomarkers of vaccine inflammation in mice. *Elife* **8**, 1–23 (2019).
  326. Fang, L., Moore, X. L., Dart, A. M. & Wang, L. M. Systemic inflammatory response following acute myocardial infarction. *J. Geriatr. Cardiol.* **12**, 305–312 (2015).
  327. Boechat, A. L. *et al.* Methotrexate-loaded lipid-core nanocapsules are highly effective in the control of inflammation in synovial cells and a chronic arthritis model. *Int. J.*

- Nanomedicine* **10**, 6603–6614 (2015).
328. Kane, D. *et al.* Reduction of synovial sublining layer inflammation and proinflammatory cytokine expression in psoriatic arthritis treated with methotrexate. *Arthritis Rheum.* **50**, 3286–3295 (2004).
329. Wang, J. *et al.* Anti-inflammatory activity of curcumin-loaded solid lipid nanoparticles in IL-1 $\beta$  transgenic mice subjected to the lipopolysaccharide-induced sepsis. *Biomaterials* **53**, 475–483 (2015).
330. Heilborn, J. D. *et al.* Low-dose oral pulse methotrexate as monotherapy in elderly patients with bullous pemphigoid. *J. Am. Acad. Dermatol.* **40**, 741–749 (1999).
331. To, H. *et al.* Therapeutic index of methotrexate depends on circadian cycling of tumour necrosis factor- $\alpha$  in collagen-induced arthritic rats and mice. *J. Pharm. Pharmacol.* **61**, 1333–1338 (2009).
332. Ishida, T., Harashima, H. & Kiwada, H. Liposome clearance. *Biosci. Rep.* **22**, 197–224 (2002).
333. Bartlett, R. L., Sharma, S. & Panitch, A. Cell-penetrating peptides released from thermosensitive nanoparticles suppress pro-inflammatory cytokine response by specifically targeting inflamed cartilage explants. *Nanomedicine Nanotechnology, Biol. Med.* **9**, 419–427 (2013).
334. Somasuntharam, I. *et al.* Knockdown of TNF- $\alpha$  by DNAzyme gold nanoparticles as an anti-inflammatory therapy for myocardial infarction. *Biomaterials* **83**, 12–22 (2016).
335. Vanniasinghe, A. S. *et al.* Targeting fibroblast-like synovial cells at sites of inflammation with peptide targeted liposomes results in inhibition of experimental arthritis. *Clin. Immunol.* **151**, 43–54 (2014).
336. Marks, J. L. & Edwards, C. J. Protective effect of methotrexate in patients with rheumatoid arthritis and cardiovascular comorbidity. *Ther. Adv. Musculoskelet. Dis.* **4**, 149–157 (2012).
337. Bălănescu, A. R., Bojincă, V. C., Bojincă, M., Donisan, T. & Bălănescu, S. M. Cardiovascular effects of methotrexate in immune-mediated inflammatory diseases (Review). *Exp. Ther. Med.* **17**, 1024–1029 (2019).
338. Asanuma, H. *et al.* Methotrexate and MX-68, a new derivative of methotrexate, limit infarct size via adenosine-dependent mechanisms in canine hearts. *J. Cardiovasc. Pharmacol.* **43**, 574–579 (2004).
339. Seshadri, G. *et al.* The delivery of superoxide dismutase encapsulated in polyketal microparticles to rat myocardium and protection from myocardial ischemia-reperfusion injury. *Biomaterials* **31**, 1372–1379 (2010).
340. Junqueira, L. C. U., Bignolas, G. & Brentani, R. R. Picrosirius staining plus polarization microscopy, a specific method for collagen detection in tissue sections. *Histochem. J.* **11**, 447–455 (1979).
341. Talman, V. & Ruskoaho, H. Cardiac fibrosis in myocardial infarction—from repair and remodeling to regeneration. *Cell Tissue Res.* **365**, 563–581 (2016).
342. Paulus, W. J., Flachskampf, F. A., Smiseth, O. A. & Fraser, A. G. How to diagnose diastolic heart failure: a consensus statement on the diagnosis of heart failure with normal left ventricular ejection fraction by the Heart Failure and Echocardiography Associations of the European Society of Cardiology. *Eur. Heart J.* **28**, 2686–2687 (2007).
343. Pacher, P., Nagayama, T., Mukhopadhyay, P., Bátkai, S. & Kass, D. A. Measurement of cardiac function using pressure-volume conductance catheter technique in mice and rats. *Nat. Protoc.* **3**, 1422–1434 (2008).

344. Nagaya, N. *et al.* Intravenous administration of mesenchymal stem cells improves cardiac function in rats with acute myocardial infarction through angiogenesis and myogenesis. *Am. J. Physiol. - Hear. Circ. Physiol.* **287**, H2670–H2676 (2004).
345. Galagudza, M. *et al.* Passive targeting of ischemic-reperfused myocardium with adenosine-loaded silica nanoparticles. *Int. J. Nanomedicine* **7**, 1671–1678 (2012).
346. Geelen, T., Paulis, L. E., Coolen, B. F., Nicolay, K. & Strijkers, G. J. Passive targeting of lipid-based nanoparticles to mouse cardiac ischemia-reperfusion injury. *Contrast Media Mol. Imaging* **8**, 117–126 (2013).
347. Verma, D. D., Levchenko, T. S., Bernstein, E. A., Mongayt, D. & Torchilin, V. P. ATP-loaded immunoliposomes specific for cardiac myosin provide improved protection of the mechanical functions of myocardium from global ischemia in an isolated rat heart model. *J. Drug Target.* **14**, 273–280 (2006).
348. Scott, R. C. *et al.* Targeting VEGF-encapsulated immunoliposomes to MI heart improves vascularity and cardiac function. *FASEB J.* **23**, 3361–3367 (2009).
349. Nobs, L., Buchegger, F., Gurny, R. & Allemann, E. Current methods for attaching targeting ligands to liposomes and nanoparticles. *J. Pharm. Sci.* **93**, 1980–1992 (2004).
350. McRae, A. & Dahlström, A. Transmitter-loaded polymeric microspheres induce regrowth of dopaminergic nerve terminals in striata of rats with 6-OH-DA induced parkinsonism. *Neurochem. Int.* **25**, 27–33 (1994).
351. Gill, S. S. *et al.* Direct brain infusion of glial cell line-derived neurotrophic factor in Parkinson disease. *Nat. Med.* **12**, 479–479 (2006).



# Appendix

## Authorisations

SPRINGER NATURE LICENSE TERMS AND CONDITIONS	SPRINGER NATURE LICENSE TERMS AND CONDITIONS
Jun 14, 2020	Jun 14, 2020
<p>This Agreement between Imperial college london -- Junyi Che ("You") and Springer Nature ("Springer Nature") consists of your license details and the terms and conditions provided by Springer Nature and Copyright Clearance Center.</p>	
License Number	4847631469482
License date	Jun 14, 2020
Licensed Content Publisher	Springer Nature
Licensed Content Publication	Nature
Licensed Content Title	Origin and physiological roles of inflammation
Licensed Content Author	Ruslan Medzhitov
Licensed Content Date	Jul 1, 2008
Type of Use	Thesis/Dissertation
Requestor type	academic/university or research institute
Format	electronic
Portion	figures/tables/illustrations
Number of figures/tables/illustrations	2
License Number	4847671084038
License date	Jun 14, 2020
Licensed Content Publisher	Springer Nature
Licensed Content Publication	Nature Reviews Immunology
Licensed Content Title	Neutrophil recruitment and function in health and inflammation
Licensed Content Author	Elzbieta Kolaczowska et al
Licensed Content Date	Feb 25, 2013
Type of Use	Thesis/Dissertation
Requestor type	academic/university or research institute
Format	electronic
Portion	figures/tables/illustrations

SPRINGER NATURE LICENSE TERMS AND CONDITIONS	ELSEVIER LICENSE TERMS AND CONDITIONS
Jun 14, 2020	Jun 14, 2020
<p>This Agreement between Imperial college london -- Junyi Che ("You") and Springer Nature ("Springer Nature") consists of your license details and the terms and conditions provided by Springer Nature and Copyright Clearance Center.</p>	
License Number	4847680068144
License date	Jun 14, 2020
Licensed Content Publisher	Springer Nature
Licensed Content Publication	Nature Medicine
Licensed Content Title	Infection-induced NETosis is a dynamic process involving neutrophil multitasking in vivo
Licensed Content Author	Bryan G Yipp et al
Licensed Content Date	Aug 26, 2012
Type of Use	Thesis/Dissertation
Requestor type	academic/university or research institute
Format	electronic
Portion	figures/tables/illustrations
License Number	4847730161540
License date	Jun 14, 2020
Licensed Content Publisher	Elsevier
Licensed Content Publication	Cell
Licensed Content Title	Anti-inflammatory Agents: Present and Future
Licensed Content Author	Charles A. Dinarello
Licensed Content Date	Mar 19, 2010
Licensed Content Volume	140
Licensed Content Issue	6
Licensed Content Pages	16
Start Page	935
End Page	950

JOHN WILEY AND SONS LICENSE TERMS AND CONDITIONS	
Jun 14, 2020	
This Agreement between Imperial college london -- Junyi Che ("You") and John Wiley and Sons ("John Wiley and Sons") consists of your license details and the terms and conditions provided by John Wiley and Sons and Copyright Clearance Center.	
License Number	4847830078713
License date	Jun 14, 2020
Licensed Content Publisher	John Wiley and Sons
Licensed Content Publication	Drug Development Research
Licensed Content Title	Viruses and their uses in nanotechnology
Licensed Content Author	Marianne Manchester, Maria J. Gonzalez, Pratik Singh
Licensed Content Date	May 11, 2006
Licensed Content Volume	67
Licensed Content Issue	1
Licensed Content Pages	19
Type of use	Dissertation/Thesis
Requestor type	University/Academic

JOHN WILEY AND SONS LICENSE TERMS AND CONDITIONS	
Jun 14, 2020	
This Agreement between Imperial college london -- Junyi Che ("You") and John Wiley and Sons ("John Wiley and Sons") consists of your license details and the terms and conditions provided by John Wiley and Sons and Copyright Clearance Center.	
License Number	4847751500364
License date	Jun 14, 2020
Licensed Content Publisher	John Wiley and Sons
Licensed Content Publication	Wiley Interdisciplinary Reviews - Nanomedicine and Nanobiotechnology
Licensed Content Title	Polymeric nanoparticles: the future of nanomedicine
Licensed Content Author	Justin L. Brown, Pouria Fattahi, Brittany L. Banik
Licensed Content Date	Aug 28, 2015
Licensed Content Volume	8
Licensed Content Issue	2
Licensed Content Pages	29
Type of use	Dissertation/Thesis

SPRINGER NATURE LICENSE TERMS AND CONDITIONS	
Aug 28, 2020	
This Agreement between Imperial college london -- Junyi Che ("You") and Springer Nature ("Springer Nature") consists of your license details and the terms and conditions provided by Springer Nature and Copyright Clearance Center.	
License Number	4897560795226
License date	Aug 28, 2020
Licensed Content Publisher	Springer Nature
Licensed Content Publication	Nature Nanotechnology
Licensed Content Title	Neutrophil-mediated anticancer drug delivery for suppression of postoperative malignant glioma recurrence
Licensed Content Author	Jingwei Xue et al
Licensed Content Date	Jun 19, 2017
Type of Use	Thesis/Dissertation
Requestor type	academic/university or research institute
Format	electronic
Portion	figures/tables/illustrations

ELSEVIER LICENSE TERMS AND CONDITIONS	
Jun 15, 2020	
This Agreement between Imperial college london -- Junyi Che ("You") and Elsevier ("Elsevier") consists of your license details and the terms and conditions provided by Elsevier and Copyright Clearance Center.	
License Number	4850261335753
License date	Jun 15, 2020
Licensed Content Publisher	Elsevier
Licensed Content Publication	Nanomedicine: Nanotechnology, Biology and Medicine
Licensed Content Title	The big picture on nanomedicine: the state of investigational and approved nanomedicine products
Licensed Content Author	Michael L. Etheridge, Stephen A. Campbell, Arthur G. Erdman, Christy L. Haynes, Susan M. Wolf, Jeffrey McCullough
Licensed Content Date	Jan 1, 2013
Licensed Content Volume	9
Licensed Content Issue	1
Licensed Content Pages	14